Improved 3D Ground Motion Simulation for Structural Response Analysis

Luis Alvarez Sanchez

Université Gustave Eiffel

Scuola Universitaria Superiore Pavia

Understanding and Managing Extremes

Thèse présentée en vue de l'obtention du titrede docteur en sciences de l'ingénieur de l'université Université Gustave Eiffel et de la scuola universitaria superiore Pavia

Luis Guillermo ALVAREZ-SANCHEZ

Improved 3D Ground Motion Simulation for Structural Response Analysis

Thèse dirigée par Luis Fabian BONILLA/Paolo BAZZURRO

Soutenu le 18/11/2022

M. Paolo BAZZURRO	Directeur de thèse
M. Luis Fabian BONILLA	Directeur de thèse
Mme. Celine GELIS	Examinatrice
M. Philippe GUEGUEN	Examinateur
M. Fernando LOPEZ-CABALLERO	Rapporteur
M. Adrian RODRIGUEZ-MAREK	Rapporteur
Mme. Paola TRAVERSA	Examinatrice
Mme. Irmela ZENTNER	Encadrante

Improved 3D Ground Motion Simulation for Structural Response Analysis

A Thesis Submitted in Partial Fulfilment of the Requirements

for the Degree of Doctor of Philosophy in

EARTHQUAKE ENGINEERING AND

ENGINEERING SEISMOLOGY

Obtained in the framework of the Doctoral Programme in

Understanding and Managing Extremes

by

Luis Guillermo Alvarez Sanchez

Supervisors:

Paolo Bazzurro PhD (IUSS Pavia)

Fabian Bonilla PhD (Université Gustave Eiffel)

Gloria Senfaute (EDF R&D)

Irmela Zentner PhD (EDF R&D)

November 2022

ABSTRACT

Stochastic ground motion simulation methods represent an attractive alternative to recorded acceleration time histories given the shortage of recorded ground motion from moderate to large magnitude events recorded in the vicinity of the seismic source, in particular when specific scenarios have to be considered. Their popularity relies in the need of relative few numbers of parameters, a comparatively simple formulation, and the successful examples when predicting the ground motion from past events. All these characteristics render these methodologies ideal for their application within an industrial context where computational times are more constrained. Nevertheless, to confidently use these simulated ground motions in realistic earthquake engineering applications, researchers and practitioners must exhaustively test the simulation methodologies. This with the intention of providing clarity not only on the thresholds of applicability of these techniques, but also on the possible bias that may be introduced in the consideration of these in lieu of recorded ground motions.

This thesis introduces a new 3D stochastic ground motion simulation method, obtained from the enhancement of state-of-the-art techniques available in the literature, and considering complementary models aiming to improve the description of the source and the spectral correlation structure of the simulated ground motions. First, the proposed technique is described in detail and assessed by means of a sensitivity analysis aiming to provide future users with a clear understanding of the simulation process and the overall importance of each input considered in the model. The proposed technique is then further evaluated by conducting a series of validations through seismological and earthquake engineering applications. These validations were achieved through a series of case studies assessing the capacity of simulated ground motions to describe the distributions of target metrics, i.e., Intensity Measures (IMs), Engineering Demand Parameters (EDPs) and Fragility curves derived from the response of simplified structural models, vis-à-vis those obtained with real ground motions. These analyses were conducted with special regard to the description of the variability related to the targeted metrics by modelling the epistemic uncertainty associated to the input parameters. Additionally, the case studies were used to showcase complementary procedures proposed for the calibration of the herein presented methodology. Results indicated that, with an appropriate calibration, the proposed simulation technique can reproduce the distributions of spectral accelerations and significant durations expected for the considered earthquake case study. The most accurate matching of the expected IMs distributions was found for simulations at short distance from the source and considering stiff soils. Finally, the consideration of simulated ground

motion for the estimation of structural response shows almost negligible biases, with respect to that obtained with recorded ground motions, when enforcing hazard consistency in the distributions of IMs relevant for the considered EDPs.

Keywords: Stochastic ground motion simulation, ground motion record selection, single building seismic risk assessment, iterative calibration procedures, hazard consistency, epistemic uncertainty modelling

RESUME

Les méthodes de simulation stochastique du mouvement du sol représentent une alternative attrayante aux séries temporels d'accélération enregistrés, étant donné le manque de mouvement du sol enregistré à partir d'événements de magnitude modérée à grande enregistrés à proximité de la source sismique, en particulier lorsque des scénarios spécifiques doivent être considérés. Leur popularité repose sur la nécessité d'un nombre relativement faible de paramètres, une formulation relativement simple et des exemples réussis de prédiction du mouvement du sol à partir d'événements passés. Toutes ces caractéristiques rendent ces méthodologies idéales pour leur application dans un contexte industriel où les temps de calcul sont plus contraints. Néanmoins, pour utiliser en toute confiance ces mouvements du sol simulés dans des applications réalistes de génie sismique, les chercheurs et les praticiens doivent tester de manière exhaustive les méthodologies de simulation. Ceci dans le but de clarifier non seulement les seuils d'applicabilité de ces techniques, mais aussi les biais possibles qui peuvent être introduits dans la prise en compte de ces mouvements au lieu des mouvements du sol enregistrés.

Cette thèse introduit une nouvelle méthode de simulation stochastique 3D des mouvements du sol, obtenue à partir de l'amélioration des techniques de pointe disponibles dans la littérature, et en considérant des modèles complémentaires visant à améliorer la description de la source et la structure de corrélation spectrale des mouvements du sol simulés. Tout d'abord, la technique proposée est décrite en détail et évaluée au moyen d'une analyse de sensibilité visant à fournir aux futurs utilisateurs une compréhension claire du processus de simulation et de l'importance globale de chaque entrée considérée dans le modèle. La technique proposée est ensuite évaluée en effectuant une série de validations par le biais d'applications sismologiques et de génie parasismique. Ces validations ont été réalisées par une série d'études de cas évaluant la capacité des mouvements de sol simulés à décrire les distributions des paramètres cibles, c'est-à-dire les mesures d'intensité (IM), les paramètres de demande d'ingénierie (EDP) et les courbes de fragilité dérivées de la réponse des modèles structurels simplifiés, par rapport à celles obtenues avec des mouvements de sol réels (enregistrées). Ces analyses ont été menées avec une attention particulière à la description de la variabilité liée aux métriques ciblées en modélisant l'incertitude épistémique associée aux paramètres d'entrée. De plus, les études de cas ont été utilisées pour présenter les procédures complémentaires proposées pour la calibration de la méthodologie présentée ici. Les résultats indiquent que, avec une calibration appropriée, la technique de simulation proposée peut reproduire les distributions des accélérations spectrales et des durées significatives attendues pour l'étude de cas de tremblement de terre considérée. La correspondance la plus précise des distributions des IMs attendues a été trouvée pour les simulations à courte distance de la source et en considérant des sols rigides. Enfin, la prise en compte du mouvement du sol simulé pour l'estimation de la réponse

structurelle montre des biais presque négligeables, par rapport à ceux obtenus avec les mouvements du sol enregistrés, lorsque l'on applique la cohérence des aléas dans les distributions des IMs pertinentes pour les EDPs considérés.

Mots clés : Simulation stochastique du mouvement du sol, sélection des enregistrements du mouvement du sol, évaluation du risque sismique pour un seul bâtiment, procédures de calibrage itératives, cohérence du risque, modélisation de l'incertitude épistémique.

RESUME LONG

L'enregistrement continu des tremblements de terre dans le monde entier a fourni aux chercheurs des données précieuses pour mieux comprendre et modéliser la physique du mouvement du sol et sa probabilité d'occurrence sur un site donné. D'un point de vue pratique, les séries temporels d'accélération, également appelés enregistrements, représentent un élément constitutif de nombreuses applications du génie sismique et de la sismologie d'ingénierie. L'une d'entre elles est l'analyse du risque sismique, où les enregistrements fournissent le lien entre le alea, généralement représenté par les résultats de l'analyse probabiliste du risque sismique, souvent appelée PSHA, et l'analyse de la réponse dynamique des structures et des systèmes. Ce lien est créé en faisant correspondre les distributions des mesures d'intensité du mouvement du sol cible (IM) obtenues à partir de l'ensemble des enregistrements sélectionnés, et celles potentiellement causées par les scénarios de séisme contribuant le plus à l'aléa sur le site. Généralement, le spectre uniforme des risques, UHS, calculé à partir des accélérations spectrales obtenues à partir du PSHA, est considéré comme la mesure d'intensité cible, cependant, différentes méthodologies ont été développées en considérant d'autres mesures d'intensité dans les algorithmes de sélection.

L'une des principales limites de ces procédures est qu'elles sont directement conditionnées par la disponibilité d'enregistrements qui pourraient modéliser collectivement la distribution des IM attendus dans la zone d'intérêt. Cette hypothèse n'est souvent pas satisfaite car les bases de données locales sur les mouvements du sol ne sont pas alimentées pour toutes les gammes de scénarios qui peuvent être intéressants, ce qui oblige les utilisateurs à sélectionner des séries temporelles avec différentes caractéristiques de mouvements du sol, c'est-à-dire différentes conditions de site, magnitude, régime tectonique, distance à la rupture, etc. Cette pratique entraîne une perte de causalité entre le scénario du mouvement du sol d'intérêt et les enregistrements sélectionnés. Si le IM, ou le vecteur de IM, considéré pour la sélection des enregistrements n'est pas suffisant, dans le sens où les paramètres d'ingénierie de la demande (EDP) qui lui sont conditionnés dépendent également d'autres caractéristiques du mouvement du sol, la perte de causalité pourrait entraîner l'estimation de réponses structurelles biaisées. Pour surmonter ces obstacles, et bien d'autres, les chercheurs se sont concentrés sur le développement et l'amélioration continue des méthodologies de simulation des mouvements du sol.

Les méthodes de simulation stochastique du mouvement du sol représentent une alternative attrayante étant donné le manque de mouvements du sol enregistrés à partir d'événements de magnitude modérée à grande enregistrés à proximité de la source sismique, en particulier lorsque des scénarios spécifiques doivent être considérés. Leur popularité repose sur la nécessité d'un nombre relativement faible de paramètres, d'une formulation relativement simple et d'exemples réussis de prédiction du mouvement du sol à partir d'événements passés. Toutes ces caractéristiques rendent ces méthodologies idéales pour leur application dans un contexte industriel où les temps de calcul sont plus contraints. Néanmoins, pour utiliser en toute confiance ces mouvements du sol simulés dans des applications réalistes de génie sismique, les chercheurs et les praticiens doivent tester de manière exhaustive les méthodologies de simulation. Ceci dans le but de clarifier non seulement les seuils d'applicabilité de ces techniques, mais aussi les biais possibles qui peuvent être introduits dans la prise en compte de ces mouvements au lieu des mouvements du sol enregistrés.

Cette thèse introduit une nouvelle méthode de simulation stochastique 3D des mouvements du sol, obtenue à partir de l'amélioration des techniques de pointe disponibles dans la littérature, et en considérant des modèles complémentaires visant à améliorer la description de la source et la structure de corrélation spectrale des mouvements du sol simulés. Le modèle proposé comprend une représentation révisée de la source, avec un modèle cinématique de la rupture et une définition de pointe de la fréquence de coin dynamique et du facteur de normalisation de l'énergie. De plus, une procédure de post-traitement a été proposée pour inclure la structure de corrélation inter-fréquence remarquée dans les bases de données de mouvements du sol enregistrés. Cette procédure, basée sur des propositions existantes, a été étendue aux simulations 3D et à la prise en compte de la structure de corrélation entre les amplitudes spectrales des différentes composantes du mouvement. La technique proposée a ensuite été évaluée au moyen d'une analyse de sensibilité visant à fournir aux futurs utilisateurs une compréhension claire du processus de simulation et de l'importance globale de chaque entrée considérée dans le modèle. Les résultats obtenus ont montré que la chute de contrainte, utilisée dans la construction du spectre de la source, est le paramètre le plus influent dans la définition du spectre du mouvement du sol. De plus, il a été observé que lorsque l'on considère différentes distributions de glissement, l'utilisation d'un facteur de normalisation de l'énergie produit des valeurs moyennes de Spectre des Amplitudes de Fourier (FAS) proches, mais que les simulations individuelles peuvent fortement différer, en particulier si l'emplacement de l'hypocentre varie également.

Une série de validations par le biais d'applications sismologiques et de génie parasismique a été réalisée pour tester la technique de simulation proposée. Ces validations ont été réalisées à travers une série d'études de cas évaluant la capacité des mouvements de sol simulés à décrire les distributions des métriques cibles, c'est-à-dire les IMs, les EDPs et les

courbes de fragilité dérivées de la réponse de modèles structurels simplifiés, par rapport à celles obtenues avec des mouvements de sol réels. Ces analyses ont été menées avec une attention particulière à la description de la variabilité liée aux métriques ciblées en modélisant l'incertitude associée aux paramètres d'entrée (épistémique). Plus précisément, les applications réalisées ont considéré des calibrations basées sur la comparaison entre des mouvements de sol simulés et de référence, ciblant non seulement le contenu spectral des mouvements de sol, mais aussi ses caractéristiques temporelles, comme la description des fenêtres de modulation temporelle, par exemple. En d'autres termes, les études de cas ont été utilisées pour présenter les procédures complémentaires proposées pour la calibration de la méthodologie présentée ici.

Le premier exercice de validation, également appelé validation sismologique, a évalué la capacité des mouvements du sol simulés à reproduire les distributions des IMs prédites par des Modèles de Mouvement du Sol (GMMs) valides pour une étude de cas définie. La validation comprenait également la comparaison des IMs et des formes d'onde par rapport à un événement de référence correspondant aux paramètres causaux de l'étude de cas considérée. Deux ensembles de simulation différents ont été considérés dans la validation, l'un considérant les variables d'entrée trouvées dans la littérature (ensemble A) et l'autre considérant les entrées dérivées de l'inversion spectrale des données locales (ensemble B). La prise en compte de deux ensembles différents avait pour but d'étudier la technique d'inversion spectrale comme une alternative au manque de données d'entrée, par exemple, dans des régions à faible sismicité ou mal caractérisées. Les résultats ont indiqué que, avec une calibration appropriée, la technique de simulation proposée peut reproduire les distributions de différents IM d'intérêt, comme les accélérations spectrales et les durées significatives attendues pour l'étude de cas de séisme considérée. En outre, en considérant la description spécifique des fenêtres de modulation temporelle, les historiques temporels des accélérations simulées correspondent aux observations des mouvements du sol enregistrés correspondant à l'étude de cas considérée. En comparant la mesure de validation communément utilisée de l'accélération spectrale à différentes périodes de vibration, il a été observé que la correspondance la plus précise, pour les composantes horizontales du mouvement, a été trouvée pour les simulations à courte distance de la source et en considérant des sols rigides. En considérant la composante verticale du mouvement du sol, on a remarqué que les simulations surestimaient systématiquement les modèles de référence du mouvement du sol et les mouvements du sol observés.

L'utilisation de mouvements de sol simulés pour l'estimation de la réponse structurelle a été réalisée dans un cadre d'évaluation des risques pour un seul bâtiment. Plus précisément, cette validation a consisté à évaluer l'adéquation de l'utilisation de mouvements de sol simulés à la place ou, mieux, en plus des enregistrements réels pour calculer les courbes de

fragilité spécifiques au site basées sur les spectres conditionnelles (CS). Les résultats ont été présentés à l'aide d'une étude de cas où une série de structures ont été supposées être situées sur un site rocheux en Italie centrale. Les structures ont été modélisées comme des systèmes d'un seul dégrée de liberté (SDoF) non linéaires avec différentes périodes fondamentales de vibration et avec deux modèles hystérétiques de matériaux alternatifs. La validation s'est concentrée sur la comparaison des EDP et des courbes de fragilité, calculées par une analyse dynamique non linéaire alimentée par des mouvements de sol réels et synthétiques. Ces derniers ont été sélectionnés sur la base de l'approche CS originale axée sur le contenu spectral et d'une variante de celle-ci, qui renforce également de manière explicite la cohérence des risques de la durée du mouvement du sol. Dans l'ensemble, la prise en compte de mouvements du sol simulés pour l'estimation de la réponse structurelle présente des biais presque négligeables par rapport à ceux obtenus avec des mouvements du sol enregistrés, lorsque l'on applique la cohérence des aléas dans les distributions des IMs pertinentes pour les EDPs considérées.

ACKNOWLEDGEMENTS

This PhD thesis embodies the product of four very formative years of my life. Not only have I been able to pursue academic and professional aspirations, but also to grow, on a personal level, in aspects I would have never imagined. Of course, this wouldn't have been possible without the support of countless persons I have met in these last years, and whom I would like to acknowledge in this section.

First, I would like to thank my supervising committee, Fabian Bonilla, Paolo Bazzurro, Gloria Senfaute, and Irmela Zentner. I am most grateful for the opportunity you gave me in selecting me for this project. Your dedication, patience and guidance were vital in the development of this thesis and has had a great impact in the way that I see my career and life. Additionally, I would like to thank all my colleagues, both at EDF R&D and IUSS-Pavia, for their support and fraternity during this period of our lives. Special mentions to "Les Fils", Nevena and Pablo.

Outside of work, I would like to thank the countless people that have been there to share a word, an advice, laughs, sadness or just time. There are so many of you I couldn't write enough theses to acknowledge you contribution. Still, I would like to specially thank Ade, Marco, Josue, Camilo, Rocio, Fausto, Andres, Basar, Petros, Mo, Marti, and Viola. You were fundamental during these past years, and I will always remember fondly the time we spent together. I would also like to specially thank Camilla, whose dedication and kindness are an inspiration to me.

Finally, I would like to thank my family. To my brother, thank you for believing in me regardless of the size of the challenge, and to my mom and my dad, whose unconditional love and support has always given me the confidence to chase my dreams.

TABLE OF CONTENTS

LIST OF FIGURES

LIST OF TABLES

LIST OF SYMBOLS AND ACRONYMS

$a_i^w{}_d$	= Acceleration time history for wave type w, sub-fault i, and component d
$A^w{}_i$	= Attenuation for wave type w, sub-fault i
AI	= Arias Intensity
Amp	= Amplitude Spectrum of the Fourier Transform for the inclusion of the correlation structure
AS16	= Afshari and Stewart (2016) Ground Motion Model for significant durations
COV	= Coefficient of variation (mean/standard deviation)
CS	= Conditional Spectrum
ς	= Covariance Matrix for the FAS of the different components of simulated ground motions
$C^w{}_{i_d}$	= Scaling constant for wave type w, sub-fault i, and component d
C_y	= Yield base shear coefficient
D	= High-frequency attenuation function
D_{i-f}	= Significant duration between the instants where i and j percentage of the Arias intensity are met
EP^w	= Energy partition factor for wave type w
EDP(s)	= Engineering Demand Parameter(s)
EPMF	= Empirical Probability Mass Function
ESM	= Engineering Strong Motion Database
f	= Frequency
f_{c0}	= Static corner frequency
$f_c^w{}_i$	= Dynamic corner frequency for wave type w, sub-fault i
f_{max}	= Cut-off frequency for the attenuation of high frequencies

f_{Tgm} = Factor modelling the elongation of the modulating function

FS^w = Free surface factor for wave type w

F_y = Yield base shear

FAS = Fourier Amplitude Spectrum(a)

G = Geometrical Spreading function

GCIM = Generalized Conditional Intensity Measure

GIT = Generalized Inversion Technique

GM = Geometrical mean of the horizontal components

GMM(s) = Ground Motion Model(s)

HVSR = Horizontal to Vertical FAS ratio

H_i^w = Energy normalization factor for wave type w, sub-fault i

IM(s) = Intensity Measure(s)

IML(s) = Intensity Measure Level(s)

LHS = Latin Hypercube Sampling

κ_0 = Slope of the high frequency attenuation

M = Frequency dependent exponent for the estimation quality factor

M_0 = Seismic Moment

M_{0_i} = Seismic Moment assigned to sub-fault *i*

M_{0ave} = Average seismic moment in the finite-fault source model

M_w = Moment Magnitude

M_{JMA} Japanese Meteorological Scale

MDoF(s) = Multi Degree of Freedom System(s)

N = Number of sub-faults in the finite-fault source model

$N_{records}$ = Number of records in a group (calibration or record selection)

n = Geometrical attenuation exponent

n_{RIK} = Integer fractions of sub-faults for the fractal distribution of the slip

NLTHA = Nonlinear Time History Analysis

PBEE = Performance Based Earthquake Engineering

PGA = Peak Ground Acceleration

PGD = Peak Ground Displacement

PGV = Peak Ground Velocity

PoE = Probability of Exceedence

PSHA = Probabilistic Seismic Hazard Analysis

Phase = Phase Spectrum of the Fourier Transform for the inclusion of the correlation structure

Q^w = Quality factor for wave type w

Q_0 = Base S-wave quality factor

q = Behaviour factor

r_i = Sub-fault i -to-reciever distance

R_0 = Reference distance for attenuation of seismic waves

RP^w = Average radiation pattern for wave type w

RDB = Reference Database

RIK = Ruiz Integral Kinematic Method

RMSA = Root-Mean-Square Average

$R_{sub-fault}$ = Sub-fault radius for fractal distribution of the slip

SA_H =Spectral acceleration of the GMRot50 component in the computation of the spectral correlation structure

SA_V =Spectral acceleration of the vertical component in the computation of the spectral correlation structure

SA_{Hx} =Spectral acceleration of the EW component in the computation of the spectral correlation structure

SA_{Hy} =Spectral acceleration of the NS component in the computation of the spectral correlation structure

$Sa(T)$ = Spectral acceleration at period T

S_0 = White noise with normalized power spectral density

$S^w{}_i$ = Source spectrum for wave type w and sub-fault i

s_i = Slip at sub-fault i

SCEC = Southern California Earthquake Center

SDB = Simulated database

SDoF(s) = Single Degree of Freedom System(s)

SNR = Signal to Noise ratio

SPDF = Spatial Probability Density Functions

SSE = Sum of the Squared Errors

$t_{i,distance}$ = Path-related duration for sub-fault i

$t_{i,source}$ = Source-related duration for sub-fault i

$\Delta t_{i_d}^w$ = Time delay for sub-fault *i*, wave type *w* and component *d*

$\Delta t_{i,rupture}$ = Rupture-related time delay for sub-fault *i*,

$\Delta t_{i,travel}^w$ = Travel-related time delay for sub-fault *i*, and wave type *w*

T = Period of vibration

T_1 = Fundamental period of vibration

T* = Conditioning period

T_{gm} = Duration of the ground motion for computation

$U_i^w{}_d$ = Mean simulated ground motion spectrum for wave type w, sub-fault i, and component d

UD = Vertical component

UHS = Uniform Hazard Spectrum

Vs_{30} = Average shear wave propagation velocity of the upper 30m

W = Fault width

w = Wave type (S or P)

$weight_i$ = Weight factor considered in the calibration process

$Z^w{}_{i_d}$ = Source effect for wave type w, sub-fault i, and component d

α = P-wave propagation velocity at the depth of the source

β = S-wave propagation velocity at the depth of the source

δ = Fault dip angle

$\delta S2S_s$ = Site-specific residuals

δB_e = Between-event residuals

λ = Fault rake angle

θ_i = Incidence angle, measured from the vertical for sub-fault i

φ_i = Azimuth angle for sub-fault I and measured with respect to the observation point

Π = Number of points in the Fourier transform for the inclusion of the correlation structure

Γ = Random vector for the inclusion of the correlation structure

ε = Intra-event residual

$\bar{\xi}$ = Average bias

ϕ = Intra-event uncertainty

τ = Inter-event uncertainty

Ψ = Weight

Ω = Overstrength factor

δ_y = Yield displacement

μ = Ductility

$\mu_{ln(Sa)}$ = Natural logarithm of the mean GMM prediction

ρ = Linear correlation factor

ρ_i = Density of the medium at sub-fault i

ρ_{H-z} = Correlation coefficient between the residuals obtained from the spectral acceleration of the horizontal and vertical components

ρ_{x-y} = Correlation coefficient between the residuals obtained from the spectral acceleration of the EW and NS components

υ_i = Wave propagation velocity for sub-fault i, and for the computation of the seismic wave attenuation

ω = Saragoni and Hart modulating function

$\Delta\sigma$ = Stress drop

3D = Tricomponent

1. INTRODUCTION

1.1 BACKGROUND AND MOTIVATION

The continuous recording of earthquakes all over the world has provided researchers with valuable data to better understand and model the physics of earthquake ground motion and its probability of occurrence at a given site. From a practical point of view, acceleration time histories, also referred to as records, represent a constituent input to many earthquake engineering and engineering seismology applications. One of these is seismic risk analysis, where records provide the link between hazard, usually represented through the results of Probabilistic Seismic Hazard Analysis, often referred to as PSHA (Cornell, 1968), and dynamic response analysis of structures and systems, (Bradley et al., 2015). This link is created by matching the distributions of target ground motion Intensity Measures (IMs) obtained from the set of selected records, and those potentially caused by earthquake scenarios most contributing to the hazard at the site. Typically, the Uniform Hazard Spectrum, UHS, computed from the spectral accelerations obtained from the PSHA, is considered as target IM, however, different methodologies have been developed considering other IMs in the selection algorithms, e.g., (Bradley, 2010)

One of the main limitations of such procedures is that they are directly conditioned on the availability of records that could collectively model the distribution of IMs expected at the area of interest. This assumption is often not met as local ground motion databases are not populated for all ranges of scenarios that may be of interest, thus forcing users to the selection of time histories with different ground motion features, i.e., different site conditions, magnitude, tectonic regime, distance to rupture, etc. This practice results in the loss of causality between the ground motion scenario of interest and the selected records. If the IM, or vector of IMs, considered for record selection is not a sufficient one, in the sense that engineering demand parameters (EDPs) conditioned to it are also dependent on other ground motion features, the loss of causality could result in the estimation of biased structural responses. To overcome these obstacles, and many others, researchers have focused on the development and continuous improvement of Ground Motion Simulation Methodologies.

Different methods have been proposed in the literature for simulating ground motion, as reviewed in Douglas & Aochi (2008). The classification of these varies from one author to the other and depending on different criteria, therefore, for the purposes of this research, and for the sake of simplicity, ground motion simulation methodologies were classified within one of three general categories, namely: Deterministic, Stochastic, and Hybrid methods.

Deterministic ground motion simulation methods, also referred to as physics-based, compute the ground motion considering numerical models that explicitly incorporate the physics of the fault rupture and seismic wave propagation, (Tsioulou et al., 2019). These methodologies consider the rupture of the fault, either through kinematic or dynamic models, and include 3D wave propagation from the source to the site, e.g., Olsen et al. (2009), Aochi & Ulrich (2015), Paolucci et al. (2015), Valentová et al., (2021), and many others. Even though these methodologies are regarded as the most accurate in terms of representation of the earthquake physical phenomenon, the frequency band and number of simulated scenarios are often limited by the heavy computational costs associated with the resolution of the fault rupture and wave propagation models. Additionally, the extensive input information required for the full characterization of the model limits their use to very well-characterized regions.

Stochastic methods model ground motion time histories as a windowed-filtered random noise. These methodologies are based on the notion that high frequencies in earthquake ground motions display a random behavior that can be modeled in the time and frequency domain, (Boore, 2003). Initial proposals were not linked to any geophysical parameter and resulted in frequency-stationary time histories often characterized by an unreasonable energy content when compared to recorded ground motions, e.g., Saragoni & Hart (1973), Vanmarcke & Gasparini (1977). Some improvements, especially the parametric modelling of the earthquake source, attenuation, site conditions, and resulting in nonstationary time series were proposed in response to these deficiencies, e.g., Beresnev & Atkinson, (1997); Boore, (1983)(2003); Motazedian & Atkinson,(2005); Otarola & Ruiz, (2016); Papageorgiou & Aki, (1983), and many others. Current simulation techniques have been proven to accurately represent the high-frequency content of earthquake ground motion at a very low computational cost, yet the simplicity of their underline models often results in a misrepresentation of the low-frequency content. Moreover, the consideration of a random phase in the representation of the acceleration time histories results in the omission of the correlation structure noticed in the Fourier Amplitude Spectrum (FAS) of earthquake ground motion.

Finally, a combination of deterministic and stochastic methods, seeking to employ both models in the frequency ranges where they are most effective, i.e., physic-based for the low frequency and Stochastic for the high frequency, results in a hybrid ground motion

simulation technique. The simulation is constructed by splicing the FAS of these different simulations at a selected frequency. Some examples of such methods are: Graves & Pitarka, (2010); Kamae et al., (1998); Pacor et al., (2005). Even though these models benefit from the advantages of both Physics-based and Stochastic methods, these are still susceptive to their limitations. For example, the same detailed information and computational cost associated with Physics-based simulations. Additionally, the selection of the splicing frequency remains somewhat arbitrary. This frequency is usually selected at a middle frequency range, i.e., 0.5 – 2 Hz, for which neither Physics-based nor Stochastic simulations provide an accurate representation, (Motazedian & Atkinson, 2005).

The use of any of the previously mentioned categories of simulation methodologies depends on the specific application at hand. However, because earthquake ground motion is subject to high uncertainties, the generation of large numbers of simulations aiming to capture the inherent variability of the phenomenon is often an important consideration in the selection of a ground motion simulation method. For this reason, and because computational resources are often limited, stochastic methods are often chosen by practitioners in need of simulated time histories. Hence, the development and validation of new accurate stochastic ground motion simulation methodologies, capable of generating realistic time histories considering most of the physics describing the earthquake process, gains importance.

1.2 SCOPE

The work presented in this thesis aims to the development and assessment of a physically sound, yet computationally efficient, stochastic ground motion simulation technique. In this context, computational efficiency refers to the capacity of the method to generate many simulations in a reasonable amount of time, whereas physical sanity refers to the correspondence of the technique with state-of-the-art models available in the research world for the characterization of the earthquake ground motion.

The proposal of the Stochastic Simulation Methodology herein presented was based on the study and improvement of a recent 3D stochastic ground motion simulation methodology introduced in Otarola & Ruiz, (2016) and S. Ruiz et al., (2018). The modifications made to the existent methodology aim to improve common deficiencies in stochastic methodologies, specifically in the modelling of the fault rupture mechanism and the correlation structure of the FAS at different frequencies.

Validation of the proposed technique was addressed in two different approaches. A seismological approach, where the distributions of IMs obtained from simulated ground motions were compared to reference Ground Motion Models, GMMs, and observations, for a case study. Complementary, a so-called engineering validation was also considered

in the assessment of the proposed simulation technique. This validation focused on the comparison of responses and fragility curves for pre-defined damage states obtained within a seismic risk assessment framework for a case study. Specifically, this section compares the responses and fragility curves obtained from sets of like records selected (and scaled) from a database of simulated and recorded ground motions.

1.3 THESIS OUTLINE

The main body of this thesis is formed around three manuscripts currently under review in first-tier peer-reviewed international journals. Readers are advised to keep this in mind since, to aid in the standalone clarity of each of the main four chapters, some statements may seem repetitive throughout the entire document. Furthermore, with the same purpose of aiding in clarity while avoiding repetitiveness, the literature review of the state-of-the-art for each topic was included in the introduction sections of their respective chapters.

Chapter 1: Introduction. This chapter provides the reader with background and motivation for the conducted research. The scope of the thesis is also stated in this chapter, briefly introducing an overview of each of the chapters forming the document.

Chapter 2: Three-dimensional Ground Motion Simulation Technique. This chapter introduces the simulation technique proposed in this thesis, emphasizing the changes with respect to the original technique introduced in Otarola & Ruiz, (2016) and Ruiz et al., (2018). Furthermore, this chapter includes a qualitative assessment and a full sensitivity study of the technique and its input parameters. This chapter is based on the manuscript entitled "***Assessment of 3D Stochastic Ground Motion Simulation Technique***", which is under review for publication in the Journal of Geophysics International, (Alvarez et al., 2022).

Chapter 3: Seismological validation of the 3D Stochastic Simulation technique – Ground Motion Prediction. This chapter presents a validation of the ground motion simulation technique for ground motion prediction purposes from a seismological point of view. The validation focuses on the comparison of distributions of IMs obtained from sets of simulated ground motions and predictions from valid GMMs for a case study matching a past earthquake scenario. Special attention is given to the calibration of the model and the propagation of the uncertainty from input to estimated IMs. This chapter is based on the manuscript entitled "***3D Stochastic Ground Motion Prediction for an event in the region of Niigata, Japan***", which is in preparation for publication in the Journal of Geophysics International.

Chapter 4: Engineering validation of the 3D Stochastic Simulation technique. This chapter presents a validation of the ground motion simulation technique within a state-of-the-art seismic risk assessment framework. This chapter focuses on the comparison of EDPs, and fragility curves obtained from the Nonlinear Time History Analysis (NLTHA)

of sets of records selected from a database of recorded and simulated records. The comparisons were performed for a case study considering different sets of simplified structures modelled as Single Degree of Freedom Systems (SDoFs) with different fundamental periods of vibration and constituent models. This chapter is based on the manuscript entitled "***A Closer Look at Hazard-Consistent Ground Motion selection for Building-Specific Risk Assessment: Part II: Use of Simulated Ground Motions***", which is in preparation for publication in the Earthquake Spectra journal.

Finally, Chapter 5: Overall Conclusions and Future Developments, serves as a summary of the main findings of the overall research, taking the key points and insights from each of the chapters in the thesis. Also, it summarizes a series of recommendations for further development based on the identified points of improvement of the herein presented work.

2.THREE-DIMENSIONAL STOCHASTIC GROUND MOTION SIMULATION TECHNIQUE

2.1 INTRODUCTION

Ground motion simulation is an active research field in seismology and earthquake engineering fields. Both communities rely on data in the form of time histories, or records, to improve the prediction of ground motion and to analyze engineering systems of interest, respectively. Yet, enough data is still missing, specifically for scenarios largely needed in the design of structures, i.e., moderate to large magnitude events recorded at close distances from the active source. In this context, stochastic ground motion methods represent an interesting alternative due to their overall capacity to accurately model the high-frequency content (> 1 Hz) of earthquake ground motion with a considerably low computational cost, (Otarola & Ruiz, 2016). This last feature becomes vital for cases where many scenarios are required in the representation of the uncertainty related to the earthquake phenomenon, (al Atik et al., 2010), more so for applications within the industry where time and resources are limited.

Arguably, stochastic simulation methods may be looped into one of two categories. Source-based methods, which model the fault rupture and propagation of the seismic waves, explicitly accounting for source path and site effects. Site-based methods, on the other hand, generate ground motion by fitting a stochastic process to a target spectrum implicitly including the source, path, and site characteristics, (Douglas & Aochi, 2008). Historically speaking, source-based methods have been mostly considered by the seismological community because the meaningful parameters used in the definition of the source, attenuation, and site effects can be inferred from data, thus resulting in the improvement of the understanding of the underlying processes of strong ground motion generation and attenuation. This feature, however, also becomes of importance for the engineering community since ground motion variability, directly affecting the derivation of fragility curves, may be directly linked to the uncertainty of the entry parameters considered by the simulation technique. For this reason and recognizing the importance of directly representing the physics of the earthquake phenomenon in the generation of realistic simulated ground motion, this work focuses on source-based stochastic methods.

Source-based Stochastic Ground Motion Simulation methods originate from the pioneering work of Hanks & Kanamori, (1979); Hanks & McGuire, (1981); McGuire & Hanks, (1980). In their work, the authors simulate ground motion by combining the FAS of strong ground motion, obtained from seismological models, with a random phase spectrum, obtained from a band-limited Gaussian white noise with a finite duration. Initially, these simulation methodologies were conceived to model far-field ground motions where the earthquake source may be considered as a point source. Boore, (1983) for example, constructs the acceleration FAS of the SH component of ground motion as a function of magnitude and distance, the method considers an instantaneous shear dislocation at a point and describes its spectrum based on the omega square model ($\boldsymbol{\omega^2}$), as defined in Aki (1967)and Brune (1970). Propagation of the seismic waves is modelled by means of semi-empirical relations considering the geometrical and anelastic attenuation, and the effects of the site are considered through filters modelling the crustal amplification, and high-frequency decay noticed in recorded ground motion. Papageorgiou and Aki (1983), on the other hand, considered a different model for the source spectrum relying on regional calibrations for the estimation of the corner frequency, yet contemplating attenuation and site effects in the same approximate manner. These initial models, however, were not accurate for the simulation of near-source earthquake scenarios. Furthermore, the consideration of a single source spectrum resulted in frequency-stationary simulations.

Beresnev & Atkinson (1997) introduced the finite-fault source model with the intention to include source geometry effects into the modelling of the source. Based on the scaling concept, dictating that a large earthquake could be modelled as the cumulative effect of smaller events, the finite-fault source considers the fault to be discretized into an array of sub-faults modelled as point sources. The ground motion is then constructed by adding the contribution of each sub-fault at the receptor, accounting for the phase lag produced by fault rupture and wave propagation. Motazedian & Atkinson (2005) further improved the finite fault model by including a dynamic corner frequency and a normalization factor. In their proposal, the authors defined the variation of the corner frequency to be inversely proportional to the ruptured area at each instant of the simulation process, i.e., number of active sub-faults during the propagation of the rupture. The normalization factor, on the other hand, was proposed to guarantee the conservation of the radiated energy and to remove the dependence of the simulation technique on the discretization of the fault. Since then, the finite-fault method has been continuously revised to address limitations on its application for earthquake engineering purposes, for example, Atkinson et al., (2009) and Boore (2009) compared estimations of point source and finite-fault models for the estimation of far-field ground motions resulting in the adaptation of the low-frequency content of the latter. Moreover, the relevance of the finite-fault simulation methodology led to its inclusion in the Southern California Earthquake Centre (SCEC) Broad Band simulation platform, (Atkinson & Assatourians, 2015); an open-source

software distribution that enables third-party users to compute broadband synthetic ground motions for engineering applications.

More recently, Otarola & Ruiz (2016) modified the finite fault method by including the FAS of the complete body-wave field spectra. The authors considered a stratified velocity model, incident and azimuthal angles, and free surface and energy partition factors to incorporate the P and SV waves in the simulation. Overall, the FAS of each body wave is computed following the same principles of the finite-fault method, i.e., considering the contribution of the source, path, and site-effects. The FAS are then decomposed based on the azimuth of each sub-source with respect to the receptor and summed into the three orthogonal components, i.e., North – South, East – West, Up-Down. Even though current stochastic methodologies have dramatically improved, simulated ground motions still present deficiencies that limit their use in earthquake engineering applications. For example, (i) the use of Gaussian white noise for the modelling of the random phase spectrum results in the miss-representation of the correlation structure noticed in the FAS at different frequencies, e.g., Bayless & Abrahamson, (2018)(2019); Bijelić et al., (2018), and (ii) the simplistic representation of source rupture results in simulation methods incapable of representing important ground motion features, specifically in the low and intermediate frequency range.

This chapter introduces an improved 3D Stochastic Ground Motion Simulation technique based on the work presented in Otarola & Ruiz (2016). The proposed technique addresses the deficiencies of the original proposal with the intention of improving its performance in the representation of earthquake scenarios to be used in seismic risk analysis. Additionally, this chapter presents an assessment of the simulated ground motions. The assessment includes the qualitative study of the simulated waveforms, a sensitivity study of the input parameters of the model aiming to provide future users a complete understanding of the herein presented simulation technique, and finally an evaluation of the improvements to the base simulation technique included in this work.

2.2 3D STOCHASTIC GROUND MOTION SIMULATION METHOD

Stochastic ground motion simulation methods, such as those described and compared in Atkinson et al. (2009), construct synthetic acceleration time histories assuming that the high-frequency motions are basically random, at least for frequencies higher than 1 Hz (Boore, 2003). These methods work in the frequency domain and model the FAS as a convolution of modulated noise with a random phase and a mean ground motion spectrum:

$$FAS = U(f, r_i, M_{0_i})\sqrt{S_0} \qquad \textbf{Equation 2.1}$$

Where U is the mean simulated ground motion spectrum, S_0 is the white noise with normalized power spectral density, f is the frequency, r_i is the sub-fault-receiver distance,

and M_{0_i} is the source seismic moment. The index "*i*" represents the ith-source (sub-fault) when modelling a finite fault, which is represented by the contribution of ground motions produced by discretized sub-faults composing the main fault structure.

2.2.1 Mean simulated ground motion spectrum ($\boldsymbol{U}$)

The definition of the mean simulated ground motion spectrum, for wave type w (P, SV, and SH), sub-source i and component d (vertical, radial, and tangential) is shown in Equation 2.2 for the case of a finite-fault source model. Where $\mathrm{C^w}_{i_d}$ is a scaling constant, $S^w{}_i(f)$ is the source spectrum, $A^w{}_i(r_i, f)$ is the attenuation due to the path and $\mathrm{Z^w}_{i_d}(f)$ represents the site-specific effects.

$$U_i^w{}_d\left(f, r_i, M_{0_i}\right) = \mathrm{C^w}_{i_d}(M_{0_i})\, S^w{}_i(f) A^w{}_i(r_i, f) \mathrm{Z^w}_{i_d}(f) \qquad \textbf{Equation 2.2}$$

2.2.1.1 *Source*

The source term of equation Equation 2.2, $S^w{}_i(f)$, models the spectral content generated at the rupture. The rupture may be modeled considering a point source or a finite-fault source model. Small earthquakes, i.e., those whose rupture dimensions are negligible when compared to the propagation distance, are typically represented by a point source, while larger earthquakes with propagation distances like or smaller than the dimensions of the source are described through finite-fault models. In this study, we focus on the description and use of the method considering the latter, however, the description of the method herein presented is valid also for point source models.

The finite-fault source model builds the total seismic moment of the simulated event by adding the contribution of smaller sub-events. Based on this concept, the fault is subdivided into a grid of sub-faults, each considered as a point source whose individual contribution is added at the observation site considering a delay in time that accounts for the rupture and traveling times. Equation 2.3 shows the omega-squared model, introduced in Aki (1967) and used to represent the source spectrum of each individual sub-fault:

$$S^w{}_i(f) = \frac{(2\pi f)^2}{1 + \left(\frac{f}{f_c^w{}_i}\right)^2} \qquad \textbf{Equation 2.3}$$

Where $f_c^w{}_i$ is the dynamic corner frequency, in Hz, of wave-type "w" and sub-source "i". Originally, the method considered a definition of the dynamic corner frequency based on the work by Motazedian & Atkinson (2005) and then adjusted to the specifics of the 3D simulation in Otarola & Ruiz (2016). More recently, authors such as Sun et al. (2010) and Dang et al. (2022) have pointed out some important deficiencies in these models; for example, the evolution of the corner frequency is entirely dependent on the rupture

sequence of the sub-faults, and thus fails to reflect the role of the distribution of asperities in the finite-fault model. For this reason, this work considered the dynamic corner frequency model proposed by Dang et al. (2022), where the dynamic corner frequency for S-waves is computed considering the distribution of the slip over the source and the static corner frequency, f_{c0}, proposed by Boore (2003): See Equation 2.4

$$f_{c0} = 4.9x10^{6}\beta\left(\frac{\Delta\sigma}{M_0}\right)^{1/3} \quad \textbf{Equation 2.4}$$

where β is the S-wave propagation velocity at the depth of the sub-fault (in km/s), $\Delta\sigma$ is the stress drop (considered constant for all sub-sources in the assumed rupture) in bars, and M_0 is the seismic moment of the target event dyne-cm. The dynamic corner frequency ($f_c^S{}_i$), in Herz, is then described by Equation 2.5:

$$f_c^S{}_i = f_0\left(1 + \left(\frac{M_{0_i}}{M_{0ave}}\right)^{\frac{1}{3}}\right) \quad \textbf{Equation 2.5}$$

The distribution of the seismic moments for each sub-source is obtained as a percentage of the total seismic moment, computed based on the ratio of the slip at the sub-fault, s_i, and the total slip of the rupture, $M_{0_i} = M_0 s_i / \sum_{i=1}^{N} s_i$, where N is the number of sub-faults considered in the discretization of the finite-fault model. Finally, M_{0ave} refers to the average seismic moment in the rupture (i.e., $M_{0ave} = M_0/N$). The estimation of the P-wave corner frequencies is done considering the ratio of P and S-wave propagation velocities as proposed in Otarola & Ruiz (2016), and shown in Equation 2.6.

$$f_0^P = \frac{\alpha}{\beta} f_0 \quad \textbf{Equation 2.6}$$

where α is the velocity of the P-wave at the hypocentral depth in km/s. The relationship of P and S-wave corner frequencies thus becomes:

$$f_c^P{}_i = \frac{\alpha_i}{\beta_i} f_c^S{}_i \quad \textbf{Equation 2.7}$$

The distribution of the slip in the fault may be considered in different ways. Earlier applications of stochastic simulation, such as those reported in Motazedian & Atkinson (2005) and Otarola & Ruiz (2016) considered random uniform and Gaussian distributions, respectively. Other authors, such as Mai & Beroza (2002) developed models to generate spatially correlated random realizations of slip distributions, based on the study of empirical data.

The development of the self-similarity concept by Hanks & Kanamori (1979) and Andrews (1980) lead to the emergence of composite source models, such as the fractal distributed models proposed in Zeng et al. (1994), and Gallovič & Brokešová (2007). More recently, Gallovič (2016) modified the Ruiz Integral Kinematic Method, RIK, (Ruiz et al., 2011) to generate a computationally efficient method for the formulation of the source. In this model, the author constructs a rupture plane composed of randomly distributed circular sub-sources. The distribution of these sub-faults follows a fractal number size distribution of 2. The sub-faults are distributed considering a sub-fault radius, $R_{sub-fault}$, equal to integer fractions, n_{RIK}, of the fault width W, i.e., $R_{sub-fault} = W/n_{RIK}$. For the number-size distribution, the number of sub-sources at level n_{RIK} is $2n_{RIK} - 1$. The sub-faults are distributed randomly along the fault or following a prescribed Spatial Probability Density Function orienting the slip of the rupture. The latter is particularly useful when studying ruptures obtained from the inversion of past earthquake events. With respect to the rupture propagation, the RIK source model considers a slip pulse dependent on the shear-wave propagation velocity of the media at the location of the sub-source. The rise time depends on the wavenumber. In the RIK model, the rise time depends on sub-source radius $R_{sub-fault}$ and the rupture velocity, which is equal to a prescribed fraction of the local S-wave propagation velocity. For this study, we considered the slip distribution and rupture propagation proposed by Gallovič (2016).

Theoretically speaking, the FAS amplitude of the simulated ground motions is insensitive to the number of sub-faults characterizing the fault. This is due to the inclusion of the energy normalization factors described in section 2.2.4. This factor is utilized to correct the differences in irradiated energy noticed when a different number or size of sub-sources was considered in previous finite fault models, (Motazedian & Atkinson, 2005). Yet, the number of sub-sources influences the non-stationarity of the simulated motion, because of the lagged summation of the contribution of the individual sub-sources.

2.2.1.2 *Path*

Otarola & Ruiz (2016) modelled seismic waves as direct rays travelling through a simplified 1D layered velocity model of the crust, with incidence angles modified at each layer interface according to Snell's law. This propagation model through a regional velocity model is the key for the computation of the free surface and energy partition parameters scaling the motion and described in section 2.2.2.

The attenuation of seismic waves due to the propagation path from each sub-source to the site, shown in Equation 2.8, is modelled through the geometrical spreading and anelastic attenuation functions. The geometrical spreading function, $G(r_i)$, shown in Equation 2.9, models the distance decay of seismic waves, r_i (mostly defined as the hypocentral distance), a reference distance, R_0, at which the source spectrum is defined

(i.e., no attenuation) and the attenuation exponent, n. Theoretically speaking, $n = 1$ represents body-wave attenuation in a semi-infinite elastic medium. However, this value is often changed in applications of other stochastic methods to better adjust the attenuation observed from data, e.g., (Atkinson & Assatourians, 2015).

The anelastic attenuation considers the intrinsic damping of the seismic waves by means of the quality factor, Q^w, the wave propagation velocity at the depth of each sub-source (v), and distance. This function usually follows the form $Q^S = Q_0 f^M$, and it is typically obtained from the spectral inversion of the S portion of the FAS of records from low magnitude events, e.g., Kinoshita (1994), Jin et al. (2000), Kinoshita & Ohike (2002), Moya & Irikura (2003). The quality factor for P-waves, Q^P, is estimated from the S-waves based on the relationship proposed by Udias (1999) and shown in Equation 2.10.

$$A^w{}_i(r_i, f) = G(r_i) exp\left(\frac{-\pi f r_i}{Q^w(f) v}\right) \quad \textbf{Equation 2.8}$$

$$G(r_i) = \frac{R_0}{r_i^n} \quad \textbf{Equation 2.9}$$

$$Q^P = \frac{3\alpha^2 Q^S}{4\beta^2} \quad \textbf{Equation 2.10}$$

2.2.1.3 *Site*

As pointed in Boore (2003), technically, site effects correspond to a modification of the ground motion due to phenomena occurring during the propagation between the sub-source and the observation point. However, these are independent from the travelled distance, a consideration that made early modelers consider best to separate them from the previously discussed path effects.

Some implementations of stochastic simulations consider the effect of the site by convolving the FAS of the ground motions with transfer functions computed from simplified velocity models. However, when simulating ground motions for generic site conditions, site effects are usually considered as a combination of amplification and attenuation functions, (Boore, 2003). Authors like Boore (2003) have considered approximations, such as the quarter-wavelength method, to estimate the amplification based on the impedance contrast from the sub-source to the site. This approximation, however, is only valid for SH-wave simulations assuming a vertical incidence. In this work, we suppose that the amplification from the source and the crustal structure is negligible with respect to the shallow soil layering, where the impedance contrast can be important.

High-frequency attenuation functions are also used in stochastic modelling. Theoretically speaking, site-specific effects include attenuation for all frequencies; nevertheless, the use of a complementary attenuation filters is still typically required in stochastic simulations, (Boore, 2003). For example, when considering site transfer functions obtained from spectral inversion, a small value of attenuation remains in the inverted source spectrum due to the use of a reference station in the separation of source and site effects. The reference station, however, is still subjected to high-frequency attenuation, thus the remaining attenuation is assigned to the source spectrum, (Oth, Bindi, et al., 2011). Anderson & Hough (1984) attributed the observed attenuation to the presence of layers of weathered materials in the crustal structure directly below the site. Hanks (1982) attributed this phenomenon mostly to propagation effects, whereas Papageorgiou & Aki (1983) related this phenomenon to the source. The most typically considered high-frequency attenuation functions are the ones proposed in Hanks (1982) and Anderson & Hough (1984), shown in Equation 2.11and Equation 2.12.

$$D(f) = \left(1 + \left(\frac{f}{f_{max}}\right)^{s}\right)^{-0.5} \qquad \textbf{Equation 2.11}$$

$$D(f) = exp\,(-\pi\kappa_0 f) \qquad \textbf{Equation 2.12}$$

Where f_{max} is the cut-off frequency and s is a variable determining the order of the filter and it is usually related to the asperities at the source. The quantity κ_0 represents the slope of the observed high-frequency decay in the FAS of ground motions directly below the site. In this study, we consider the κ_0-model proposed by Anderson & Hough (1984).

2.2.2 Scaling constant

The amount of energy released by the event is represented by the scaling constant, which depends on earthquake magnitude, media properties and ray propagation through the regional velocity model. The scaling constant reads:

$$\frac{M_{0_i}(RP^w\ FS^w{}_i\ EP^w{}_i)}{4\pi\rho_i {v_i}^3 R_0} \qquad \textbf{Equation 2.13}$$

Where RP^w is the radiation pattern, $FS^w{}_i$ is the free surface factor, $EP^w{}_i$ is the energy partition factor, ρ_i is the density at the level of the sub-source, and v_i is the wave propagation velocity at the level of the sub-source. The model considers average radiation patters, computed based on the theoretical isotropic high-frequency, fault dependent relationships proposed in Onishi & Horike (2004).

$$R^P = \sqrt{\frac{4}{15}} \qquad \text{Equation 2.14}$$

$$R^{SV} = \frac{1}{2}\sqrt{\sin^2(\lambda)\left(\frac{14}{15}+\frac{1}{3}\sin^2(2\delta)\right)+\cos^2(\lambda)\left(\frac{14}{15}+\frac{2}{3}\cos^2(\delta)\right)} \qquad \text{Equation 2.15}$$

$$R^{SH} = \frac{1}{2}\sqrt{\frac{2}{3}\cos^2(\lambda)\,(1+\sin^2(\delta))+\frac{1}{3}\sin^2(\lambda)\,(1+\cos^2(2\delta))} \qquad \text{Equation 2.16}$$

Where λ and δ are the rake and dip angles of the ruptured fault, respectively. The energy partition factors are used to decompose the particle movement into a convenient coordinate system. Considering that P and SV-waves generate displacements alongside the incidence of the seismic rays, and SH waves perpendicular to this plane, the energy partition factors are computed for a system composed of a tangential (t), radial (r) and vertical (z) components:

$$\begin{bmatrix} {EP^{P_r}}_i \\ {EP^{P_z}}_i \\ {EP^{SV_r}}_i \\ {EP^{SV_z}}_i \\ {EP^{SH_t}}_i \end{bmatrix} = \begin{bmatrix} -\sin(\theta) \\ \cos(\theta) \\ \cos(\theta) \\ \sin(\theta) \\ 1 \end{bmatrix} \qquad \text{Equation 2.17}$$

where θ is the incidence angle measured from the vertical. The amplification factors due to the free surface effect is computed as a function of the incidence angle and according to the elastic close-form solutions presented in Evans (1984)

2.2.3 Random noise and modulating window

The phase spectrum is modelled as a random variable in the form of a band limited Gaussian white-noise with finite duration. The duration of the noise is obtained as the sum of source and propagation components, $t_{i,source} + t_{i,distance}$, where t_{source} is defined as a fraction of the rise time, and $t_{distance}$ is a function modelling the concept of signal elongation with distance. A modulating function is then applied to the white noise with the intention to include the characteristic temporal non-stationary nature of ground motion time series. The Saragoni and Hart modulating function, $\omega(t, e, \eta, t_\eta)$ (Saragoni & Hart, 1973), shown in Equation 18, is often considered in stochastic simulation

methods, e.g., Boore (2003), Motazedian & Atkinson (2005), Otarola & Ruiz (2016), Ruiz et al., (2018).

$$\omega(t, e, \eta, t_\eta) = a\left({}^{t}/_{t_\eta}\right)^{b} \exp\left(-c\left({}^{t}/_{t_\eta}\right)\right) \qquad \textbf{Equation 2.18}$$

Where e and η are parameters defining the shape of the function, $a = \exp(1)/e$, $b = -e\ln(\eta)/(1 + e\,(\ln(e) - 1))$, $c = b/e$, $t_\eta = f_{Tgm}T_{gm}$. T_{gm} is the duration of the signal for the computation of the window function, and f_{Tgm} is a factor modeling the elongation of the windows. Previous implementations of this modulating function have considered different combinations of parameters. These are often adjusted for matching reference signals, e.g., Boore (2003), Otarola & Ruiz (2016), Ruiz et al., (2018).

As in previous applications of the method, due to the lack of information, this study considers the same window description for all wave types (P, SV, and SH). Next, the FAS of the modulated noise is normalized by the square-root of the mean square of its amplitude spectrum, and then multiplied by the ground motion spectrum $U_{i\ d}^{w}\left(f, r_i, M_{0_i}\right)$. The acceleration time history of each sub-source and wave type, a_i^w, is finally obtained by computing its inverse Fourier transform.

2.2.4 Summation scheme

The aggregation of the signals from all sub-faults, and for each wave-type, is performed at the site considering a time delay $\Delta t_{i_d}^{w} = \Delta t_{i,rupture} + \Delta t_{i,travel}^{w}$. The first component of the delay, $\Delta t_{i,rupture}$, corresponds to the time that takes the rupture front to propagate from the hypocentre to the sub-fault. The second component of the delay, $\Delta t_{i,travel}^{w}$, represents the time it takes the seismic ray to travel through the regional velocity model from the sub-fault to the site. The acceleration time history at the site, for each wave-type and component, $a_d^w(t)$, is computed according to Equation 2.19. The equation includes an energy normalization factor, H_i^w, whose function is to balance and conserve the radiated energy from all sub-faults at high frequencies, (Otarola & Ruiz, 2016). Originally, this factor was computed based on the ratio of the velocity spectrum, e.g.,Motazedian & Atkinson, (2005); Otarola & Ruiz, (2016), this consideration, however, neglected the contribution of the asperities for the radiation of high-frequency energy and thus hid important features produced by the non-uniformity of the asperities in the source model (Dang et al., 2022). To correct this issue, Dang et al., (2022) proposed to weight the contribution of the radiated energy based on the slip at each sub-source, as shown in Equation 2.20 for a generic wave type (the author's proposal considered only S waves). The technique presented in this work considers this energy normalization factor.

$$a_d^w(t) = \sum_{i=1}^{N} a_{i\ d}^{w}\, \Delta t_{i_d}\, H_i^w \qquad \text{Equation 2.19}$$

$$H_i^w = \sqrt{\frac{\sum_{f_k}\left[\frac{f_k}{1+\left(\frac{f_k}{f_0^w}\right)^2}\right]^2}{\sum_{f_k}\left[\frac{f_k}{1+\left(\frac{f_k}{f_{c\ i}^{w}}\right)^2}\right]^2}\,\frac{\sum_{i=1}^{N} s_i}{s_i}} \qquad \text{Equation 2.20}$$

As last step, the coordinate system of the time histories is changed from cylindrical to Cartesian coordinates. The coordinate transformation matrix is constructed based on the azimuth angles, φ_i, of each sub-fault. The system of equations used to transform the coordinate system is shown in Equation 2.21.

$$\begin{bmatrix} a_{i_{NS}}^w \\ a_{i_{EW}}^w \\ a_{i_{UD}}^w \end{bmatrix} = \begin{bmatrix} \cos(\varphi_i) & -\sin(\varphi_i) & 0 \\ \sin(\varphi_i) & \cos(\varphi_i) & 0 \\ 0 & 0 & 1 \end{bmatrix} \begin{bmatrix} a_{i_r}^w \\ a_{i_t}^w \\ a_{i_z}^w \end{bmatrix} \qquad \text{Equation 2.21}$$

2.2.5 Ground Motion Simulation Summary

The following list summarizes the information and parameters required to perform a full simulation with the herein proposed methodology:

Observation point

- Location of the observation point: Overall position of the observation point. The observation point should be located in an X-Y-Z coordinate system consistent with the one used for the location of the source model.

Source model

- Geometry of the source: Dimensions of the considered rupture plane, if finite fault model is considered.
- Location of the source model: Overall position of the each of the sub faults, if finite fault model is considered, in an X-Y-Z coordinate system consistent with the one used for the location of the observation point.

- Hypocentre: Location of the hypocentre in the rupture plane, if finite fault model is considered, or in in case of point source, relative location of the hypocentre with respect to the observation point.
- Rupture propagation model: Instant at which the rupture front arrives to each sub fault (from the hypocentre) if finite fault model is considered. Here given directly by the kinematic source model, (Gallovič, 2016).
- Slip model: Distribution of the slip on the rupture plane if finite fault model is considered. Here given directly by the kinematic source model, (Gallovič, 2016).

Propagation model

- Stratified velocity model: Including wave propagation velocity (of S and P-waves) and density at each of the layers composing the stratified velocity model. Furthermore, the depth of the interface between layers must also be included. The properties of the stratified velocity model should match the ones considered in the conception of the source model.

Site effects

- Transfer functions (optional): Transfer functions including the effect of the superficial soil layers. The model allows for the consideration of the changes produced to the phase of the ground motion.

Ground Motion Spectrum

- Stress drop ($\Delta\sigma$)
- Geometrical spreading function, $G(r_i)$, including the reference distance at which the source spectrum is computed R_0
- Quality function for the S-waves, $Q^S = Q_0 f^M$,
- High-frequency attenuation function modelled either with the f_{max} or κ_0 functions.

A summary of the simulation procedure is shown in Figure 2.1.

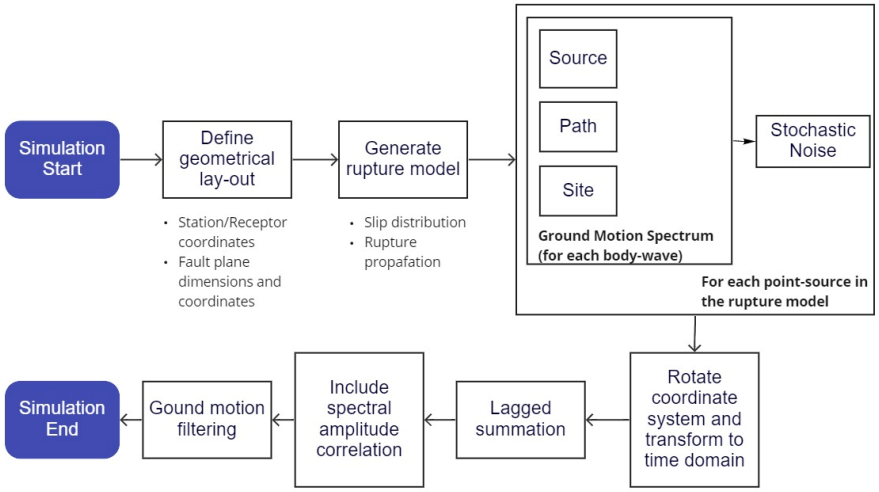

Figure 2.1. Ground motion simulation flow chart

2.4 Simulation post-processing

2.4.1 Correlation structure of spectral amplitudes

Different studies have demonstrated the existence of a correlation structure between residuals computed with respect to a ground motion model of spectral accelerations, e.g., Baker & Cornell (2006), Baker & Jayaram (2008), Bayless & Abrahamson (2018, 2019), Kohrangi et al. (2020). The correlation of spectral accelerations may be computed between two periods of vibration T_i and T_j, for the same component: $SA_V(T_i) - SA_V(T_j)$, $SA_{Hx,y}(T_i) - SA_{Hx,y}(T_j)$, or for different components of the ground motion: $SA_H(T_i) - SA_V(T_j)$. Furthermore, the correlation between spectral accelerations at the same period of vibration and different components, i.e., $SA_{Hx}(T_i) - SA_{Hy}(T_i)$ and $SA_H(T_i) - SA_V(T_i)$, has also been studied in the past, (Baker & Cornell, 2006).

The appropriate representation of the spectral correlation structure is of interest for engineering purposes because the frequency content of the input ground motion directly affects the nonlinear response of Single Degree of Freedom (SDoF) and of Multi-Degree of Freedom Systems (MDoF). Without the adequate correlation structure embedded in the simulation process of ground motions, amplitude and variability in the structural response may be underestimated, leading to non-conservative estimates of seismic risk, (Bayless & Abrahamson, 2018). For clarification purposes, whenever we refer to the correlation to the horizontal component, SA_H, we refer to the orientation-independent measure in terms of GMRot50 (Boore et al., 2006). The individual horizontal components are labelled as SA_{Hy} and SA_{Hx} for the NS and EW components, respectively.

Studies such as Burks & Baker (2014) have shown that stochastic ground motion simulations display an unrealistic decay of the correlation between neighbouring periods. This is due to the use of white noise in the construction of the ground motions, which is, by definition, a sequence of serially uncorrelated random variables with zero mean and finite variance. To correct this deficiency, at least partially, Wang et al. (2019) proposed a post processing procedure to include, within the simulated ground motions, the correlation structure coming from the analysis of within-site residuals (the correlation structure obtained from the between event residuals has not yet been included in the procedure). The procedure presented by the authors introduces the correlation structure in the horizontal components of the ground motion by adding vectors constructed with it. Further details on the implementation of this technique may be found in Wang et al. (2019).

In this work, the procedure proposed in Wang et al. (2019) was extended to take into consideration the vertical component of the motion. The following steps summarize this procedure:

1. Obtain the Fourier transform of the acceleration time histories of the three simulated components. Let $\Pi_{x,y,z}$, $Amp_{x,y,z}$ and $Phase_{x,y,z}$ be the number of points, the amplitude and the phase of the Fourier transform of each component.
2. For each of the components, generate a vector of length of length $\Pi_{x,y,z}$, $\Gamma_{x,y,z}$. Each entry in the vectors is sampled from a normally distributed random variable with zero mean, and standard deviation consistent with the standard deviation of the simulated ground motions.
3. Create a covariance matrix expressing the link between the spectral amplitudes of different components, see Equation 2.22. The coefficients ρ_{x-y} and ρ_{H-z} model the correlation between spectral accelerations at the same frequency, but from different ground motion components. According to Baker & Cornell (2006), the correlation factor between horizontal components, ρ_{x-y}, varies linearly between 0.9 - 0.75 for periods of vibration between 0.05s and 5.0s. A constant value of $\rho_{x-y} = 0.90$ is considered in this work. Finally, for the correlation factor between horizontal and vertical components, ρ_{H-z}, we considered a constant value of $\rho_{H-z} = 0.63$, as reported by the authors.

$$\varsigma = \begin{bmatrix} 1 & \rho_{x-y} & \rho_{H-z} \\ \rho_{x-y} & 1 & \rho_{H-z} \\ \rho_{H-z} & \rho_{H-z} & 1 \end{bmatrix} \qquad \textbf{Equation 2.22}$$

4. Apply Cholesky decomposition to covariance matrix ς and obtain the 3x3 upper triangular matrix B (Equation 2.23). Multiply the matrix $[\Gamma_x, \Gamma_y, \Gamma_z]$ by B to obtain the correlated random vectors $\left[R_x^{Corr}, R_y^{Corr}, R_z^{Corr}\right]$.

$$\varsigma = BB^T \quad \textbf{Equation 2.23}$$

$$\left[\Gamma_x^{Corr}, \Gamma_y^{Corr}, \Gamma_z^{Corr}\right] = [R_x, R_y, R_z]B \quad \textbf{Equation 2.24}$$

5. Apply Cholesky decomposition to the correlation matrix $Corr_{Bayless}$ reported in (Bayless & Abrahamson, 2018), to obtain the lower triangular matrix L. The correlation matrix is defined in the frequency range 0.1-24 Hz. For frequencies outside this range, we consider no correlation between the spectral amplitudes.

$$Corr_{Bayless} = LL^T \quad \textbf{Equation 2.25}$$

6. For each of the components, left multiply the correlated random vector $\Gamma_{x,y,z}^{Corr}$ by L. For frequency points outside of the frequency range of $Corr_{Bayless}$ we considered $S = \Gamma_{x,y,z}^{Corr}$. See Equation 2.26. At this point, it is important to highlight the fact that we are explicitly considering the correlation structure obtained for the horizontal components also for the vertical. However, considering the lack of a correlation matrix for the vertical component of the FAS, and the similitude in the functional shape of the correlation structures between spectral accelerations of horizontal and vertical components, e.g., Kohrangi et al. (2020), we expect this to be a good approximation.

$$S_{x,y,z} = L\Gamma_{x,y,z}^{Corr} \quad \textbf{Equation 2.26}$$

7. Construct the FAS for each of the components following Equation 2.27. The Fourier transform for each of the components is completed by adding the original phase $Phase_{x,y,z}$. The time histories are then obtained by applying the inverse Fourier transform.

$$Amp_{x,y,z}^{corr} = Amp_{x,y,z} \exp(S_{x,y,z}) \quad \textbf{Equation 2.27}$$

8. The inclusion of the correlation structure through the modification of the FAS results in the modification of the energy of the simulated time histories. To correct this issue, apply a correction factor computed as the ratio of the Arias intensity of the time history before and after the procedure described in the previous steps. See Equation 2.28

$$E_{norm} = \sqrt{\frac{AI}{AI^C}} \qquad \text{Equation 2.28}$$

2.4.2 Ground Motion filtering

Displacement time histories, obtained from the integration of the simulated ground motions, often displayed residual displacements due to the presence of artificial low-frequency content in the FAS of the motion. This artificial content is generated by the finite frequency step of the simulations, resulting in a constant FAS for frequencies lower than the frequency step. To remedy this inconsistency with the herein considered model, simulated ground motions in this work are treated with acausal Butterworth high-pass filter of third order. This in agreement with the post-processing recommendations in Boore & Bommer (2005). The proposed filter considers a high-pass corner frequency given by the intersection of the FAS with a f^2 model, and a low-pass corner frequency defined by the maximum frequency for which the correlation structure is defined, i.e., 24 Hz, (Bayless & Abrahamson, 2019).

2.3 EVALUATION OF THE SIMULATION TECHNIQUE

This section presents the results obtained from the evaluation of the proposed ground motion simulation technique. This evaluation consisted in the study of the sensitivity of the technique to its input parameters, and in the assessment of the features included in the simulation technique as part of this work, i.e., the post processing procedure proposed to include spectral correlation structure.

These analyses were based on sets of ground motions simulated for a hypothetical earthquake considered as case study. Specifically, the simulations were generated for a magnitude 6.6 ($M_w = 6.6$) earthquake in the region of Niigata, Japan. The observation points considered in the evaluation, located at different distances and azimuths from the source (defined in section 2.3.1.2), are shown in Figure *2*.2.

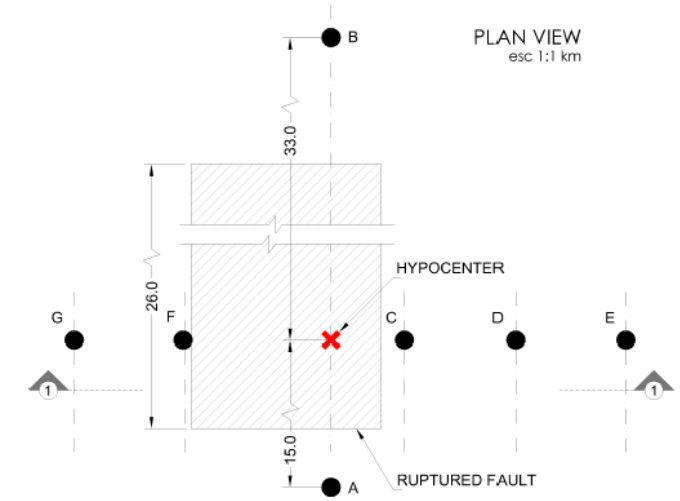

(a)

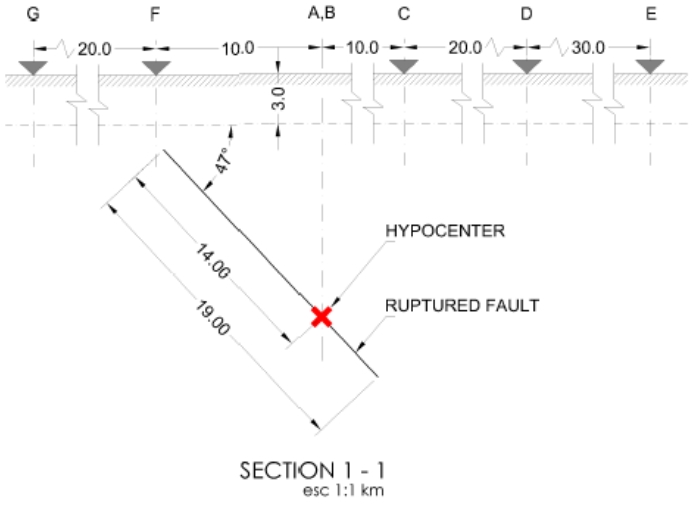

(b)

Figure 2.2. Geometrical setup for the ground motions and sensitivity analysis. (a) - Plan view, (b) - transverse section. The position of the fixed hypocentre considered in the analysis is marked in the figures.

2.3.1 Sensitivity analysis

The sensitivity analysis was based on the comparison of the FAS of simulated ground motions for different likely values of input. The comparisons were focused on the FAS because the technique constructs the ground motions based on its modelling, hence the impact of the analysed variables is directly seen. Overall, two different categories of input parameters were considered: (i) the parameters used in the construction of the simulated ground motion spectrum (section 2.2.1), namely $\Delta\sigma$, Q_0, M, and κ_0, found in Equation 2.4, Equation 2.8 and Equation 2.12, respectively, and (ii) the entry models used to describe the propagation medium and the distribution of the slip in the source. The following sections describe the sampling spaces of each of these variables as considered in the sensitivity analysis.

2.3.1.1 *Ground motion spectrum*

The ground motion spectrum was constructed considering the seismological characterization of a point source model for the area of Niigata, Japan, and reported in Oth et al. (2010) and Oth et al. (2011a, 2011b). These studies provided distributions of the variables describing the FAS of the S-wave portion of the ground motions recorded by the Japanese monitoring networks: K-NET and KiK-Net (National Research Institute for Earth Science and Disaster Resilience, 2019). According to these sources, Japanese crustal events are characterized by a stress drop following a log-normal distribution with a mean of 11 Bar (1.1 MPa) and a log standard deviation of 0.7. The authors a geometrical attenuation function $G(R) = R_0/R_{hypocentral} = 5/R_{hypocentral}$, and a quality factor function of the form $Q^S(f) = Q_0 f^M$, where $Q_0 = 55 \pm 4$ and $M = 0.77 \pm 0.04$. Finally, the authors define the crustal-related high-frequency attenuation considering the filter proposed in Anderson & Hough, (1984) and dependent on κ_0. According to the results reported in Oth et al., (2010), and for crustal earthquakes, this parameter follows a Gaussian distribution with a mean of 0.029s and a standard deviation of 0.008s.

2.3.1.2 *Source*

The geometry of the source was defined in agreement with an actual earthquake scenario matching the causative parameters of the case study, the 2004 Niigata M6.6 earthquake, (Asano & Iwata, 2009). According to the authors, this event was generated by a planar rupture with a length of 26 km and width of 19 km, oriented with a strike, dip, and rake angles of 0°, 47° and 93°, respectively. Figure *2*.2 shows the disposition of the ruptured plane, and the assumed hypocentre location, with respect to the considered station arrangement.

Two different spatial density functions were considered in the definition of the slip for the study of the sensibility of the method to this input. First, a uniform density function, where each sub-source has equal probability of allocating a given slip, and second, a spatial

probability density function (herein named as IPF), considered as the normalized slip inversion of the reference event. Each of the finite-fault models considered in this work were discretized by a total of 100 sub-faults.

2.3.1.3 *Path*

The propagation medium was defined considering two different stratified models proposed for the area of interest, a mostly homogeneous and fast model proposed in Aoi et al. (2008), and the model proposed by Hikima-Koketsu (HK), characterized by a progressive increase in the propagation velocity with depth, (Aochi et al., 2013). Figure 2.3 shows these regional velocity models.

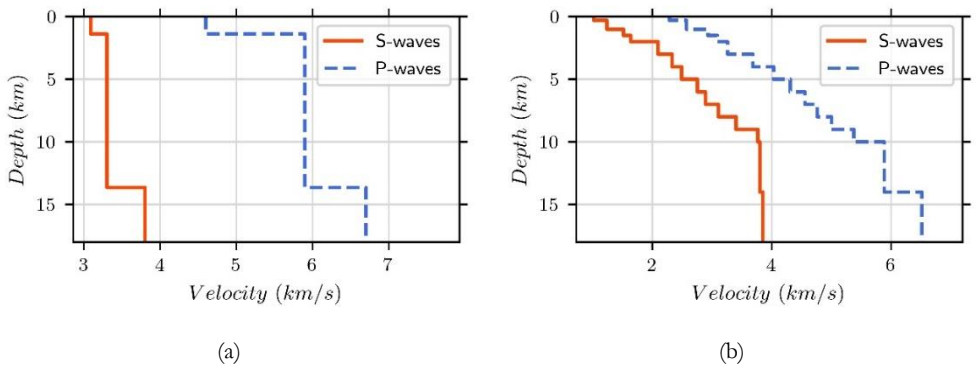

Figure 2.3. Regional velocity models considered in this study. (a) – Aoi et al. (2008) and (b) – Hikima-Koketsu (HK), (Aochi, et al., 2011). The hypocentre is located at 13 km depth.

2.3.1.4 *Site*

The simulations considered in this chapter were generated considering an outcropping crystalline rock site, hence free of any site-effects related to superficial soil layers. Also, for simplicity, amplification due to the impedance contrast between the source and the reference rock condition was not considered either.

2.3.1.5 *Definition of a reference model*

To simplify the comparison performed as part of the sensitivity analysis, a reference model was defined. This model considered the uniform spatial density function for the definition of the slip distribution of the source, the regional velocity model proposed by Aoi et al. (2008), and the mean value of the random variables used in the construction of the ground motion spectrum, i.e., $\Delta\sigma = 11$ bar, $Q_0 = 55$, $M = 0.79$ and $\kappa_0 = 0.029$s. Figure 2.4 shows the acceleration, velocity, and displacement time histories of one simulation conducted with the parametrization of the base model, for station A (identical figures for the remaining stations are included in the appendix of this document). The shown

scenario corresponds to the simulation with the median geometric mean of the Peak Ground Acceleration (PGA) of all three components, from a set of 50 simulations where the only variable is the random seed of the stochastic noise used to construct the acceleration time histories. The acceleration time histories have been post-processed according to the procedure described in section 2.4.2, padding zeros at the beginning and end of the signals. The arrival times of P and S waves, based on the minimum travel times among all sub-faults is also shown in the figure. The waveforms clearly show the different frequency content dominating the acceleration, velocity, and displacement time histories. Furthermore, the effect of the alignment of the fault and the observation point may also be noticed by comparing the amplitude of the motion in the NS and EW components, see Equation 2.21. Finally, the effect of the proximity to the source may also be noticed by the amplitude of the simulated vertical component.

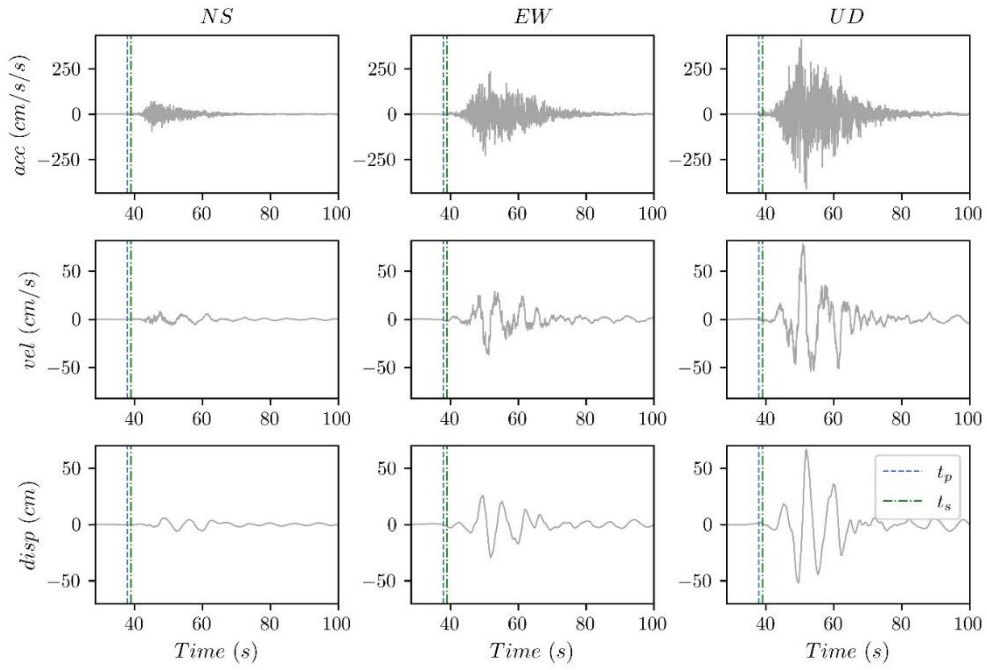

Figure 2.4. Base model time histories for station A. The time histories for North-South, East-West and Upward-Downward components are shown in the left, centre, and right column, respectively.

2.3.1.6 *Sensitivity to parameters defining the ground motion spectrum*

The sensitivity of the technique to the parameters defining the ground motion spectrum was studied by correlating the variation of the FAS to the variation of the considering parameters, i.e., $\Delta\sigma$, Q_0, M and κ_0. To do so, the following steps were followed:

1. Construct a total of 100 different ground motion simulation models by sampling parameter combinations considering the Latin Hypercube Sampling (LHS) technique and the distributions of each of these random variables (described in section 2.3.1.1).
2. For each of the ground motion simulation models, generate a single set of time histories considering a constant random seed. This consideration will eliminate the aleatory component added by the sampling of the Gaussian white noise.
3. Compute the FAS for all 3 components of the simulated ground motion. Combine the horizontal components into their geometrical mean.
4. Construct a pair with the Fourier Amplitude ordinates (for a given frequency) of each model and the value of each of the input parameter constituting the ground motion simulation model.
5. Aggregate the pairs, for each of the input parameters and for each of the considered frequencies into a cloud of points.
6. Finally, compute the Spearman correlation coefficient relating the input parameter and Fourier Amplitude ordinate at the considered frequency.

Figure 2.6 shows the FAS ordinates at two different frequencies for the considered range of variation of $\Delta\sigma$ and for the Geometrical Mean of the Horizontal components (GM component). The plots illustrate the linear tendency computed for the cloud of points and the respective linear correlation factor. From Figure 2.6a one can observe that $\Delta\sigma$ is directly linked to the variation of the FAS for $f = 1.0Hz$ with a correlation factor of $\rho \approx 1.0$. The influence of this parameter, however, decreases with frequency, as noticed in Figure 2.6b for $f = 10.0Hz$ where $\rho = 0.77$.

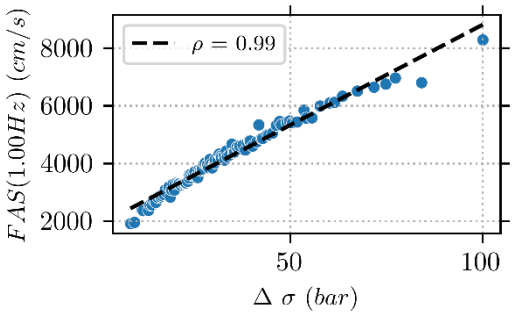

(a)

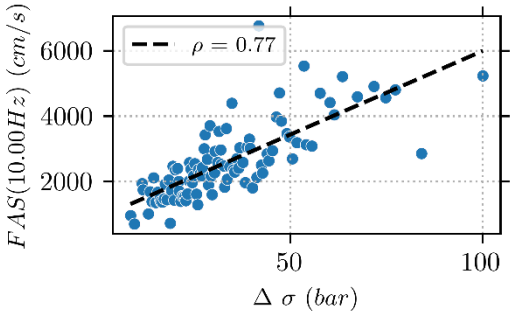

(b)

Figure 2.5. Variation of FAS_{GM} as a function of stress drop at station A, for (a) - $f = 1.0Hz$, and (b) - $f = 10.0Hz$. The dashed line represents the linear regression for the data used in the computation of the linear correlation factor.

The aggregation of the correlation factors for all considered frequencies provides a representation of the importance of each model parameter to the different frequency ranges of the FAS. Figure 2.6 shows these functions for each of the considered stations, thus allowing to distinguish different effects depending on the location of with respect to the source. For example, Figure 2.6a shows that the stress drop was found to be the most important parameter in the definition of the FAS for all considered stations and for frequencies below 10 Hz. After this frequency, however, the exponential decrement produced by κ_0 starts to control the shape of the FAS. A decay in the importance of this parameter was noticed in the lowest frequency range for stations C, F and E. The noticed decay was caused by the direct location of the stations over the source (stations C and F), for which the rupture plays a key role, and due to the distance with respect to the source (station E), for which propagation effects start to gain importance. This observation is also supported by the parameters related to the attenuation themselves, Q_0 and M, shown in Figure 2.6b and Figure 2.6c, for which station E shows features the biggest importance.

Identical results were obtained on the vertical component of the simulated ground motions.

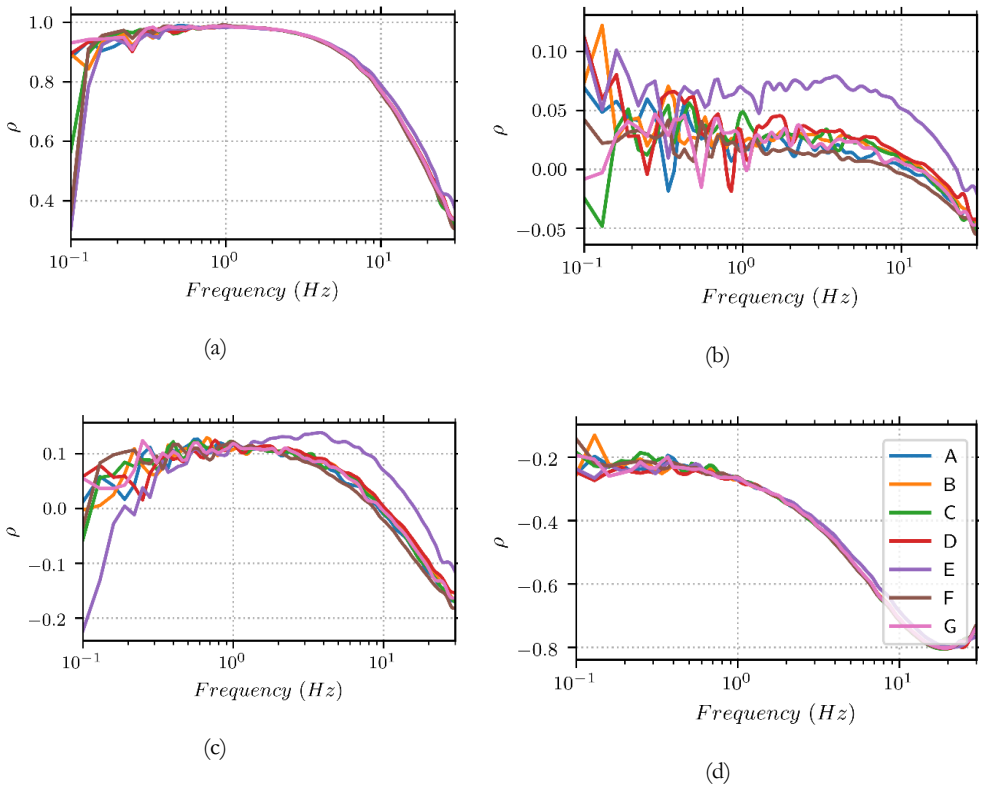

Figure 2.6. Correlation of the input parameters and FAS_{GM} as a function of frequency. (a) – $\Delta\sigma$, (b) - Q_0, (c) – M, and (d) - κ_0.

2.3.1.7 *Sensitivity to the slip distribution and hypocentre location*

The effect of slip distribution in the source was studied by comparing three different sets of simulations constructed from the base model and varying only the description of the source. The first set was generated considering a uniform spatial probability density function for the slip distribution and a constant hypocentre. The second was constructed considering the IPF spatial probability density function, defined in section 2.3.1.2, and the same fixed hypocentre location. Finally, the third set was assembled considering a uniform spatial probability density function but with varying position of the hypocentre (varying uniformly between the length and the lower half of the width of the fault). Each of these sets was composed of a total of 100 different scenarios, each with a different stochastic random seed and a different source idealization (constructed with their respective spatial probability function).

The comparison of sets considering a constant hypocentre location and different spatial probability density functions is shown in Figure 2.7a for the geometrical mean of the horizontal components (GM), and in Figure 2.7b for the vertical component (UD) at station A. The FAS of the simulated sets resulted in identical distributions for the analysed frequency range, both in terms of median and coefficient of variation COV (mean/standard deviation). The similarity of the distribution of the simulated FAS at all stations is due to the use of the energy normalization factor, H_i^W, which normalizes the far-field received energy of each sub-source based on the ratio of the source spectra and the slip with that of the static fault model (see Equation 2.4) and the total slip in the source, respectively, (Dang et al., 2022).

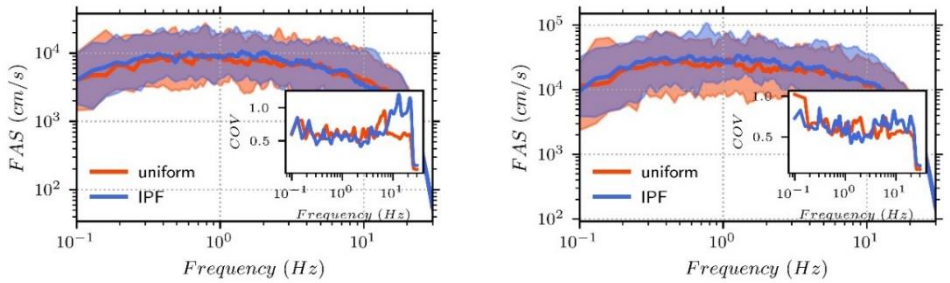

Figure 2.7. Sensitivity to the slip distribution at station A. Comparison of the FAS of sets of simulations considering two different spatial probability density function models and a fixed hypocentre. Comparisons for the (a) the geometrical mean of the horizontal components, and (b) the vertical component. The shaded areas represent the area between the 5^{th} and 95^{th} percentiles. The comparison of the coefficient of variation of the distributions is included in each figure

The similarity of the simulated FAS does not mean that the model is insensitive to the slip distribution. Figure 2.8 shows the comparison of two scenarios simulated with different source realizations considering a uniform spatial probability density function and constant hypocentre locations (see Figure 2.8a and Figure 2.8b). The comparison of the time histories obtained from these two sources shows similar amplitudes; however, the location of individual peaks varies from one simulation to the other.

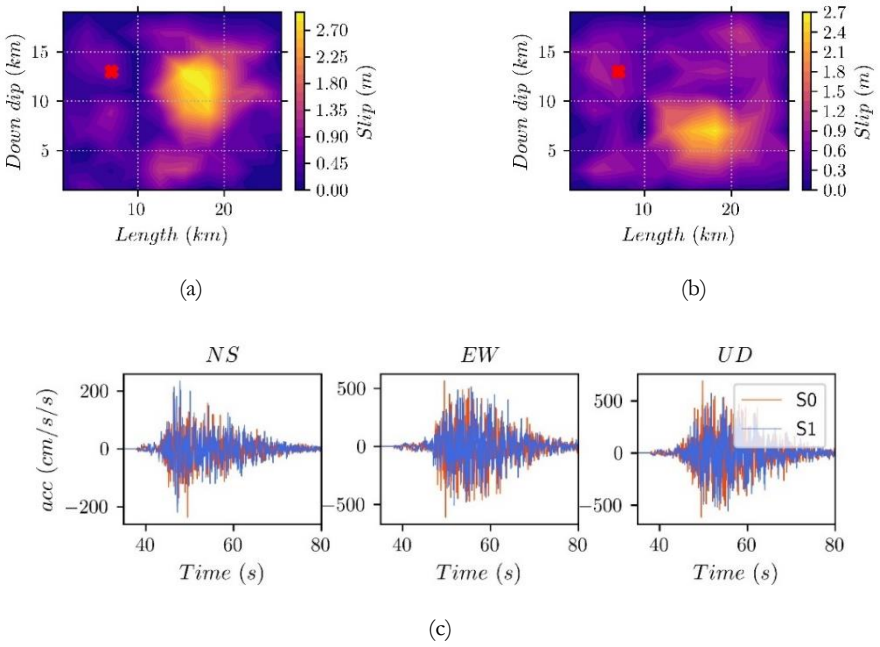

Figure 2.8. (a) -Comparison of individual scenarios from station A, generated from different realizations of the source, considering a uniform spatial probability function and a constant hypocentre. (a) – Source model No. 0 (S0), (b) - Source model No. 1 (S1).

Differences in the median of the distribution of the simulated FAS were noticed when considering a variable hypocentre location (i.e., by comparing the first and third sets). These differences were noticeable at all stations, specifically for frequencies larger than 1Hz. See for example Figure 2.9a and Figure 2.9b for the comparisons of the GM and UD components of simulations for stations A, respectively. The effect of the variation of the hypocentre, from an individual simulation-point of view, is shown in Figure 2.10. The most evident effect is the translation of the signals in time due to the variation of the distance of the initiation of the rupture and the station at which the time history is aggregated.

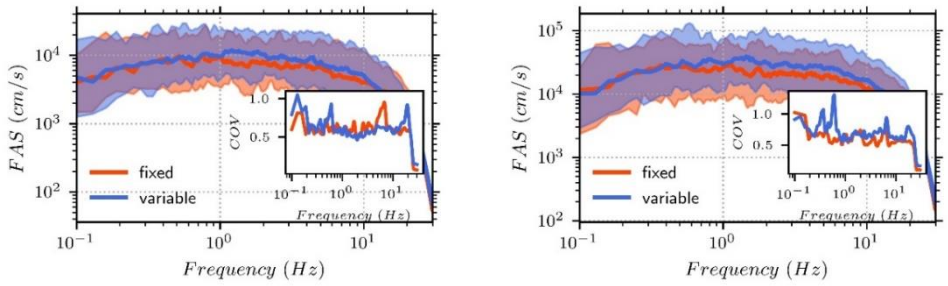

(a) (b)

Figure 2.9. Sensitivity to the slip distribution at station A. Comparison of the FAS of sets of simulations considering – A uniform density function and variable hypocentres. Comparisons for the (a) the geometrical mean of the horizontal components, and (b) the vertical component. The shaded areas represent the area between the 5^{th} and 95^{th} percentiles. The comparison of the coefficient of variation of the distributions is included in each figure

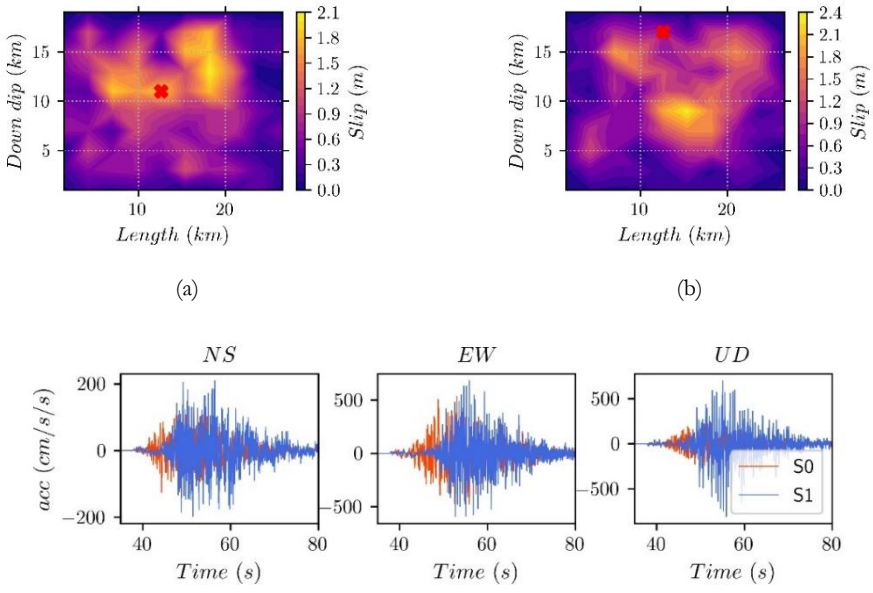

(a) (b)

(c)

Figure 2.10. (a) -Comparison of individual scenarios from station A, generated from different realizations of the source, considering a uniform spatial probability function and a variable hypocentre. (a) – Source model No. 0 (S0), (b) - Source model No. 1 (S1).

2.3.1.8 *Sensitivity to the regional velocity model*

The effect of the regional velocity model was studied by comparing the FAS obtained from sets of simulations conducted considering the regional velocity models described in section 2.3.1.3. The results obtained for two stations, A and E, are shown in Figure 2.11. In general, ground motions simulated with the HK velocity model (gradient-like model) result in larger FAS when compared to those considering the Aoi velocity model (step-like model). The differences decrease as the distance from the source increases (station A is closer to the source than station E), specifically at frequencies higher than 2 Hz, see for example Figure 2.11b. This condition was not observed for in the analyses of the vertical components were, as shown in Figure 2.11c and Figure 2.11d.

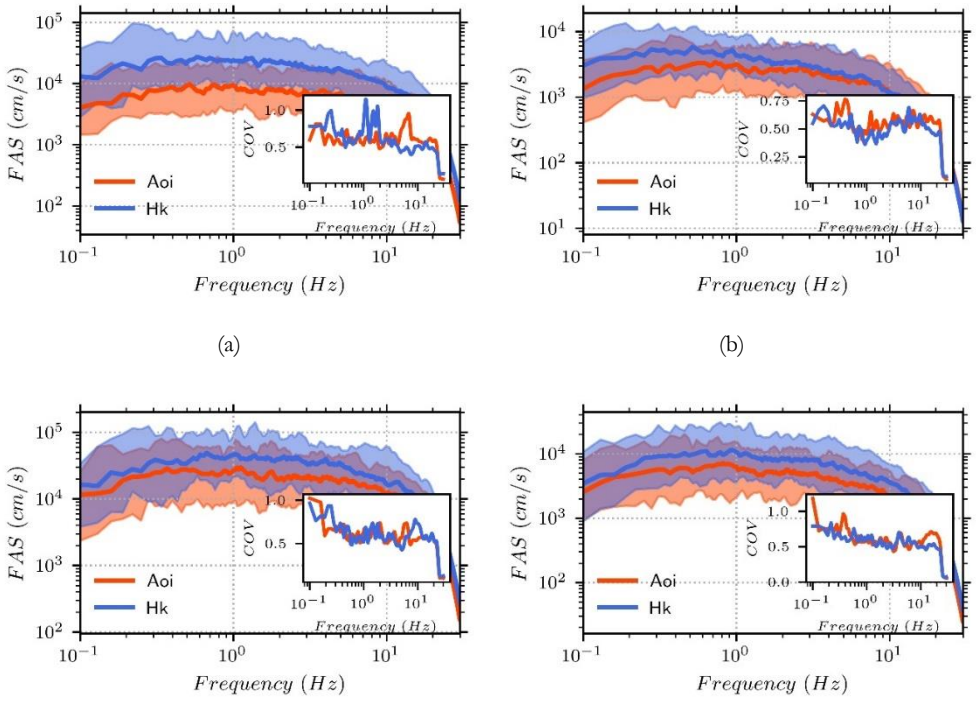

Figure 2.11. Sensitivity to the regional velocity model. Comparison of the FAS of the geometrical mean of the horizontal components at stations A (a) and E (b). Comparison of the FAS of the vertical components at stations A (c) and E (d), respectively. The shaded areas represent the 5^{th} and 95^{th} percentiles. The comparison of the coefficient of variation of the distributions is included in each figure.

The differences observed in the comparison of the FAS considering different regional velocity models were caused by several factors. First, the propagation velocity of the medium, at the depth of the sub-fault, scales the motion to the power of 3 (refer to section 2.2.2). For the herein conducted evaluation, the gradient-like model results in a wide distribution of scaling factors, whereas the Aoi model results in a more compact representation for all sub-sources. Additionally, the free surface and energy partition factors, included in Equation 2.13 and computed for each set with their respective incidence angle distributions affect the amplitude of the FAS. Figure 2.12a shows the free surface factors (FS) as a function of the incidence angle. The same figure also shows the distribution of incidence angles obtained for the P-wave at station A. The inspection of this figure shows that the HK model yielded low incidence angles (closest to the vertical), resulting in larger free surface factor values. The Aoi model, on the other hand, yielded larger incidence angles due to fewer layers and strong impedance contrast among individual layers. The difference between the distributions of incidence angles obtained from different regional velocity models is important and affects the ground motion estimation at different distances from the source. By comparing the FAS of the ground motion component of simulations with both regional velocity models, it was observed that, for stations far from the source, the FAS are similar in the high-frequency range (Figure 2.9a). In fact, the differences between the different FAS for each station increase with the proximity to the source. A couple of factors contribute to this phenomenon. First, the consideration of a different regional velocity model affects the arrival times of the individual sub-fault waves at the site, thus affecting the summation scheme. A gradient-like model, such as HK, results in a wider distribution of arrival of waves at the site (distribution of arrival times for P-waves at station E, Figure 2.12b). In contrast, for the Aoi model, the obtained results showed a narrower distribution of arrival times. This type of spaced summation contributes to lower frequency content in the ground motion for stations farther from the source. These differences in wave arrivals are not noticed for stations closest to the source, as for example for station A (Figure 2.12c).

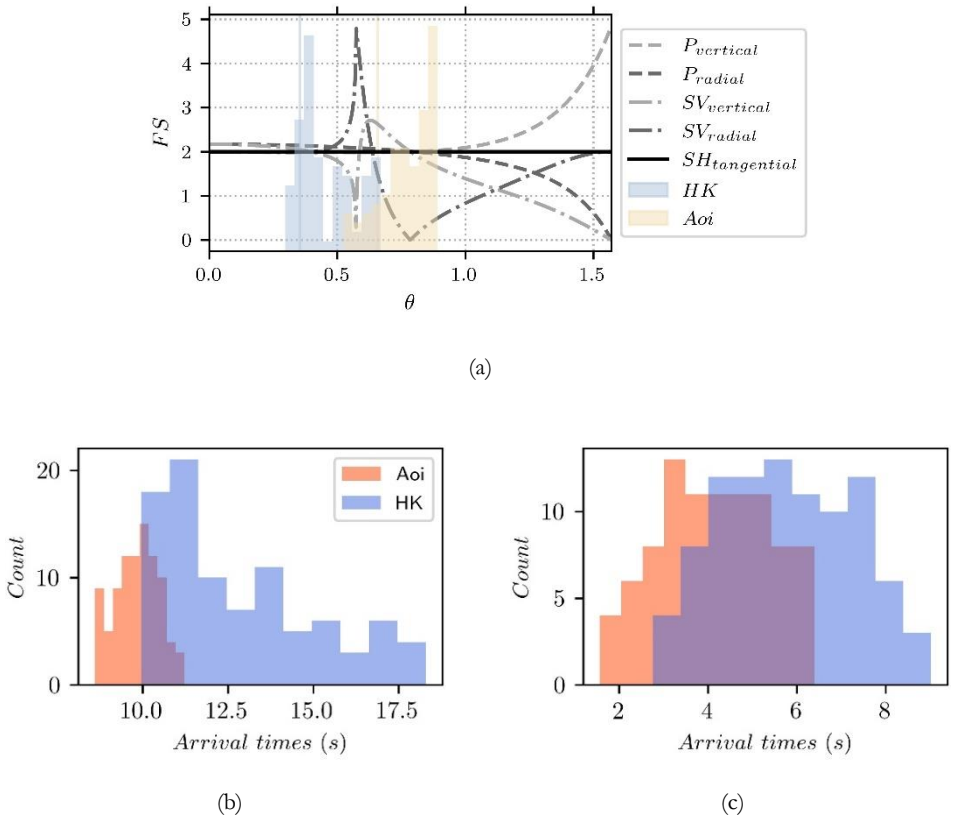

Figure 2.12. (a) - Comparison of the Free Surface factors and incidence angles of P-waves for a simulation at station A. P-wave arrival times for simulations at stations (b) - E, and (c) – A.

The regional velocity structure also impacts the shape of the simulated FAS by affecting the attenuation model described in Equation 2.8. This equation includes the effects of geometrical and anelastic attenuation; however, differences due to the regional velocity model, frequency content, or wave types are included only in the latter. In this equation, a lower propagation velocity at the depth of the sub-fault will increase the attenuation of the waves due to propagation effects. Figure 2.13 shows the attenuation computed following this equation for each of the sub-sources of stations A and E, for frequencies of 0.5 Hz and 5.0 Hz, and considering the two different velocity models. In general, largest attenuation was observed for the gradient-like model due to the presence of layers with lower propagation velocities (Figure 2.13).

The effect of attenuation increases with frequency (when comparing estimates for the same velocity model). See for example the comparison of circular and squared markers in Figure 2.13c for the attenuation at station E, and for frequencies of 0.5 Hz and 5.0Hz, respectively. Figure 2.11b shows a clear example of the importance of attenuation at

higher frequencies, and its enhancing by the consideration of a slower velocity model. Here, the differences in the attenuation computed considering the HK and Aoi models are significantly reduced. With respect to the attenuation of the different wave types, comparisons showed no important difference in the attenuation of P waves considering different velocity models because the anelastic attenuation is lower (Q^P higher than Q^S). This results in the constant offset of the FAS of the vertical component (Figure 13b).

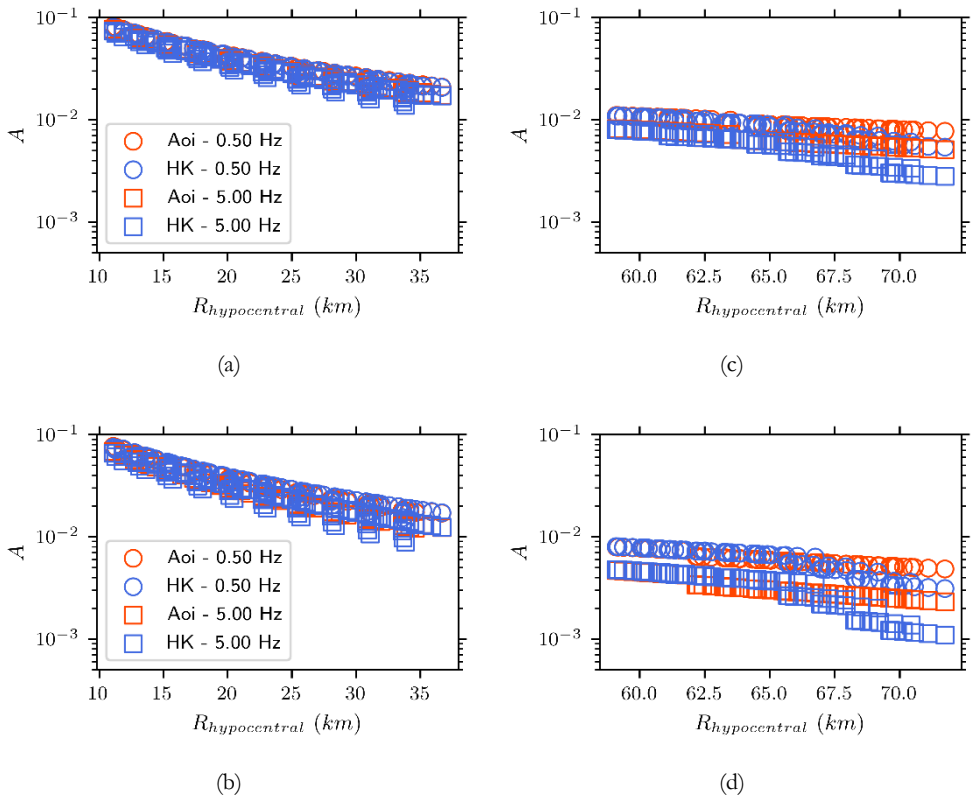

Figure 2.13. Attenuation at station A, (a) - P waves and (b) – S waves. Attenuation at station E, (c) – P waves and (d) – S waves

Finally, Figure 2.14 shows the comparison of envelopes of the acceleration time history for the East-West (EW) and North-South (NS) components simulated at station C. These figures show the differences in amplitude, previously discussed, but also the dissimilarity in overall duration and shape. These divergences are mainly due to the difference in the arrival time of the waves from each sub-source due to the velocity model. A fast model, such as the one proposed in Aoi et al. (2008) results in seismic waves arriving to the observation point without much delay between individual sub-sources, thus resulting in a more compact time history. A slower model, such as the HK model, on the other hand,

results in longer time histories, characterized by the delayed arrival of the contribution from each individual sub-fault. In general, the most important differences are generated by the contrast of propagation velocities at the depth of each sub-source, i.e., for a velocity model having high contrast at different depths, sub-faults located at shallower and slower layers will produce waves that will travel with moderate angles through the slowest layers, resulting in longer propagation times and delayed arrival times of different peaks of energy. Additionally, direct rays produced in deeper and faster layers, will cross the slowest layers with steeper angles resulting in slower travelling times. This behaviour is a consequence of the simplistic discretization of the media and wave propagation mechanisms and could be improved by incorporating more realistic 2D or 3D regional velocity models, which is beyond of the scope of this work.

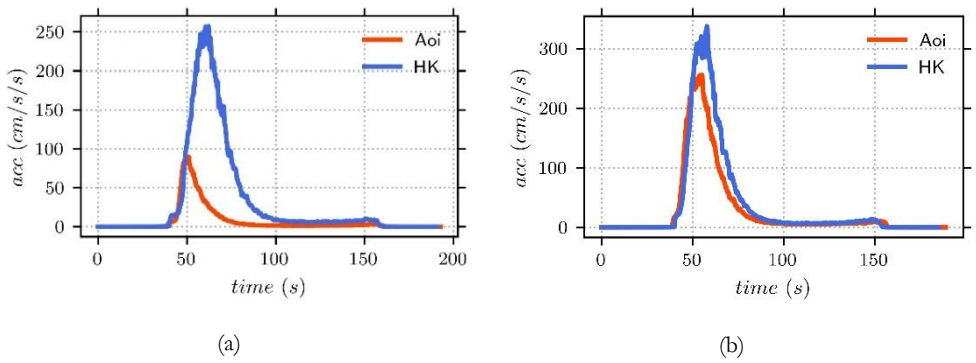

Figure 2.14. Comparison of the envelope of acceleration time histories simulated for station A. (a) EW, and (b) NS components.

2.3.2 Evaluation of the spectral acceleration correlation structure

Section 2.4.1 introduced the proposed post processing produce for the inclusion of the spectral correlation structure in the FAS of simulated ground motions. This section presents the evaluation of this procedure considering the pseudo spectral accelerations due to its traditional role as metric in Earthquake Engineering applications. Specifically, this section presents the analysis of the intra-event residuals, ε, calculated at different periods of vibration, at each station considered in the case study presented in this chapter. These residuals are computed considering the 5% damped response spectra of the stochastic sets and the prediction from a GMM, as shown in Equation 2.29.

$$\varepsilon = \frac{\ln(Sa_{sim}) - (\mu_{\ln(Sa)} + \tau)}{\phi} \qquad \textbf{Equation 2.29}$$

Where $ln(Sa_{sim})$ is the natural logarithm of the spectral acceleration of the simulation, $\mu_{ln(Sa)}$ is the natural logarithm of the mean GMM prediction, τ and ϕ are the inter-event

and intra-event standard deviation terms of the GMM, respectively. In this study, the following GMMs were considered: i) BSSA14 for the RotD50 component, (Boore et al., 2014), ii) Boore1997 for the arbitrary horizontal components, (Boore et al., 1997) and iii) SBSA16 for the vertical component (Stewart et al., 2016). These were selected because of their relevance for the case study, nevertheless, because the correlation structures have been noticed to be unsensitive to the GMM, (Baker & Jayaram, 2008), results are expected to be valid regardless of the considered models Once the residuals were computed for all periods of vibration, the correlation structure between the spectral acceleration at different periods of vibration was estimated with the linear correlation coefficient between residuals at a conditioning period (T_i) and all other periods of vibration (T_j).

Figure 2.15 shows the comparison of the different inter-period correlation structures, for a conditioning period of 1.0s ($T_j = 1.0s$), and for two sets of ground motions, one simulated considering the post processing procedure detailed in section 2.4.1 and one without. These results show that the correlation structure of the simulations, with no post processing procedure, decays too quickly when compared with the empirical models for $SA_V(T_i) - SA_V(T_j)$, $SA_H(T_i) - SA_H(T_j)$, $SA_H(T_i) - SA_V(T_j)$. This is due the use of white noise in the construction of the simulated time histories as pointed out by Burks & Baker (2014) in their evaluation of the EXSIM stochastic ground motion simulation method (Motazedian & Atkinson, 2005). The inspection of the correlation structure for the processed sets demonstrates the capacity of the methodology to embed the empirical correlation structure within the simulated ground motions. An improved match was observed for all inter-period correlation structures, notably, the correlation between spectral accelerations of the horizontal component, $SA_H(T_i) - SA_H(T_j)$, shows the closest fit. Slight discrepancies were observed for the correlation structure related to the vertical component, namely $SA_V(T_i) - SA_V(T_j)$, and $SA_H(T_i) - SA_V(T_j)$. For these cases, the correlation structure was slightly underestimated for periods of vibration closest to the conditioning period T_j. This underestimation was attributed to the use of an inconsistent correlation matrix for the vertical component of the motion. Indeed, in the absence of specific correlation structure for the vertical component, this work extended the horizontal correlation values to this direction. Despite this approximation, that the functional forms of the correlation structures for $SA_V(T_i) - SA_V(T_j)$ and $SA_H(T_i) - SA_V(T_j)$ closely follow those of the reference empirical models.

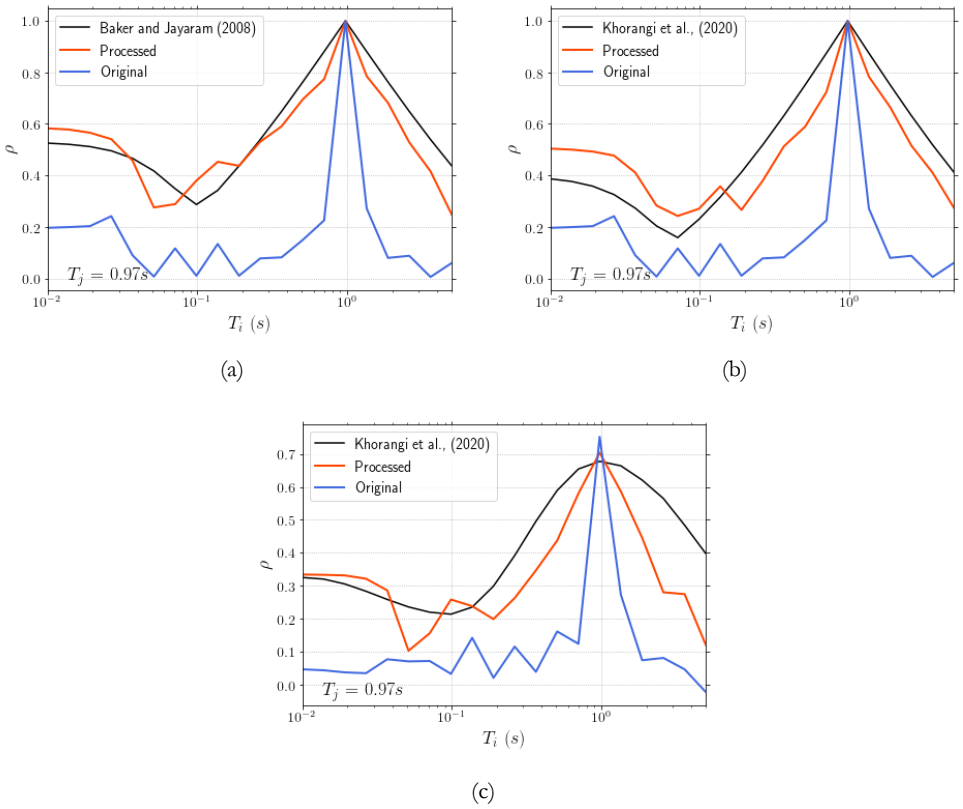

Figure 2.15. Inter-period correlation structure: (a) - $SA_H(T_i) - SA_H(1.0s)$ computing residuals with the BSSA14 model, (b) - $SA_V(T_i) - SA_V(1.0s)$ computing residuals with the SBSA16 model. (c) - $SA_H(T_i) - SA_V(1.0s)$ computing residuals with the BSSA14 model for the horizontal component and the SBSA16 model for the vertical component

The results obtained from the evaluation of the inter-component correlation structure are shown in Figure 2.16. Figure 2.16a shows the correlation structure between horizontal components, $SA_{Hx}(T_i) - SA_{Hy}(T_i)$, whereas Figure 2.16b shows it for the vertical to horizontal component, $SA_H(T_i) - SA_V(T_i)$. The obtained results showed that the post-processed simulations closely approach the reference empirical models in both cases. The slightly larger correlation values when compared to the reference by Baker & Cornell (2006), noticed even for the unprocessed simulations, may be attributed to the missing transformation of P to SV-waves (and vice-versa) due to the reflection and refraction of the waves at each interface of the regional velocity model. Finally, the absence of surface waves in this stochastic model may produce an underestimation of energy at long periods.

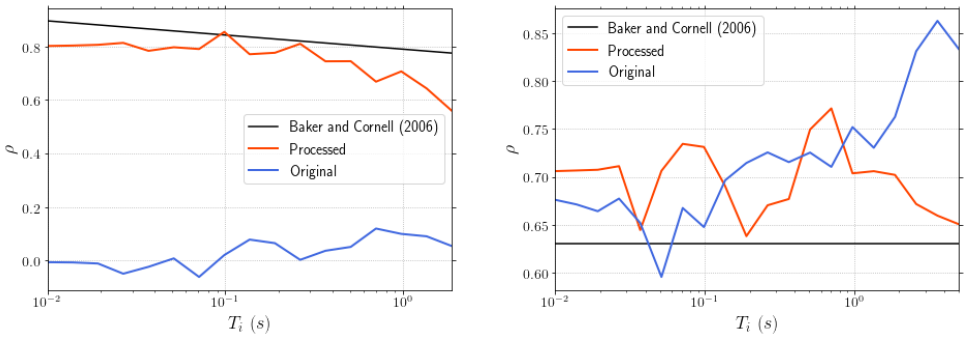

Figure 2.16. Inter-component correlation structure for: (a) - $SA_{Hx}(T_i) - SA_{Hy}(T_i)$ computing the residuals with the Boore 1997 model, (b) - $SA_H(T_i) - SA_V(T_i)$ computing the residuals with the Boore 1997 model for the horizontal components and the SBSA16 model for the vertical component

It is important to acknowledge that for a given pseudo spectral acceleration (for a specific period of vibration) there is a range of frequencies in the ground motion affecting the response of the oscillator. In fact, the relationship between the period of vibration and the contributing range of frequencies in the ground motion is nonlinear, (N. Wang et al., 2019). The adequate representation of the correlation structure in the FAS of the ground motion is thus reflected in the correlation structure of the herein presented spectral accelerations.

2.4 Summary and Conclusions

An improved version of Otarola & Ruiz (2016) 3D stochastic ground motion simulation method was presented in this chapter. The proposed model includes a revised representation of the source, featuring a kinematic model of the rupture and the state-of-the-art definition of the dynamic corner frequency and energy normalization factor, as described by Dang et al., (2022). Additionally, a post-processing procedure to include the inter-frequency correlation structure noticed in databases of recorded ground motions was proposed. This procedure built from the original proposal of Wang et al., (2019) but was herein extended to 3D simulations and to consider the correlation structure between spectral amplitudes in different components of the motion.

In addition, this chapter presents a qualitative assessment of the proposed simulation technique. The assessment included a thorough sensitivity analysis of the input variables considered in the simulation of the ground motion and an evaluation of the features included as part of this work, i.e., the correlation structure of the spectral amplitudes of simulated ground motions. Based on the results obtained from this assessment, the following conclusions may be drawn:

- The stress drop is the most influential parameter in the definition of the ground motion spectrum, like what has been found from other studies of stochastic simulation methods (i.e., Boore et al., 1997)
- When considering different slip distributions, the use of an energy normalization factor produces close mean values of FAS. Individual simulations, however, may strongly be different, especially if the hypocentre location also varies.
- Important differences were observed in the computed FAS when considering different regional velocity models. They include the shape of the simulated accelerograms (in the time domain) and the FAS amplitude. These differences are caused by the direct effect of the regional velocity model in the computation of the incidence angles, the wave arrival times, and their attenuation.
- The herein proposed procedure to include the inter-frequency correlation structure considerably improves this feature in simulated ground motions. This method, however, relies on the assumption that the frequency content of the vertical component of the ground motion is described by the same correlation matrix as that of the horizontal components.

3. SEISMOLOGICAL VALIDATION OF THE 3D STOCHASTIC SIMULATION TECHNIQUE – GROUND MOTION PREDICTION

3.1 INTRODUCTION

As highlighted previously, the development of ground motion simulation methodologies has been an active research field due to their promising capacity to overcome the limited availability of real records. However, to confidently consider these methodologies in earthquake engineering applications, simulated ground motions must be properly tested and validated. Generally, authors have conducted these validations by comparing: (i) seismological features of the simulated and recorded ground motions, considering IMs as reference metric, (ii) The response of structural systems, considering EDPs as reference metric, or (ii) a combination of both.

This chapter focuses on the seismological validation, or testing, of the simulation technique proposed in this work. Seismological validation, or validation through IMs has been traditionally used in studies aiming to introduce or improve ground motion simulation techniques e.g., Atkinson & Silva, (2000); Motazedian & Atkinson, (2005); Otarola & Ruiz, (2016); Pugliese & Sabetta, (1996); S. Ruiz et al., (2018), and many others. The Southern California Earthquake Centre (SCEC) has also set up a platform to implement such a validation scheme for a collection of broadband simulation methods (Dreger et al., 2015; Dreger & Jordan, 2015; Goulet et al., 2015). Due to its wide-spread use by engineers, the most employed validation IM is the spectral acceleration at several periods of interest. Nevertheless, other IMs have also been used in past studies, such as Peak Ground Velocity (PGV), Peak Ground Displacement (PGD), Arias Intensity (AI), significant duration, etc. In addition to these, researchers have also focused on the proposal of validation schemes including proxies for key features of recorded ground motions, such as for example the evolutionary character of the frequency content, signal polarization, non-linear response, and correlation of spectral accelerations in response spectra, (Burks & Baker, 2014). These types of validations often focus on the comparison of simulated ground motions against recordings from historical events, yet empirical statistical models such as GMMs have also been used as reference in the past, e.g., Atkinson & Assatourians, (2015); Bijelić et al., (2018); Burks & Baker, (2014); Frankel, (2009); Lee et al., (2020); Petrone et al., (2021); Star et al., (2011). Most of these studies,

however, have not evaluated the capacity of the simulation techniques to reproduce the inherent uncertainty related to earthquake ground motion, a key feature in the use of simulation techniques for ground motion prediction purposes. In particular, the question that has not been addressed concerns the capacity of the techniques to propagate the uncertainty from input parameters to IMs estimates consistent with the variability observed in recorded ground motions.

This chapter focuses on this aspect, in the validation of the 3D stochastic simulation technique for its use within a ground motion prediction framework, i.e., evaluating not only the correspondence of the simulated and predicted IMs, but also the capacity of technique to reproduce the uncertainty associated to these estimates through the consideration of the uncertainty of the input variables. The comparisons were conducted for a case study considering a generic earthquake scenario and valid GMMs as reference. Finally, this chapter also explores the use of local data for the derivation of the input parameters required for the simulation of ground motions. This as an alternative for regions not very well characterized or for the capturing of site-effects not well represented in analytical models typically considered in ground motion simulation schemes.

3.2 CASE STUDY: NIIGATA, JAPAN

This work considered a magnitude 6.6 (Mw = 6.6) earthquake in the region of Niigata, Japan, as case study. In addition to the definition of this generic scenario, a **reference event**, the 2004 Mw 6.6 Niigata earthquake was also considered in the comparisons conducted for the seismological test of the 3D stochastic simulation technique.

Acknowledging that the main objective of this chapter is the assessment of the simulation technique for ground motion prediction purposes, i.e., in consideration of the uncertainty related to the predicted IMs, the intention of the case study is not to replicate the reference event, but rather the predictions given by valid GMMs for an event matching its causative features. The consideration of a reference event provides an actual observation to the comparisons of simulated and reference IMs, furthermore, it allows for the direct comparison of waveforms not currently available in GMMs.

3.2.1 Observed data

Recorded ground motion time histories of the observed reference event were obtained from the K-NET and KiK-net network databases, (National Research Institute for Earth Science and Disaster Resilience, 2019). The comparisons in this chapter focused on ground motions recorded at a maximum hypocentral distance of 70 km, and for sites with a minimum average shear wave propagation velocity in the upper 30m of 500 m/s ($V_{s30} \geq 500\, m/s$). These filtering criteria intend to exclude, or minimize the influence, of phenomena not included explicitly included in the assumptions of the simulation technique, such as surface waves and non-linear response of the soil, respectively.

Figure 3.1a shows the location of the source model of the observed reference event, as reported in Asano & Iwata, (2009), and the location of the stations of interest with respect to the rupture. Additionally, the description of the shear wave propagation velocity profiles of the soil columns for each of the stations of interest is also shown in Figure 3.1b.

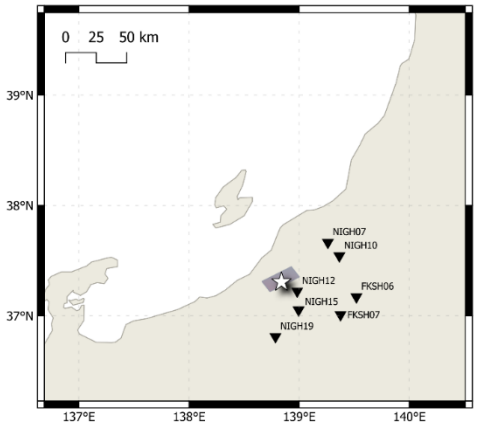

(a)

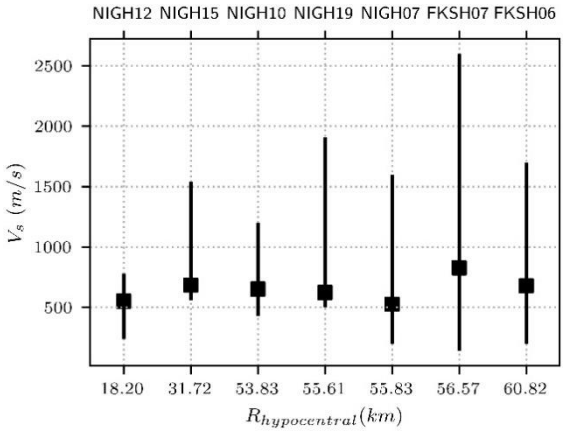

(b)

Figure 3.1. (a) – Projection of the rupture model of the observed reference event, and location of the stations of interest. (b) – Shear wave propagation velocity for all statins of interest, where the point represents Vs_{30}, the upper and lower end of the bars represent the maximum and minimum vs of the soil columns of each station

All downloaded time histories were treated before any manipulation. The processing of the time histories consisted of the following steps:

1. Base line correction by subtraction of the average of the time series.
2. 5% cosine tapering at the beginning and at the end of the signal.
3. Application of a bandwidth (acausal) filter to eliminate the low-frequency noise and the response of the measuring instrument.

This study considered Butterworth filter ($n = 3$), with a with a high-pass corner frequency given by the maximum between (i) The frequency at which the signal-to-noise ratio, SNR, of the motion was above the value of 3, or (ii) The interception of the FAS with a f^2 function, (Boore, 2005). The low-pass corner frequency of the filter was set at 30 Hz since this is the frequency at which an anti-aliasing filter, to account for the effects of the instruments, is applied(Oth, Parolai, et al., 2011).

3.2.2 Input parameters for Ground Motion Simulation

The following sections describe the input parameters considered in the description of the case study for the purpose of ground motion simulation. These sections describe the sampling space of each of the considered input variables, the characterization of the model, i.e., the modelling of the epistemic uncertainty related to the consideration of the different input is discussed in later sections.

3.2.2.1 *Crustal structure*

Two velocity models were considered for the description of the propagation medium. The Aoi and HK models introduced in section 2.3.1.3, and shown in Figure 2.3. These models were thought to be equally likely.

3.2.2.2 *Source model*

A total of 100, equally likely ruptures varying in terms of geometry and slip distribution, were considered for the description of the source. The variability of their geometry was considered with the relationship proposed by Wells & Coopersmith (1994), where the length and width of the fault depend on the size and mechanism of the rupture. Figure 3.2a and Figure 3.2b show the distributions of fault length and width from the source models considered in this study, respectively. The length and width of the observed reference event, as indicated in Asano & Iwata (2009), are also marked in the figures. The depth of the hypocentre was kept constant with respect to that of the observed reference event, therefore, only source idealizations resulting in physically sound ruptures were considered, i.e., rupture geometry lies beneath the floor level. Each of the fault planes was oriented with dip and strike angles sampled randomly from uniform distributions varying between 10°-90° and 0°-359°, respectively. Finally, for the definition of the slip

distribution at each generated rupture, the RIK source model (see section 2.2.1.1) was employed to generate distributions of 1000 asperities uniformly distributed along the rupture surface. Figure 3.2c shows one of the generated source idealizations.

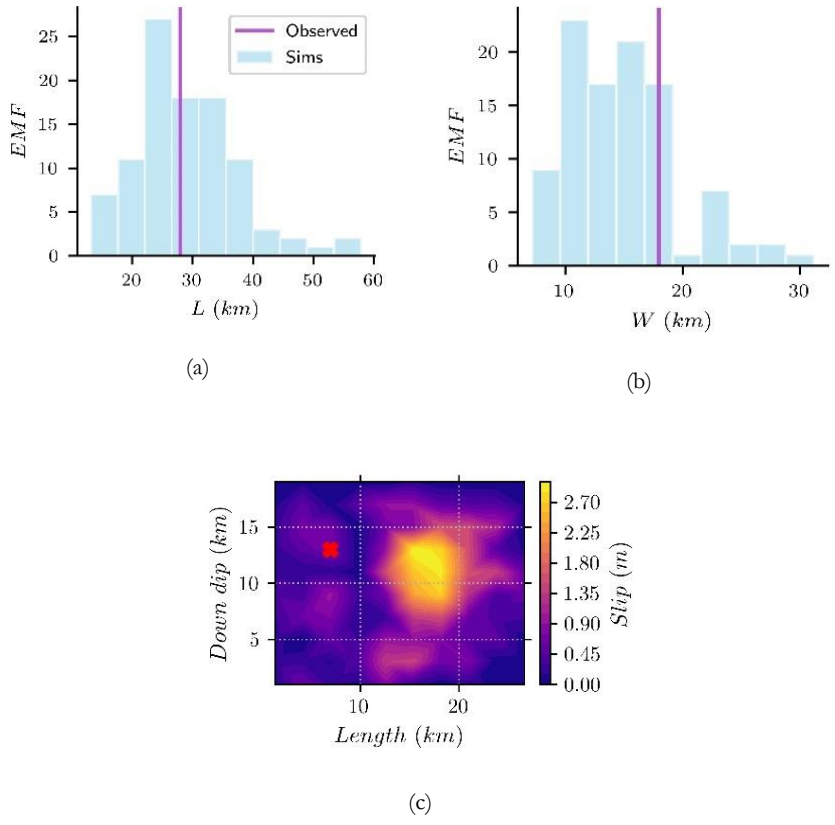

Figure 3.2. Distributions of (a) – fault length and (b) – fault width in the considered source models. The geometry of the reference event, (Asano & Iwata, 2009), is marked with a vertical line. (c) – Source slip distribution example. The hypocentre of the scenario is marked in the figure.

3.2.2.3 *Site effects*

Site effects related to superficial soil layers were considered by means of analytical elastic transfer functions computed with the Haskell-Thompson transfer matrix method, (Haskell, 1953). This method delivers complex transfer functions dependent on the wave type (P, SV, and SH), the 1D column velocity profile, damping and angle of incidence of the seismic wave.

The transfer functions employed in this study were constructed with the soil profiles reported for each station, (National Research Institute for Earth Science and Disaster Resilience, 2019), and considering them to be directly on top of the velocity model considered for the crustal structure. In other words, the computation of the transfer functions considers the uppermost layer of the crustal structure as the infinite half-space over which the soil column lies. Thus, the uncertainty related to the site effects, at each station, comes from considering either of the crustal models in the computation of the transfer functions. It is important to highlight that, because the analytical transfer functions are elastic, the nonlinear response of the soil layers that may occur due to the amplitude of the simulated ground motion is not accounted.

3.2.2.4 *Ground Motion Spectrum*

This study considered the seismological characterization of the area of Niigata introduced in section 2.3.1.1. According to the authors, Japanese crustal earthquakes are characterized by with stress drops following a log-normal distribution with a mean of 11 Bar (1.1 MPa) and a log standard deviation of 0.7. This estimation, however, considers many low-magnitude events and may not be appropriate for the description of the source spectrum of an event in the magnitude range of the case study, (C. Ji & Archuleta, 2021). To better constrain the estimation of the source spectrum, a distribution of stress drop was built with the regressed estimates reported by the authors for the magnitude range of interest i.e., $6 \leq M_w < 7$. A total of 7 events were identified from figure 2 in Oth et al., (2010), with reported stress drops of: 17.65, 20.05, 25.45, 28.03, 28.05, 46.26, 80.90 Bar. These were found to be well represented by a log-normal distribution with a mean of 30.8 Bar and a log-standard deviation of 0.48.

Regarding the attenuation, and as mentioned previously in section 2.3.1.3, the authors reported a geometrical attenuation function $G(R_{hypocentral}) = R_0/R_{hypocentral} = 5/R_{hypocentral}$, and a quality factor function of the form $Q^S(f) = Q_0 f^M$, where $Q_0 = 55 \pm 4$ and $M = 0.77 \pm 0.04$. In the same line, the crustal-related high-frequency attenuation was modelled with the κ_0.parameter following a Gaussian distribution with a mean of 0.029s and a standard deviation of 0.008s.

3.2.2.5 *Site specific S-wave spectral inversion*

This work included the spectral inversion of local recorded ground motions, i.e., generated at approximately the same location as the target event, as an alternative to derive the parameters used in the definition of the simulated ground motion spectrum in areas where such information is not readily available. Furthermore, by considering earthquake scenarios generated at approximately the same location as the reference event, and ground motion recorded at the stations of interest, one could expect the inversion exercise to capture any endemic features that may have been averaged out in the results presented by studies performed at a larger scale, e.g., Oth, Bindi, et al., (2011); Oth et al., (2010); Oth,

Parolai, et al., (2011), or not properly captured by analytical models, such as for example the site specific transfer functions described in section 3.2.2.3.

To mirror a situation with scarce information, the spectral decomposition considered the recorded time histories of 10 low magnitudes events, between 4.0 and 5.0 in the Japan Meteorological Seismic Scale, M_{JMA}, and generated at locations within a buffer distance of 30 km from the epicentre of the reference event. The relative location and key features of these events are summarized in Table 3.1 and shown in, respectively Figure 3.1.

Table 3.1. Low magnitude events considered in the inversion of the FAS

Date	ID	HHMMSS	M_{JMA}	Latitude	Longitude	Depth (km)
18/01/2005	18012005	21:50:00	4.7	37.37	138.99	8.0
25/10/2004	25102004	01:27:00	4.7	37.17	138.76	6.0
25/12/2004	25122004	10:23:00	4.4	37.41	138.96	4.4
02/01/2001	02012001	19:53:00	4.4	37.27	138.6	15.0
02/02/2002	02022002	05:09:00	4.3	37.4	139.85	11.0
21/02/1998	21021998	09:55:00	5.0	37.29	138.76	21.0
08/01/2009	08012009	11:41:00	4.0	37.22	138.83	10.0
09/01/2005	09012005	20:15:00	4.2	37.27	138.94	10.0
02/06/2011	02062011	11:33:00	4.7	37.02	138.71	6.0
05/12/2012	05122012	08:02:00	4.1	37.25	138.94	11.0
07/09/2005	07092005	19:22:00	4.3	37.21	138.83	11.0
08/01/2007	08012007	18:59:00	4.8	37.26	138.92	13.0

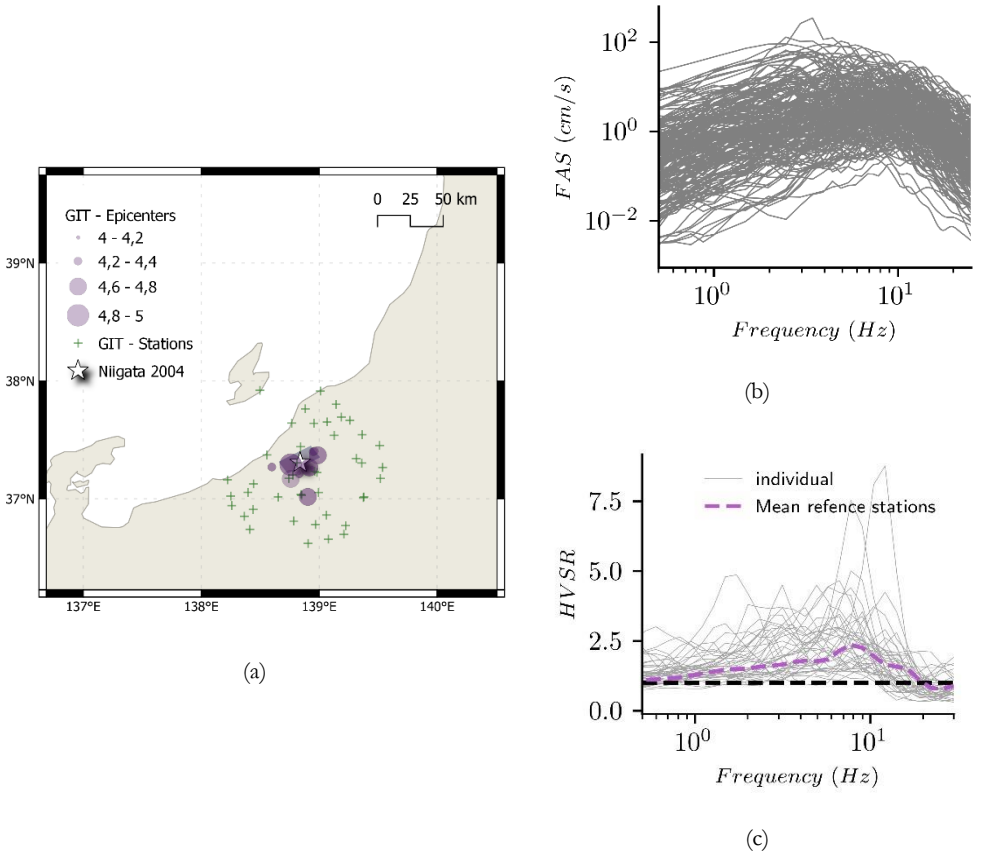

Figure 3.3. (a) – Geographical location of the events and stations considered in the spectral inversion. The figure also shows, for reference, the epicentre of the observed reference event. (b) – S wave FAS of the records considered in the spectral inversion. (c) – Horizontal-to-vertical spectral ratio (HVSR) of all stations considered in the spectral inversion. The dashed line represents the logarithmic mean of the stations considered as reference

A total of 207 tri-component acceleration time histories were downloaded from the K-NET and KiK-Net networks databases, (National Research Institute for Earth Science and Disaster Resilience, 2019), considering a maximum hypocentral distance of 100 km and a minimum Vs_{30} of 250 m/s. All records were processed before performing the inversion by considering the following steps: (i) base line correction by subtraction of the average of the time series. (ii) Application of a band pass (acausal) filter based on the criteria mentioned in section 3.2.1 of this document, (iii) isolation of the S-wave portion of the motion by considering a 5% cosine-tapered time window starting two seconds before S-wave arrival. S-wave arrival was considered as the instant at which 5% of the record's Arias Intensity ($0.05AI$) is reached. The end of the window is considered as the

instant at which $0.80AI$ is reached, however, a minimum and maximum duration of 10s and 15s were considered to provide a minimum frequency step and to avoid the presence of secondary events, respectively. These windows, defined according to Oth, Parolai, et al., (2011), were then checked to verify that the PGA of the record was contained in the considered portion. Finally, iv) computation of the smoothed FAS for all time histories, considering the Konno-Ohmachi window function with $b = 40$, (Konno & Ohmachi, 1998), and combining the horizontal components of each record into their root-mean-square average (RMSA). Figure 3.1b shows the resultant FAS for the RMSA component of the processed ground motions considered in this study.

The spectral decomposition of the FAS was performed with the Generalized Inversion Technique, GIT. This technique was used to isolate frequency dependent attenuation, source, and site characteristic response, much as done in studies such as Bonilla et al., (1997); Castro et al., (1990); Oth, Bindi, et al., (2011). In general, and considering that the isolated windows are characterized mainly by the most energetic SH-waves, the FAS of ground motion may be expressed as follows:

$$U_{jk}(f, Mw_j, R_{jk}) = S_{jk}(f, M_{0j})A(R_{jk}, f)Z_k(f) \qquad \textbf{Equation 3.1}$$

Where $U_{jk}(f, M_j, R_{jk})$ represents the observed spectral amplitude at frequency f, observed at station k, and located at a hypocentral distance R_{jk} from the source of earthquake j with magnitude M_w. $S_{jk}(f, M_{0j})$ represents the source component of the ground motions. Finally, $A(R_{jk}, f)$ and $Z_k(f)$ represent the attenuation due to the path and the site-specific effects, respectively. By taking the logarithm, Equation 3.1 becomes a linear system of the form:

$$\begin{aligned} log_{10}U_{jk}(f, Mw_j, R_{jk}) \\ = log_{10}S_{jk}(f, M_{0j}) + log_{10}A(R_{jk}, f) \\ + log_{10}Z_k(f) \end{aligned} \qquad \textbf{Equation 3.2}$$

Equation 3.2 may be considered a system of the common form $Bx = b$. Where b is a vector containing the observed spectral logarithmic amplitudes and x is a vector containing the logarithmic source, path, and site contributions. Finally, B is the system matrix relating observations and model contributions. This system was solved considering two constraints. First, to obtain the path attenuation component, $A(R_{jk}, f)$ was constrained to be a smooth decreasing function with distance, additionally, attenuation was set as 1.0 at the reference distance R_0. The reference distance was taken as the minimum hypocentral distance from the pool of analysed FAS, in this case $R_0 = 7.5\ km$. Finally, to separate source and site effects, a constraint to the site component of the FAS was set. Typically, this constraint is considered by setting the site term of a reference station to 1.0 for all considered frequencies. This directly implies that the reference site is

subject to no site-effects, a condition very rarely met. Alternatively, the source component of an event j may be considered as reference, e.g., Boatwright et al., (1991). This, however, would require the assumption of a functional form, and would thus constrain from the beginning both site and source effects. In this study, the former option was considered. Figure 3.1c shows a distribution of the horizontal-to-vertical spectral ratio (HVSR) for all stations involved in the inversion exercise and reported in Zhu et al., (2021). From the figure, one may observe that all considered stations show some site-related effect at different frequency ranges. Under these circumstances, the selection of a single station as reference constraint would result in an inversion heavily biased to the shape of the site component of that station. To limit this effect, and to spread the bias resulting from not having an adequate reference station, the average of the site terms of all stations with $Vs_{30} > 500\, m/s$ was selected as reference. This resulted in an almost constant site reference terms with $HVSR < 2.0$, for all considered frequencies, instead of a functional form specific of the site conditions of any of the individual stations.

The system of equations was solved in one step and in a non-parametric fashion for a total of 65 frequencies between 0.5-30 Hz, considering an LSQR solver algorithm and the previously mentioned constraints. This inversion considered the same frequency limits as in Oth, Bindi, et al., (2011) because of the overall quality of the considered data. The minimum frequency of 0.5 Hz relates to the frequency at which the authors found that 75% of the studied time histories have a spectral-to-noise ratio higher than 3 ($SNR > 3$), and the maximum frequency of 30 Hz to the frequency at which the response of the instrument is flat, (Oth, Bindi, et al., 2011). The confidence levels of the estimations obtained from the inversion procedure were obtained by means of Jack-knife resampling of the data (Friedl & Stampfer, 2001). Figure 3.4 shows the non-parametric attenuation functions obtained from the spectral inversion for all considered frequencies. Overall, the attenuation functions were best constrained for the highest frequency range ($f > 10\, Hz$), as it may be noticed from the compact group of attenuation functions. Low frequencies, on the other hand, were characterized by a more erratic decay with distance. Oth, Bindi, et al., (2011) attributed this behaviour to two main causes: i) Considering the low magnitude of the events included in the inversion, low frequencies are usually characterized by higher levels of noise which would affect the spectral decomposition, even after filtering for $SNR > 3$, and ii) low frequencies show an important deterministic component of the radiation pattern, as pointed out in Takenaka et al., 2003); which is incompatible with the point source model considered in the spectral decomposition.

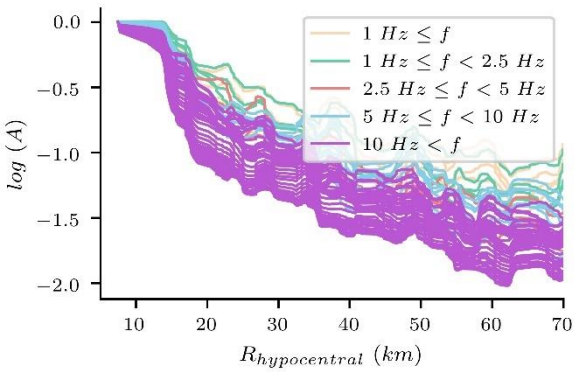

Figure 3.4. Attenuation functions for all considered frequencies as obtained from the GIT

The attenuation functions shown in Figure 3.4 were parametrized for its use within the simulation technique. For this, the typical functional form described in Equation 2.8, and revisited in Equation 3.3, was considered. This equation includes the modelization of the geometrical spreading and the anaelastic attenuation. In this equation, R_0 is the reference distance, $R_{hypocentral}$ is the hypocentral distance to the observation, n is the geometrical attenuation exponent, Q is the quality factor and v_s is the shear wave propagation velocity. Many researchers have discussed about the trade-offs between the definition of geometrical spreading and anaelastic attenuation functions, e.g., Castro et al., (1990) and Oth, Bindi, et al., (2011). Typically, the determination of stable estimates of n and Q, depends on the assumption of either of these parameters, (Oth, Bindi, et al., 2011). In this study, and considering that the simulation technique contemplates only direct body waves, the geometrical attenuation exponent was set to 1 ($n = 1$), this decision allows focusing the parametrization on the quality factor function by means of the minimization of the difference between the non-parametric and parametric attenuation functions.

$$A = \frac{R_0}{R_{hypocentral}} \exp\left[\frac{\pi f (R - R_0)}{Q(f) v_s}\right] \qquad \textbf{Equation 3.3}$$

The minimization procedure was conducted for all 65 considered frequencies, contemplating a sequential least squares algorithm and a functional form $Q(f) = Q_0 f^M$. Before conducting the minimization, the non-parametric attenuation ordinates were grouped in bins of 2 km with the intention of smoothing out the effect of stations at similar distances, but with very different attenuation components. The parametrization procedure resulted in a median quality factor function $Q(f) = 124 f^{0.47}$, with standard errors of 60 and 0.14 for the mean estimates of Q_0 and M, respectively. The large margins of error of these estimates in comparison to those reported in Oth, Bindi, et al., (2011) is due to the limited number of records considered in the inversion process.

Overall, the spectral inversion resulted in less important attenuation when compared to the results reported in Oth, Bindi, et al., (2011). Figure 3.5 exemplifies this observation in the comparison of the attenuation functions for two different frequencies. The figure also shows the increasing importance of the uncertainty in the attenuation estimates with distance. The initial offset of the curves is due to the reference distance considered in the inversions, Oth et al., (2011) consider a reference distance of 5.0 km, whereas the reference in the herein conducted inversion is 7.5 km.

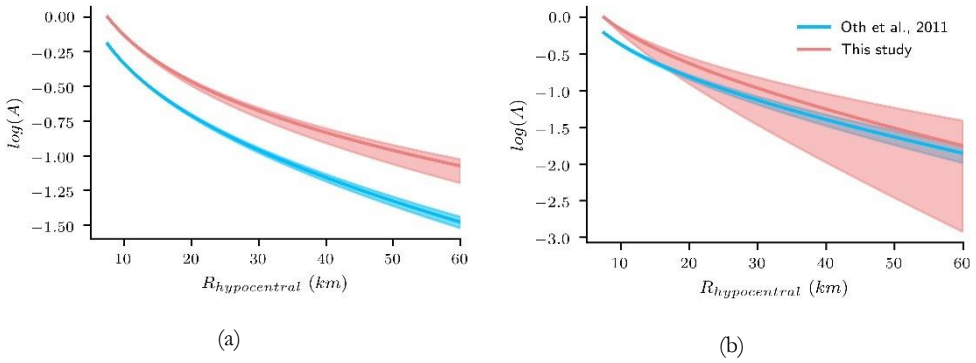

Figure 3.5. Parametric attenuations considered in the generation of the simulated sets. Attenuation for (a) - $f = 1.0\ Hz$, ad (b) - $f = 20.0\ Hz$

The source spectra and site-effects components were also obtained from the one-step spectral decomposition. The site-effect component of the inversion is represented for the stations of interest in Figure 3.6. The figure also shows the transfer functions computed analytically with the Haskell-Thompson methodology, (Haskell, 1953), considering both crustal structures and for a vertical incidence angle. The comparison of these transfer functions shows some similarities between the analytical and empirical results. Nevertheless, important differences in the functional form may be found for some stations, for example, the peak around 8Hz noticed in the transfer function of station FKSH06. Features such as this one may not be captured by analytical models or depend heavily on the assumptions regarding damping and the uncertainties related to soil properties.

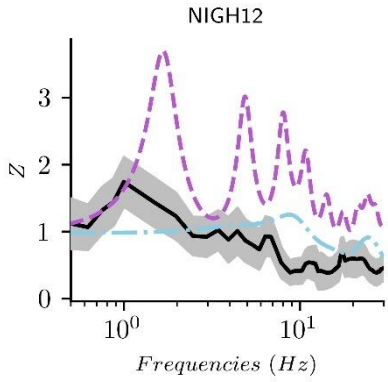
NIGH12
Z
Frequencies (Hz)

(a)

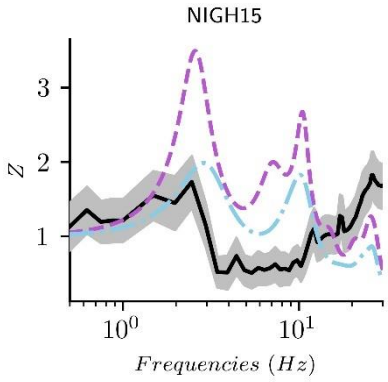
NIGH15
Z
Frequencies (Hz)

(b)

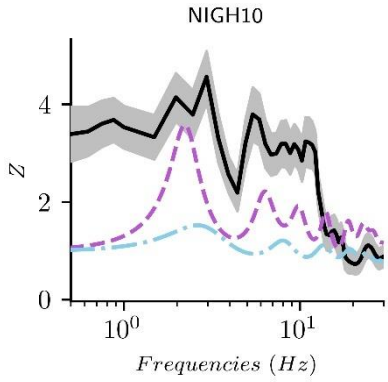
NIGH10
Z
Frequencies (Hz)

(c)

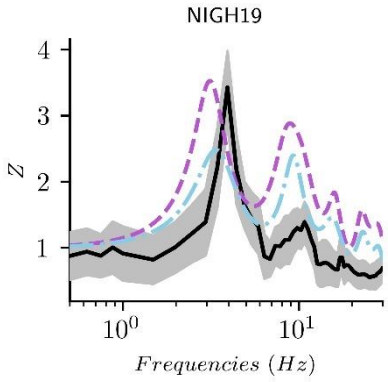
NIGH19
Z
Frequencies (Hz)

(d)

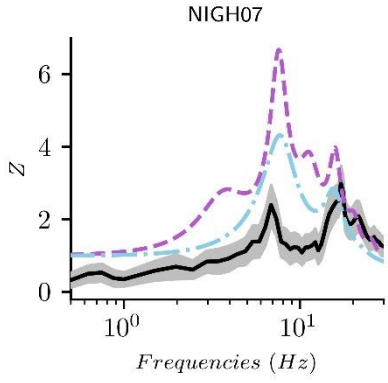
NIGH07
Z
Frequencies (Hz)

(e)

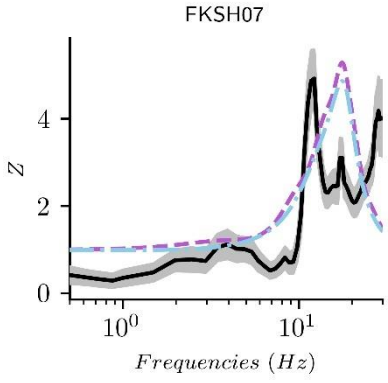
FKSH07
Z
Frequencies (Hz)

(f)

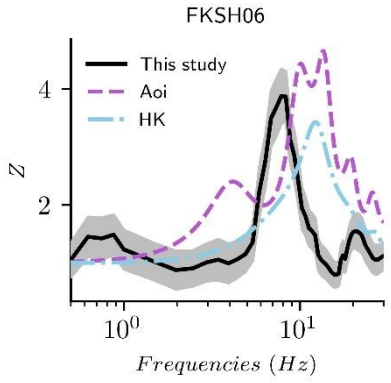

(g)

Figure 3.6. Transfer functions for our stations of interest as obtained from the GIT procedure. Stations (a) – NIGH12, (b) – NIGH15, (c) – NIGH10, (d) – NIGH19, (e) – NIGH07, (f) – FKSH07, and (e) – FKSH06. The figure shows the comparison with the analytical transfer functions computed for the two considered crustal models.

Finally, the source spectra of the events considered in the GIT is shown in Figure 3.7. The figures also display the parametric source spectra obtained from the point-source model described in Equation 3.4, and constructed through the least squares regression of its input parameters, i.e., $\Delta\sigma$, M_0, and κ_0. The point source model shown in Equation 3.4 is identical to that described in section 2.2.1.1, where the corner frequency defining the source spectrum, f_c, is computed considering $\Delta\sigma$ and M_0, as per Equation 2.4. The parametric source spectrum model considered for the regression was completed considering generic parameters consistent with those reported in Oth et al., (2010), i.e., a generic free surface factor, FS, of 2.0, an energy partition factor, EP, of $1/\sqrt{2}$, an average radiation pattern, RP, of 0.55, a medium density, ρ, of 2800 kg m^{-3} and a shear wave propagation velocity, v, of 3500 m/s. The reference distance, R_0, was taken as 7.5 km in agreement with the data considered in the GIT.

$$S(f) = \frac{M_0(RP\ FSEP)}{4\pi\rho v^3 R_0} \frac{(2\pi f)^2}{1+\left(\frac{f}{f_c}\right)^2}\ exp\ (-\pi\kappa_0 f) \qquad \textbf{Equation 3.4}$$

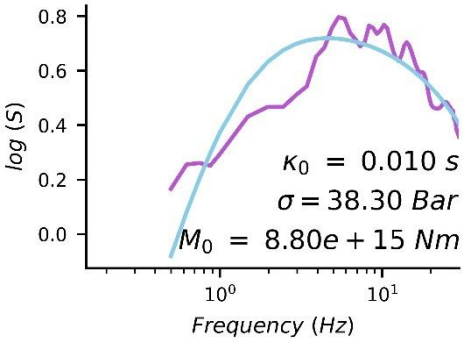
log (S)
Frequency (Hz)
κ0 = 0.010 s
σ = 38.30 Bar
M0 = 8.80e + 15 Nm

(a)

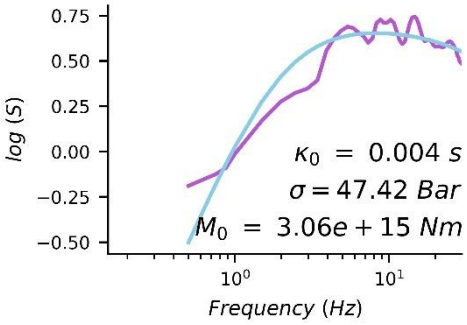
log (S)
Frequency (Hz)
κ0 = 0.004 s
σ = 47.42 Bar
M0 = 3.06e + 15 Nm

(b)

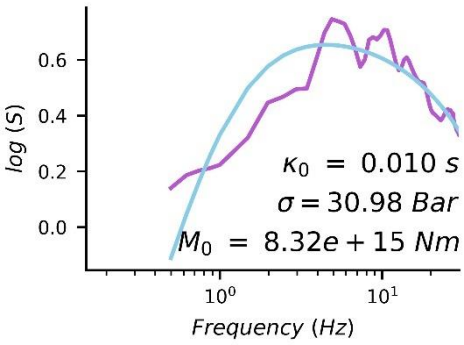
log (S)
Frequency (Hz)
κ0 = 0.010 s
σ = 30.98 Bar
M0 = 8.32e + 15 Nm

(c)

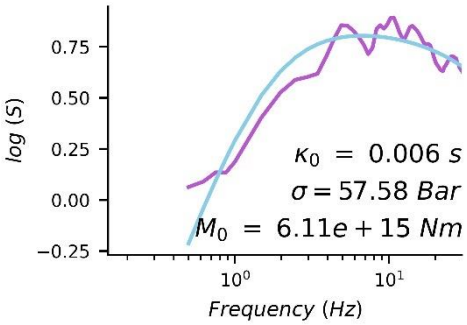
log (S)
Frequency (Hz)
κ0 = 0.006 s
σ = 57.58 Bar
M0 = 6.11e + 15 Nm

(d)

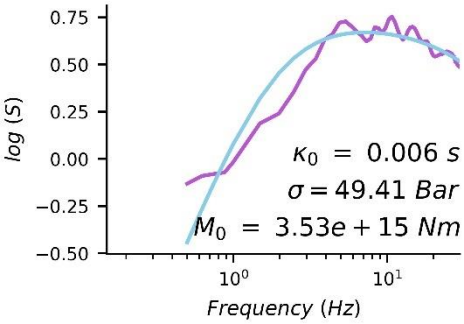
log (S)
Frequency (Hz)
κ0 = 0.006 s
σ = 49.41 Bar
M0 = 3.53e + 15 Nm

(e)

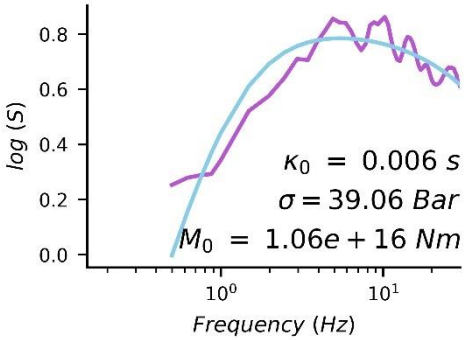
log (S)
Frequency (Hz)
κ0 = 0.006 s
σ = 39.06 Bar
M0 = 1.06e + 16 Nm

(f)

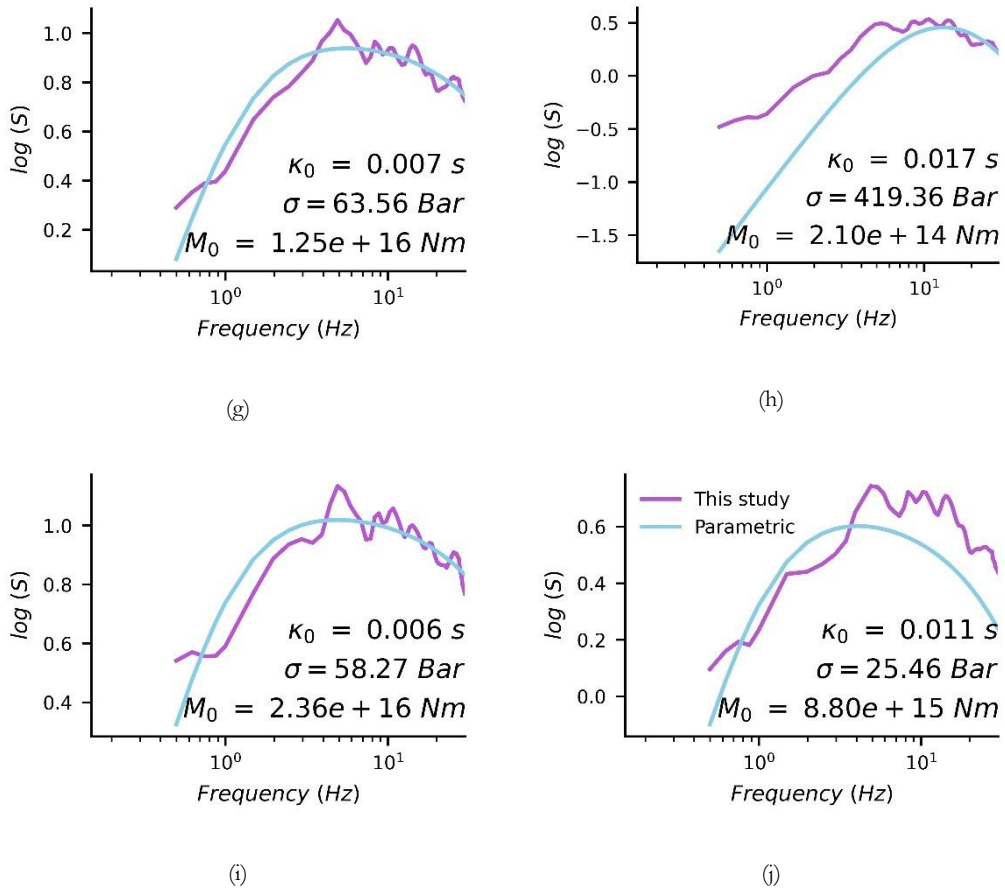

Figure 3.7. Source spectra of the events considered in the GIT, namely: (a)- 020122001, (b) - 02022002, (c) - 25102004, (d) - 25122004, (e) - 01092005, (f) - 18012005, (g) - 08012007, (h)- 08012009, (i) -21021998 and (j) - 02062011. The purple functions represent the non-parametric source spectra obtained from the inversion, whereas the light blue correspond to their parametric representation. The parameters displayed correspond to the values used in the construction of the parametric source spectra.

3.2.3 Modulating window and duration

The description of the simulation technique is completed with the definition of the white noise used in the construction of the time histories. Typically, the duration of the noise, for a given sub fault, is given by the sum of a source related duration, $t_{source} = 1/f_c$, where f_c is the corner frequency of the source spectrum, and a distance related duration term, in this case considered as $t_{distance} = 0.07R_{hypocentral}$, (Atkinson & Assatourians, 2015). These terms, however, were not associated to any uncertainties and

thus the variability of the duration is completely dictated by that of the corner frequency. In addition, no information is currently available, to the authors knowledge, for the modelling of the time modulating window functions, at least not in consideration of the uncertainty related to this feature.

In this study, the Saragoni-Hart modulating window, (Saragoni & Hart, 1973), introduced in Equation 2.18, was considered as modulating function. In this application, the parameters used in the construction of the modulating function were employed to model the uncertainty related to ground motion duration and overall shape of the simulated time histories. A grid search algorithm was considered to define the distributions of the input parameters: e, η and f_{Tgm}, modelling the location of the peak, decay and elongation of the modulating window, respectively. This algorithm to directly compared a target duration and the duration of sets of simulations for the defined stations of interest. Three significant durations, predicted by the ground motion model reported in Afshari & Stewart, (2016) and herein referred to as AS16, were considered as target. These are, the duration between 5% - 95% (D_{5-95}), 5% - 75% (D_{5-75}), and 20% - 80% (D_{20-80}) of the ground motions arias intensity of the GM component.

The following points describe the grid search process considered in this study:

- Definition of the window models

  First, the sampling space for each the variables was specified. These were considered as uniform and with the following boundaries: $e \in \{0.05, 0.5\}$, $\eta \in \{0.001, 0.5\}$, and $e \in \{0.1, 3.0\}$. Next, a total of 100 combinations of these parameters was defined by mean of LHS sampling. Each of these represents a possible model for the modulating window.

- Definition of the target scenarios

  A total of 100 target scenarios were defined. These scenarios include the three significant durations, computed with the AS16 GMM, for each of the stations of interest.

- Grid search

  A set of 100 three-component simulations was generated for each station of interest, and for each possible window model. A total of 10000 simulations were conducted for each station. Next, a score was given to each simulation set (defined by the considered window model) measuring the divergence between the mean and the standard deviation of the target and simulated durations. Finally, the window model with the lowest score was selected and the parameters defining the model were stocked.

The results obtained from the grid search process are summarized in Figure 3.8. Overall, the elongation factor, f_{Tgm}; shown in Figure 3.8a follows a lognormal distribution of mean 0.51 and log standard deviation 0.80, whereas the parameters e and η, modelling the location of the peak and the decay, respectively, do not seem to follow such a clear distribution thus suggesting the little relevance of these variables for the definition of the overall duration. A correlation coefficient of 0.3 was found between e and η, this correlation is evidenced in the scatter plot shown in Figure 3.8b. Other variable combinations show no relevant correlations.

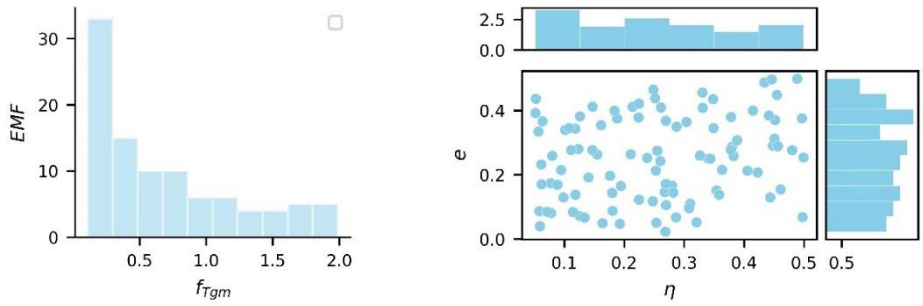

(a) (b)

Figure 3.8. Results from the grid search procedure. (a) – Histogram of f_{Tgm}, and (b) – Joint dispersion plot and histogram for e, η

3.3 RESULTS

The evaluation focused on the comparison of spectral acceleration at different periods of interest, and significant duration for different thresholds of energy (measured with percentages of the arias intensity). The comparisons were conducted considering valid GMMs as reference. Specifically, this work considered the ground motion model developed by Kotha et al., (2018) for the spectral accelerations of the GM component, Stewart et al., (2016) for the spectral acceleration of the UD component, and Afshari & Stewart, (2016) for the significant durations of the GM component. In addition, the comparisons considered the IMs obtained from the observed reference event (see section 3.2.1).

The simulated ground motions were conceived by means of Monte Carlo sampling of the crustal and source models, the variables constructing the simulated ground motion spectrum and the site-effects. Two different sets of simulated ground motions were considered in the comparisons, **Set A,** which represents a case where information is readily available, was generated considering the input variables for the construction of the simulated ground motion spectrum reported in Oth, Bindi, et al., (2011); Oth et al., (2010); Oth, Parolai, et al., (2011), and the analytical site effects computed with the soil columns

of each station of interest. **Set B,** on the other hand, represents a case where no information is readily available. This condition was represented using the attenuation and site effects obtained from the inversion of local data. The source spectra and the high-frequency attenuation, however, were modelled with the distributions of $\Delta\sigma$, κ_0 reported in Oth et al., (2010), respectively. This with the intention to maintain the causality of the simulations since the GIT inversion did not consider events in the magnitude range of the case study. To account for the intra-evet variability, all simulations were conducted considering different random seeds in the construction of the white noise. Same as with observed reference event, the simulated ground motions were treated before the computation of any IM. The post processing of the simulated time histories was conducted following the procedure detailed in section 3.2.1.

The number of simulations per station, and within each simulated set, was defined by evaluating the stability of the distributions of the IMs of interest. Stability was measured with the relative variation of the mean and standard deviation of spectral accelerations, at different periods of vibration and for incremental numbers of simulations. Figure 3.9 shows the evolution of these variations for the dominating case in this study, PGA at station NIGH12 and considering the model for description for **set B**. By setting a maximum target variation of the mean and standard deviation of 5%, a minimum of 100 simulations was defined.

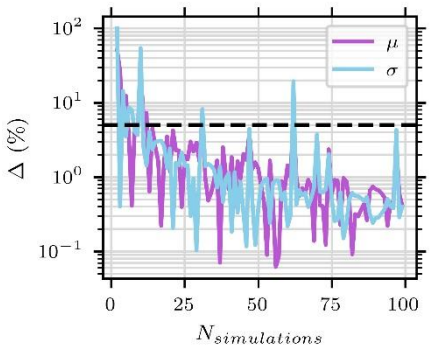

Figure 3.9. Percentual variation of the mean and standard deviation of PGA at station NIGH12 between incremental number of simulations. The dashed line represents the defined performance limit (of maximum variation) of 5%.

A comparison of the simulated and observed FAS, acceleration, and velocity time histories (for all stations of interest and simulated sets) is included in the appendix. Figure 3.10 and Figure 3.11 show these comparisons for the stations closest and furthest to the source, i.e., stations NIGH12 and FKSH06, located at a hypocentral distances of 18.2 km and 60.8 km, respectively. The time histories shown in the figure correspond to the scenario with the median Arias intensity of the GM component, $\mathbf{AI_{GM}}$. To facilitate the

comparison of the these, the observed and synthetic acceleration time histories were aligned at the instant at which 0.01AI is achieved. Overall, both simulated sets resulted in similar acceleration time history waveforms for all considered stations. The median scenarios were observed to agree with the waveforms of the reference event, not only in terms of maximum amplitude, but also in the evolution of the amplitude over the duration of the ground motion. This agreement, and the overall match of the target and simulated ground motions durations shown in ,Figure 3.12 are mainly attributed to the calibration of the modulating windows discussed in section 3.2.3. For the sake of brevity, the figure shows only the results from set A (considering the results obtained from simulations considering both crustal models), however, the conclusions drawn from the comparisons with set B are identical.

The comparison of the FAS allowed the assessment of the differences between the different simulated sets. For example, in Figure 3.10, its seen that the median scenario obtained from set B was able to capture the distinctive peak noticed in the reference event at 8 Hz, whereas that obtained from set A was not. This observation leads to believe that the transfer functions computed from the inversion of local data allowed for the modelling of an endemic features not properly captured by the analytical transfer functions. The comparison of FAS also exposes the divergences in the intermediate and low frequency content noticed between observed and simulated ground motions, a condition also noticed in the comparison of the velocity time histories, shown Figure 3.10b and Figure 3.11b.

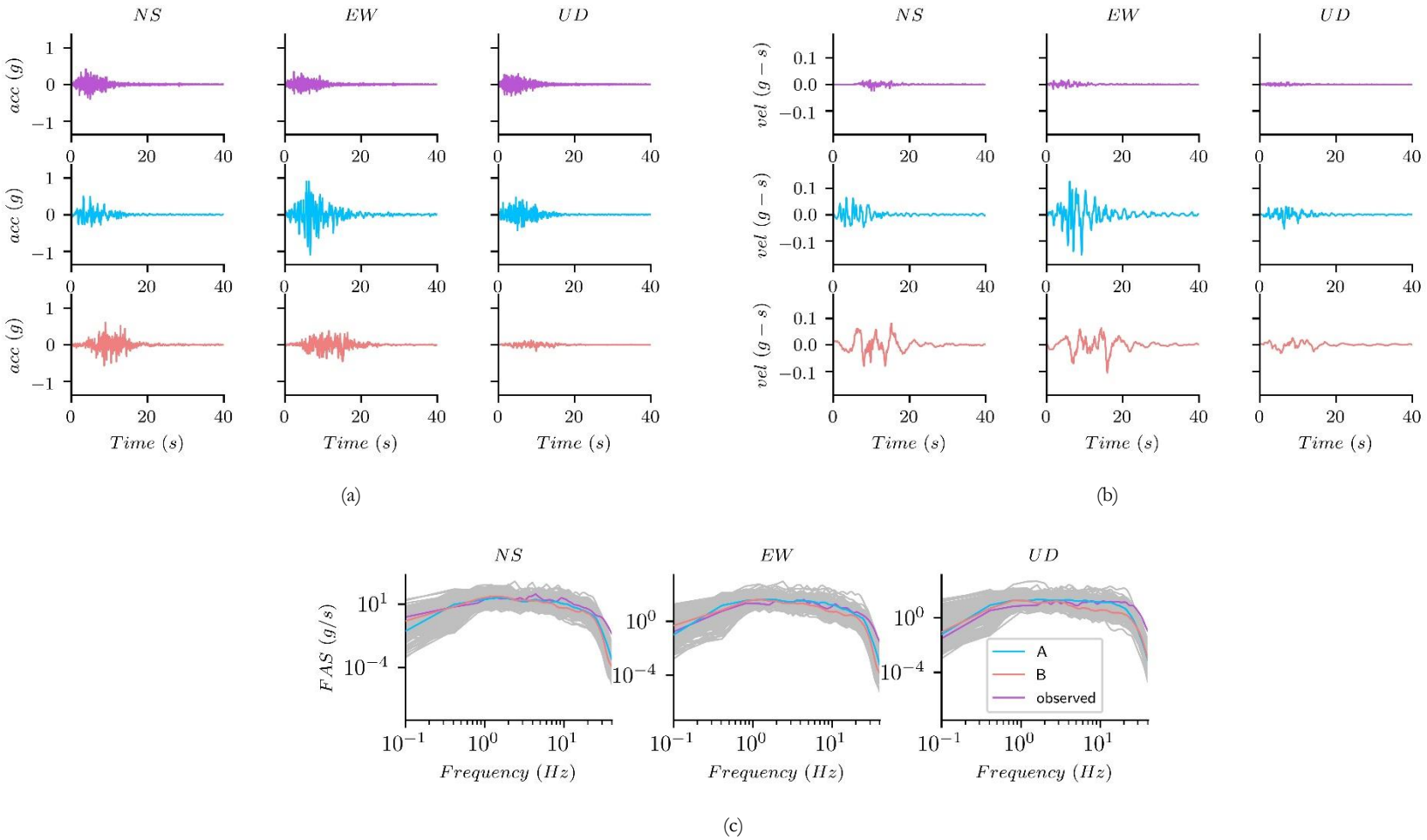

Figure 3.10. Comparison between observed and simulated ground motions for station NIGH12. (a) –Acceleration and (b) – velocity time histories. To facilitate the comparison of the time histories, these were aligned at instant where 1% of the maximum arias intensity (AI) is reached. The shown simulated scenarios correspond to the median AI of the GM component. (c) – Comparison of smoothed FAS, the grey lines correspond to individual simulations and the highlighted scenarios correspond to the median of the distributions.

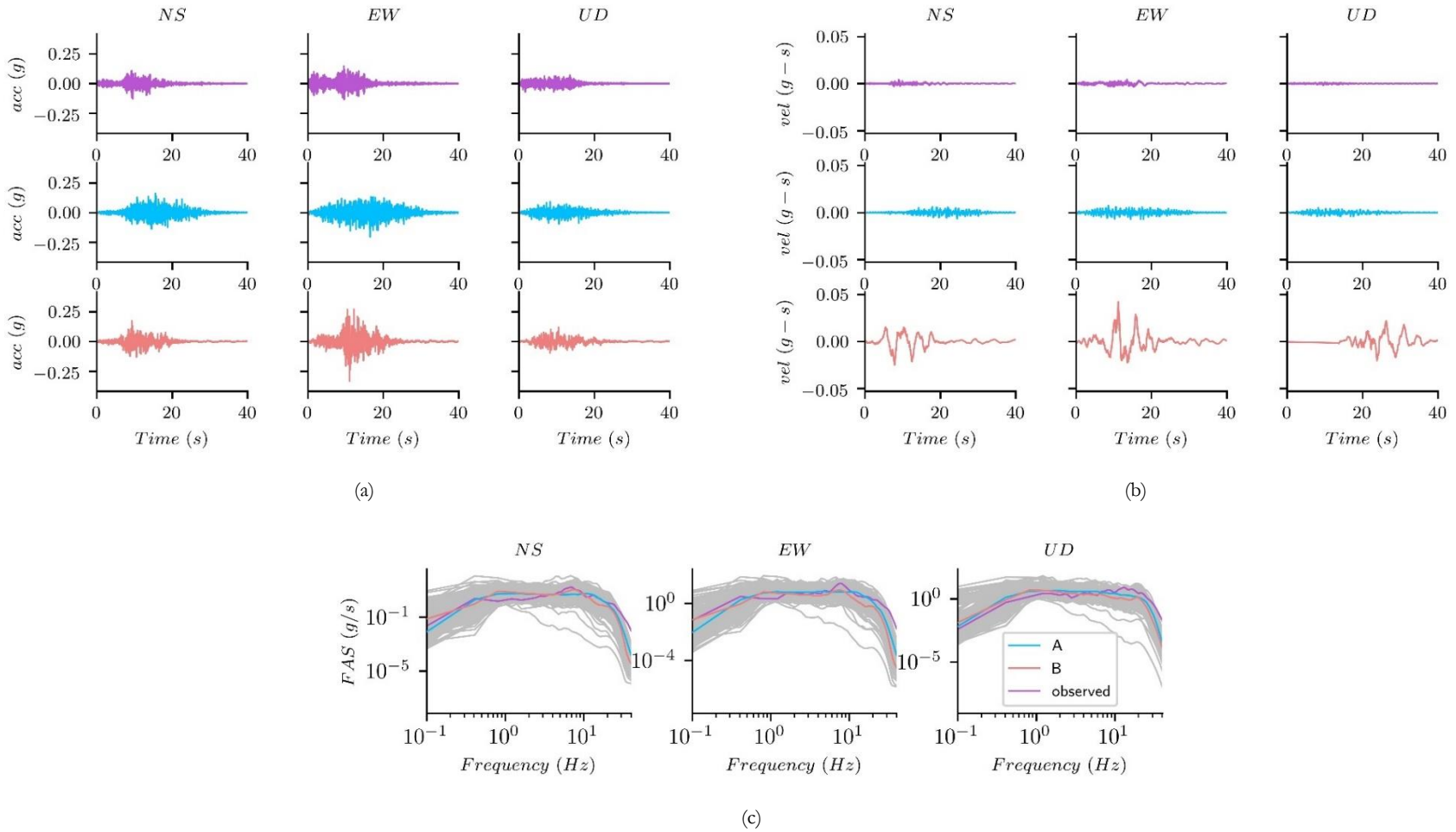

Figure 3.11. Comparison between observed and simulated ground motions for station FKSH06. (a) –Acceleration and (b) – velocity time histories. To facilitate the comparison of the time histories, these were aligned at the instant where 1% of the maximum arias intensity (AI) is reached. The shown simulated scenarios correspond to the median AI of the GM component. (c) – Comparison of smoothed FAS, the grey lines correspond to individual simulations and the highlighted scenarios correspond to the median of the distributions.

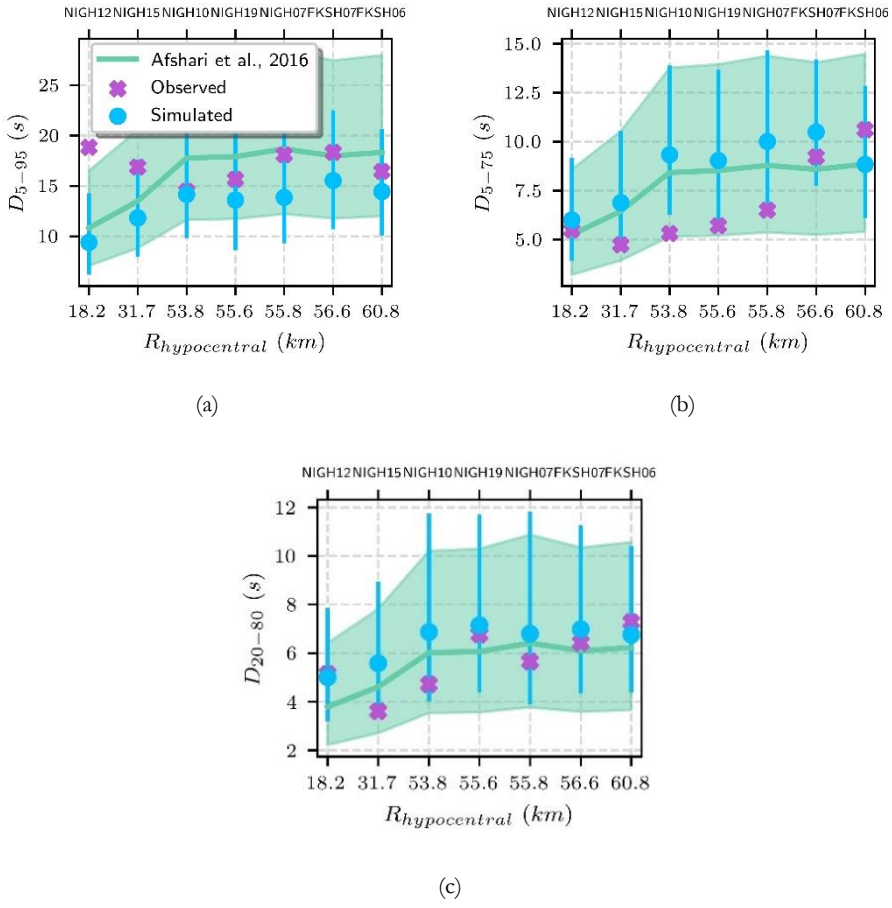

Figure 3.12. Comparison of different significant durations for the stations of interest and simulated set A. Duration between (a) – 5%-95%, (b) – 5%-75%, and (c) – 20%-80% of the Arias intensity of the geometrical mean of the horizontal components. The shaded area and the bars represent the space between $\pm 1\sigma$ for the predictions considering the Afshari et al., (2016) and simulated models, respectively.

A comparison of spectral accelerations at different periods of vibration is shown in Figure 3.13 and Figure 3.14 for the GM and UD components, respectively. The figures show the comparison of the predictions from the reference ground motion model, the simulated sets, and the observed spectral accelerations from the reference event. Due to the availability of the site-specific residuals resulting from the calibration of the GMM model, this work considered an ergodic and a site-specific reference prediction. The ergodic estimation refers to a "regular" application of the GMM, where one considers that the

variability in ground motion at a single site-source pair is the same as the variability in ground motion observed in a more global dataset,(al Atik et al., 2010). The site-specific application, on the other hand, considers the site-specific residuals ($\delta S2S_s$) obtained from the regressions performed in the construction of the GMM. The site-specific application may be regarded as a partial non-ergodic prediction because the ergodic assumption remains for the between event term (δB_e) of the uncertainty. This estimation results in a more realistic representation of the ground motion, associated not only to a reduced uncertainty, but also to a much closer agreement with the herein presented simulated scenario, i.e., in consideration of magnitude specific source parameters, site-specific transfer functions, and for the GIT case, local attenuation curves and empirical transfer functions.

Figure 3.13 shows that the mean spectral accelerations computed from the simulated sets fairly match the predictions from the reference GMM for all considered periods of vibration. The spectral accelerations from the observed event coincided with the predictions from the GMM and simulated sets for periods of vibration below or equal to 1.0s. When considering higher periods of vibration, the simulated ground motions resulted in spectral accelerations closer to the reference GMM than the observed reference event. The comparison of the predictions from the simulated sets indicated that set B matched better the predictions from the reference for all stations but NIGH10. This improvement was mainly due to the consideration of empirical transfer functions better modelling the site-effects. The quality of these, however, is completely dependent on the quality of the records considered in the GIT (representative of the variability of the ground motion). One of its main drawbacks it's the absence of a clear reference station, or set of stations, for the deconvolution of the source and site components. The lack of such a reference led to the inaccurate approximation of the site effects at station NIGH10 as noticed from the overall offset of the empirical transfer function with respect to those estimated by the analytical models. In addition to the comparison of the mean spectral accelerations, the figures also display the comparison of the standard deviation associated to the predictions of GMM and the simulated sets.

The standard deviation from the simulated sets was found to be between the ergodic and site-specific estimations of the reference GMM for periods of vibration below 1.0s. In fact, the standard deviation of the simulated sets increases with the period of vibration for all considered stations, thus leading to believe that the increase in the uncertainty is directly linked to the epistemic modelling of the source and the overall modelling simplistic modelling of the rupture of the fault. Some exceptions, where standard deviation of the simulated sets exceeds that of the reference GMM for all periods of vibration, were noticed. Specifically for simulation set B and station NIGH07, which is characterized by the lowest Vs_{30} and one of the highest contrasts in the velocities of the soil column, thus leading to believe that site effects considerably affect the response at this station. Finally, the

comparison of the uncertainty estimates between both simulated sets showed little differences, except for the case of NIGH07, for periods of vibration below 2.0s. This match was attributed to the fact that both sets of simulations consider the same distribution of $\Delta\sigma$, κ_0 and for the construction of the source spectrum and the attenuation of the high frequencies, respectively. These parameters were noticed to be the most influential in the simulation of the high-frequency component (see section 2.3.1.1), and thus their uncertainty dictates that of the spectral accelerations for the shortest period range. For larger periods of vibration, set B was noticed to result in higher standard deviation values due to the larger error associated to the attenuation and site effects obtained from the GIT. The overall estimates of standard deviation are completely dependent on the epistemic modelling considered for the input variables, for example, different standard deviations would be expected if only one crustal model was considered of if more weight was given to any of the two options.

The comparison of spectral accelerations computed from the vertical component of the ground motions is shown in and Figure 3.14. These comparisons consider only the ergodic application of the reference GMM due to the lack of the site-specific residuals. The obtained results indicated that simulations consistently overestimated the amplitude of the vertical component of the motion when compared to the considered reference model and the observed reference event. In general, the estimations obtained from simulated set B were closer to the references when compared to those from set A. This observation is specifically true for stations furthest from the source, which indicates that the attenuation functions estimated from the GIT were a better approximation to the context of the region that the generic values obtained from the literature. The overestimation of the vertical component may be due to different factors such as the simplistic approximation of the corner frequency of P-waves based on the ratio of propagation velocities at the depth of the sub-faults (Equation 2.6). Another likely cause may be the limitations of the model in the representation of phenomena such as the transformation of P to SV waves, and vice versa, due to the reflection of seismic waves at the interface of the layers of the velocity models. These limitations need to be further explored. Finally, the analysis of the compared standard deviations leads to the same conclusions as those obtained from the analysis of the horizontal components.

Figure 3.15 and Figure 3.16 show the bias, for set B, of the spectral acceleration for different periods of vibration (logarithmic ratio of the reference and simulated), and as a function of hypocentral distance and $\boldsymbol{Vs_{30}}$, respectively. These comparisons included all the stations considered in the GIT, and not only the reference stations mentioned in previous comparisons. In general, the analysis of the biases showed that the simulation technique is more accurate in the representation of the high-frequency content, thus matching the observed reference in the short-period range better. The comparisons indicated that adequate matches were found (for the stations of interest) for periods of

vibration of 2.0s and 0.5s for the GM and vertical component, respectively. The analysis of the biases as a function of distance, shown in Figure 3.15, revealed that the simulation technique was more accurate in representing the spectral content of the observed reference for stations closest to the source, specifically below 75 km. This is due to the increasing importance of surface waves, not explicitly modelled in the methodology, in ground motions recorded at stations far from the source. Finally, regarding the comparison of the biases as a function of the site, here measured by Vs_{30}, the obtained results suggested that the technique was more accurate for stations with $Vs_{30} > 400\ m/s$, where the hypothesis of linear soil response was more valid. These conclusions were found to be applicable also for the biases computed with set A (shown in the appendix).

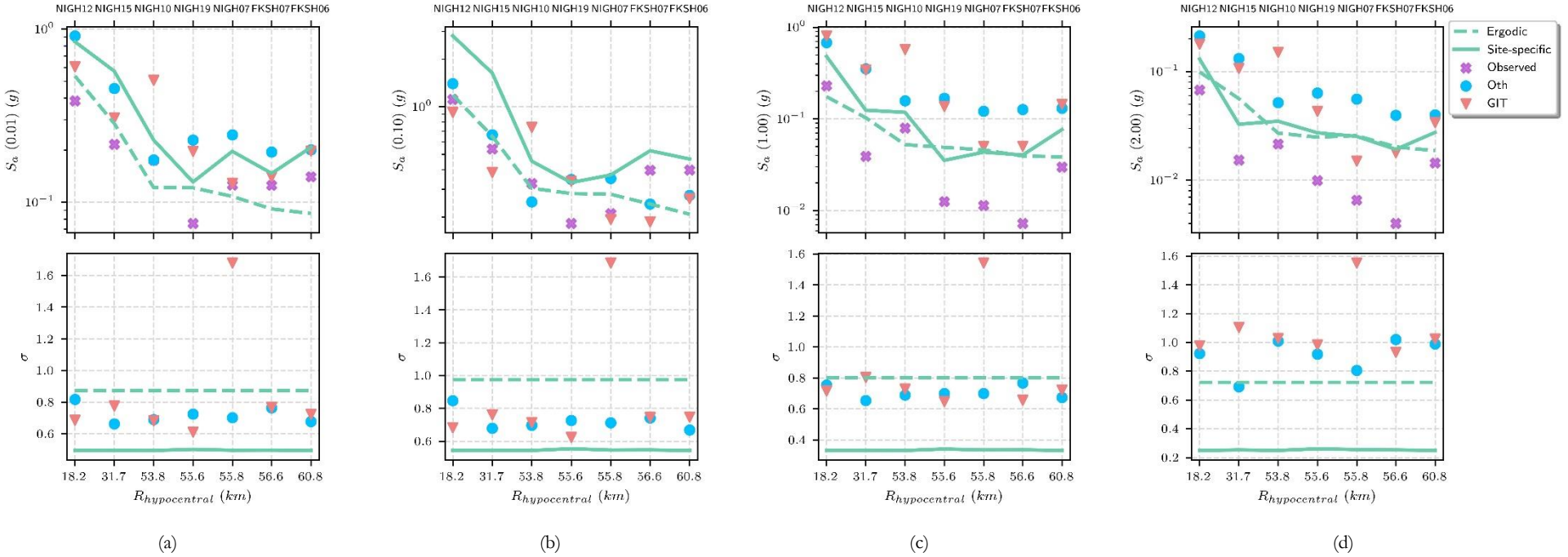

Figure 3.13. Comparison of mean and standard deviation of spectral accelerations for the geometrical mean of the horizontal components (GM). Observed, simulated, and predicted for the stations of interest and at different periods of vibration, (a) - $Sa(0.01s)$ or PGA, (b) - $Sa(05s)$, (c) - $Sa(1.0s)$, and (d) - $Sa(2.0s)$.

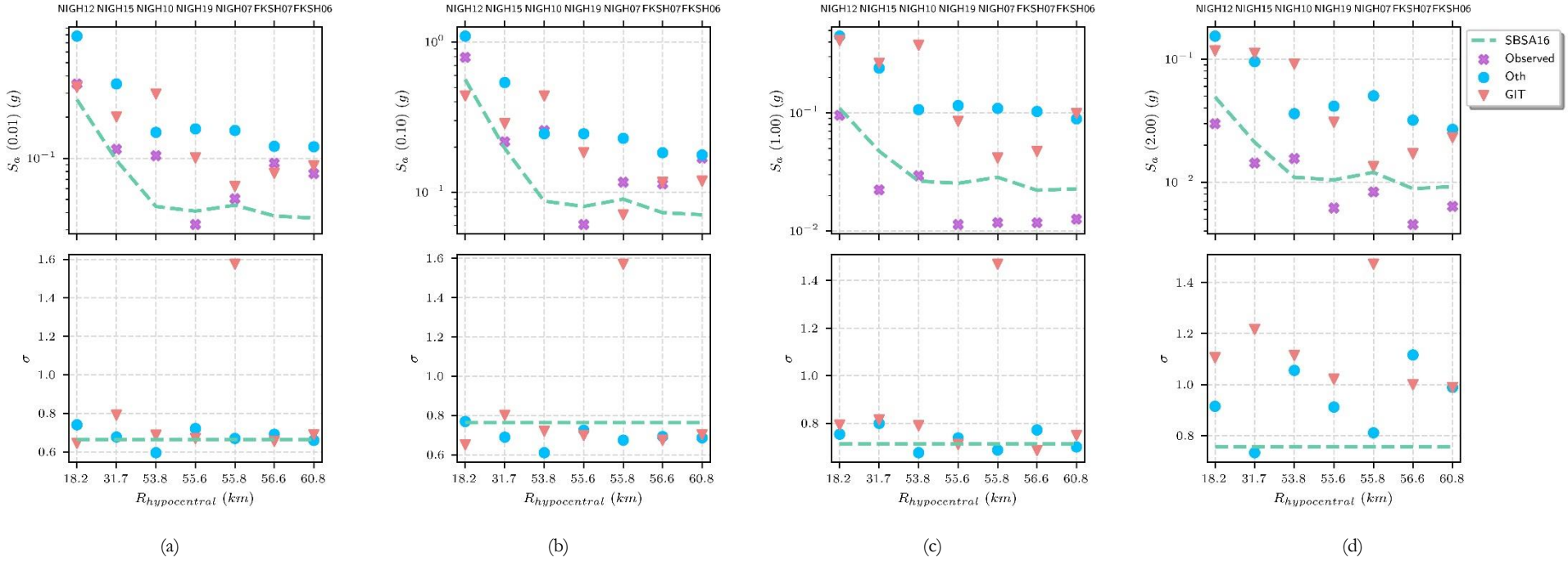

Figure 3.14. Comparison of mean and standard deviation of spectral accelerations for the vertical component (UD). Observed, simulated, and predicted for the stations of interest and at different periods of vibration, (a) - $Sa(0.01s)$ or PGA, (b) - $Sa(05s)$, (c) - $Sa(1.0s)$, and (d) - $Sa(2.0s)$.

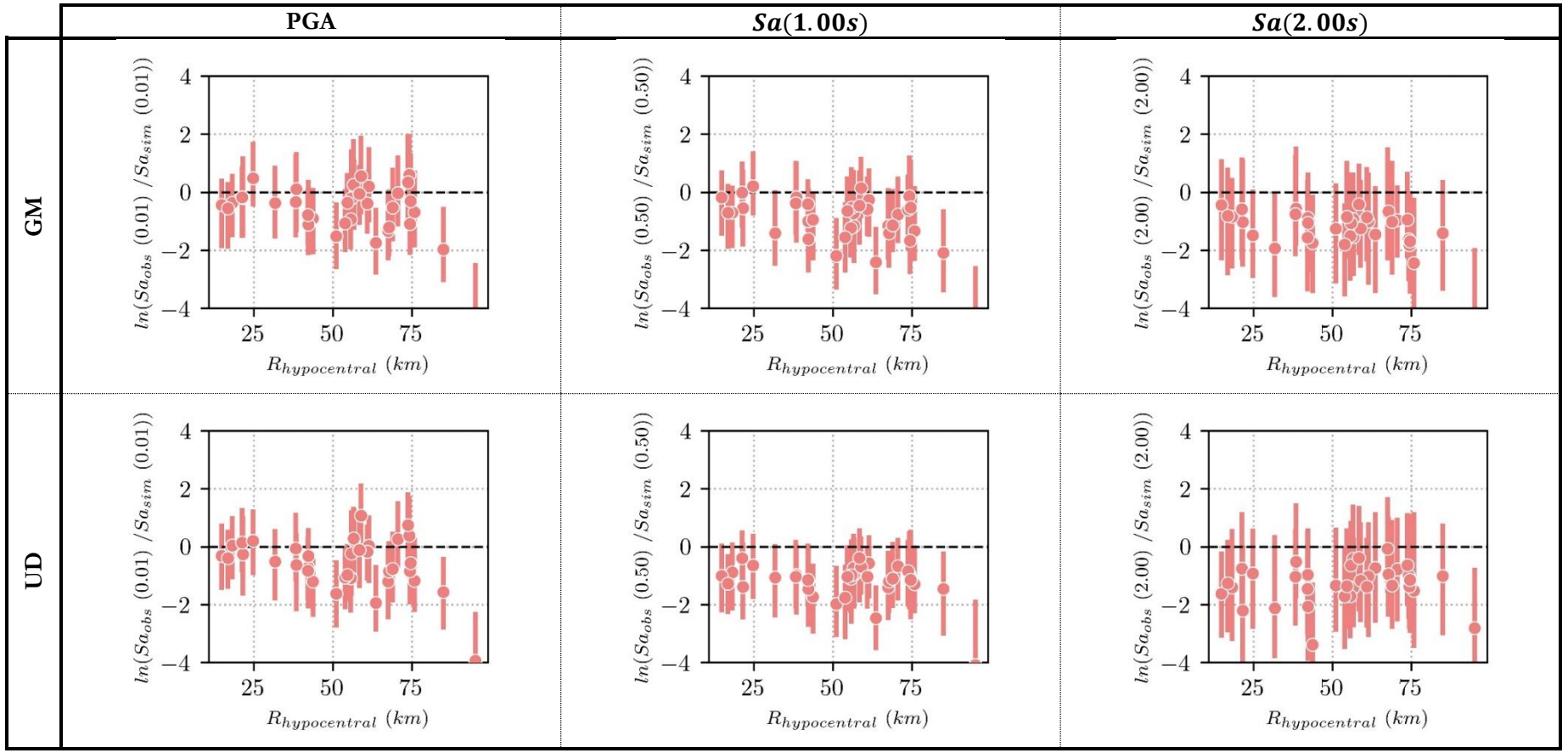

Figure 3.15. Bias in the spectral acceleration of set B with respect to the observed reference. The results are presented for different periods of vibration and as a function of hypocentral distance

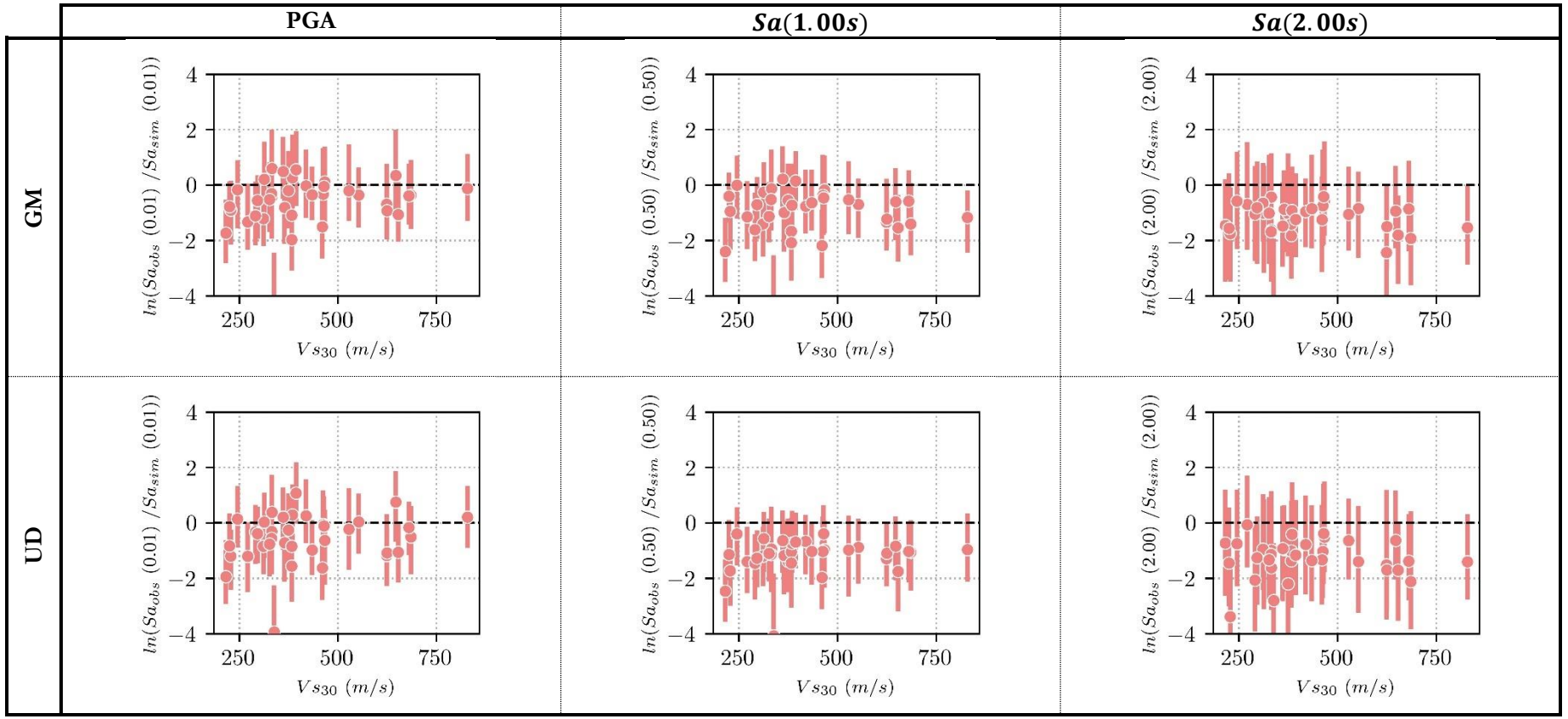

Figure 3.16. Bias in the spectral acceleration of set B with respect to the observed reference. The results are presented for different periods of vibration and as a function of Vs_{30}

3.4 SUMMARY AND CONCLUSIONS

This chapter presented the validation of the ground motion simulation technique through a ground motion prediction case study. This validation, also referred to as seismological validation, evaluated the capacity of the simulated ground motions to replicate the distributions of IMs predicted by valid GMMs for a defined case study. The validation also included the comparison of IMs and waveforms with respect to a reference event matching the causative parameters of the considered case study. Two different simulation sets were considered in the validation, one considering input variables found in the literature (set A) and another one considering input derived from the spectral inversion of local data (set B). The consideration of two different sets was intended to study the spectral inversion technique as an alternative to the lack of input data, for example, at regions with low seismicity or not well characterized. Based on the results obtained from this assessment, the following conclusions were be drawn:

- The waveforms of the simulated ground motions were found to be consistent with those of the reference event. This similarity was obtained because of the calibration of the modulating window functions. This calibration additionally lead to the agreement of the distributions of the significant durations of simulated and reference GMM.
- The simulated ground motions could represent the distributions of spectral content for the GM component of the ground motion expected for the target scenario for periods of vibration below 2.0s. Both sets of simulated ground motions were closer to the long-period prediction from the reference model than the observed reference. Simulated set B was found to be closer to the observed reference event for most studied cases.
- Regarding the comparison of the uncertainty. The results indicated that the proposed epistemic modelling of the uncertainty resulted in standard deviations of the simulated IMs (both spectral acceleration and significant duration) like that of the GMMs prediction. The standard deviation was noticed to increase in the simulated sets for longer periods of vibration, this due to the simplistic modelling of the source and the increasing importance of the uncertainty in the attenuation and site effects for the spectral content at low frequencies.
- The UD component of the simulated ground motions was noticed to be consistently larger than the prediction of the GMM for periods of vibration other than PGA. Specifically, simulated set B was noticed to be closer to the observed reference event, thus indicating that the analytical transfer functions considered in this work may not be a well representation of the site effects expected for the vertical component of the motion. Several factors are thought to cause this miss interpretation of the vertical component, e.g., the simplified estimation of the corner frequency for P-waves, and the transformation of P to SV waves, and vice

versa, due to the reflection of seismic waves at the interface of the layers of the velocity models. These limitations need to be further explored. Regarding the uncertainty of the IMs estimates, the same conclusions as those delivered for the GM component applied for the vertical component.

- The analysis of the biases obtained from the comparison of spectral accelerations at different periods of vibration, and as a function of different variables, indicated that the simulation technique performs better in description of the short-period range, for stations closest to the source ($R_{hypocentral} \leq 75km$) and with stiff soil conditions ($Vs_{30} > 400\ m/s$).
- The consideration of local data for the derivation of the variables describing the mean simulated ground motion spectrum, U, allows for the empirical modelling of spectral features averaged in similar studies consideration data from larger studied regions. These features are mostly evidenced through the attenuation and site-specific transfer functions obtained from the spectral inversion. The estimates of source, attenuation and site obtained from the GIT highly depend on the quality of the data. If the records considered in the inversion scheme are not very representative of the variability of the ground motion, and if a very low number of records is considered, the results may be biased and associated with a large error in the estimation of the regressed parameters.

4.ENGINEERING VALIDATION OF THE 3D STOCHASTIC SIMULATION TECHNIQUE – SINGLE BUILDING RISK ASSESSMENT

4.1 INTRODUCTION

State-of-the-art building-specific risk assessment is conducted by means of Performance-Based Earthquake Engineering, PBEE, (Cornell & Krawinkler, 2000). In this context, the performance of a structure is assessed via its response to ground motions coherent with seismic hazard at the site of interest. The estimation of the seismic hazard, which is conducted through PSHA, (Cornell, 1968), is defined as the rate of exceeding (or equalling), over a defined period of time, an IM or IMs at the site of interest, due to all possible identified earthquake scenarios. Structural response, on the other hand, is typically estimated by means of nonlinear time history analysis (NLTHA) carried out for sets of ground motions selected based on the conditioned IM, or IMs, values considered in the PSHA. The response of the structure is often represented through the development of fragility curves (or surfaces) describing the probability of exceeding certain limit states whose occurrence is monitored through EDPs.

This process assumes that the response of the structure is accurately predicted by the conditioning IM, and that all the other IMs have, conditionally speaking, a much lower importance in affecting the EDPs that measure structural response. This is not the case for most types of structures as structural response is controlled by several IMs. Moreover, different IMs may be good predictors for different EDPs of the same structure. Therefore, the selection of an appropriate conditioning IM directly affects the record selection procedure, the development of the ensuing fragility curves and, in the end, the outcome of the seismic risk assessment, (Luco & Cornell, 2007). In this regard, researchers have developed methodologies for the enforcement of hazard-consistent record selection. The Conditional Spectrum method, CS, proposed by Jayaram et al., (2011), for example, enforces hazard consistency by selecting records coherent with the distribution of spectral

accelerations at all vibration periods conditional on the spectral acceleration at a period of interest, $Sa(T^*)$. The Generalized Conditional Intensity Measure (GCIM) approach developed by Bradley, (2010) simply provides a generalization of the CS to include IMs other than spectral quantities.

To limit any possible bias, analysts usually screen the database before record selection, for instance, by retaining records from events of magnitude, distance, and soil shear velocity to be consistent with the scenarios most influential to the hazard at the site. Furthermore, limitations are also usually imposed to the considered scaling factors. While some level of screening of the database is, of course, recommended, strictly adhering to the site conditions or the magnitude events pertinent to the case at hand can cause a significant reduction in the number of candidate records. This, in turn, may lead to the undesirable consequence of a poor fit to the target spectrum (Tarbali & Bradley, 2016). Thus, the analyst often faces a trade-off between the number of available records and the desired level hazard consistency of the selected sets of ground motions. In addition, databases of recorded real records are not sufficiently populated, or diverse, to provide sets of records that match in a satisfactory manner the target distribution of the considered IMs. Such is the case of rock sites, for which ground motions are often scarce, particularly those representing severe shaking, e.g., those from events of large magnitudes close to the source. In the past, this limitation has been circumvented by using real recordings on both rock and soil sites appropriately scaled to the amplitude levels desired by the application at hand. While this approach is practical, it might bias the results because: i) time histories recorded at soil sites usually present distributions of IMs inherently different than those recorded at rock sites due to the presence of site-effects (Bommer et al., 2004; Chandramohan, et al., 2016; Ji et al., 2018) and, ii) weak but scaled ground motions are arguably different than strong ground motions naturally at high amplitude levels. To help solving the issue of scarcity of adequate real ground motion recordings, an injection of simulated ground motions has been seen as a viable alternative option. However, before simulated ground motions are confidently adopted by engineers in lieu of real ones they need to pass some sanity checks to show that they are statistically indistinguishable from real recordings caused by earthquakes with the same characteristics.

The previous chapter presented a validation from a seismological point of view by comparing the distributions of IMs and waveforms generated for a case study within a ground motion prediction framework. This chapter complements this assessment from an earthquake engineering point of view by evaluating the performance of simulated ground motions in a risk assessment case study. This study considered a set of structures modelled as SDoF systems characterized by different constitutive models and fundamental periods of vibration and located at a rock site. The assessment focused on the comparison of the structural response and fragility curves generated by sets of records with similar characteristics of the causative event and of soil conditions selected from databases of

recorded and simulated ground motions. This chapter starts with the introduction of the reference and simulated databases considered in the record selection procedure. Next, the case study is introduced alongside the record selection procedure. Finally, the results obtained from the record selection procedure, and the comparison of the seismological features of the selected sets of records and the response of SDoF systems is presented.

4.2 CASE STUDY

As alluded to earlier, the prime objective of this chapter was the validation, from an engineering point of view, of the ground motions produced by the proposed simulation technique. This validation was conducted from a single building seismic risk assessment framework, contrasting the structural responses and fragility curves obtained from the NLTHA of simplified structures to sets of records selected from databases of record and simulated ground motions.

The case study considered a fictitious location in Perugia, Italy, at 43.11°N and 12.39°E on a rock site with Vs_{30}= 800 m/s. Here, a wide group of structures represented by SDoF systems with different fundamental periods of vibration and characterized by two different hysteretic models. Specifically, the degradation (pinching) and the elastic-hardening models represented in Figure 4.1.

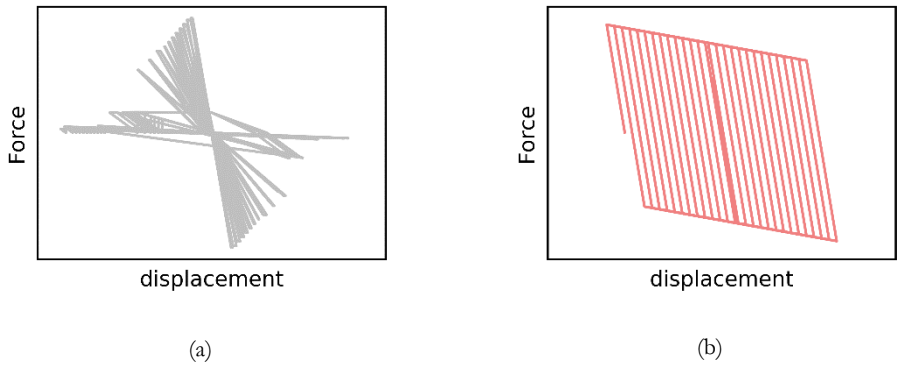

Figure 4.1. Illustration of the hysteretic models considered in the definition of the SDoF systems, (a) – Degradation (pinching) and (b) – Elastic hardening.

The SDoF systems correspond to 5 elastic fundamental periods of vibration: $T_1 = 0.2s, 0.5s, 1.0s, 1.5s$, and $2.0s$. These were designed with the yield base shear coefficient (C_y). This coefficient is representative of a lateral strength equivalent to that of the PSHA-based spectral acceleration value of 10% in 50 years at the fundamental period of each SDoF. C_y represents the yield base shear F_y normalized by the weight Ψ, which is

numerically equivalent to the yield spectral acceleration Sa_y in units of g. Namely $Sa_y/g=F_y/\Psi$, is obtained by $C_y = Sa_{des}(T_1) \cdot \Omega/q \cdot g$, where $Sa_{des}(T_1)$ is the design spectral acceleration at T_1, q is the behavior factor assumed equal to 4.0 for new ductile buildings, and $\Omega = 2$ is the over-strength factor. Accordingly, the corresponding yield displacement, δ_y, of the SDoF is obtained by $\delta_y = Sa_y \left[\frac{T_1}{2\pi}\right]^2$. Conventionally, it is assumed that collapse of the considered systems occurs once a ductility value of 8 is exceeded. As for the dynamic properties, the models were assumed to have a 5% mass proportional Rayleigh damping.

4.3 GROUND MOTION DATABASES

The following sections describe the databases considered for the selection of ground motion sets. The records selected from these databases constitute the two groups considered in the comparisons presented in this chapter.

4.3.1 Recorded Ground Motions Database (RDB)

For this study, a subset of the Engineering Strong-Motion database (ESM) of recorded ground motions was considered as reference, (Lanzano et al., 2019). This database collects the earthquake ground motions recorded in Europe and Middle East, including records from a total of 2179 earthquakes and 2080 stations. The ESM is complemented by a flat file that includes verified metadata and intensity measures of the manually processed waveforms in the database. The subset considered in this study, herein referred simply as RDB, contains the information from earthquakes with moment magnitudes between 4-8 ($4 \leq M_w < 8$), hypocentral distances below 100 km ($R_{hypocentral} \leq 75\,km$) and average shear wave propagation velocities in the upper 30m above 400 m/s ($Vs_{30} \geq 400\,m/s$). These constraints are adequate for the case study and limit the comparisons to the cases where we expect the simulation technique to perform well, i.e., ground motions from short-distance scenarios less impacted by surface waves not explicitly modelled by the method, and to sites characterized by stiff soil or rock, where severe non-linearities in the soil response are not expected (see section 3.3). After considering this screening, a total of 6912 three-component recordings constitutes the RDB. A representation of the main parameters of these scenarios is shown in Figure 4.2.

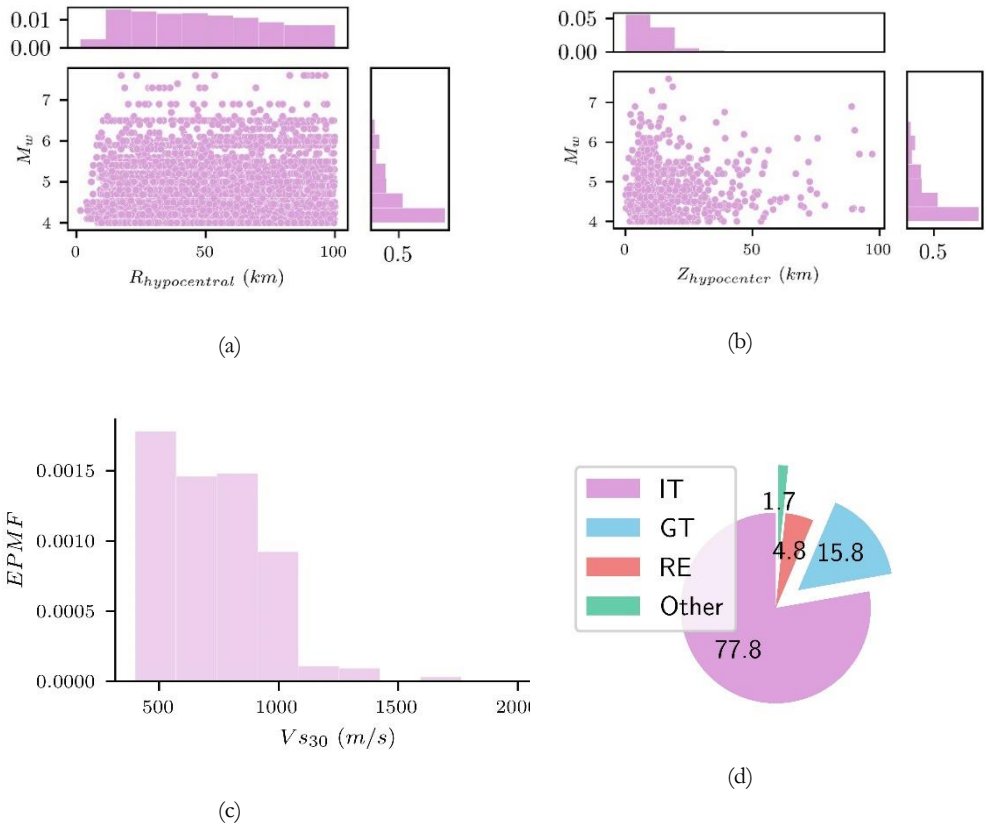

Figure 4.2. Empirical Probability Mass Function (EPMF) of ground motion features within the RDB database. (a) - Moment magnitude (M_w)-Hypocentral distance ($R_{hypocentral}$), (b) – Moment magnitude-Hypocentral depth ($Z_{hypocentre}$). (c) – Histogram of V_{s30}, and (d) – Distribution of countries of origin of the recorded scenarios (IT=Italy; GT=Greece and Turkey, RE=Central Europe).

4.3.2 Simulated Ground Motions Database (SDB)

The database of simulated ground motions, referred to as the SDB, by design, was made consistent with the characteristics of RDB described in the previous section. The consistency was enforced in terms of the joint probability distributions of the main causative parameters of the scenarios contained in the RDB, namely: moment magnitude (M_w), source-to -site distance (in this case considered as the hypocentral distance, $R_{hypocentral}$), hypocentral depth ($Z_{hypocentre}$), and site characteristics (in this case considered with the average shear wave propagation velocity in the upper 30m (Vs_{30}). The following sections discuss the calibration of the simulation and generation of the SDB.

4.3.2.1 *Input parameters for ground motion simulation*

Much like for the case study described in section 3.2, one of the key aspects to consider in this ground motion simulation exercise is the variability of the IMs computed from the simulated ground motions. The following sections describe the input parameters considered in the description of the case study for the purpose of ground motion simulation.

- **Crustal structure**

The considered crustal structure, in the form of a 1D velocity model, was that defined in (Boore & Joyner, 1997) for hard rock. This model provides a generic S-wave propagation velocity profile for the crust as a function of depth. The P-wave velocity profile was approximated considering a constant velocity ratio of S-to-P wave of 0.67 ($\beta/\alpha = 0.67$), which corresponds to a Poisson ratio of 0.25. The density of the crust was estimated with the generic function for hard rock proposed in Boore & Joyner (1997).

- **Source model**

The geometry of the sources was based on the regression model proposed by Wells & Coopersmith, (1994). The distribution of the slip in the source was specified based on a uniform spatial density function, thus allocating the scenario-consistent slip with equal probability to each of the sub-faults defining the finite-fault model. All finite-fault models were discretized into 100 sub-faults. Due to the lack of specific information for each of the scenarios in the RDB, dip, strike, and rake of the source were sampled as random variables with uniform distributions. The ranges of variation of these variables were considered as 10°-90° for the dip, 0°-360° for the strike and 0°-90° for the rake. Finally, the location of the hypocentre was random within the length and the deepest (down-dip) half of the ruptured plane. Sources unphysically possible due to the geometry of the fault, hypocentre location ad prescribed hypocentral depth were not considered.

- **Site effects**

Site effects related to superficial soil layers were considered by sampling site-specific elastic transfer functions as a function of Vs_{30} from a database of pre-computed function. These transfer functions were computed for soil columns constructed with the soil profiles reported for the stations considered in the GIT described in section 3.2.2.5, and the generic crustal structure considered for this case study. This work considered the stations from the Japanese network due to the availability of a high number of soil column profiles. Considering that site-effects are completely conditioned on Vs_{30}, the fact that these profiles come from a different region should not impose a conflict in the simulation methodology. The transfer functions were constructed with Haskell-Thompson method (Haskell 1953) and considering a constant 10% damping.

- **Ground Motion Spectrum**

Finally, the input variables defining the ground motion spectrum were taken from Bindi & Kotha, (2020). In their study, the authors used the Generalized Inversion technique to parameterize the FAS of earthquake ground motions contained in the complete ESM database.

- **Calibration of the ground motion simulation technique**

Currently, there are no available studies providing any guidance on the modelling of the shape of simulated ground motions within a finite-fault context. The lagged summation of sub-fault contributions does not allow for the definition of a single set of parameters suiting all simulation possibilities. Additionally, and as discussed in the previous chapter, the consideration of stress drops estimates obtained from the spectral inversion of large number of events results in estimates heavily biased towards the source physics of lower magnitude events, in the sense that these are comparatively more abundant than earthquakes of medium or large magnitudes.

These identified deficiencies were addressed by an iterative calibration of the time modulating window parameters and a scaling factor to the stress drop. This process consisted in the minimization of the differences between the distributions of IMs of interest extracted from the RDB ground motions, and those extracted from sets of synthetic replicas computed with different combinations of the searched parameters. The replicas were constructed by generating simulated ground motions from scenarios with the same causative parameters, i.e., M_w, $R_{hypentral}$, and $Z_{hypentre}$, as those contained in the RDB. The error of a certain set of searched parameters was defined as the median bias, $\bar{\xi}$, from the distribution of biases computed from the comparison of the IMs from the reference and simulated ground motions. The computation of the median bias for a given IM is shown in equation Equation 4.1.

$$\bar{\xi} = \frac{1}{N_{records}} \sum_{i=1}^{N_{records}} ln\left({IM_{reference}}_i / {IM_{simulation}}_i\right)^2 \qquad \textbf{Equation 4.1}$$

Where $N_{records}$ is the number of records considered in the computation of the median bias. The consideration of more than one IM in the computation of the error requires the combination of the individual errors according to Equation 4.2:

$$Error = \sum_{i=1}^{n_{IM}} weight_i \bar{\xi}_i \qquad \textbf{Equation 4.2}$$

Where $weight_i$ represents a weighting factor allowing the prioritization of the match of IM_i, $i=1,\ldots, n_{IM}$ considered in this procedure. The IMs considered in the computation of the error were: (i) the ordinates of the response spectra of the geometric mean of the horizontal components, $Sa_{GM}(t)$, at periods of vibration of PGA, 0.1, 0.3, 0.5 and 1.0s, the Peak Ground Acceleration of the vertical component, PGA_{UD}, and the Arias intensity of the geometric mean of the horizontal components, AI_{GM}. Table 4.1 shows the weighting scheme considered in the computation of the error.

Table 4.1. Weighting scheme considering in this study for the computation of the error in the calibration procedure

IM	w
PGA_{GM}	0.1
$Sa_{GM}(0.1, 0.3, 0.5, 1.0)$	0.1, 0.1, 0.1, 0.1
PGA_{UD}	0.1
AI_{GM}	0.4

The iterative minimization procedure was applied to different groups of data in search of a more accurate estimation of the searched input parameters. A total of 12 groups were defined based on the following criteria: $4 < M_w \leq 5$, $5 < M_w \leq 6$ and $M_w > 6$, $R_{hyp} \leq 50\ km$ and $50km < R_{hyp} \leq 100\ km$, $400\ m/s \leq Vs_{30} < 600\ m/s$ and $Vs_{30} \geq 600\ m/s$.

The results obtained from the calibration procedure, for the scenarios closest to the source, i.e. $R_{hypocentral} \leq 50\ km$, are shown in Figure 4.3 and Figure 4.4. Figure 4.3a and Figure 4.3b show the time-modulating functions for simulations at soil ($400\ m/s \leq Vs_{30} < 600\ m/s$) and rock sites ($Vs_{30} \geq 600\ m/s$), respectively. These results show the importance of the site-effects in the duration and overall distribution of the amplitude in the simulated ground motions, where the changes in the phase produced by softer soil layers disguise the differences in the arrival times of the energy of events with different magnitudes. The scaling factor for the stress drop, SF, shown in Figure 4.4,shows that obtained values consistently decrease with magnitude, except for the simulations at soil sites and for the largest magnitude bin. The decreasing scaling factor as a function of magnitude is related to the influence of the size of the considered finite-source model. The point-source model concentrates the source at a single point thus resulting in attenuation effects computed for a single hypocentral distance. Finite-source models, on the other hand, are subject to different values of attenuation for every sub-source composing the model, and this results in more energy from sub-sources closer to the observation point

and, therefore, requiring a smaller scaling factor. The case of the scaling factor related to simulations for soil sites and for the highest magnitude bin is influenced by the non-linear response of the soil in the recorded events. This is a feature not captured in our simulated ground motions as site effects were computed considering linear elastic transfer functions not capable of modelling the dissipation of energy produced by non-linear soil response. This limitation is compensated by the scaling factor affecting the overall amplitude of the high-frequency content of our synthetic ground motions.

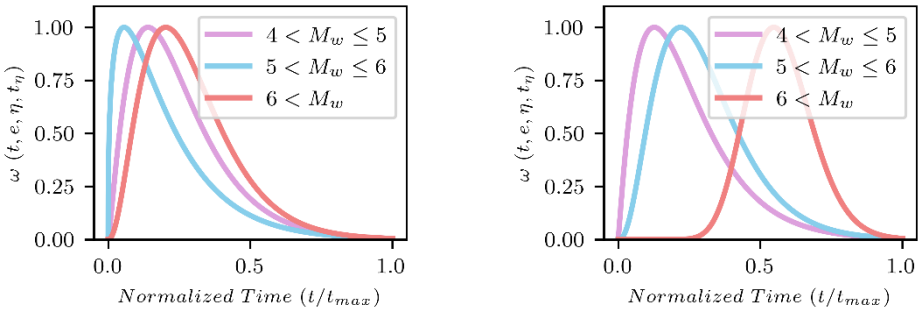

Figure 4.3. Time modulating functions obtained in the calibration procedure for the ranges of distances $R_{hypocentral} \leq 50\ km$ for (a) - $400\ m/s \leq Vs_{30} < 600\ m/s$, and (b) - $Vs_{30} \geq 600\ m/s$

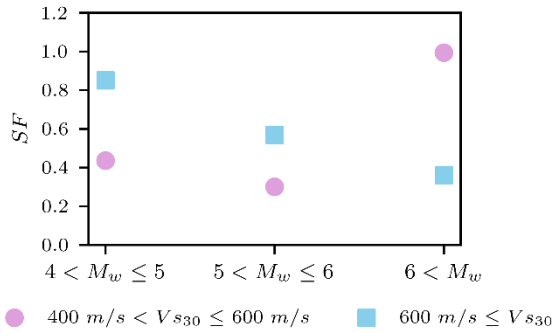

Figure 4.4. Stress drop scaling factors, SF, obtained in the calibration procedure for the range of distances $R_{hypocentral} \leq 50\ km$

As an illustrative example, Figure 4.5 shows a comparison of the distribution of IMs of the reference and simulated scenarios for the group characterized by $5 < M_w \leq 6$, $R_{hypocentral} \leq 50\ km$ and $Vs_{30} \geq 600\ m/s$. This figure shows a close fit of the spectral shapes and Arias Intensity included in the weighting scheme. More important differences, however, were noticed in the distribution of Husid duration (defined as the duration between the instants at which the signal reaches 5% and 95% of its total energy) which was

not included in the calibration. The importance of each IM considered in the calibration procedure may be adjusted by considering different weighting schemes. For this application, however, the spectral shape was prioritized because of its important role in CS-based record selection. Additional figures, showing the comparison of the IMs for all other calibration groups are included in the appendix.

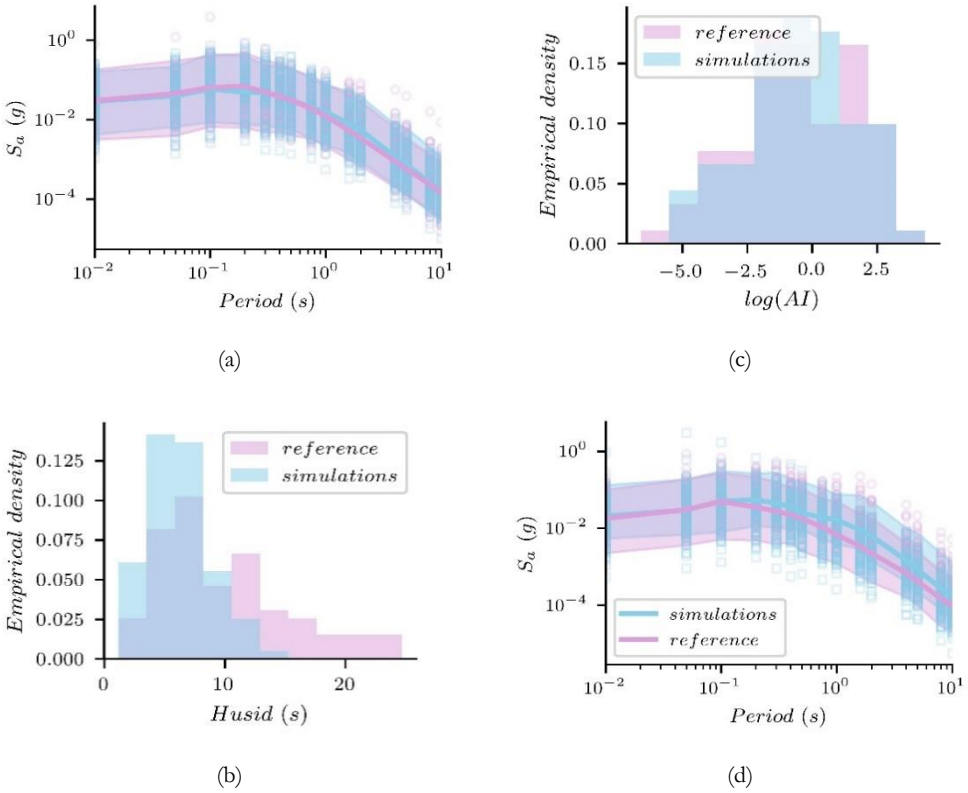

Figure 4.5. Comparison of reference and simulated distributions of the IMs of interest considered during the calibration process of scenarios for the group with $5 \leq M_w < 6$, $R_{hypocentral} \leq 50\ km$ and $Vs_{30} \geq 600\ m/s$. (a) – Geometric mean of the horizontal response spectra, (b) – Geometrical mean of the horizontal Husid durations, (c) – Geometrical mean of the horizontal AI, d) – Response spectra of the vertical component.

4.3.2.2 *Generation of the Ground Motion Simulation Database*

The SDB was populated with 7000 3D acceleration time histories. The causative parameters describing these were obtained by Monte Carlo sampling of the joint probability density function of $M_w, R_{hypocentral}$ and $Z_{hypocentre}$ and considering the description of the model input discussed in the previous section. Figure 4.6a shows the distribution of

causative parameter, $M_w - R_{hypocentral}$, of the simulated ground motions contained in the SDB. The differences in the distributions of the Vs_{30}, shown in Figure 4.6b, are mainly due to the limited number of sites contained in the considered database of transfer functions.

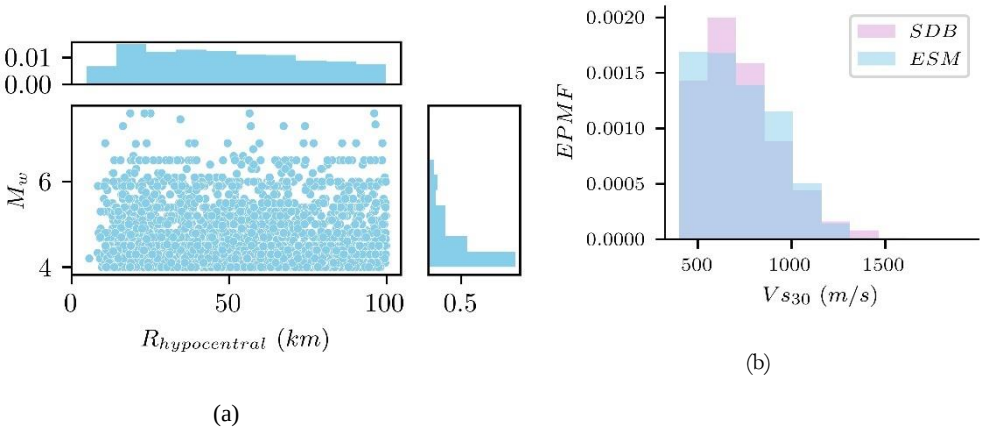

Figure 4.6. (a) - Distribution of Magnitude-Hypocentral distance for the SDB, and (b) – Comparison of the distribution of Vs_{30} for the ground motions in the RDB and SDB.

Figure 4.7 shows a comparison of acceleration time histories for one of the scenarios found in the group constrained by $6 < M_w$, $R_{hypocentral} \leq 50\ km$ and $Vs_{30} \geq 600\ m/s$. This group is of special interest due to the number of records considered in the record selection procedure to be discussed next. The figure shows three simulated records that match in terms of the causative parameters with the shown event from the RDB. Here, only one of the simulated scenarios resembled the event from the RDB. The differences in the waveforms are due to the random characterization of the source and the sampling of the input variables in the simulation process. Figure 4.8 shows a comparison of the IMs for all the events constituting the previously mentioned group. The comparisons indicated an overall similarity between SDB and RDB distributions of intensity measures. Some differences, however, were noticed in the overall dispersion of the $Sa(t)_{GM}$. This condition was mostly found in the groups where the RDB was constituted by few records coming mostly from a few scenarios, i.e., most of the records have the same source. This represents a fundamental difference with the simulation scheme here considered, where each simulated record comes, from definition, by a different earthquake scenario defined by the Monte Carlo sampling of all the input parameters.

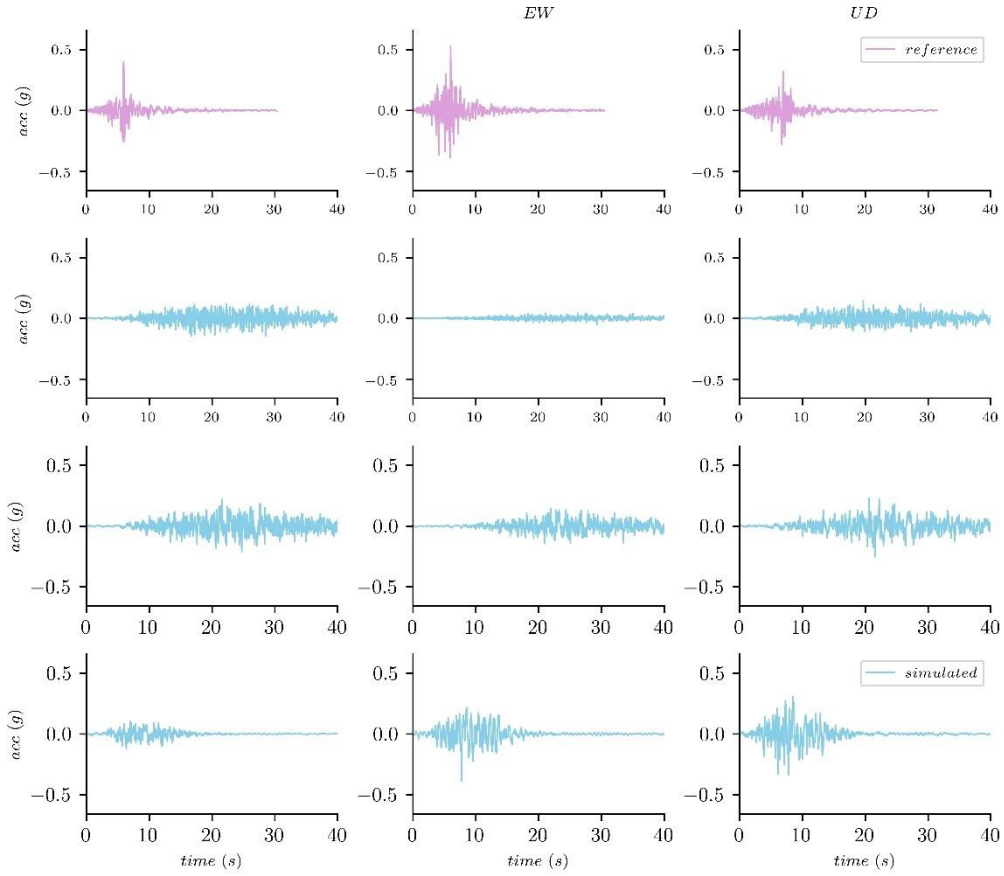

Figure 4.7. Comparison of reference and simulated time histories for one of the replicated scenarios ($M_w = 6.50, R_{hypocentral} = 27.96km, Z = 9.20km$).

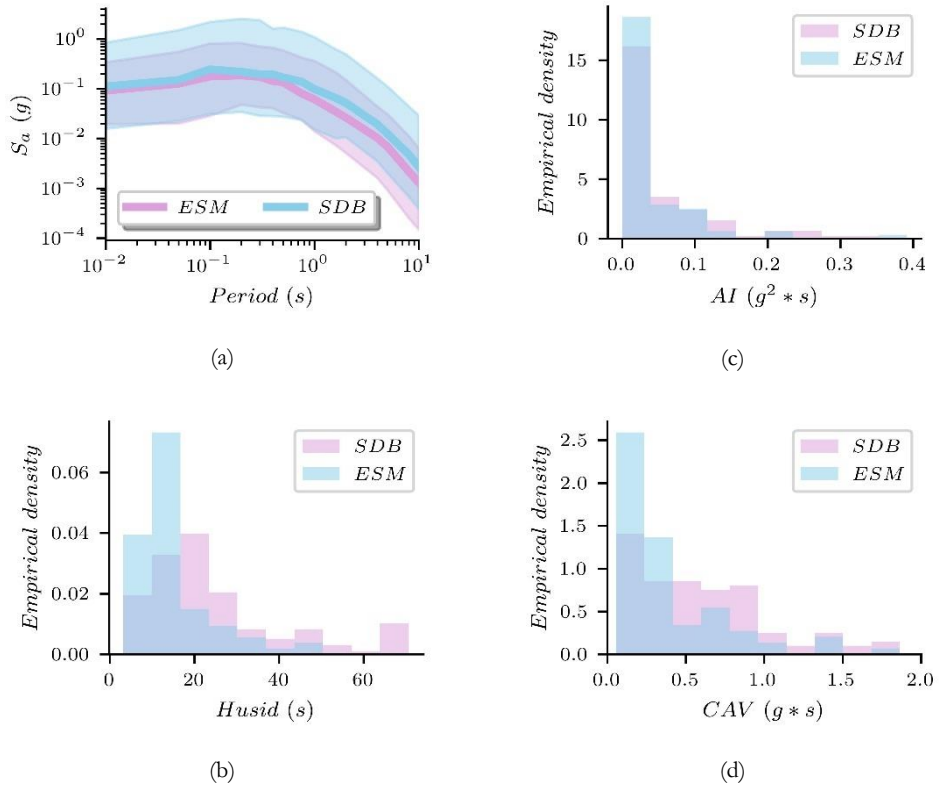

Figure 4.8. Comparison of the distribution of IMs for the ground motion record group with $6 < M_w$, $R_{hypocentral} \leq 50\ km$ and $Vs_{30} \geq 600\ m/s$ in the RDB and SDB databases. (a) – Response spectra (Sa_{GM}), (b) – Arias Intensity (AI_{GM}), (c) – Husid duration ($Husid_{GM}$), and (d) – Cumulative Absolute Velocity (CAV_{GM})for the Geometrical Mean of the Horizontal components

4.4 RECORD SELECTION

This study considered CS as primary record selection methodology, (Jayaram et al., 2011). Here three main steps constitute the selection of ground motion sets. (i) First, perform PSHA for the site of interest (including local soil conditions, here rock) and IM of choice. Additionally, perform seismic hazard disaggregation to identify the event characteristics most contributing to the estimated mean hazard. (ii) Second, evaluate the distribution of the spectral quantities conditioned on the IM of choice for a considered representative $M_w - R_{hypocentral}$ scenario, e.g., mean, mode, or more accurately the totality of the scenarios. (iii) Finally, select a suite of records that collectively describes the estimated target distributions for the CS at all considered Intensity Measure Levels (IMLs).

Table 4.2 shows the values of spectral acceleration obtained from PSHA analysis for the case study site and considering the fundamental periods of vibration of the SDoF systems, $Sa(T_1)$, as conditioning IM. To validate the use of simulated ground motions in different response ranges, i.e., linear, and nonlinear, these IMs were computed for IMLs covering values ranging between 0.2% probability of exceedance (PoE) in 50 years (i.e., return period of 25,000 years) to 70% PoE in 50 years (i.e., return period of 40 years). These calculations were carried out with the OpenQuake software (Pagani et al., 2014) and considering the Boore & Atkinson, (2008) GMM and the area source model developed for the SHARE project[a].

[a] www.share-eu.org

Table 4.2 Values of the IMs at the 10 levels of intesity at the Perugia site. IML 4 corresponds to the 10% PoE in 50 years (i.e., the design level).

IML	PoE in 50 years [%]	Return period	$S_a(0.2s)$	$S_a(0.5s)$	$S_a(1s)$	$S_a(1.5s)$	$S_a(2s)$
1	70	42	0.2	0.09	0.042	0.025	0.017
2	50	72	0.26	0.13	0.057	0.034	0.023
3	30	140	0.35	0.18	0.08	0.049	0.034
4	10	475	0.58	0.32	0.146	0.09	0.064
5	5	975	0.78	0.43	0.203	0.13	0.091
6	2	2475	1.12	0.64	0.305	0.19	0.139
7	1.5	3310	1.25	0.72	0.343	0.22	0.158
8	1	4975	1.44	0.83	0.402	0.26	0.187
9	0.6	8310	1.71	1	0.485	0.32	0.229
10	0.2	24975	2.12	1.42	0.697	0.47	0.337

The CS was constructed for the GMRotD50 component of the ground motion, considering the same GMM used in the computation of the PSHA, the mean M_w and $R_{hypocentral}$ values of the causative earthquakes contributing to the hazard, and the intra period spectral acceleration correlation model proposed in Baker & Jayaram, (2008). Next, sets of records were selected to match the CS of every IML considering a simulation approach and the 'greedy' optimization technique, (Baker & Lee, 2018). The selected sets of records are sought to collectively match the mean target spectrum and the full *Sa*(*T*) distribution, for all *T*s, within some specified tolerance. In this study, the misfit between the empirical distributions of the final set of records and the target ones was measured with the sum of squared errors (SSE_s) (Baker & Lee, 2018):

$$SSE_s = \sum_{k=1}^{p} \left[\left(m_{lnIM_k} - \mu_{lnIM_k} \right)^2 + w \left(s_{lnIM_k} - \sigma_{lnIM_k} \right)^2 \right] \qquad \textbf{Equation 4.3}$$

Where IM_k is the spectral acceleration at T_k, m_{lnIM_k} is the sample mean of $lnIM_k$ and s_{lnIM_k} is the sample standard deviation of $lnIM_k$ both estimated from the selected motions. The quantities μ_{lnIM_k} and σ_{lnIM_k} are the target conditional means and standard deviations, p is the number of periods of interest in the target spectrum, and w is a weight factor here arbitrarily assumed to be equal to 2. This latter value is meant to assign a higher degree of importance to the mismatches in the standard deviation rather than the target mean. In agreement with Garcia et al., (2022) a value of $SSE_s = 0.12$ is considered as the acceptable threshold.

The assessment presented in this chapter considered sets of 40 hazard consistent records selected considering $Sa(T_1)$ as conditioning IM and for each of the IMLs mentioned previously. Figure 4.9 shows the overall fit of these selected suites of records by comparing the $\mathrm{SSE_s}$ for all considered conditioning periods. Additionally, the threshold defined as reference for the adequacy of the fit is also displayed in the figure. Overall, the match to the target CS deteriorated with increasing IMLs, specifically for the RDB and for the highest periods of vibration. This indicates that the RDB lacks the diversity of scenarios required to match the spectral content described by the CS at the highest amplitudes. The deterioration of the match was not as severe for the SDB because the records within it were generated each with a different $M_w - R_{hypocentral}$ pair. In contrast, for the case of the RDB, many of the $M_w - R_{hypocentral}$ pairs come from the same earthquake scenario (rupture), thus limiting the diversity of the available records.

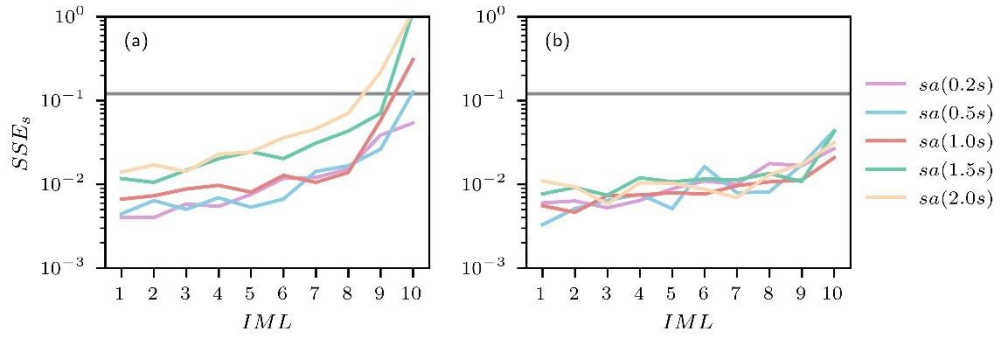

Figure 4.9. SSE_s for the (a) RDB and (b) SDB records sets for different conditioning periods. The acceptable error of 0.12 is illustrated as a grey dashed line.

4.5 RESULTS

The following sections present the results obtained from the validation of the ground motion simulation technique within a single building seismic risk assessment framework. The comparisons considered two groups of sets of records: (1) those selected from the RDB, and (2) those selected from the SDB, and included the contrast of the distributions of ground motion causative parameters, IMs, EDPs and fragility curves within the selected sets of ground motions.

4.5.1 Comparison of causative parameters

Figure 4.10 shows the comparison of the median causative parameters and scaling factor obtained from the sets of records selected for three of the five SDoFs, namely: 0.2, 1.0 and 2.0s. Overall, there is an acceptable match of the median values for $M_w, R_{hypocentral}$ and Vs_{30} for all conditioning periods (the same holds when comparing the standard deviation of the samples not shown here). The median values of SF also match reasonably well for the $T_1 = 0.2s$ SDoF but larger differences were noticed for the SDoFs with longer vibration periods, specifically for the highest IMLs. More precisely, records selected from the RDB required larger scaling factors to match the target CS, thus indicating that the selected records from the SDB systematically presents larger spectral accelerations for the longest periods of vibration cases. The comparison of median and standard deviation of the distributions of causative parameters, for the sets of records selected for all considered SDoFs, is added in the appendix.

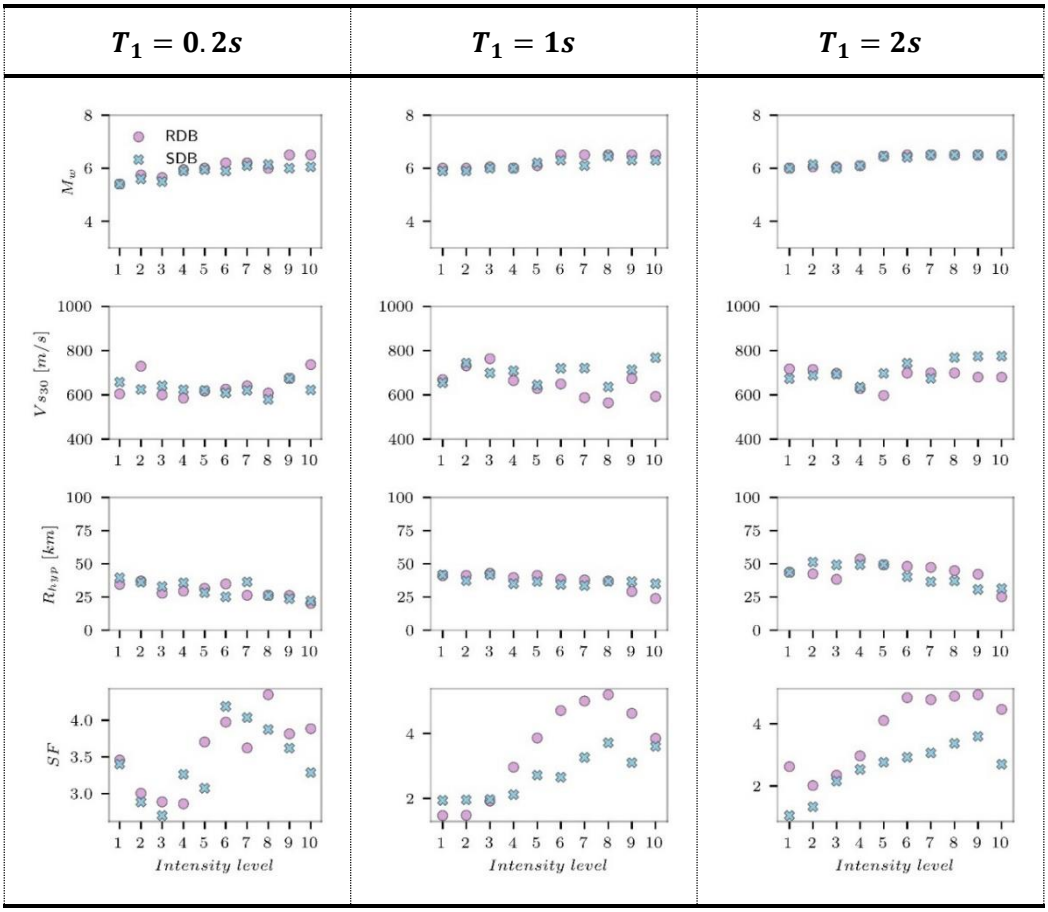

Figure 4.10 – Median of the causative parameters of the selected records, namely moment magnitude (M_w), average shear propagation velocity of the upper 30m (Vs_{30}), hypocentral distance (R_{hyp}), and scaling factor (SF), from first to the last row, respectively.

4.5.2 Comparison of Intensity Measures (IMs)

Figure 4.11 and Figure 4.12 show the median and standard deviation of the distributions of IMs computed from the selected suites of records of the RDB and SDB, respectively. These figures compare a series of IMs considered in the calibration procedure, i.e., PGA, AI, and Husid duration. Furthermore, these figures present the comparison of two complementary IMs: Cumulative Absolute Velocity (CAV), which is a measure of the damage potential of an earthquake, computed as $CAV = \int_0^{t_{max}} |a(t)|\, dt$, where t_{max} is the total duration of the ground motion, and Spectral intensity (SI), which is computed as $SI = \int_{0.1s}^{2.5s} SA(\tau) d\tau$, where τ is the oscillator period and SA is the pseudo-spectral acceleration.

The obtained results showed a close fit for the median and standard deviation of IMs related to the spectral content of the ground motions, i.e., PGA and SI, for all considered conditional periods of vibration. Nevertheless, the comparison of the distributions of the IMs related to duration of the ground motions showed discrepancies in terms of median and standard deviation. When considering Husid duration, for example, a systematically larger median duration and standard deviation for conditioning periods below $T_1 = 2.0s$ was noticed. The differences in duration, in addition, impact the distribution of CAV and AI.

The discrepancies in duration related IMs were noticed to be more important for higher amplitudes of the motions, namely for higher IMLs. Considering that differences in duration are independent from the scaling factor used to adjust the amplitude of the motions, its evident that the overall duration of the simulated ground motions was not very well captured during the calibration of the simulation technique. This may be attributed to three reasons: (i) Higher weights, hence, more importance, was given to the spectral content in the calibration procedure rather than to duration. (ii) The number of events considered for the calibration of the group containing the largest magnitudes was the smallest within the reference ESM subset, thus limiting the available information for its characterization, and iii) the use of transfer functions sampled only by Vs_{30} does not guarantee similar changes in the phase of the ground motions. This because different distributions of soil layers may result in comparable Vs_{30} but completely different phase modifications. In other words, Vs_{30} is not a sufficient variable to describe site effects.

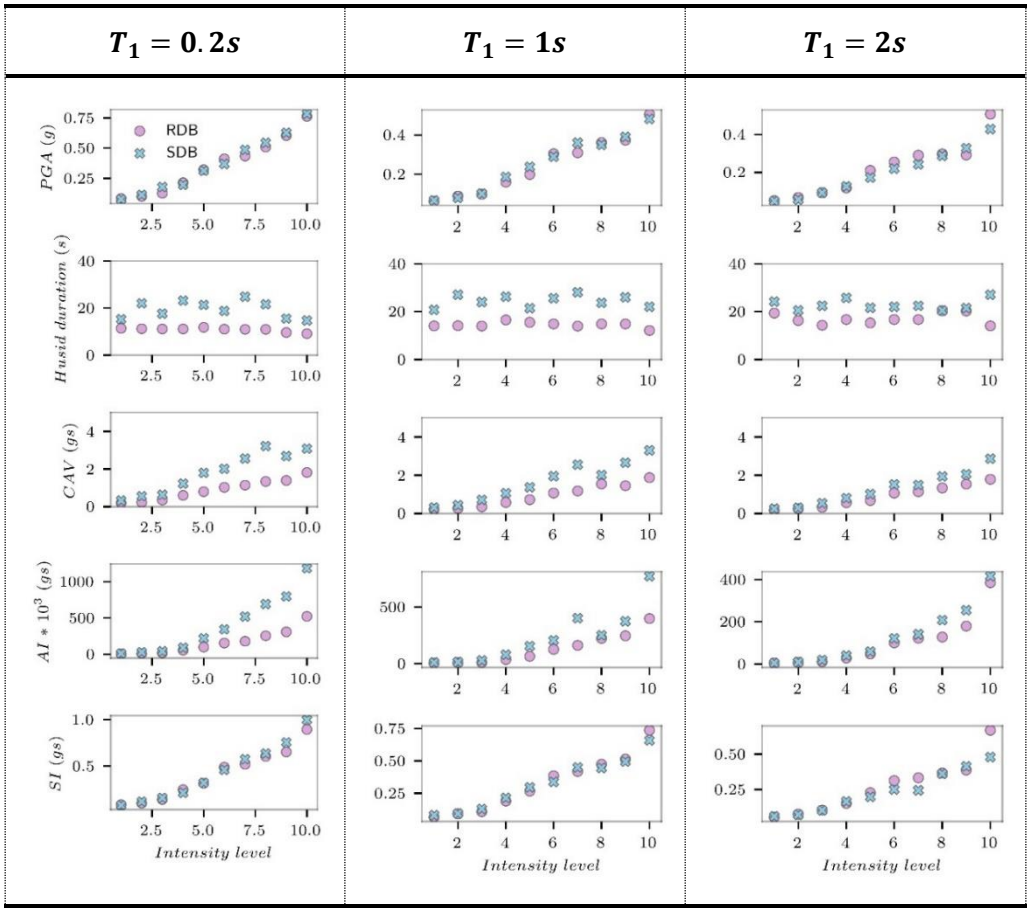

Figure 4.11 – Medians of the distributions of different IMs, namely peak ground acceleration (PGA), Husid duration, Cumulative absolute velocity (CAV), Arias intensity (AI), and Spectral intensity (SI), from first to the last row, respectively.

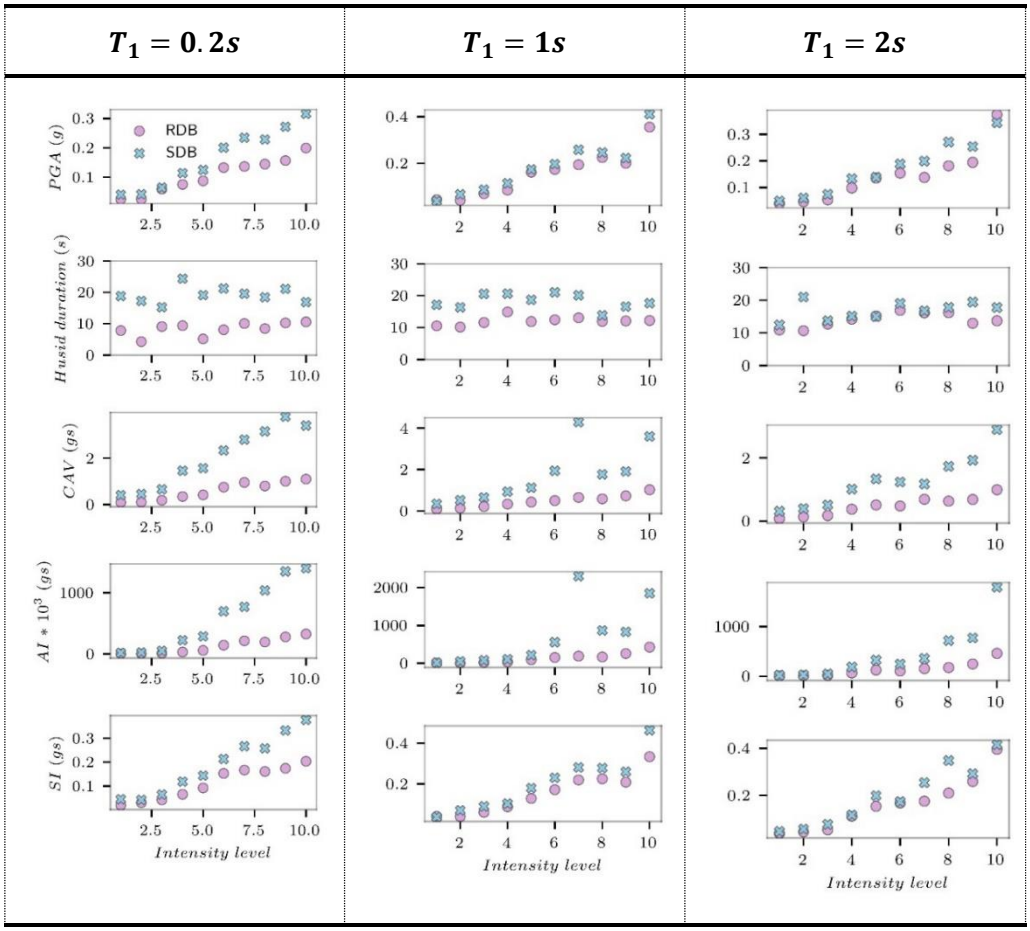

Figure 4.12 – Standard deviations of the distributions of different IMs, namely peak ground acceleration (PGA), Husid duration, Cumulative absolute velocity (CAV), Arias intensity (AI), and Spectral intensity (SI), from first to the last row, respectively.

4.5.3 Comparison of structural response (EDPs)

The structural response of the considered SDoFs to the selected sets of records was obtained by means of NLTHA and assessed through the monitoring of different EDPs, namely: ductility ratio (μ), maximum acceleration and velocity of the system, and the dissipated energy. Figure 4.13 shows the comparison of the response of these EDPs, for the same three SDoFs discussed so far, and for the pinching material model. The EDP comparisons for the remaining SDoFs and hysteresis model, which show similar trends, are included in the appendix.

In this analysis, cases with ductility ratio above eight were treated as collapses, and, for illustration, they were lumped at the dashed horizontal grey line defining the maximum limit for each EDP. When more than 50% of data points were collapse cases, the median ductility is infinite and is omitted in the figure. For the case of dissipated energy, a value of 1.0 was fixed for records resulting in a linear response of the SDoF, i.e., $\mu < 1.0$.

In general, the median responses obtained for the records selected from the RDB and the SDB databases agreed for all considered SDoFs and IMLs. The comparisons of 5th and 95th percentiles, however, showed considerable differences. These differences were more important for the EDPs related to the displacement response of the SDoF, such as ductility and dissipated energy. When comparing the acceleration response, on the other hand, smaller differences were noticed, except for the case of $T_1 = 0.2s$.

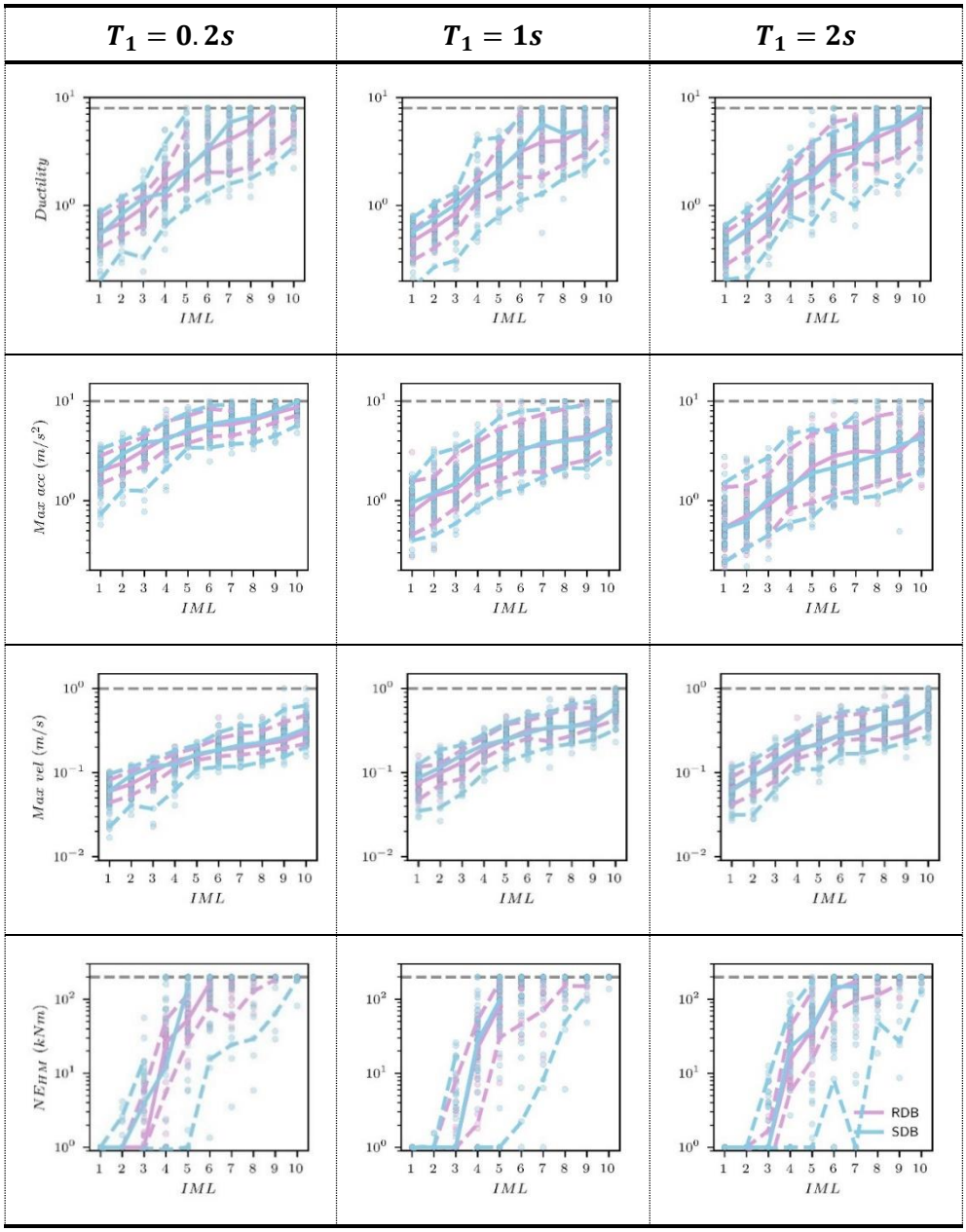

Figure 4.13 – EDPs for three SDoFs with pinching hysteresis model obtained via NLTHA using 40 records at each IML, selected from the RFD and SDB. Ductility ratio, Peak Floor acceleration, Peak floor velocity, and dissipated energy, from first to the last row, respectively. In the figure, the median is represented by the solid line and 5th and 95th percentiles by the dashed lines.

The assessment of the structural response was complemented by the generation of fragility curves showing the probabilities of exceeding different limit states defined here by different ductility ratio levels, namely: 2, 4 and 8. These thresholds could be associated to the onset of minor damage, moderate damage, and collapse states. The curves for the three SDoFs with pinching hysteresis model are contrasted in Figure 4.14, whereas those obtained for the complementary SDoFs and hysteresis model are added in the appendix material. The discrepancies in the distribution of the EDP were evidenced in the fragility curves shown in Figure 4.14. The comparisons indicated some level of bias in the SDB-based estimates of the median capacity when compared with those obtained with the RDB records for all considered limit states and SDoFs. As expected, the larger variability in the SDB-based EDPs causes the generally flatter shape of the SDB-based fragility curves.

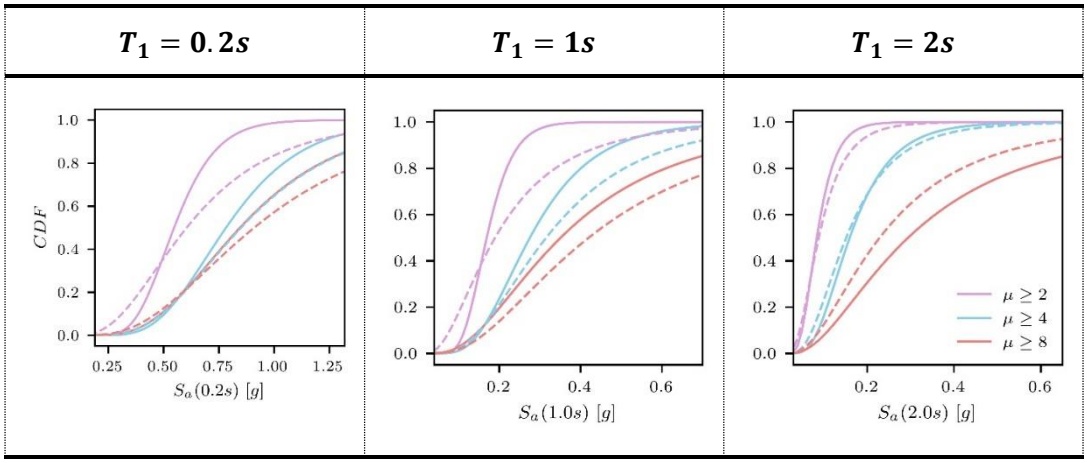

Figure 4.14 – Comparison between the fragility curves obtained from RDB records (solid line) and from SDB records (dashed line) for three different ductility levels and SDoF systems with T_1=0.2s, T_1=1s and T_1=2s vibration periods and pinching hysteresis model.

In addition, the SDB was assessed by studying the fragility curves generated for a different EDP. Figure 4.15 shows the comparison of the fragility curves derived considering the case of a floor acceleration sensitive equipment, mounted at the centre of mass of the SDoF system. For this exercise, the Low Voltage Switchgear (LVSG) equipment was considered. The LVSG is a centralized collection of circuit breakers, fuses, and switches (circuit protection devices) typically used in Nuclear Power Plants to ensure and protect the performance of 480V-AC (alternative current) electrical systems, (M. Z. Wang, 2018). The response of this equipment is typically defined by two different limit states: (i) the capacity limit state, which entails repairable damages such as jamming of the controls, and (ii) the failure limit state, when structural failure of the equipment is reached. According to EPRI, (1994), the onset of the capacity limit state is achieved when the mean spectral acceleration of the story motion, between the periods of 0.1s-0.2s, is larger than 1.8g. The onset of the

failure limit state, on the other hand, is reached when the minimum spectral acceleration in the range of 0.0625s to 0.33s is larger than 1.8g. The results shown here correspond to the pinching model and SDoFs with natural vibration period of $T_1 = 0.2s, T_1 = 1.0s$, and $T_1 = 2.0s$. The results for the remaining hysteresis models and SDoF systems are included in the appendix. Apart for the case of $T_1 = 0.2s$ and the failure limit state, the obtained results showed a much better match than that achieved for the ductility-related fragility curves. This result was expected as results evidenced a better correspondence of the distribution of the responses in terms of Peak Floor Acceleration (see Figure 4.12). The full agreement of the fragility curves for the capacity limit state and for $T_1 = 0.2s$ was obtained because the spectral amplitude of the story motion surpasses the threshold for all IMLs.

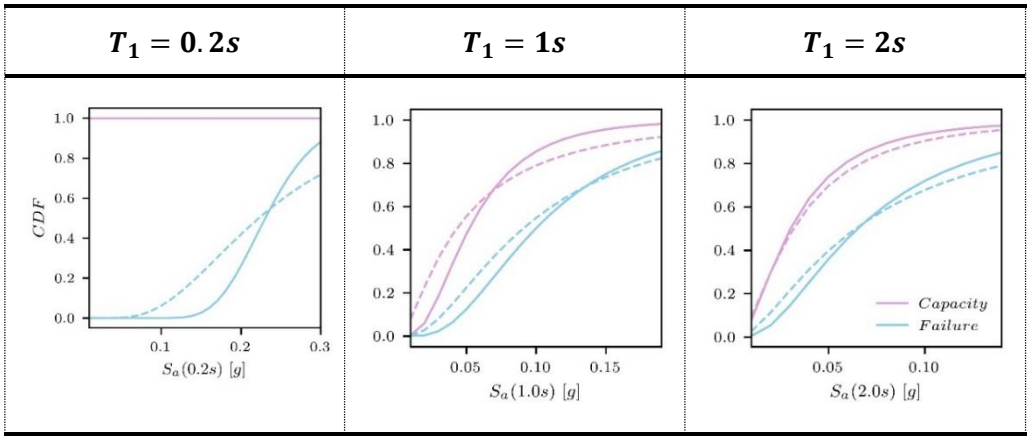

Figure 4.15 – Comparison between the fragility curves obtained from RDB records (solid line) and SDB records (dashed line) for two different system acceleration levels and SDoF systems with T_1=0.2s, T_1=1s and T_1=2s vibration periods and pinching hysteresis model.

4.5.4 Importance of complementary conditioning IMs

The differences in distributions of EDPs, and consequently, of fragility curves computed via CS-based selection, point towards the insufficiency of the spectral ordinates as conditioning IM when comparing sets of real and simulated ground motions. In other words, the observed differences in EDPs were likely caused by the systematic differences in the distributions of IMs related to ground motion duration, namely Husid duration and CAV. To test this conjecture, and to evaluate the importance of duration and the role of its inconsistency in the computed fragility curves, record selection was repeated considering the methodology proposed in Chandramohan, Jack W. Baker, et al., (2016). This methodology simply adds an extra IM to the vector of response spectral ordinates considered in the standard CS approach, thus enforcing the consistency of the selected records also in terms of the extra IM. Theoretically, any IM for which a GMM and correlation models exist can be used in addition to the spectral ordinates. For this case, the

considered complementary IM was the Husid duration. This IM was included in the record selection scheme considering the GMM proposed in Afshari & Stewart, (2016) and the correlation coefficients developed by Bradley, (2011). This complementary record selection scheme is referred to as $CS(D_s)$.

Figure 4.16 and Figure 4.17 show the comparison of the median and standard deviation of IM distributions for a pool of sets of selected records considering the $CS(D_s)$. As expected, the comparison of the new distributions of IMs shows how the differences in the metrics of the duration distributions essentially vanished. Some discrepancies, however, were still present in terms of standard deviation, especially for the case of $T_1 = 0.2s$, this due to the limit variability of the considered databases.

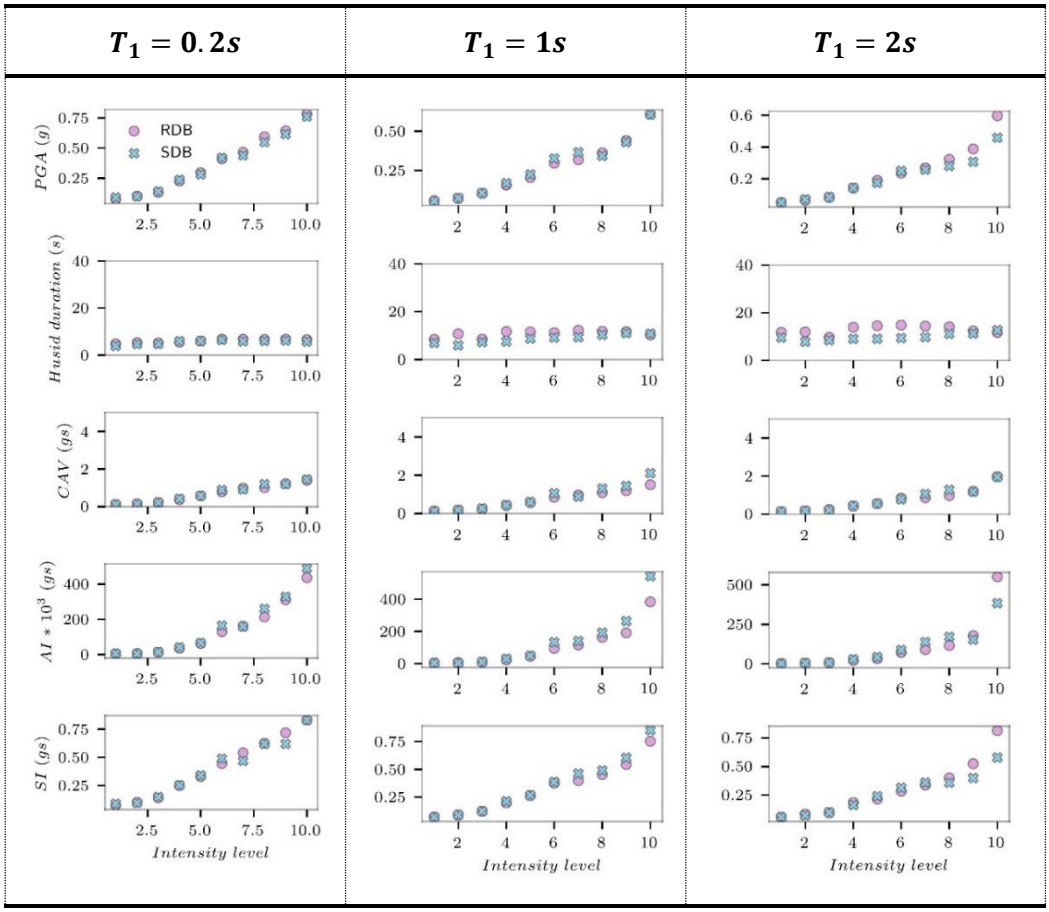

Figure 4.16 – Medians of the distribution of different IMs, namely peak ground acceleration (PGA), Husid duration, Cumulative absolute velocity (CAV), Arias intensity (AI), and Spectral intensity (SI), from first to the last row, respectively, obtained with records selected via $CS(D_s)$.

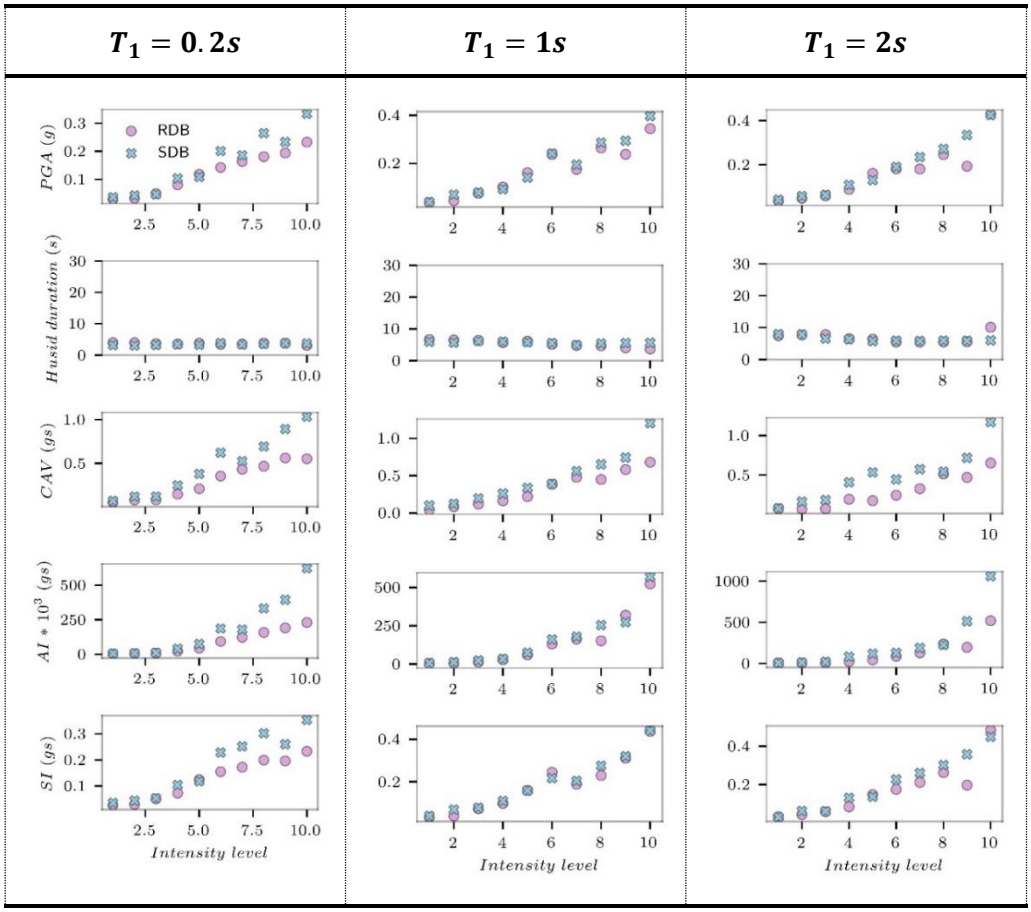

Figure 4.17 – Standard deviations of the distributions of different IMs, namely peak ground acceleration (PGA), Husid duration, Cumulative absolute velocity (CAV), Arias intensity (AI), and Spectral intensity (SI), from first to the last row, respectively, obtained with records selected via $CS(D_s)$.

By analysing the fragility curves computed with the new selected sets of records, shown in Figure 4.18 and Figure 4.19, a clear improvement in the match for all limit states may be noticed. Essentially, the consideration of duration as complementary conditioning IM effectively eliminates the bias introduced by the insufficient calibration of the simulation technique i.e., deficiencies in the match of the distributions of IMs.

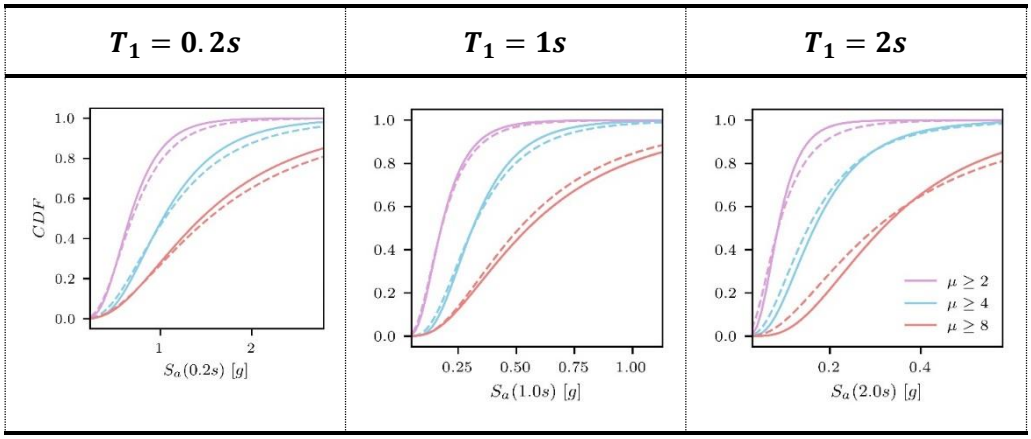

Figure 4.18 – Comparison between the fragility curves obtained with the $CS(D_s)$-based records extracted from RDB (solid line) and SDB (dashed line) for three different ductility levels of SDoF systems with T_1=0.2s, T_1=1s and T_1=2s vibration periods and pinching hysteresis model.

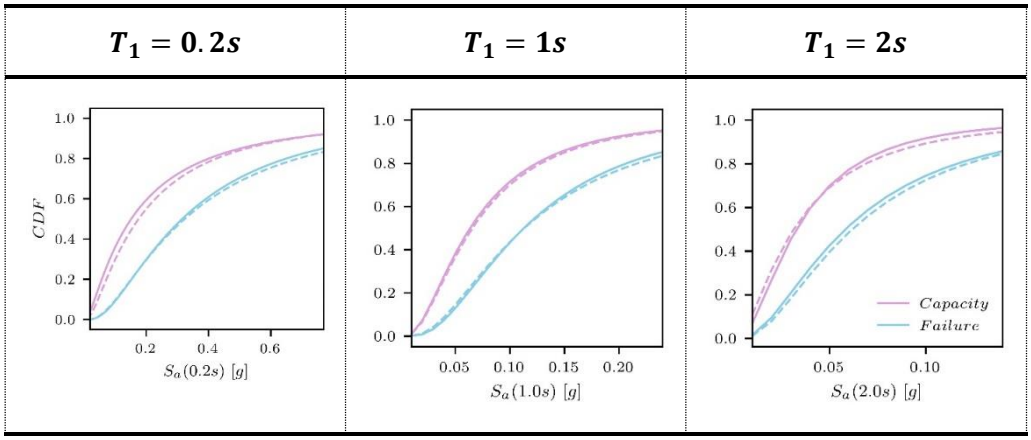

Figure 4.19 – Comparison between the fragility curves obtained with the $CS(D_s)$-based records extracted from RDB (solid line) and SDB (dashed line) for two different acceleration levels of SDoF systems with T_1=0.2s, T_1=1s and T_1=2s vibration periods and pinching hysteresis model.

4.6 SUMMARY AND CONCLUSIONS

This chapter presented a validation for the use of the ground motion simulation technique for its use within a single building risk assessment framework. Specifically, this validation consisted in the evaluation of the adequacy of using simulated ground motions in lieu of or, better, in addition to real records for computing site specific CS-based fragility curves. Like for the previous chapter, the results were showcased with a case study where a suite of structures were assumed to be located at a rock site in central Italy. The structures were modelled as nonlinear SDoF systems with different fundamental periods of vibration and with two alternative material hysteretic models. The validation was focused on the

comparison of EDPs, and fragility curves, computed via nonlinear dynamic analysis fed by both real and synthetic ground motions. These were selected based on the original spectral-content-focused CS approach and a variant of it, which also explicitly enforces the hazard consistency of ground motion duration.

The recorded ground motions were selected from a database of real records (RDB) constructed from a subset of the ESM database. To remove the sample size variability of the IMs that matter for predicting the EDPs that control the limit states for which the fragility curves are sought, a database of synthetic ground motions (SDB) was constructed. The SDB was designed to be fully consistent with the characteristics of the causative events and the soil conditions of the ground motions included in the RDB. The synthetic ground motions populating the SDB were generated with the simulation technique introduced in this work and considering a calibration process aiming to match the distribution of spectral ordinates and energy of the reference database.

Based on the results obtained from this assessment, the following conclusions may be drawn:

- Considering a CS selection method, the selected sets of records matched in terms of the distributions of the causative parameters for all considered cases, thus validating the capacity of the simulation technique to represent the spectral content of the motions for all groups of ground motions populating the reference database.
- The calibration of the simulation technique, based on the matching of spectral content and energy only, resulted in an inaccurate representation of distributions of other IMs in the reference database, i.e., Husid duration and cumulative absolute velocity (CAV)
- The differences in duration-related IMs impact the distribution of the EDPs computed using hazard consistent sets of ground motions extracted from both the RDB and the SDB via the original spectral-quantity-oriented CS approach. The fragility curves related to the exceedance of ductility levels and, to a less extent, those related to the exceedance of acceleration-based showed a considerable bias. This bias was, to a large extent, removed when the consistency of Husid was also enforced.

5.GENERAL CONCLUSIONS AND FUTURE DEVELOPMENTS

5.1 CONCLUSIONS

Stochastic ground motion simulation methodologies have gained popularity amongst researchers and practitioners due to their easiness of application and constant improvement in the description of the earthquake phenomenon. These methods, however, need to be properly tested before simulated ground motions may be considered in lieu of or alongside recorded ground motions. In this thesis, an improved 3D stochastic ground motion simulation method was proposed. This method improves a state-of-the-art stochastic ground motion simulation technique by incorporating a more realistic representation of the source and correlation structure between spectral ordinates of the simulated ground motions. The proposed method was then validated from a seismological and engineering point of view through ground motion prediction and single building risk assessment case studies, respectively. The consideration of these case studies allowed for the presentation of proposed calibration and ground motion simulation schemes complementary to the simulation technique and which may be of interest for future users. In the following, the main conclusions drawn from the research performed are be outlined, however, in addition to the full account of conclusions drawn in each of the main chapters in this thesis.

From the introduction and assessment of the 3D stochastic ground motion simulation technique:

- The proposed simulation methodology generated consistent 3D acceleration time histories. The consideration of the herein proposed post-processing procedure allowed for the significant improvement of the spectral correlation structure with respect to other stochastic simulation techniques. Additionally, the consideration of a more realistic source model aided in the proper modelling of the waveform.

From the seismological validation of the simulation technique

- The distributions of spectral accelerations and significant duration, estimated from GMMs suitable for a case study, were properly matched by the simulated ground motions. The modelling of the uncertainty of the input variables allowed for the

accurate representation of the distributions of significant duration and spectral accelerations of the horizontal components up to a period of vibration of 2s.

- The comparison of the simulated ground motions with the reference GMM and observed event indicated that the simulation technique performed better in the representation of the short period/high frequency content range of the earthquake ground motion. The simulation technique was found to be more accurate in the simulation of scenarios close to the source and characterized by stiff soils. These constraints respond to the lack of modelling of surface-waves and non-linear site response, respectively.
- Simulated ground motions were found to overestimate the spectral content of the vertical component for increasing periods of vibration and distance to the source. These differences may be due to different simplifications considered in the modelling of the P and SV-waves.

From the engineering validation of the simulation technique

- Hazard consistency was found to be key for the limited-biased estimation of the structural response when considering simulated ground motions. The use of an insufficient conditioning IM vector resulted in important differences in the comparison of fragility curves for ductility and floor acceleration limit states.
- The enforcement of hazard consistency in terms of spectral acceleration and significant duration of motion resulted in the agreement of structural responses and fragility curves computed with sets of recorded and simulated ground motions. However, and considering that some bias was still noticed, specifically for the collapse-related fragility curves, this study recommends the use of these simulated ground motions in regions where the GMMs considered in the record selection scheme are well constraint.

5.2 FUTURE DEVELOPMENTS

During the development of this thesis, some subjects were identified as valuable axes of improvement, yet not pursued because they were either out of the scope or could not be explored due to insufficient resources. These constitute the following list of recommendations for future developments:

- It was observed, during the various applications of the simulation technique, that the vertical component of the simulated ground motions was often overestimated with respected to the reference ground motions, either recorded or from GMMs. This observation indicated that the simulated FAS of P and SV waves is larger than observed in natural records. Considering that the overall decay of spectral content in simulated ground motions, obtained from the spectral acceleration estimates for different distances and matching soil conditions, is very similar to that of the

observed references, we considered the deficiency to be in the estimation of the source spectrum and thus in the estimation of the stress drop used in its construction. Currently, the model estimates the stress drop of P-waves as a factor (α/β) of the prescribed S wave stress drop. This model is rather simplistic and could be improved by adopting a more physical description of the P-wave source spectrum.

- The postprocessing procedure proposed in this document assumed that the intra-frequency correlation structure derived from the analysis of the horizontal components was also valid for the vertical component of the motion. This had to be considered due to the inexistence, to the authors knowledge, of such models in current available literature. The derivation of such model would benefit the herein proposed procedure to include the inter frequency correlation structure.
- The analysis of biases from the comparison of spectral accelerations of recorded and simulated ground motions showed that simulations for scenarios considering softer soils, i.e., $Vs_{30} \leq 400\ m/s$, were systematically different to those obtained from reference GMMs or observed events. More so for simulations considering higher magnitudes. The main cause of this deficiency is the use of linear elastic transfer functions for the computation of site-effects. These functions are limited to the elastic response of the soil layer configurations and thus become irrelevant for scenarios where the amplitude of the simulation causes the nonlinear response of the soil. The consideration of complementary methodologies approximating the propagation of the wave in nonlinear media would, in theory, improve the quality of the simulated ground motions for some scenarios currently miss-represented.

REFERENCES

Afshari, K., & Stewart, J. P. (2016). Physically Parameterized Prediction Equations for Significant Duration in Active Crustal Regions. *Earthquake Spectra*, *32*, 2057–2081. https://doi.org/10.1193/063015EQS106M

Aki, K. (1967). Scaling Law of Seismic Spectrum. *Journal of Geophysical Research*, *72*(4), 1217–1231.

al Atik, L., Abrahamson, N., Bommer, J. J., Scherbaum, F., Cotton, F., & Kuehn, N. (2010). The variability of ground-motion prediction models and its components. *Seismological Research Letters*, *81*(5), 794–801. https://doi.org/10.1785/gssrl.81.5.794

Alvarez, L., Bonilla, L., Bazzurro, P., Aochi, H., Zentner, I., & Senfaute, G. (2022). 3D Stochastic Ground Motion Prediction for an event in the region of Niigata, Japan. *Journal Geophysics International* .

Anderson, J. G., & Hough, S. E. (1984). A MODEL FOR THE SHAPE OF THE FOURIER AMPLITUDE SPECTRUM OF ACCELERATION AT HIGH FREQUENCIES. In *Bulletin of the Seismological Society of America* (Vol. 74, Issue 5).

Andrews, D. J. (1980). A stochastic fault model: 1. Static case. *Journal of Geophysical Research: Solid Earth*, *85*(B7), 3867–3877. https://doi.org/10.1029/JB085iB07p03867

Aochi, H., Ducellier, A., Dupros, F., Delatre, M., Ulrich, T., de Martin, F., & Yoshimi, M. (2013). Finite difference simulations of seismic wave propagation for the 2007 Mw 6.6 Niigata-ken Chuetsu-Oki earthquake: Validity of models and reliable input ground motion in the near field. *Pure and Applied Geophysics*, *170*(2). https://doi.org/10.1007/s00024-011-0429-5ï

Aochi, H., & Ulrich, T. (2015). A Probable Earthquake Scenario near Istanbul Determined from Dynamic Simulations. *Bulletin of the Seismological Society of America*, *105*(3), 1468–1475. https://doi.org/10.1785/0120140283

Aoi, S., Honda, R., Morikawa, N., Sekiguchi, H., Suzuki, H., Hayakawa, Y., Kunugi, T., & Fujiwara, H. (2008). Three-dimensional finite difference simulation of long-period

ground motions for the 2003 Tokachi-oki, Japan, earthquake. *Journal of Geophysical Research: Solid Earth*, *113*(7). https://doi.org/10.1029/2007JB005452

Asano, K., & Iwata, T. (2009). Source rupture process of the 2004 Chuetsu, Mid-Niigata Prefecture, Japan, earthquake inferred from waveform inversion with dense strong-motion data. *Bulletin of the Seismological Society of America*, *99*(1), 123–140. https://doi.org/10.1785/0120080257

Atkinson, G. M., & Assatourians, K. (2015). Implementation and validation of EXSIM (a stochastic finite-fault ground-motion simulation algorithm) on the SCEC broadband platform. *Seismological Research Letters*, *86*(1), 48–60. https://doi.org/10.1785/0220140097

Atkinson, G. M., Assatourians, K., Boore, D. M., Campbell, K., & Motazedian, D. (2009). A guide to differences between stochastic point-source and stochastic finite-fault simulations. *Bulletin of the Seismological Society of America*, *99*(6), 3192–3201. https://doi.org/10.1785/0120090058

Atkinson, G. M., & Silva, W. (2000). Stochastic Modeling of California Ground Motions. In *Abrahamson and Silva* (Vol. 90, Issue 2). Seismological Society of America.

Baker, J. W., & Cornell, C. A. (2006). Spectral shape, epsilon and record selection. *Earthquake Engineering and Structural Dynamics*, *35*(9), 1077–1095. https://doi.org/10.1002/eqe.571

Baker, J. W., & Jayaram, N. (2008). Correlation of spectral acceleration values from NGA ground motion models. *Earthquake Spectra*, *24*(1), 299–317. https://doi.org/10.1193/1.2857544

Baker, J. W., & Lee, C. (2018). An Improved Algorithm for Selecting Ground Motions to Match a Conditional Spectrum. *Journal of Earthquake Engineering*, *22*(4), 708–723. https://doi.org/10.1080/13632469.2016.1264334

Bayless, J., & Abrahamson, N. A. (2018). Evaluation of the interperiod correlation of ground-motion simulations. *Bulletin of the Seismological Society of America*, *108*(6), 3413–3430. https://doi.org/10.1785/0120180095

Bayless, J., & Abrahamson, N. A. (2019a). An empirical model for the interfrequency correlation of epsilon for fourier amplitude spectra. *Bulletin of the Seismological Society of America*, *109*(3), 1058–1070. https://doi.org/10.1785/0120180238

Bayless, J., & Abrahamson, N. A. (2019b). An empirical model for the interfrequency correlation of epsilon for fourier amplitude spectra. *Bulletin of the Seismological Society of America*, *109*(3), 1058–1070. https://doi.org/10.1785/0120180238

Beresnev, I. A., & Atkinson, G. M. (1997). Modeling Finite-Fault Radiation from the o) n Spectrum. In *Bulletin of the Seismological Society of America* (Vol. 87, Issue 1). Atldnson and Boore.

Bijelić, N., Lin, T., & Deierlein, G. G. (2018). Validation of the SCEC Broadband Platform simulations for tall building risk assessments considering spectral shape and duration of the ground motion. *Earthquake Engineering and Structural Dynamics*, *47*(11), 2233–2251. https://doi.org/10.1002/eqe.3066

Bindi, D., & Kotha, S. R. (2020). Spectral decomposition of the Engineering Strong Motion (ESM) flat file : regional attenuation , source scaling and Arias stress drop. *Bulletin of Earthquake Engineering*, *18*(6), 2581–2606. https://doi.org/10.1007/s10518-020-00796-1

Boatwright, J., Fletcher, J. B., & Fumal, T. (1991). A general inversion scheme for source, site, and propagation characteristics using multiply recorded sets of moderate-sized earthquakes. *Bulletin of the Seismological Society of America*, *81*, 1754–1782.

Bommer, J. J., Magenes, G., Hancock, J., & Penazzo, P. (2004). The influence of strong-motion duration on the seismic response of masonry structures. *Bulletin of Earthquake Engineering*, *2*(1), 1–26. https://doi.org/10.1023/B:BEEE.0000038948.95616.bf

Bonilla, L. F., Steidl, J. H., Lindley, G. T., Tumarkin, A. G., & Archuleta, R. J. (1997). Site Amplification in the San Fernando Valley, California: Variability of Site-Effect Estimation Using the S-Wave, Coda, and H/V Methods. In *Bulletin of the Seismological Society of America* (Vol. 87, Issue 3). http://pubs.geoscienceworld.org/ssa/bssa/article-pdf/87/3/710/2709133/BSSA0870030710.pdf

Boore, D. M. (1983). STOCHASTIC SIMULATION OF HIGH-FREQUENCY GROUND MOTIONS BASED ON SEISMOLOGICAL MODELS OF THE RADIATED SPECTRA. In *Bulletin of the Se~smologmal Society of America* (Vol. 73, Issue 6).

Boore, D. M. (2003). Simulation of Ground Motion Using the Stochastic Method. *Pure and Applied Geophysics*, *160*, 635–676.

Boore, D. M. (2005). On pads and filters: Processing strong-motion data. *Bulletin of the Seismological Society of America*, *95*(2), 745–750. https://doi.org/10.1785/0120040160

Boore, D. M. (2009). Comparing Stochastic Point-Source and Finite-Source Ground-Motion Simulations: SMSIM and EXSIM. *Bulletin of the Seismological Society of America*, *99*(6), 3202–3216. https://doi.org/10.1785/0120090056

Boore, D. M., & Atkinson, G. M. (2008). Ground-motion prediction equations for the average horizontal component of PGA, PGV, and 5%-damped PSA at spectral periods between 0.01 s and 10.0 s. *Earthquake Spectra*, *24*(1), 99–138. https://doi.org/10.1193/1.2830434

Boore, D. M., & Bommer, J. J. (2005). Processing of strong-motion accelerograms: Needs, options and consequences. *Soil Dynamics and Earthquake Engineering*, *25*(2), 93–115. https://doi.org/10.1016/j.soildyn.2004.10.007

Boore, D. M., & Joyner, W. B. (1997a). Site amplifications for generic rock sites. *Bulletin of the Seismological Society of America*, *87*(2), 327–341. https://doi.org/10.1785/bssa0870020327

Boore, D. M., & Joyner, W. B. (1997b). Site Amplifications for Generic Rock Sites. In *Bulletin of the Seismological Society of America* (Vol. 87, Issue 2).

Boore, D. M., Joyner, W. B., & Fumal, T. E. (1997). Equations for Estimating Horizontal Response Spectra and Peak Acceleration from Western North American Earthquakes: A Summary of Recent Work. *Seismological Research Letters*, *68*, 128–153.

Boore, D. M., Stewart, J. P., Seyhan, E., & Atkinson, G. M. (2014). NGA-West2 Equations for Predicting PGA, PGV, and 5% Damped PSA for Shallow Crustal Earthquakes. *Earthquake Spectra*, *30*(3), 1057–1085. https://doi.org/10.1193/070113EQS184M

Bradley, B. A. (2010). A generalized conditional intensity measure approach and holistic ground-motion selection. *Earthquake Engineering & Structural Dynamics*, *39*, 1321–1342. https://doi.org/10.1002/eqe

Bradley, B. A. (2011). Correlation of significant duration with amplitude and cumulative intensity measures and its use in ground motion selection. *Journal of Earthquake Engineering*, *15*(6), 809–832. https://doi.org/10.1080/13632469.2011.557140

Bradley, B. A., Burks, L. S., & Baker, J. W. (2015). Ground motion selection for simulation-based seismic hazard and structural reliability assessment. *Earthquake Engineering and Structural Dynamics*, *44*(13), 2321–2340. https://doi.org/10.1002/eqe.2588

Brune, J. N. (1970). Tectonic stress and the spectra of seismic shear waves from earthquakes. *Journal of Geophysical Research*, *75*(26), 4997–5009. https://doi.org/10.1029/JB075i026p04997

Burks, L. S., & Baker, J. W. (2014). Validation of ground-motion simulations through simple proxies for the response of engineered systems. *Bulletin of the Seismological Society of America*, *104*(4), 1930–1946. https://doi.org/10.1785/0120130276

Castro, R. R., Anderson, J. G., & Singh, S. K. (1990). SITE RESPONSE, ATTENUATION AND SOURCE SPECTRA OF S WAVES ALONG THE GUERRERO, MEXICO, SUBDUCTION ZONE. In *Bulletin of the Seismological Society of America* (Vol. 80, Issue 6). http://pubs.geoscienceworld.org/ssa/bssa/article-pdf/80/6A/1481/2706754/BSSA08006A1481.pdf

Chandramohan, R., Baker, J. W., & Deierlein, G. G. (2016). *Quantifying the influence of ground motion duration on structural collapse capacity using spectrally equivalent records Digital Appendix*.

Cornell, C. A. (1968). Engineering seismic risk analysis. *Bulletin of the Seismological Society of America*, *58*(5), 1583–1606. https://doi.org/10.1785/BSSA0580051583

Cornell, C. A., & Krawinkler, H. (2000). *Progress and challenges in seismic performance assessment* (pp. 1–3). PEER Center News, 3.

Dang, P., Cui, J., Liu, Q., & Xia, S. (2022). Slip-Correlated High-Frequency Scaling Factor for Stochastic Finite-Fault Modeling of Ground Motion. *Bulletin of the Seismological Society of America*. https://doi.org/10.1785/0120210293

Douglas, J., & Aochi, H. (2008). A survey of techniques for predicting earthquake ground motions for engineering purposes. *Surveys in Geophysics*, *29*(3), 187–220. https://doi.org/10.1007/s10712-008-9046-y

Dreger, D. S., Beroza, G. C., Day, S. M., Goulet, C. A., Jordan, T. H., Spudich, P. A., & Stewart, J. P. (2015). Validation of the SCEC broadband platform v14.3 simulation methods using pseudospectral acceleration data. *Seismological Research Letters*, *86*(1), 39–47. https://doi.org/10.1785/0220140118

Dreger, D. S., & Jordan, T. H. (2015). Introduction to the focus section on validation of the SCEC broadband platform V14.3 simulation methods. *Seismological Research Letters*, *86*(1), 15–16. https://doi.org/10.1785/0220140233

EPRI. (1991). *Generic seismic ruggedness of power plant equipment (Revision 1)*.

Evans, R. (1984). *Effects of the free surface on shear wavetrains* (Vol. 76).

Frankel, A. (2009). A Constant Stress-Drop Model for Producing Broadband Synthetic Seismograms: Comparison with the Next Generation Attenuation Relations. *Bulletin of the Seismological Society of America*, *99*(2A), 664–680. https://doi.org/10.1785/0120080079

Friedl, H., & Stampfer, E. (2001). Jackknife Resampling. In *Encyclopedia of Environmetrics*. Wiley. https://doi.org/10.1002/9780470057339.vaj001

Gallovič, F. (2016). Modeling velocity recordings of the mw 6.0 south napa, California, earthquake: Unilateral event with weak high-frequency directivity. *Seismological Research Letters*, *87*(1), 2–14. https://doi.org/10.1785/0220150042

Gallovič, F., & Brokešová, J. (2007). Hybrid k-squared source model for strong ground motion simulations: Introduction. *Physics of the Earth and Planetary Interiors*, *160*(1), 34–50. https://doi.org/10.1016/j.pepi.2006.09.002

Garcia, P., Šipčić, N., Alvarez, L., Kohrangui, M., & Bazzurro, P. (2022). A Closer look at Hazard COnsistent Ground Motion Selection for Building Specific Risk Assessment. Effect of Soil Chracteristics and Scaling or Real Accelerograms. *Earthquake Spectra*.

Goulet, C. A., Abrahamson, N. A., Somerville, P. G., & Wooddell, K. E. (2015). The SCEC broadband platform validation exercise: Methodology for code validation in the context of seismic-hazard analyses. *Seismological Research Letters*, *86*(1), 17–26. https://doi.org/10.1785/0220140104

Graves, R. W., & Pitarka, A. (2010). Broadband ground-motion simulation using a hybrid approach. *Bulletin of the Seismological Society of America*, *100*(5 A), 2095–2123. https://doi.org/10.1785/0120100057

Hanks, T. C. (1982). *f* max. *Bulletin of the Seismological Society of America*, *72*(6A), 1867–1879. https://doi.org/10.1785/BSSA07206A1867

Hanks, T. C., & Kanamori, H. (1979). A moment magnitude scale. *Journal of Geophysical Research B: Solid Earth*, *84*(B5), 2348–2350. https://doi.org/10.1029/JB084iB05p02348

Hanks, T. C., & McGuire, R. K. (1981). The character of high-frequency strong ground motion. *Bulletin of the Seismological Society of America*, *71*(6), 2071–2095. https://doi.org/10.1785/BSSA0710062071

Haskell, N. A. (1953). The dispersion of surface waves on multilayered media. *Bulletin of the Seismological Society of America*, *43*(1), 17–34. https://doi.org/10.1785/BSSA0430010017

Jayaram, N., Lin, T., & Baker, J. W. (2011). A Computationally efficient ground-motion selection algorithm for matching a target response spectrum mean and variance. *Earthquake Spectra*, *27*(3), 797–815. https://doi.org/10.1193/1.3608002

Ji, C., & Archuleta, R. J. (2021). Two empirical double-corner-frequency source spectra and their physical implications. *Bulletin of the Seismological Society of America*, *111*(2), 737–761. https://doi.org/10.1785/0120200238

Ji, D., Wen, W., Zhai, C., & Katsanos, E. I. (2018). Residual displacement ratios of SDOF systems subjected to ground motions recorded on soft soils. *Soil Dynamics and Earthquake Engineering*, *115*(September), 331–335. https://doi.org/10.1016/j.soildyn.2018.09.001

Jin, A., Moya, C. A., & Ando, M. (2000). Simultaneous Determination of Site Responses and Source Parameters of Small Earthquakes along the Atotsugawa Fault Zone, Central Japan. In *Bulletin of the Seismological Society of America* (Vol. 90). https://pubs.geoscienceworld.org/ssa/bssa/article-pdf/90/6/1430/2710509/1430_ssa99140.pdf

Kamae, K., Irikura, K., & Pitarka, A. (1998). A Technique for Simulating Strong Ground Motion Using Hybrid Green's Function. In *Bulletin of the Seismological Society of America* (Vol. 88, Issue 2).

Kinoshita, S. (1994). Frequency-dependent attenuation of shear waves in the crust of the southern Kanto area, Japan. *Bulletin of the Seismological Society of America*, *84*(5), 1387–1396.

Kinoshita, S., & Ohike, M. (2002). Scaling relations of earthquakes that occurred in the upper part of the Philippine Sea plate beneath the Kanto region, Japan, estimated by

means of borehole recordings. *Bulletin of the Seismological Society of America*, *92*(2), 611–624.

Kohrangi, M., Papadopoulos, A. N., Bazzurro, P., & Vamvatsikos, D. (2020). Correlation of spectral acceleration values of vertical and horizontal ground motion pairs. *Earthquake Spectra*, *36*(4), 2112–2128. https://doi.org/10.1177/8755293020919416

Konno, K., & Ohmachi, T. (1998). Ground-motion characteristics estimated from spectral ratio between horizontal and vertical components of microtremor. *Bulletin of the Seismological Society of America*, *88*(1), 228–241. https://doi.org/10.1785/BSSA0880010228

Kotha, S. R., Cotton, F., & Bindi, D. (2018). A new approach to site classification: Mixed-effects Ground Motion Prediction Equation with spectral clustering of site amplification functions. *Soil Dynamics and Earthquake Engineering*, *110*, 318–329. https://doi.org/10.1016/j.soildyn.2018.01.051

Lanzano, G., Sgobba, S., Luzi, L., Puglia, R., Pacor, F., Felicetta, C., D'Amico, M., Cotton, F., & Bindi, D. (2019). The pan-European Engineering Strong Motion (ESM) flatfile: compilation criteria and data statistics. *Bulletin of Earthquake Engineering*, *17*(2), 561–582. https://doi.org/10.1007/s10518-018-0480-z

Lee, R. L., Bradley, B. A., Stafford, P. J., Graves, R. W., & Rodriguez-Marek, A. (2020). Hybrid broadband ground motion simulation validation of small magnitude earthquakes in Canterbury, New Zealand. *Earthquake Spectra*, *36*(2), 673–699. https://doi.org/10.1177/8755293019891718

Luco, N., & Cornell, A. (2007). Structure-Specific Scalar Intensity Measures for Near-Source and Ordinary Earthquake Ground Motions. *Earthquake Spectra*, *23*, 357–392. http://peer.berkeley.edu/news/2000spring/performance.html

Mai, M. P., & Beroza, G. C. (2002). A spatial random field model to characterize complexity in earthquake slip. *Journal of Geophysical Research: Solid Earth*, *107*(B11), ESE 10-1-ESE 10-21. https://doi.org/10.1029/2001jb000588

McGuire, R. K., & Hanks, T. C. (1980). RMS accelerations and spectral amplitudes of strong ground motion during the San Fernando, California earthquake. *Bulletin of the Seismological Society of America*, *70*(5), 1907–1919. https://doi.org/10.1785/BSSA0700051907

Motazedian, D., & Atkinson, G. M. (2005). Stochastic finite-fault modeling based on a dynamic corner frequency. *Bulletin of the Seismological Society of America*, *95*(3), 995–1010. https://doi.org/10.1785/0120030207

Moya, A., & Irikura, K. (2003). Estimation of Site Effects and Q Factor Using a Reference Event. In *Bulletin of the Seismological Society of America* (Vol. 93, Issue 4). https://pubs.geoscienceworld.org/ssa/bssa/article-pdf/93/4/1730/2718533/1730_934_02220.1730_1745.pdf

National Research Institute for Earth Science and Disaster Resilience. (2019). *NIED K-NET, KiK-net*.

Olsen, K. B., Day, S. M., Dalguer, L. A., Mayhew, J., Cui, Y., Zhu, J., Cruz-Atienza, V. M., Roten, D., Maechling, P., Jordan, T. H., Okaya, D., & Chourasia, A. (2009). ShakeOut-D: Ground motion estimates using an ensemble of large earthquakes on the southern San Andreas fault with spontaneous rupture propagation. *Geophysical Research Letters*, *36*(4). https://doi.org/10.1029/2008GL036832

Onishi, Y., & Horike, M. (2004). The Extended Stochastic Simulation Method for Close-Fault Earthquake Motion Prediction and Comments for its Application to the Hybrid Method. *Journal of Structural and Construction Engineering*, *69*, 37–44.

Otarola, C., & Ruiz, S. (2016). Stochastic generation of accelerograms for subduction earthquakes. *Bulletin of the Seismological Society of America*, *106*(6), 2511–2520. https://doi.org/10.1785/0120150262

Oth, A., Bindi, D., Parolai, S., & di Giacomo, D. (2010). Earthquake scaling characteristics and the scale-(in)dependence of seismic energy-to-moment ratio: Insights from KiK-net data in Japan. *Geophysical Research Letters*, *37*(19). https://doi.org/10.1029/2010GL044572

Oth, A., Bindi, D., Parolai, S., & di Giacomo, D. (2011). Spectral analysis of K-NET and KiK-net data in Japan, Part II: On attenuation characteristics, source spectra, and site response of borehole and surface stations. *Bulletin of the Seismological Society of America*, *101*(2), 667–687. https://doi.org/10.1785/0120100135

Oth, A., Parolai, S., & Bindi, D. (2011). Spectral analysis of K-NET and KiK-net data in Japan, Part I: Database compilation and peculiarities. *Bulletin of the Seismological Society of America*, *101*(2), 652–666. https://doi.org/10.1785/0120100134

Pacor, F., Cultrera, G., Mendez, A., & Cocco, M. (2005). Finite fault modeling of strong ground motions using a hybrid deterministic-stochastic approach. *Bulletin of the Seismological Society of America*, *95*(1), 225–240. https://doi.org/10.1785/0120030163

Pagani, M., Monelli, D., Weatherill, G., Danciu, L., Crowley, H., Henshaw, P., Butler, L., Nastasi, M., Panzeri, L., Simionato, M., & Vigano, D. (2014). OpenQuake Engine : An Open Hazard (and Risk) Software for the Global Earthquake Model. *Seismological Research Letters*, *85*(3), 692–702. https://doi.org/10.1785/0220130087

Paolucci, R., Mazzieri, I., & Smerzini, C. (2015). Anatomy of strong ground motion: Near-source records and three-dimensional physics-based numerical simulations of the Mw 6.0 2012 may 29 po plain earthquake, Italy. *Geophysical Journal International*, *203*(3), 2001–2020. https://doi.org/10.1093/gji/ggv405

Papageorgiou, A. S., & Aki, K. (1983). A specific barrier model for the quantitative description of inhomogeneous faulting and the prediction of strong ground motion. Part II. Applications of the model. *Bulletin of the Seismological Society of America*, *73*(4), 953–978. https://doi.org/10.1785/bssa0730040953

Petrone, F., Abrahamson, N., McCallen, D., & Miah, M. (2021). Validation of (not-historical) large-event near-fault ground-motion simulations for use in civil engineering applications. *Earthquake Engineering & Structural Dynamics*, *50*(1), 116–134. https://doi.org/10.1002/eqe.3366

Pugliese, A., & Sabetta, F. (1996). Simulation of nonstationary time histories scaled for magnitude, distance and soil conditions A new methodology for the seismic risk assessment of structures View project Seismic Hazard Assessment View project Estimation of Response Spectra and Simulation of Nonstationary Earthquake Ground Motions. In *Bulletin of the Seismological Society of America* (Vol. 86, Issue 2). https://www.researchgate.net/publication/236142883

Rezaeian, S., Zhong, P., Hartzell, S., & Zareian, F. (2015). Validation of simulated earthquake ground motions based on evolution of intensity and frequency content. *Bulletin of the Seismological Society of America*, *105*(6), 3036–3049. https://doi.org/10.1785/0120140210

Ruiz, J. A., Baumont, D., Bernard, P., & Berge-Thierry, C. (2011). Modelling directivity of strong ground motion with a fractal, k-2, kinematic source model. *Geophysical Journal International*, *186*(1), 226–244. https://doi.org/10.1111/j.1365-246X.2011.05000.x

Ruiz, S., Ojeda, J., Pastén, C., Otarola, C., & Silva, R. (2018). Stochastic strong-motion simulation in borehole and on surface for the 2011 m w 9.0 tohoku-oki megathrust earthquake considering p, sv, and sh amplification transfer functions. *Bulletin of the Seismological Society of America*, *108*(5), 2333–2346. https://doi.org/10.1785/0120170342

Saragoni, R. G., & Hart, G. C. (1973). Simulation of Artificial Earthquakes. *Earthquake Engineering & Structural Dynamics*, *2*, 249–267.

Star, L. M., Stewart, J. P., & Graves, R. W. (2011). Comparison of Ground Motions from Hybrid Simulations to NGA Prediction Equations. *Earthquake Spectra*, *27*(2), 331–350. https://doi.org/10.1193/1.3583644

Stewart, J. P., Boore, D. M., Seyhan, E., & Atkinson, G. M. (2016). NGA-West2 equations for predicting vertical-component PGA, PGV, and 5%-damped PSA from shallow crustal earthquakes. *Earthquake Spectra*, *32*(2), 1005–1031. https://doi.org/10.1193/072114EQS116M

Sun, X., Tao, X., & Chen, F. (2010). Improvements of corner frequency and scaling factor for stochastic finite-fault modeling. *Earthquake Engineering and Engineering Vibration*, *9*(4), 503–511. https://doi.org/10.1007/s11803-010-0032-2

Takenaka, H., Mamada, Y., & Futamure, H. (2003). Near-source effect on radiation pattern of high-frequency S waves: strong SH–SV mixing observed from aftershocks of the 1997 Northwestern Kagoshima, Japan, earthquakes. *Physics of the Earth and Planetary Interiors*, *137*(1–4), 31–43. https://doi.org/10.1016/S0031-9201(03)00006-2

Tarbali, K., & Bradley, B. A. (2016). The effect of causal parameter bounds in PSHA-based ground motion selection. *Earthquake Engineering and Structural Dynamics*, *45*(9), 1515–1535. https://doi.org/10.1002/eqe.2721

Tsioulou, A., Taflanidis, A. A., & Galasso, C. (2019). Validation of stochastic ground motion model modification by comparison to seismic demand of recorded ground motions. *Bulletin of Earthquake Engineering*, *17*(6), 2871–2898. https://doi.org/10.1007/s10518-019-00571-x

Udias, A. (1999). *Principles of Seismology*. Cambridge University Press.

Wang, M. Z. (2018). *A framework for seismic risk assessment based on artificial neural networks Composition du Jury*. Universite Paris-Saclay.

Wang, N., Takedatsu, R., Olsen, K. B., & Day, S. M. (2019). Broadband ground-motion simulation with interfrequency correlations. *Bulletin of the Seismological Society of America*, *109*(6), 2437–2446. https://doi.org/10.1785/0120190136

Wells, D. L., & Coopersmith, K. J. (1994). New Empirical RelationShips among Magnitude, Rupture Length, Rupture Width, Rupture Area , and Surfce Displacement. *Bulletin of the Seismological Society of America*, *84*, 974–1002.

Zeng, Y., Anderson, J. G., & Yu, G. (1994). A composite source model for computing realistic synthetic strong ground motions. *Geophysical Research Letters*, *21*(8), 725–728. https://doi.org/10.1029/94GL00367

Zhu, C., Weatherill, G., Cotton, F., Pilz, M., Kwak, D. Y., & Kawase, H. (2021). An open-source site database of strong-motion stations in Japan: K-NET and KiK-net (v1.0.0). *Earthquake Spectra*, *37*(3), 2126–2149. https://doi.org/10.1177/8755293020988028

APPENDIX

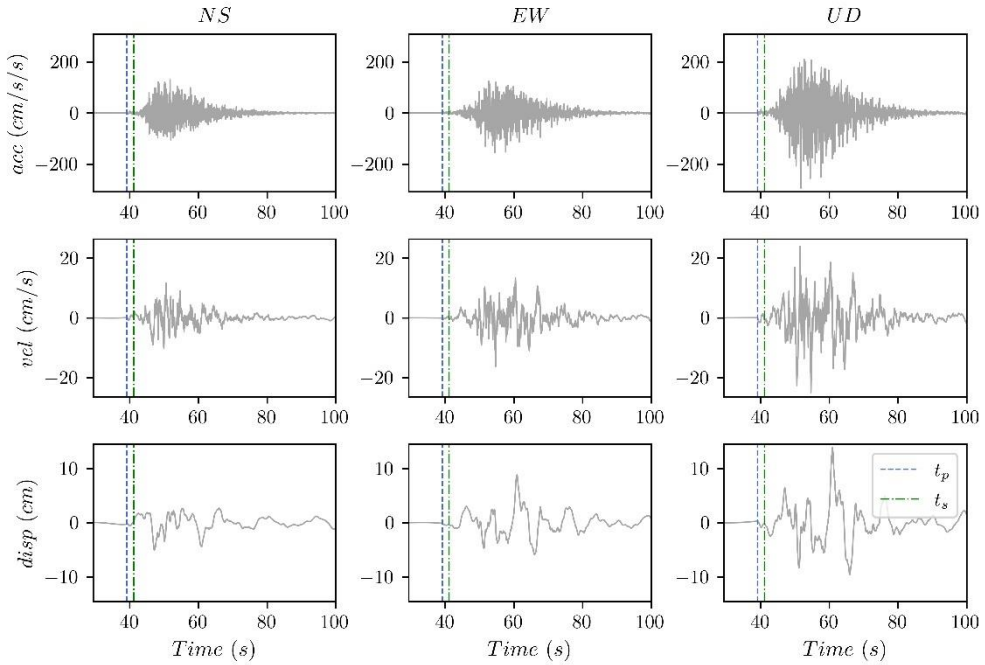

Appendix 1. Base model time histories for station B. The time histories for North-South, East-West and Upward-Downward components are shown in the left, centre, and right column, respectively

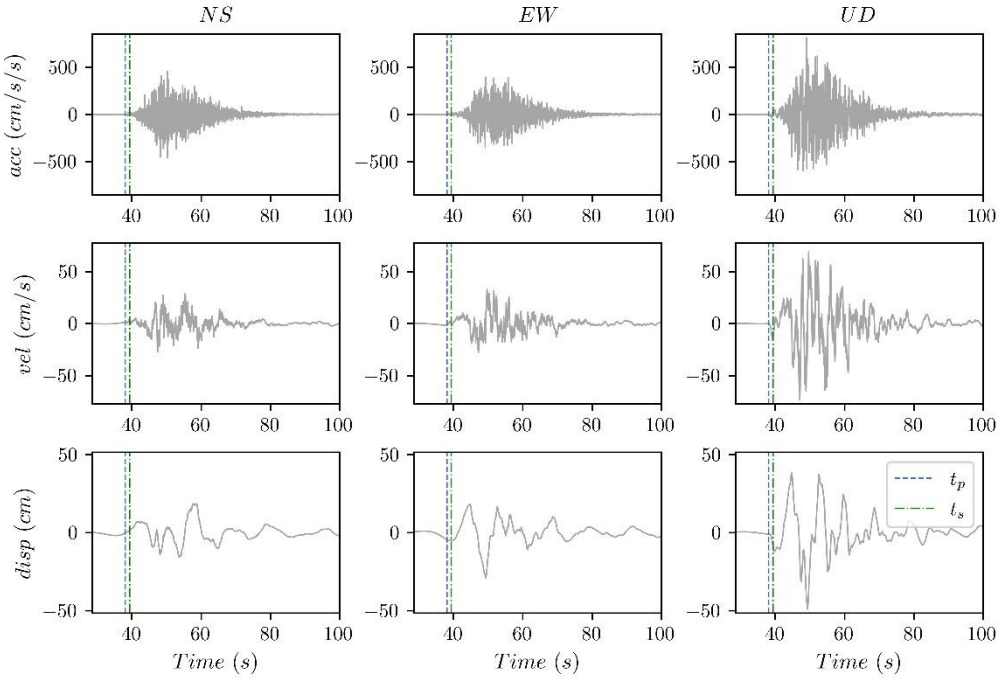

Appendix 2. Base model time histories for station C. The time histories for North-South, East-West and Upward-Downward components are shown in the left, centre, and right column, respectively

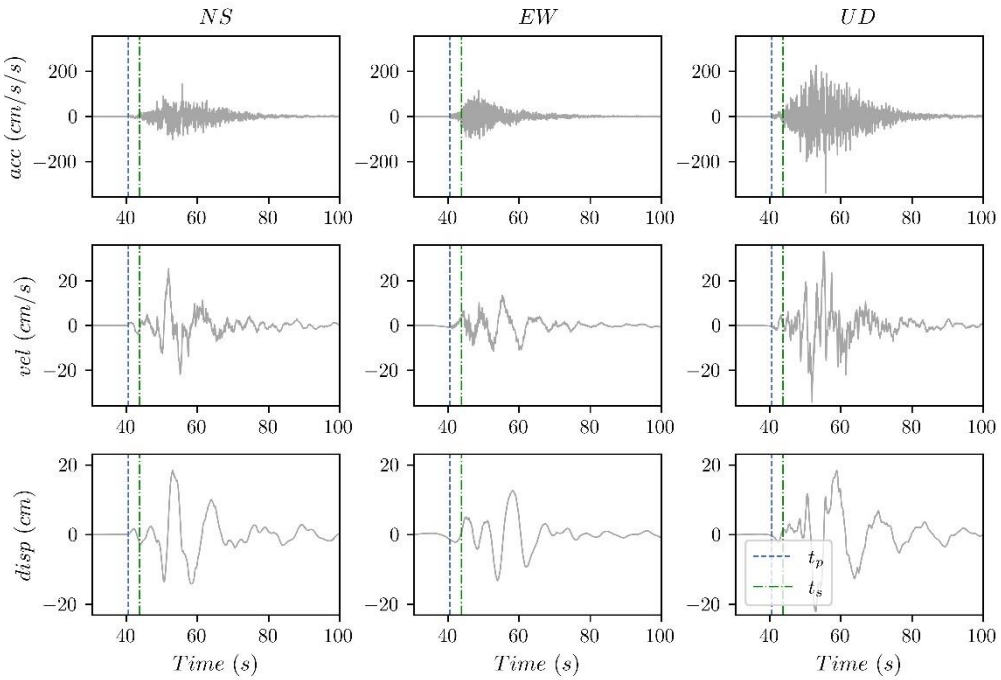

Appendix 3. Base model time histories for station D. The time histories for North-South, East-West and Upward-Downward components are shown in the left, centre, and right column, respectively.

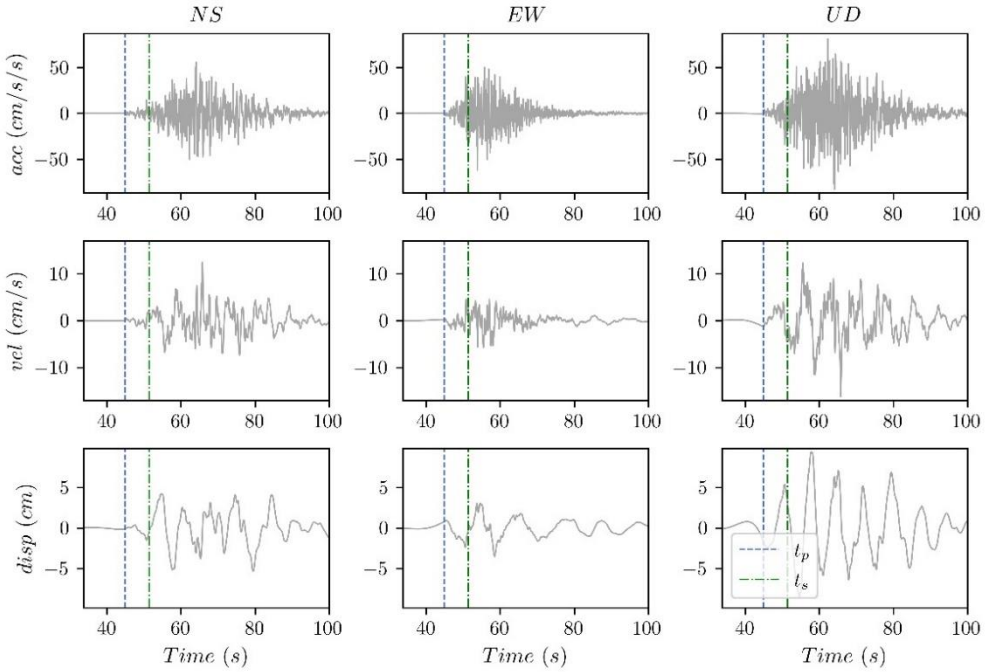

Appendix 4. Base model time histories for station E. The time histories for North-South, East-West and Upward-Downward components are shown in the left, centre, and right column, respectively.

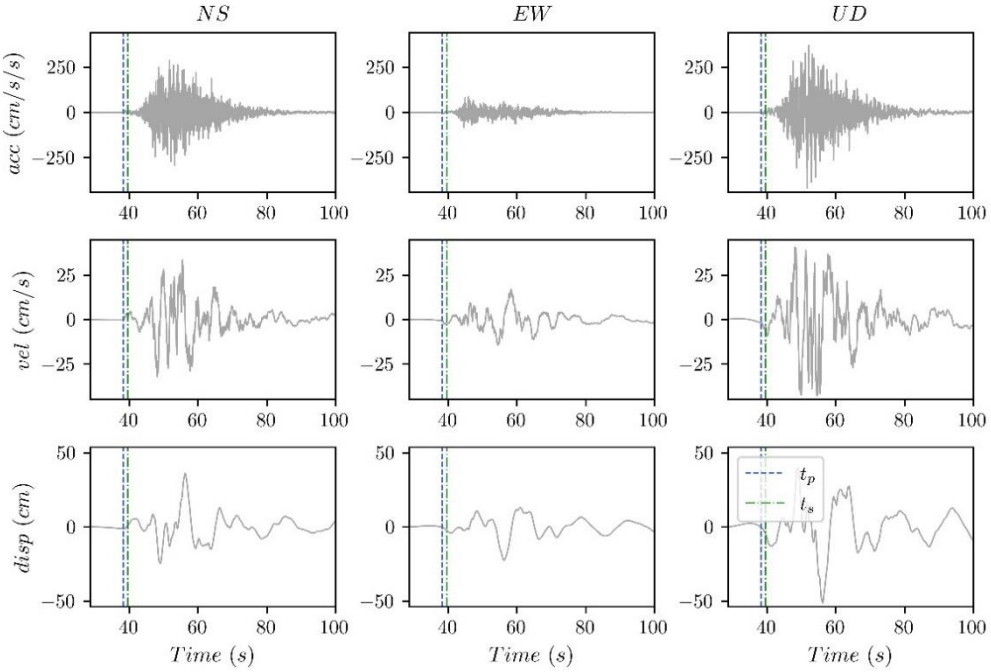

Appendix 5. Base model time histories for station F. The time histories for North-South, East-West and Upward-Downward components are shown in the left, centre, and right column, respectively.

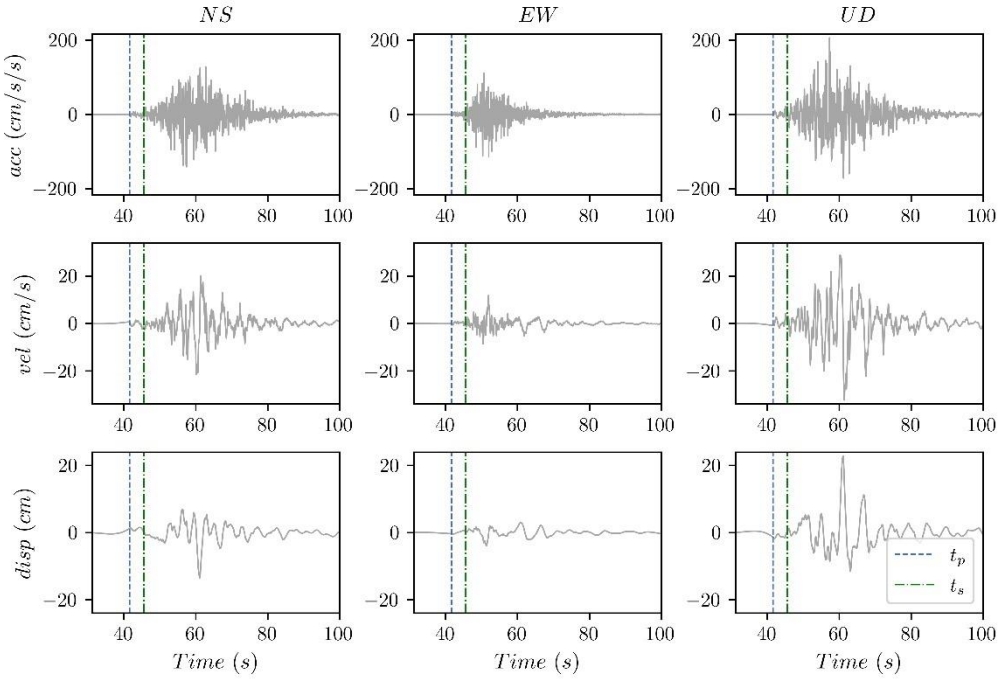

Appendix 6. Base model time histories for station G. The time histories for North-South, East-West and Upward-Downward components are shown in the left, centre, and right column, respectively.

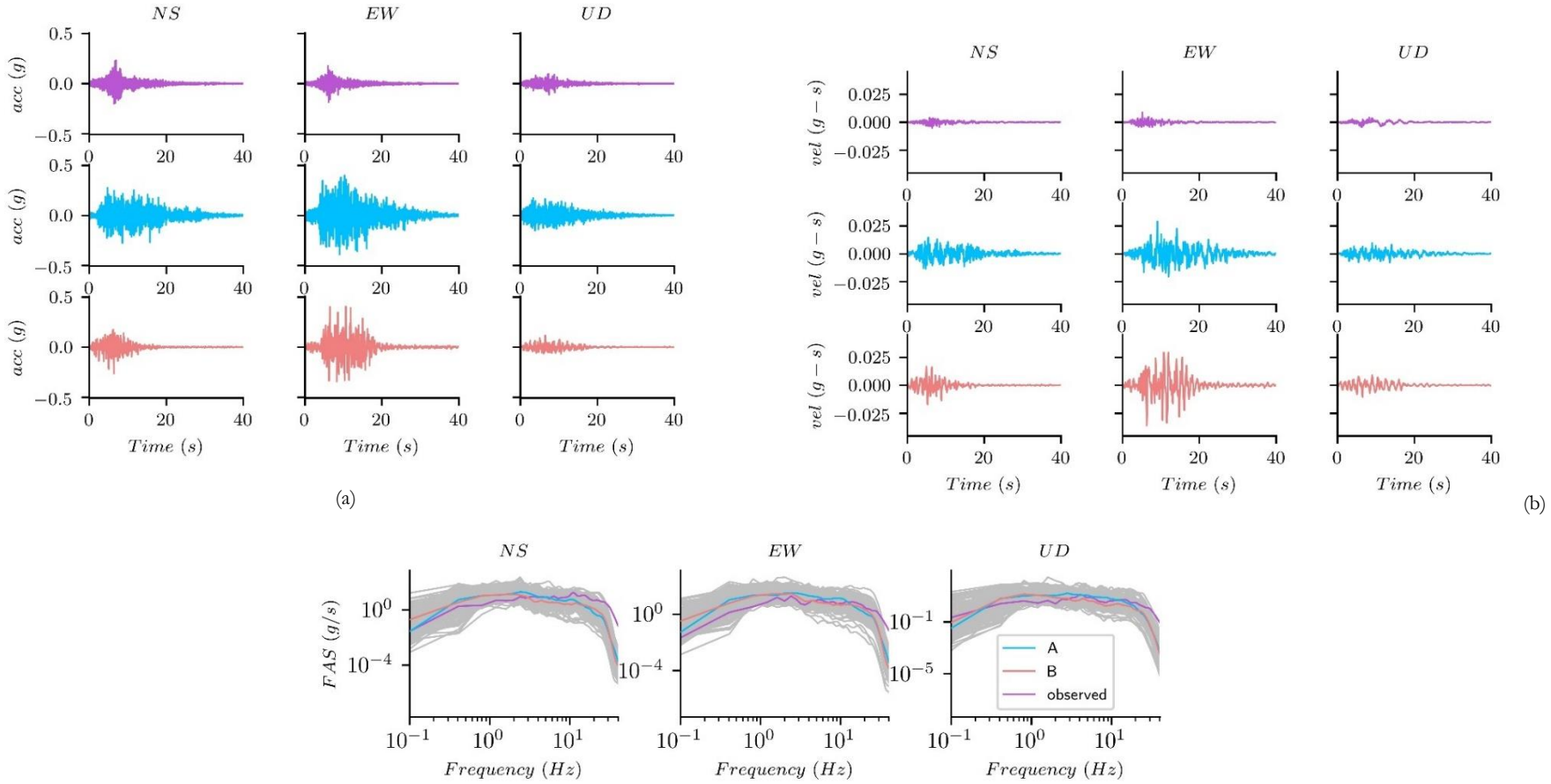

Appendix 7. Comparison between observed and simulated ground motions for station NIGH15. (a) –Acceleration and (b) – velocity time histories. To facilitate the comparison of the time histories, these were aligned at the instant where 1% of the maximum arias intensity (AI) is reached. The shown simulated scenarios correspond to the median AI of the GM component. (c) – Comparison of smoothed FAS, the grey lines correspond to individual simulations and the highlighted scenarios correspond to the median of the distributions.

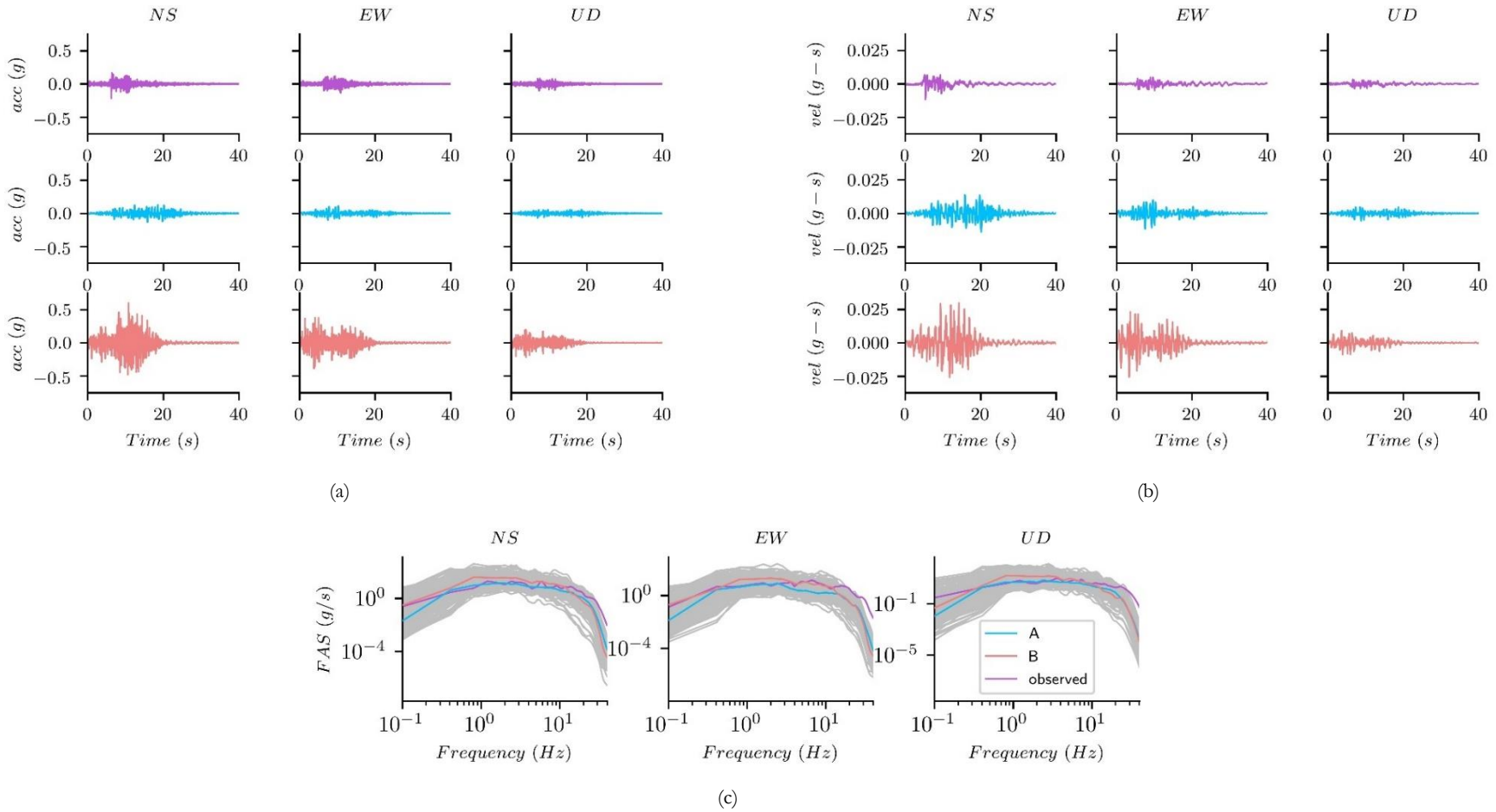

Appendix 8. Comparison between observed and simulated ground motions for station NIGH10. (a) –Acceleration and (b) – velocity time histories. To facilitate the comparison of the time histories, these were aligned at the instant where 1% of the maximum arias intensity (AI) is reached. The shown simulated scenarios correspond to the median AI of the GM component. (c) – Comparison of smoothed FAS, the grey lines correspond to individual simulations and the highlighted scenarios correspond to the median of the distributions.

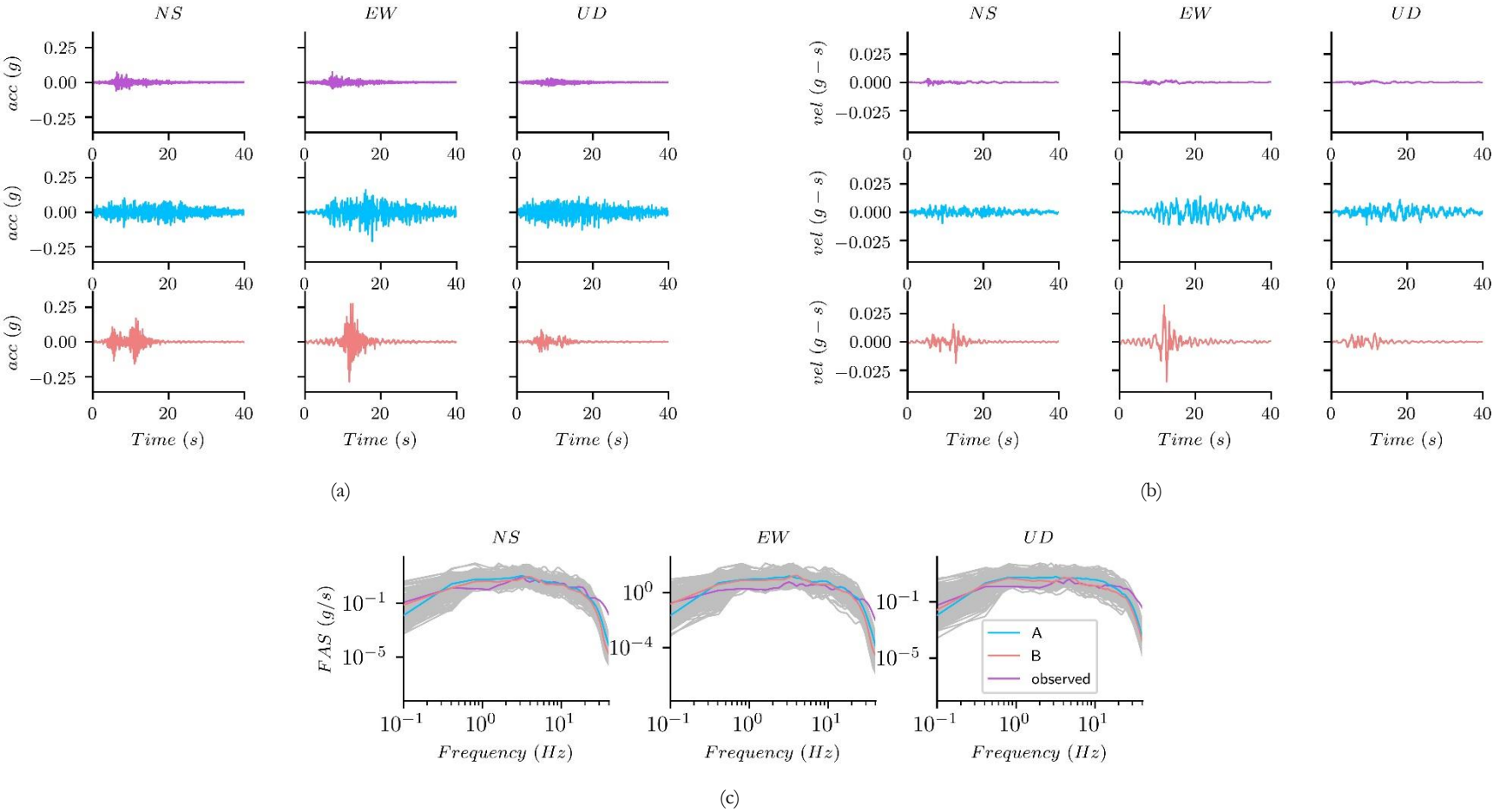

Appendix 9. Comparison between observed and simulated ground motions for station NIGH19. (a) –Acceleration and (b) – velocity time histories. To facilitate the comparison of the time histories, these were aligned at the instant where 1% of the maximum arias intensity (AI) is reached. The shown simulated scenarios correspond to the median AI of the GM component. (c) – Comparison of smoothed FAS, the grey lines correspond to individual simulations and the highlighted scenarios correspond to the median of the distributions.

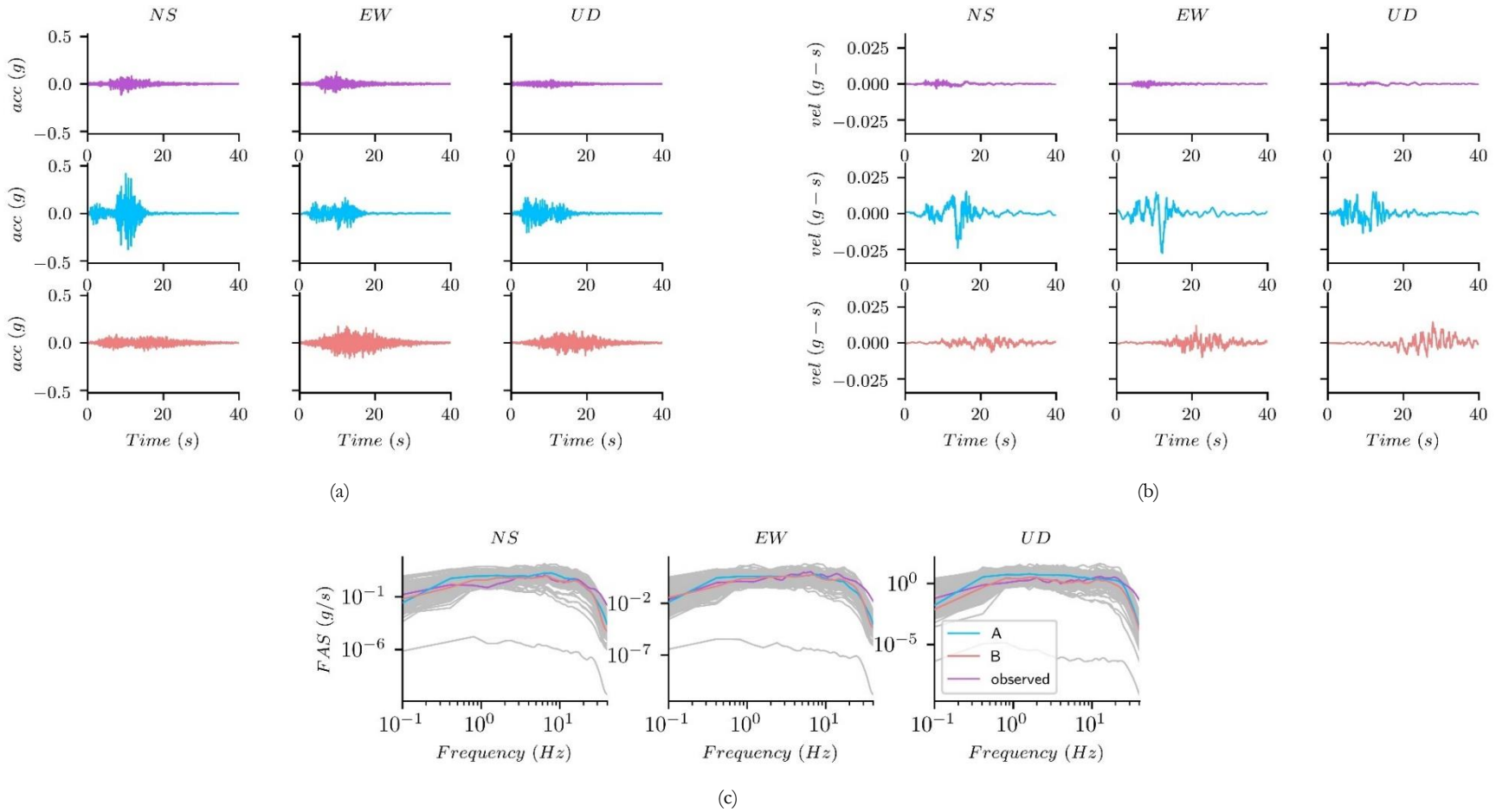

Appendix 10. Comparison between observed and simulated ground motions for station NIGH07. (a) –Acceleration and (b) – velocity time histories. To facilitate the comparison of the time histories, these were aligned at the instant where 1% of the maximum arias intensity (AI) is reached. The shown simulated scenarios correspond to the median AI of the GM component. (c) – Comparison of smoothed FAS, the grey lines correspond to individual simulations and the highlighted scenarios correspond to the median of the distributions.

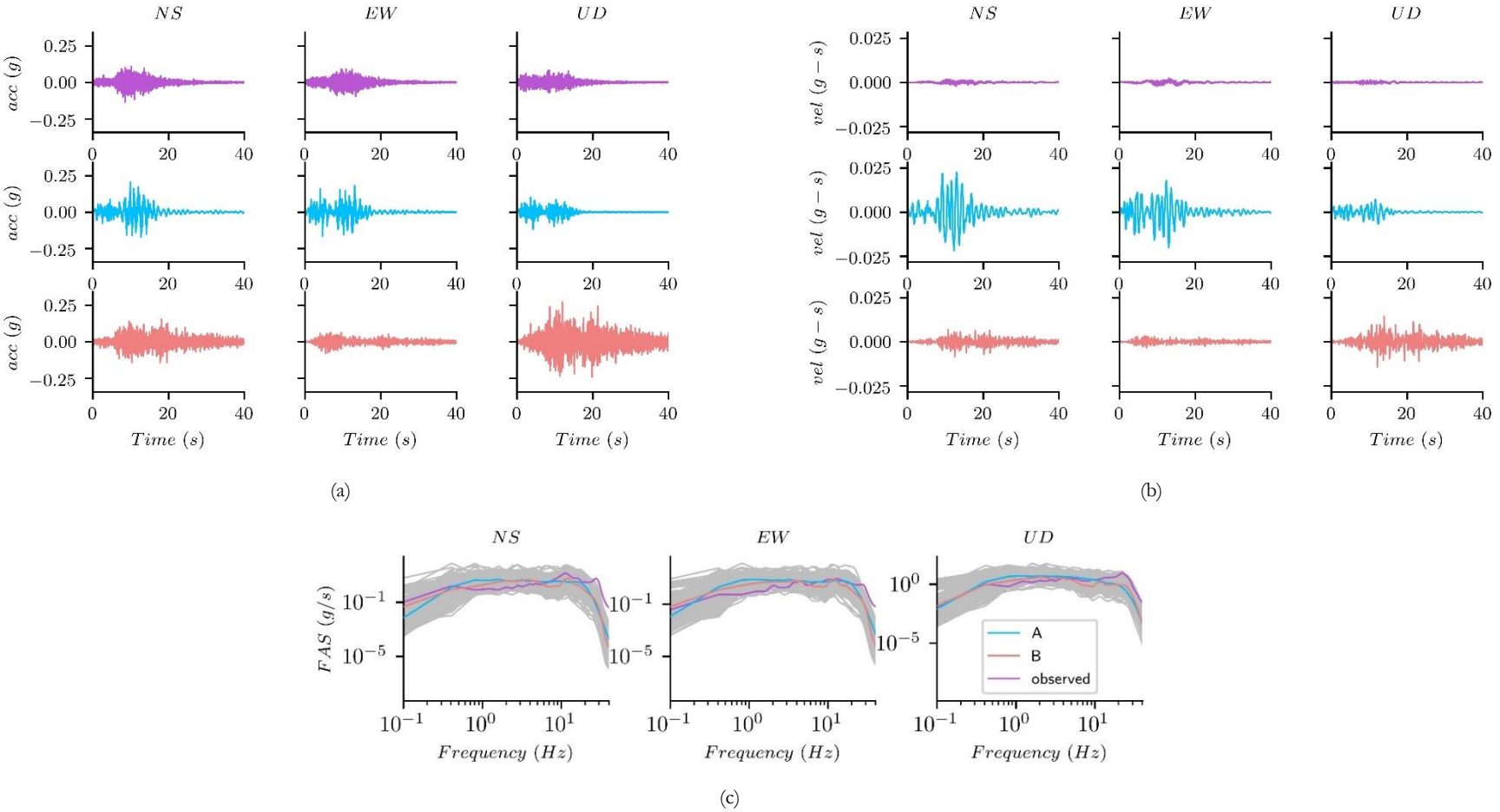

Appendix 11. Comparison between observed and simulated ground motions for station FKSH07. (a) –Acceleration and (b) – velocity time histories. To facilitate the comparison of the time histories, these were aligned at the instant where 1% of the maximum arias intensity (AI) is reached. The shown simulated scenarios correspond to the median AI of the GM component. (c) – Comparison of smoothed FAS, the grey lines correspond to individual simulations and the highlighted scenarios correspond to the median of the distributions.

PGA	$Sa(1.00s)$	$Sa(2.00s)$

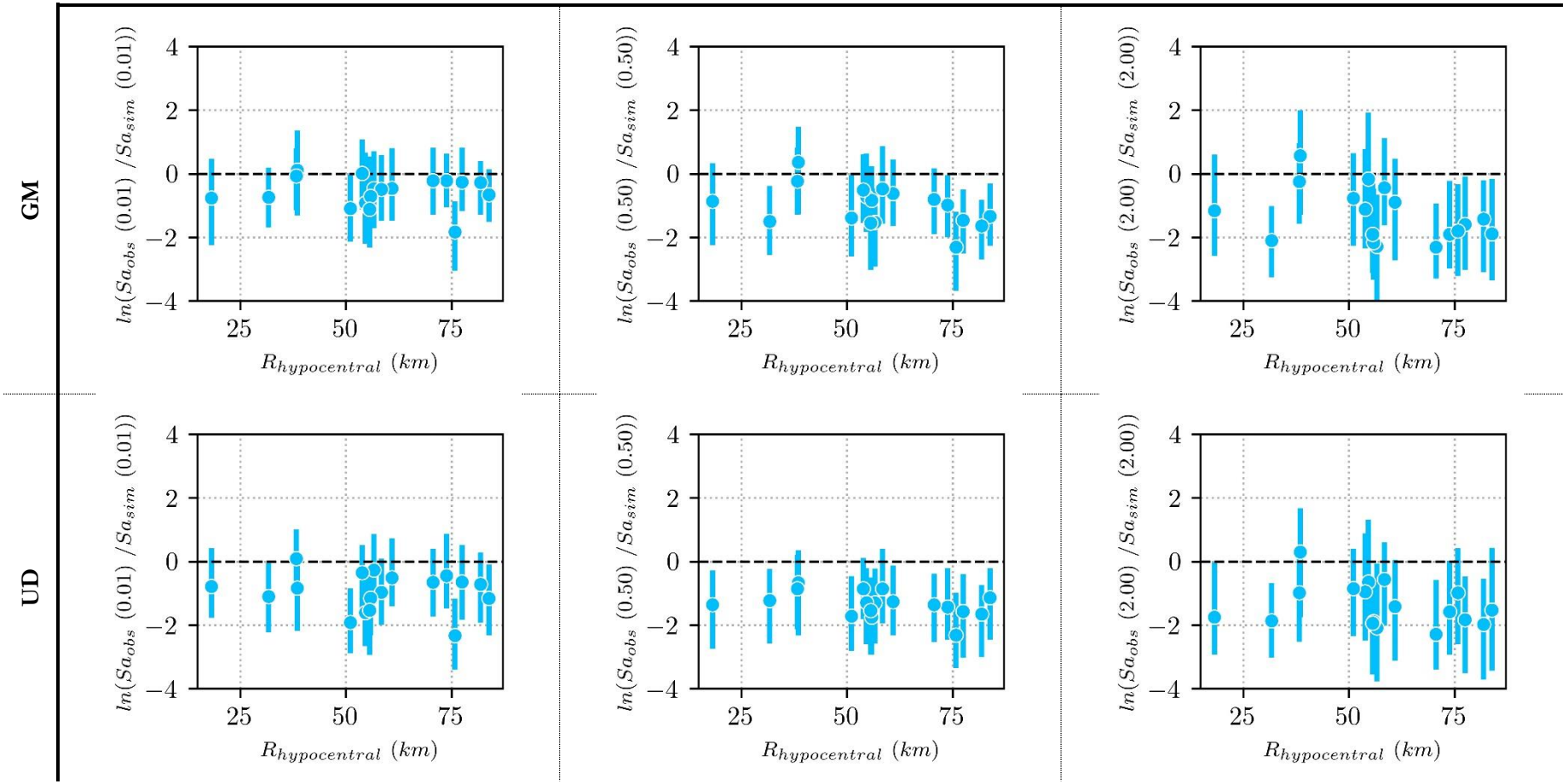

Appendix 12. Bias in the spectral acceleration of set A with respect to the observed reference. The results are presented for different periods of vibration and as a function of hypocentral distance

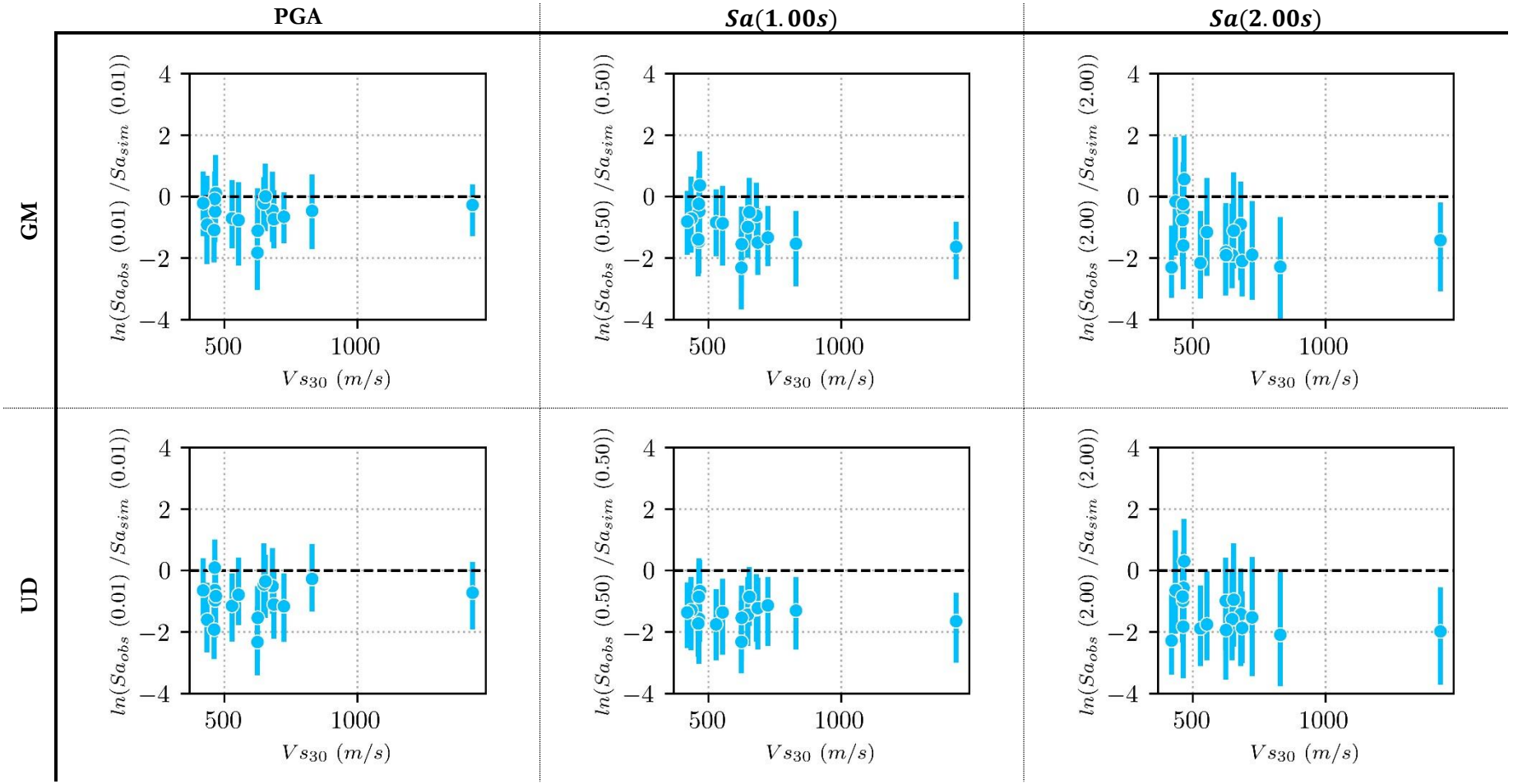

Appendix 13. Bias in the spectral acceleration of set A with respect to the observed reference. The results are presented for different periods of vibration and as a function of Vs_{30}.

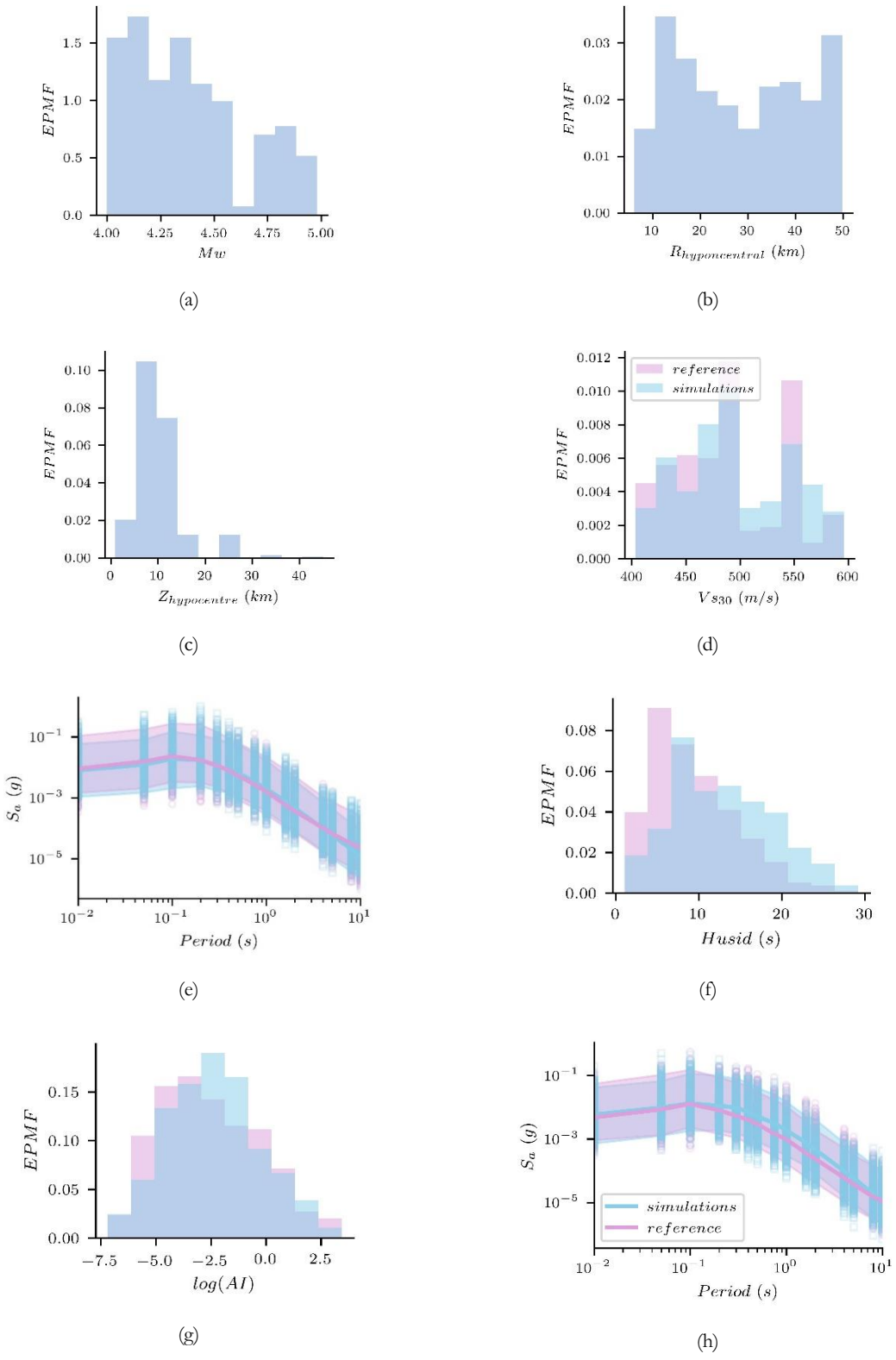

Appendix 14. Comparison of reference and simulated distributions of the causative parameters and IMs of interest considered during the calibration process of scenarios for the group with $4 < M_w \leq 5$, $R_{hypocentral} \leq 50\ km$ and $400\ m/s \leq Vs_{30} < 600\ m/s$. (a) - M_w, (b) - $R_{hypocentral}$, (c) - $Z_{hypocentre}$, (d) - Vs_{30}, (e) – Geometric mean of the horizontal response spectra, (f) – Geometrical mean of the horizontal Husid durations, (g) – Geometrical mean of the horizontal AI, and (h) – Response spectrum of the vertical component.

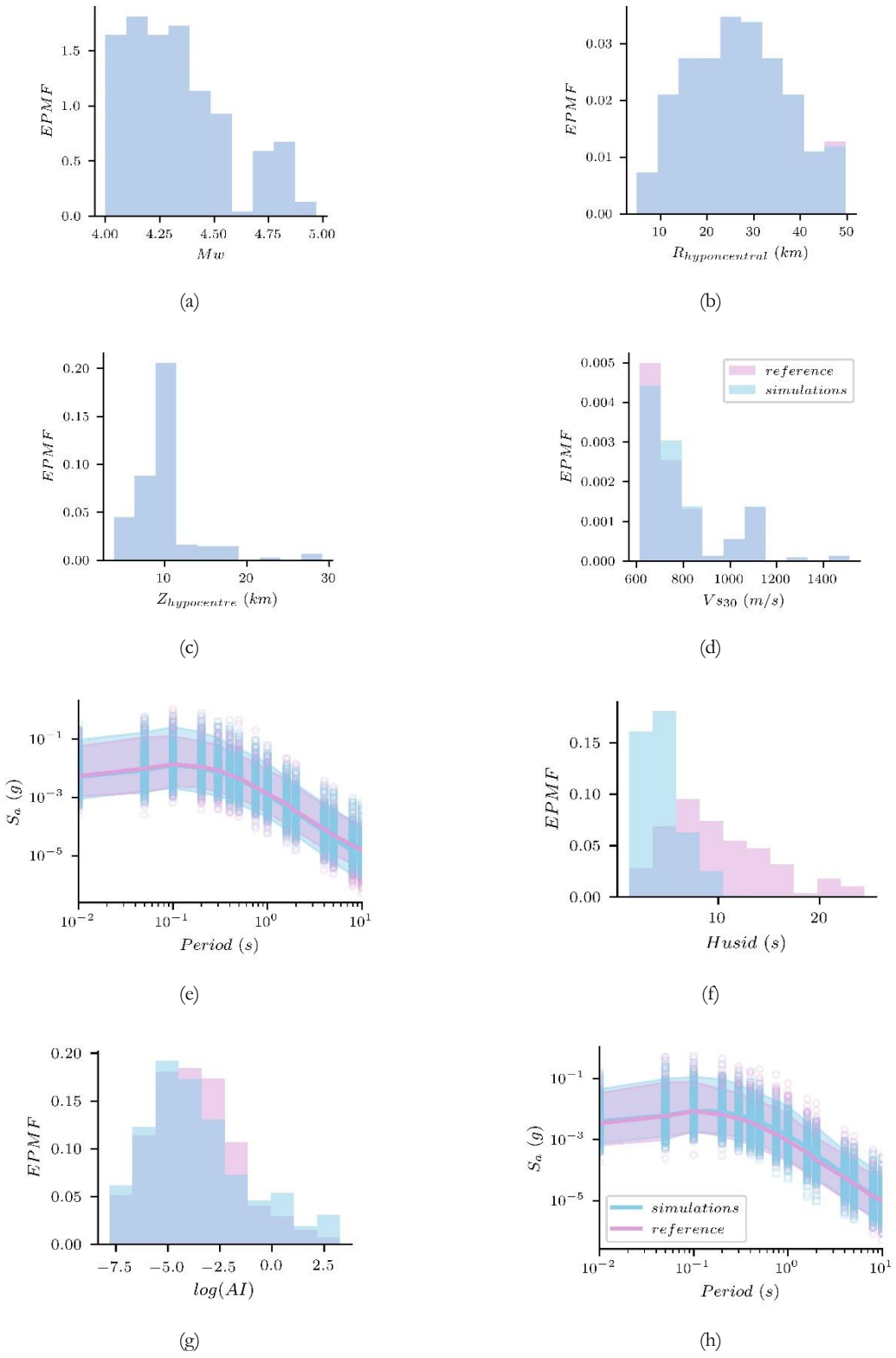

Appendix 15. Comparison of reference and simulated distributions of the causative parameters and IMs of interest considered during the calibration process of scenarios for the group with $4 < M_w \leq 5$, $R_{hypocentral} \leq 50\ km$ and $Vs_{30} \geq 600\ m/s$. (a) - M_w, (b) - $R_{hypocentral}$, (c) - $Z_{hypocentre}$, (d) - Vs_{30}, (e) – Geometric mean of the horizontal response spectra, (f) – Geometrical mean of the horizontal Husid durations, (g) – Geometrical mean of the horizontal AI, and (h) – Response spectrum of the vertical component.

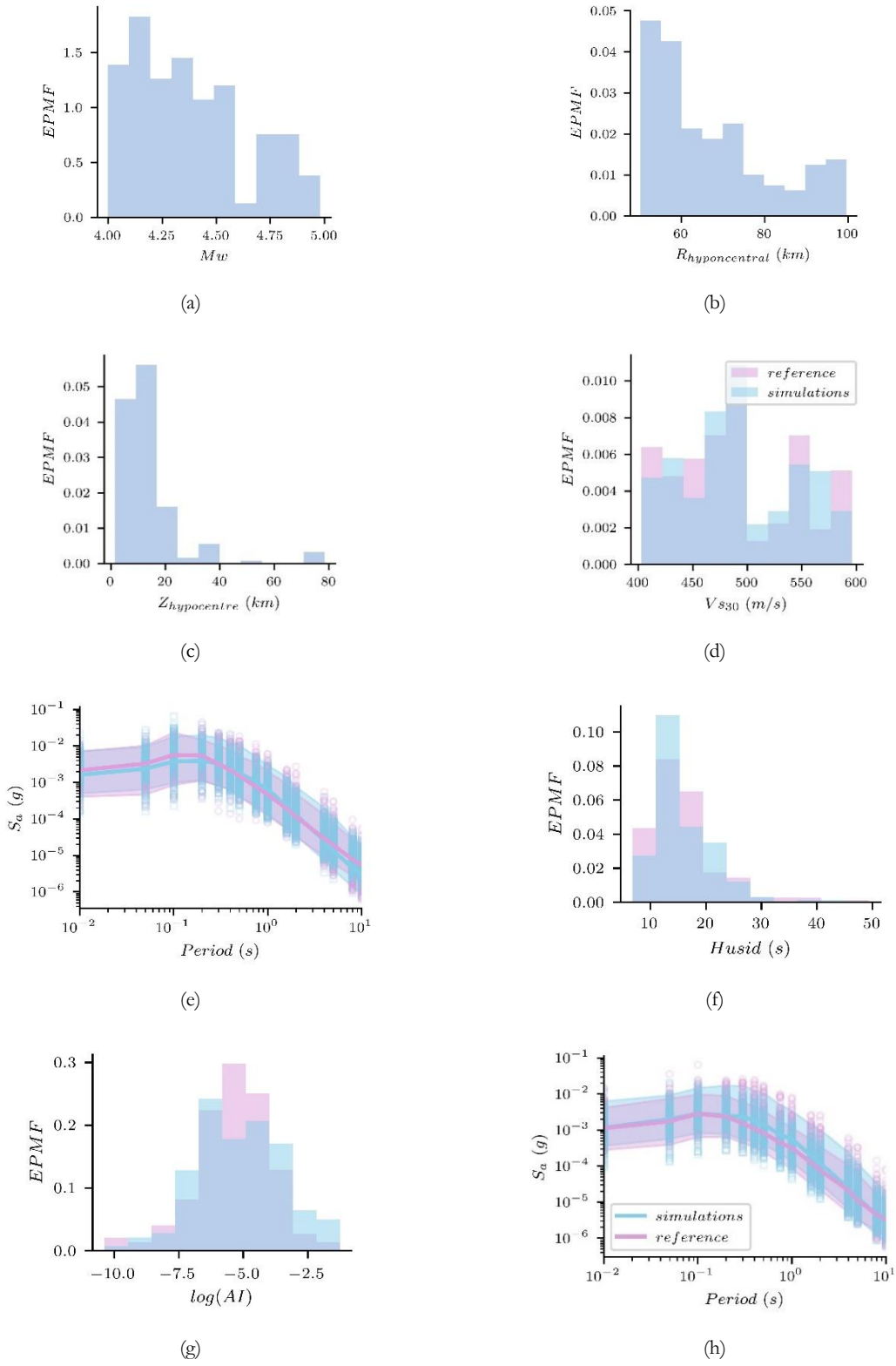

Appendix 16. Comparison of reference and simulated distributions of the causative parameters and IMs of interest considered during the calibration process of scenarios for the group with $4 < M_w \leq 5, 50 < R_{hypocentral} \leq 100\ km$ and $400\ m/s \leq Vs_{30} < 600\ m/s$. (a) - M_w, (b) - $R_{hypocentral}$, (c) - $Z_{hypocentre}$, (d) - Vs_{30}, (e) – Geometric mean of the horizontal response spectra, (f) – Geometrical mean of the horizontal Husid durations, (g) – Geometrical mean of the horizontal AI, and (h) – Response spectrum of the vertical component.

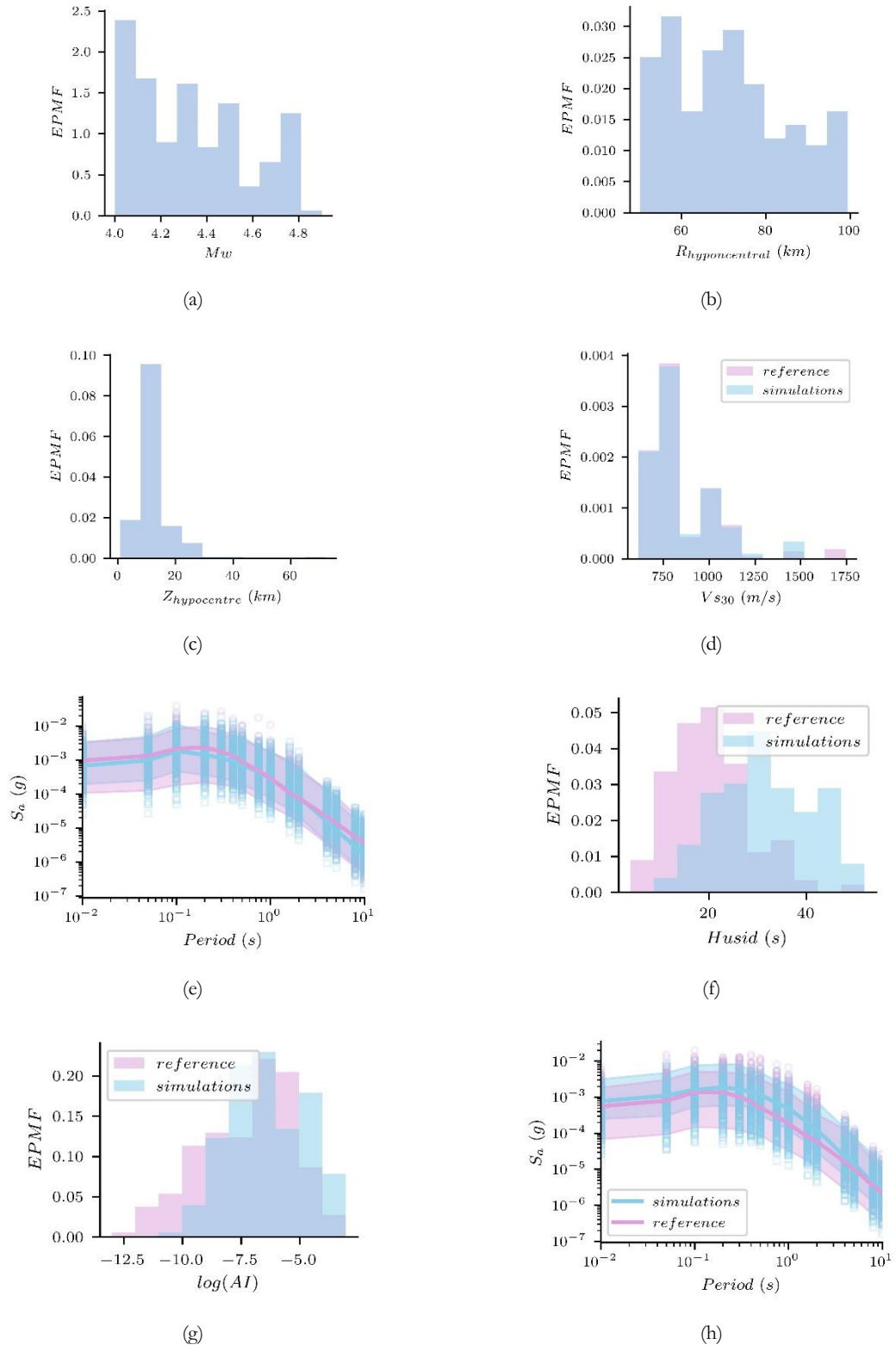

Appendix 17. Comparison of reference and simulated distributions of the causative parameters and IMs of interest considered during the calibration process of scenarios for the group with $4 < M_w \leq 5, 50 < R_{hypocentral} \leq 100\ km$ and $Vs_{30} \geq 600\ m/s$. (a) - M_w, (b) - $R_{hypocentral}$, (c) - $Z_{hypocentre}$, (d) - Vs_{30}, (e) – Geometric mean of the horizontal response spectra, (f) – Geometrical mean of the horizontal Husid durations, (g) – Geometrical mean of the horizontal AI, and (h) – Response spectrum of the vertical component.

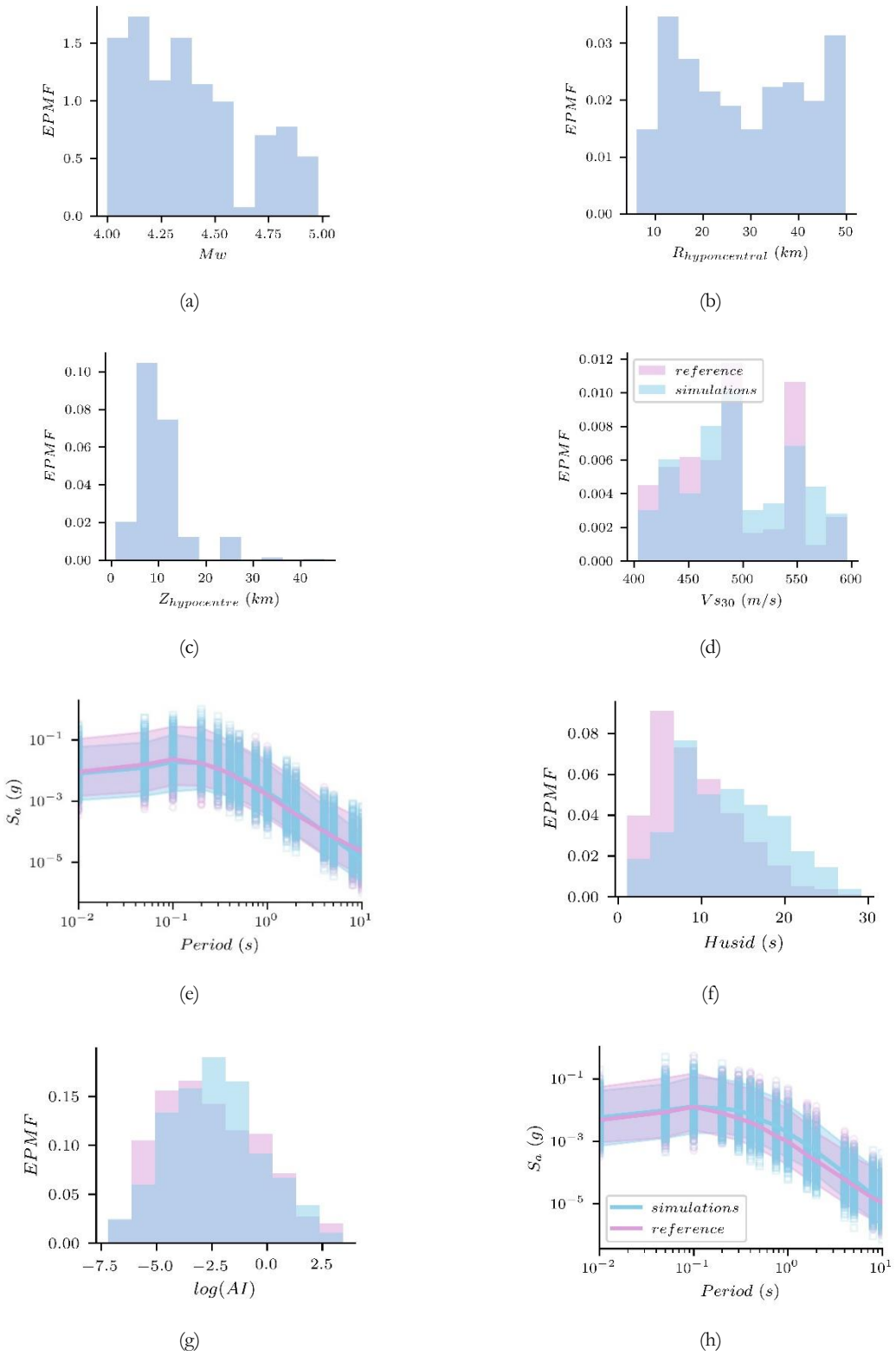

Appendix 18. Comparison of reference and simulated distributions of the causative parameters and IMs of interest considered during the calibration process of scenarios for the group with $4 < M_w \leq 5$, $R_{hypocentral} \leq 50\ km$ and $400\ m/s \leq Vs_{30} < 600\ m/s$. (a) - M_w, (b) - $R_{hypocentral}$, (c) - $Z_{hypocentre}$, (d) - Vs_{30}, (e) – Geometric mean of the horizontal response spectra, (f) – Geometrical mean of the horizontal Husid durations, (g) – Geometrical mean of the horizontal AI, and (h) – Response spectrum of the vertical component.

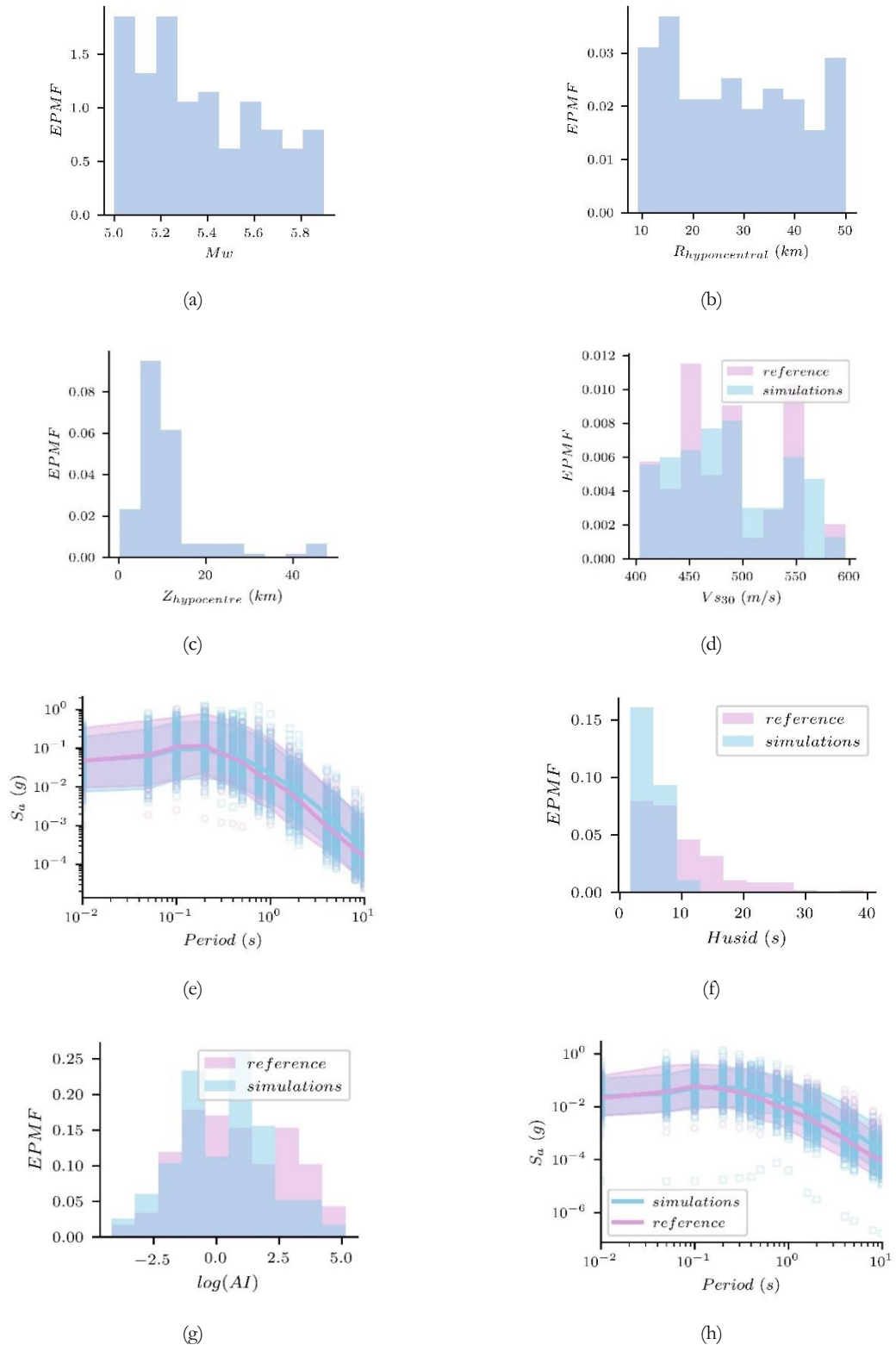

Appendix 19. Comparison of reference and simulated distributions of the causative parameters and IMs of interest considered during the calibration process of scenarios for the group with $5 < M_w \leq 6$, $R_{hypocentral} \leq 50\ km$ and $400 \leq Vs_{30} < 600\ m/s$. (a) - M_w, (b) - $R_{hypocentral}$, (c) - $Z_{hypocentre}$, (d) - Vs_{30}, (e) – Geometric mean of the horizontal response spectra, (f) – Geometrical mean of the horizontal Husid durations, (g) – Geometrical mean of the horizontal AI, and (h) – Response spectrum of the vertical component.

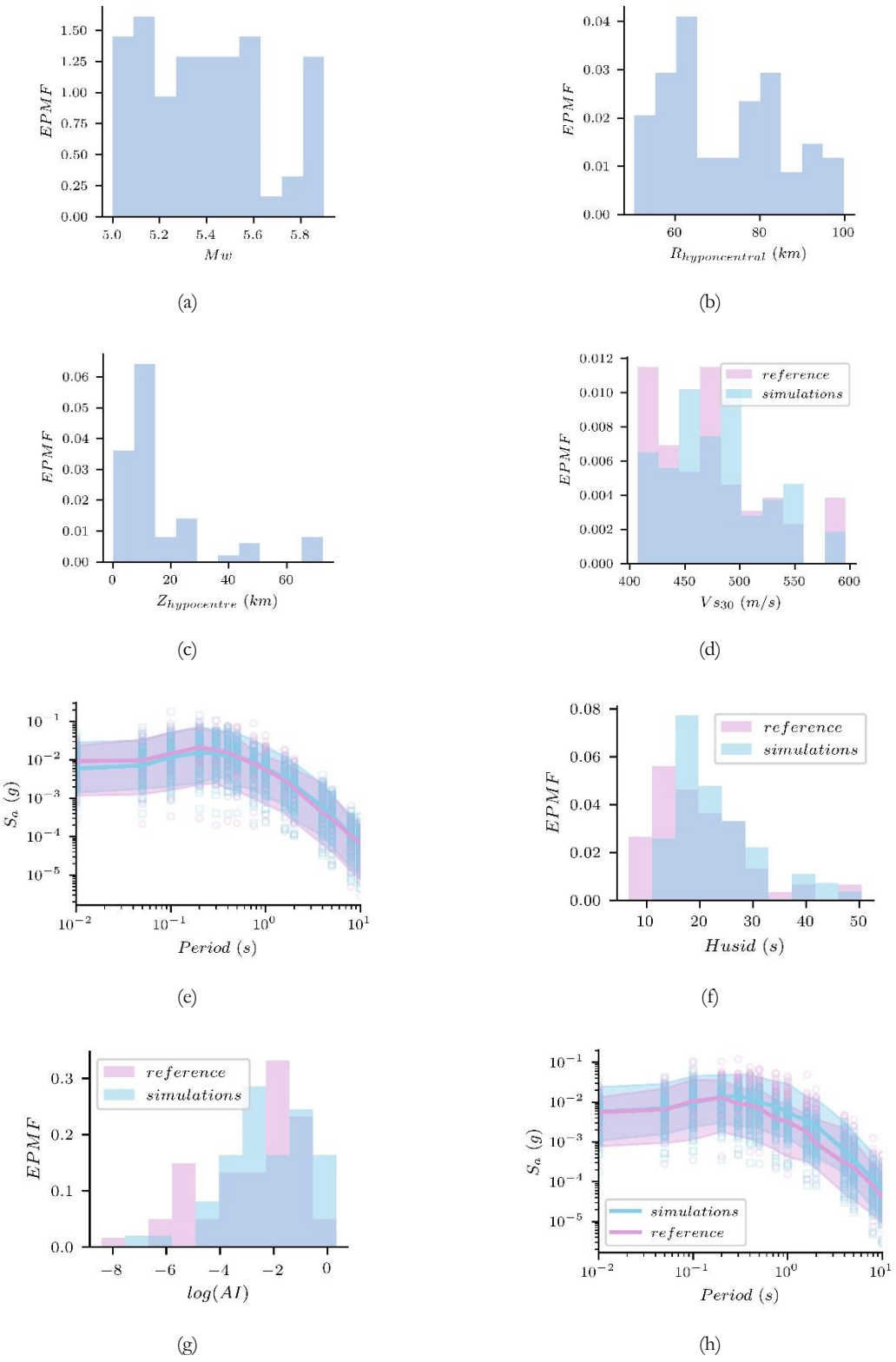

Appendix 20. Comparison of reference and simulated distributions of the causative parameters and IMs of interest considered during the calibration process of scenarios for the group with $5 < M_w \leq 6, 50 < R_{hypocentral} \leq 100\ km$ and $400\ m/s \leq Vs_{30} < 600\ m/s$. (a) - M_w, (b) - $R_{hypocentral}$, (c) - $Z_{hypocentre}$, (d) - Vs_{30}, (e) – Geometric mean of the horizontal response spectra, (f) – Geometrical mean of the horizontal Husid durations, (g) – Geometrical mean of the horizontal AI, and (h) – Response spectrum of the vertical component.

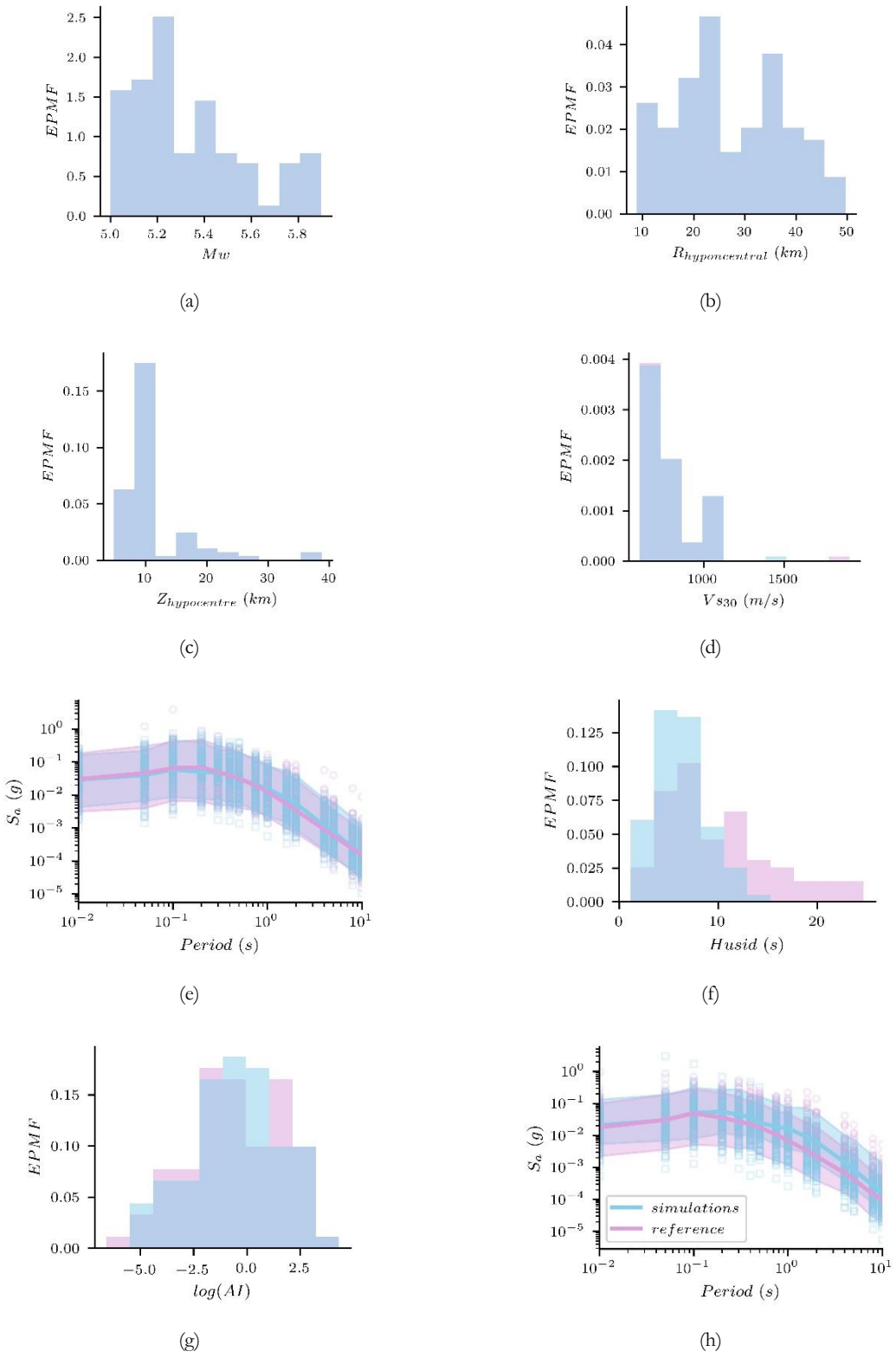

Appendix 21. Comparison of reference and simulated distributions of the causative parameters and IMs of interest considered during the calibration process of scenarios for the group with $5 < M_w \leq 6$, $R_{hypocentral} \leq 50\ km$ and $Vs_{30} \geq 600\ m/s$. (a) - M_w, (b) - $R_{hypocentral}$, (c) - $Z_{hypocentre}$, (d) - Vs_{30}, (e) – Geometric mean of the horizontal response spectra, (f) – Geometrical mean of the horizontal Husid durations, (g) – Geometrical mean of the horizontal AI, and (h) – Response spectrum of the vertical component.

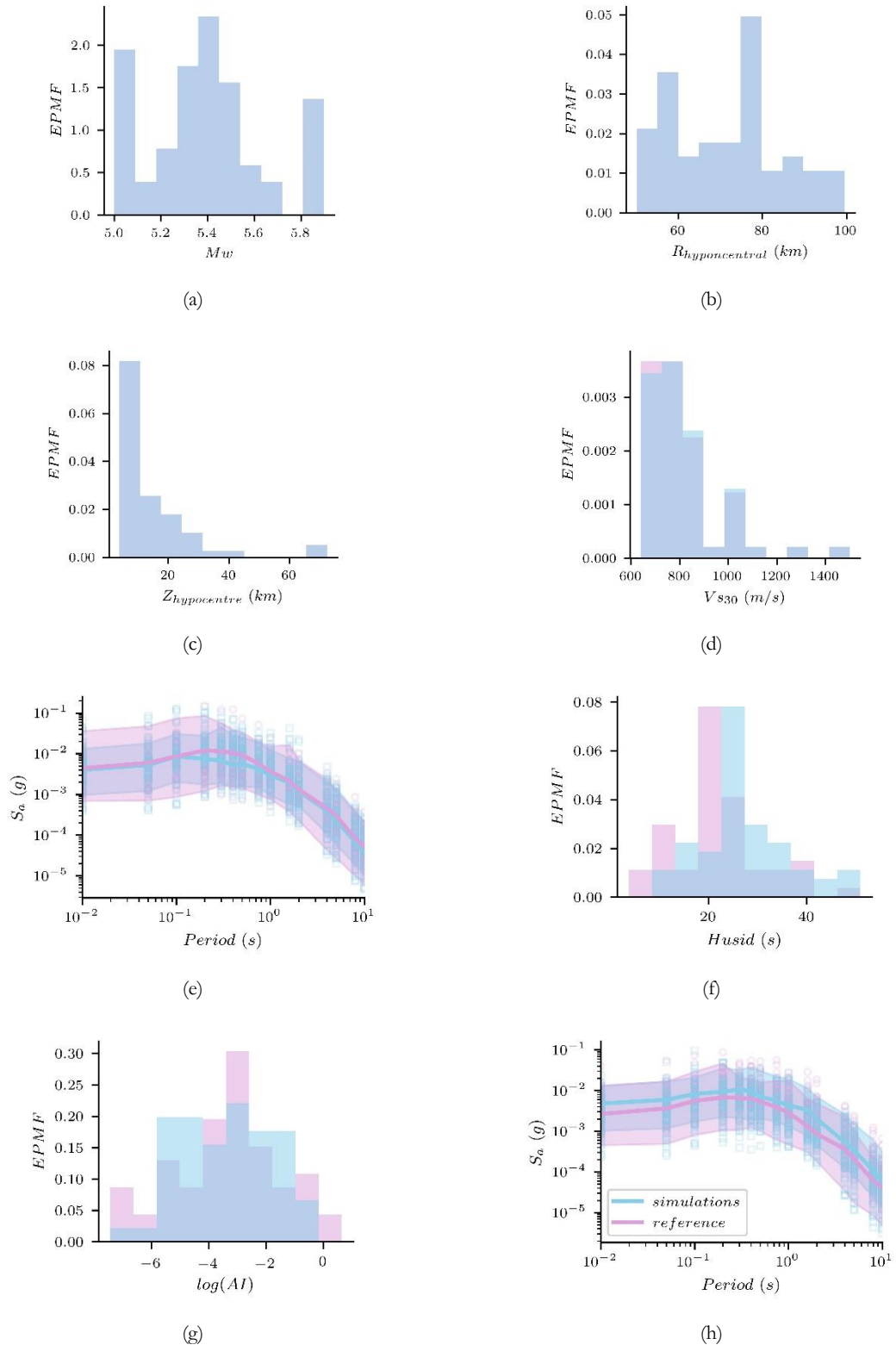

Appendix 22. Comparison of reference and simulated distributions of the causative parameters and IMs of interest considered during the calibration process of scenarios for the group with $5 < M_w \leq 6, 50 < R_{hypocentral} \leq 100\ km$ and $Vs_{30} \geq 600\ m/s$. (a) - M_w, (b) - $R_{hypocentral}$, (c) - $Z_{hypocentre}$, (d) - Vs_{30}, (e) – Geometric mean of the horizontal response spectra, (f) – Geometrical mean of the horizontal Husid durations, (g) – Geometrical mean of the horizontal AI, and (h) – Response spectrum of the vertical component.

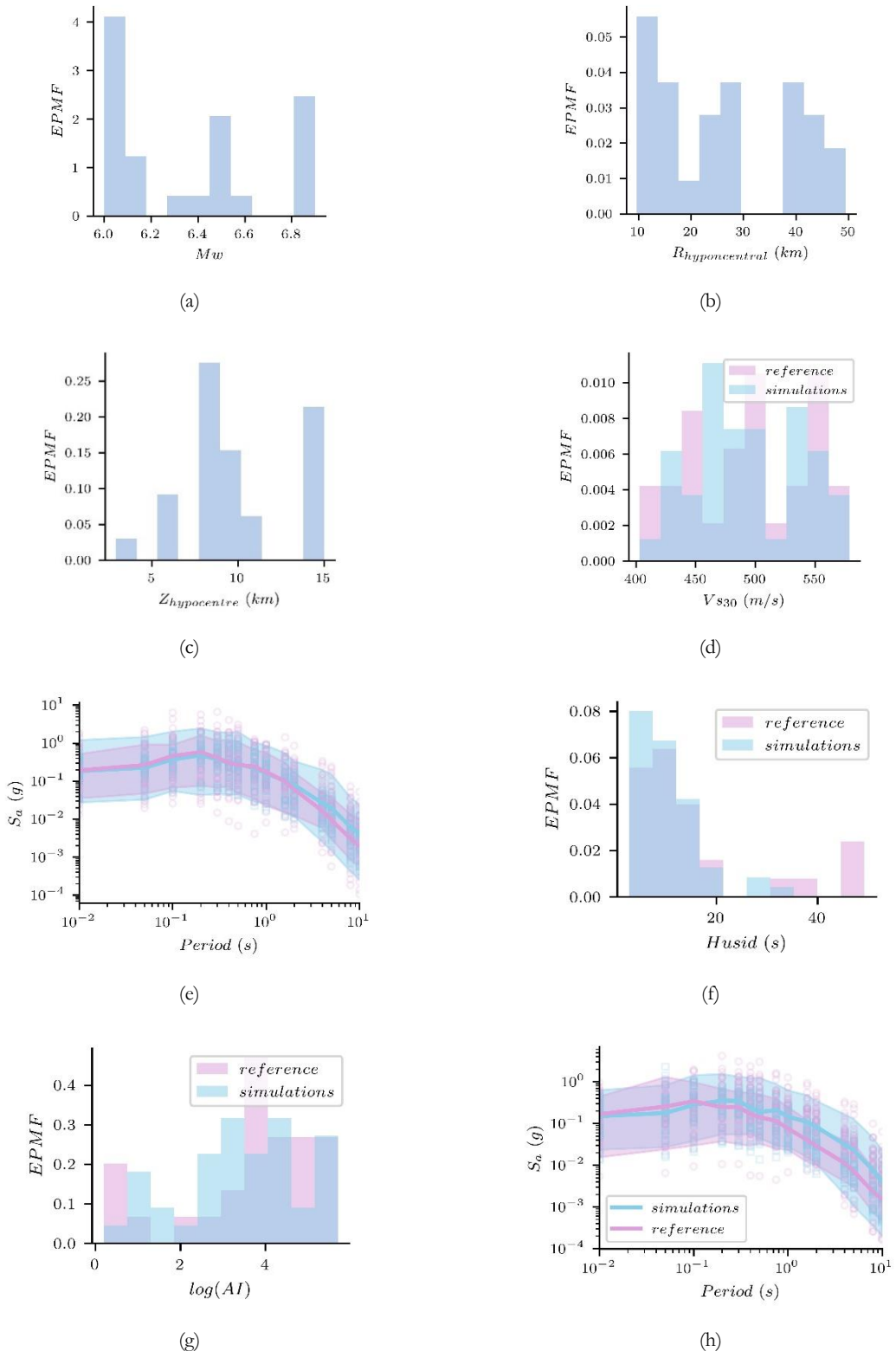

Appendix 23. Comparison of reference and simulated distributions of the causative parameters and IMs of interest considered during the calibration process of scenarios for the group with $M_w > 6$, $R_{hypocentral} \leq 50\ km$ and $400 \leq Vs_{30} < 600\ m/s$. (a) - M_w, (b) - $R_{hypocentral}$, (c) - $Z_{hypocentre}$, (d) - Vs_{30}, (e) – Geometric mean of the horizontal response spectra, (f) – Geometrical mean of the horizontal Husid durations, (g) – Geometrical mean of the horizontal AI, and (h) – Response spectrum of the vertical component.

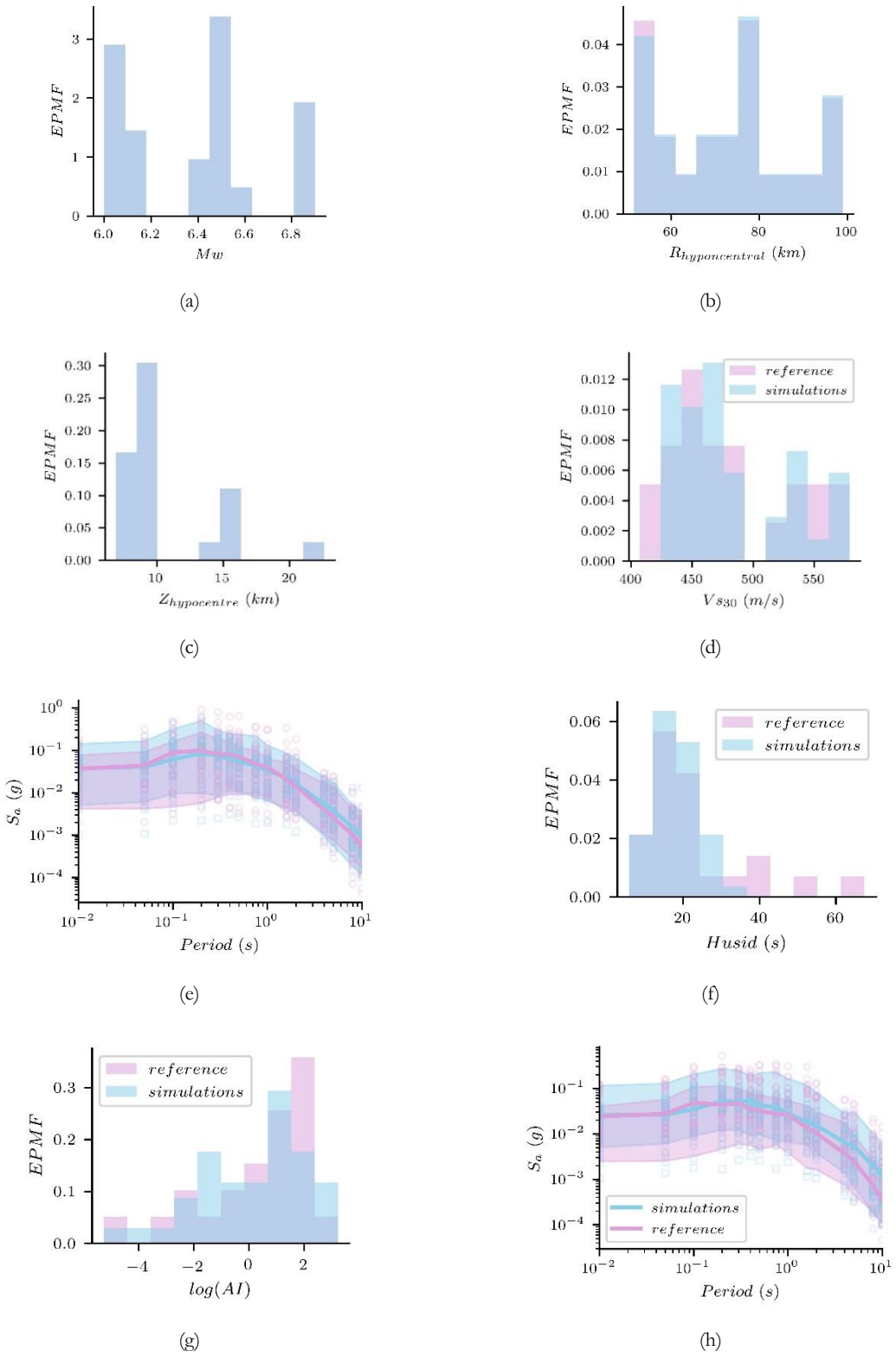

Appendix 24. Comparison of reference and simulated distributions of the causative parameters and IMs of interest considered during the calibration process of scenarios for the group with $M_w > 6, 50 < R_{hypocentral} \leq 100\ km$ and $400\ m/s \leq Vs_{30} < 600\ m/s$. (a) - M_w, (b) - $R_{hypocentral}$, (c) - $Z_{hypocentre}$, (d) - Vs_{30}, (e) – Geometric mean of the horizontal response spectra, (f) – Geometrical mean of the horizontal Husid durations, (g) – Geometrical mean of the horizontal AI, and (h) – Response spectrum of the vertical component.

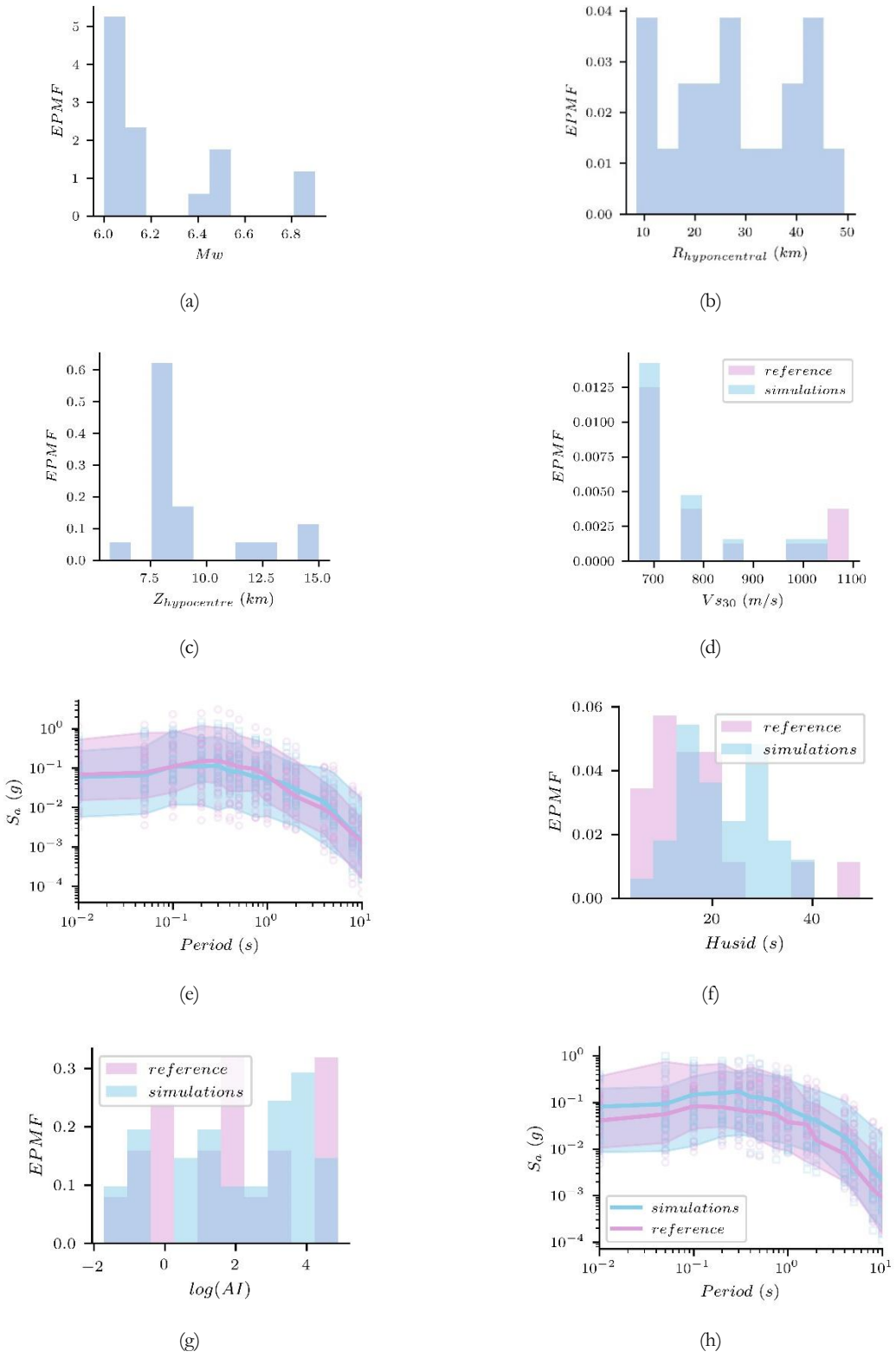

Appendix 25. Comparison of reference and simulated distributions of the causative parameters and IMs of interest considered during the calibration process of scenarios for the group with $M_w > 6$, $R_{hypocentral} \leq 50\ km$ and $Vs_{30} \geq 600\ m/s$. (a) - M_w, (b) - $R_{hypocentral}$, (c) - $Z_{hypocentre}$, (d) - Vs_{30}, (e) – Geometric mean of the horizontal response spectra, (f) – Geometrical mean of the horizontal Husid durations, (g) – Geometrical mean of the horizontal AI, and (h) – Response spectrum of the vertical component.

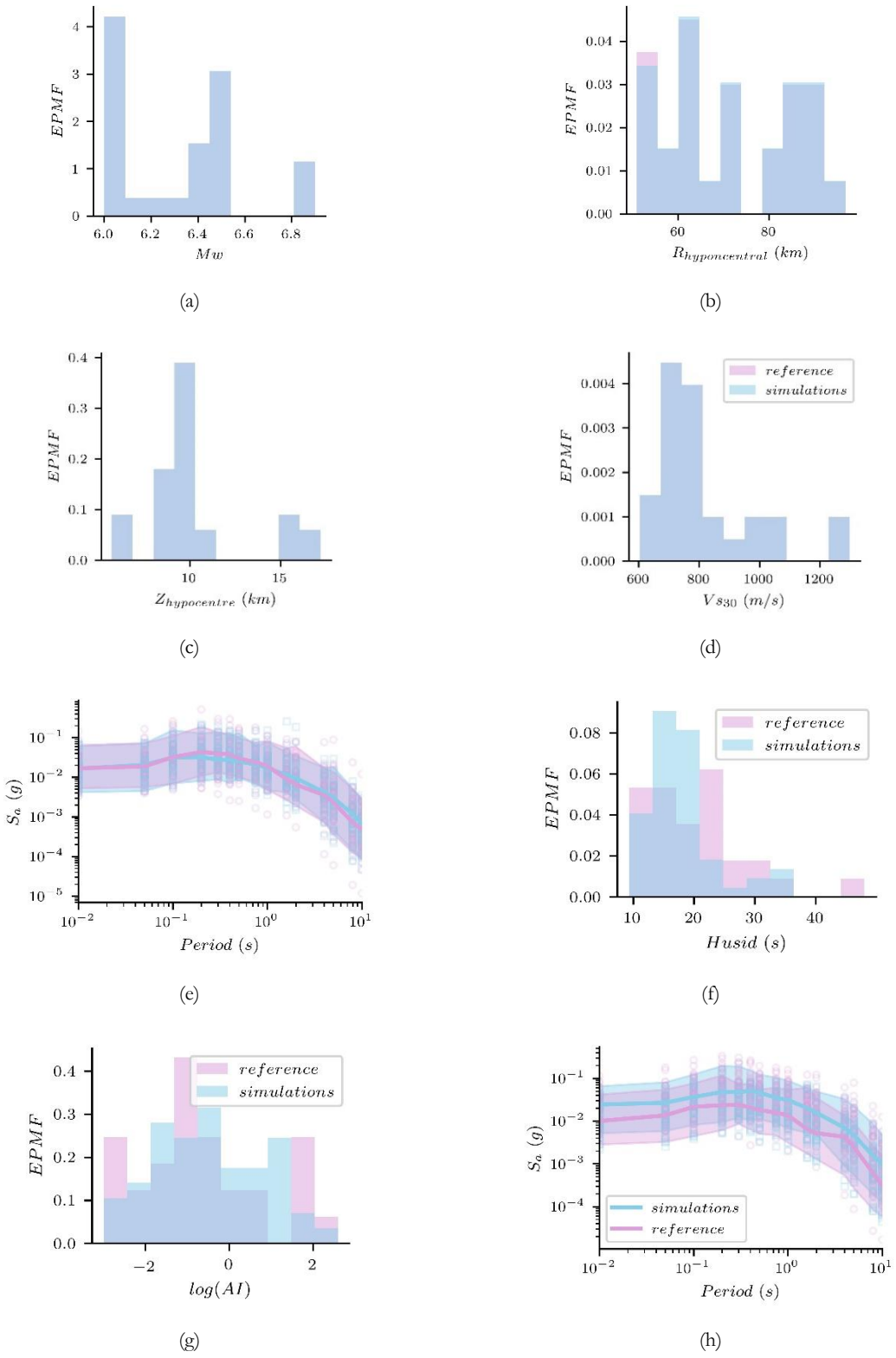

Appendix 26. Comparison of reference and simulated distributions of the causative parameters and IMs of interest considered during the calibration process of scenarios for the group with $M_w > 6, 50 < R_{hypocentral} \leq 100\ km$ and $Vs_{30} \geq 600\ m/s$. (a) - M_w, (b) - $R_{hypocentral}$, (c) - $Z_{hypocentre}$, (d) - Vs_{30}, (e) – Geometric mean of the horizontal response spectra, (f) – Geometrical mean of the horizontal Husid durations, (g) – Geometrical mean of the horizontal AI, and (h) – Response spectrum of the vertical component.

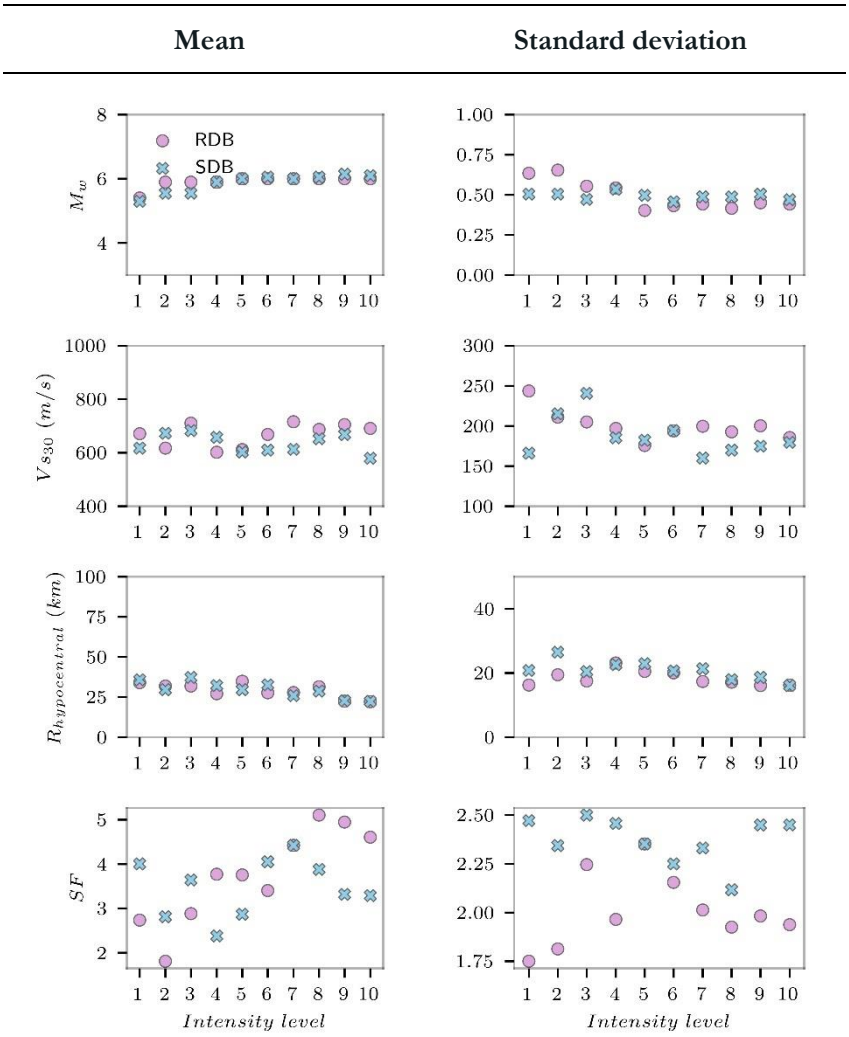

Appendix 27. Causative parameters of the CS-selected records for $Sa(T_1) = 0.2s$, namely moment magnitude (M_w), average shear propagation velocity of the upper 30m (Vs_{30}), hypocentral distance (R_{hyp}), and scaling factor (SF), from first to the last row, respectively.

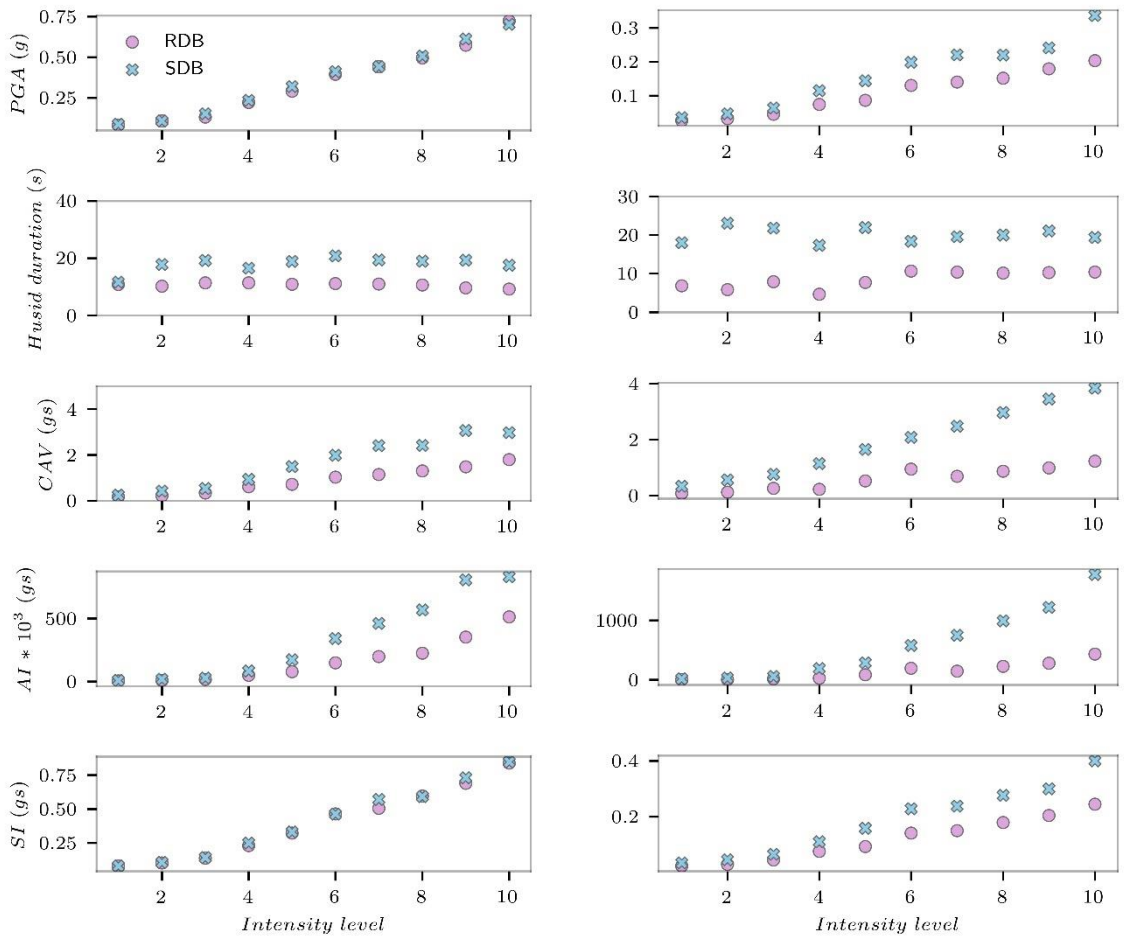

Appendix 28. IMs of the CS-selected records for $Sa(T_1) = 0.2s$, namely moment magnitude (M_w), average shear propagation velocity of the upper 30m (Vs_{30}), hypocentral distance (R_{hyp}), and scaling factor (SF), from first to the last row, respectively.

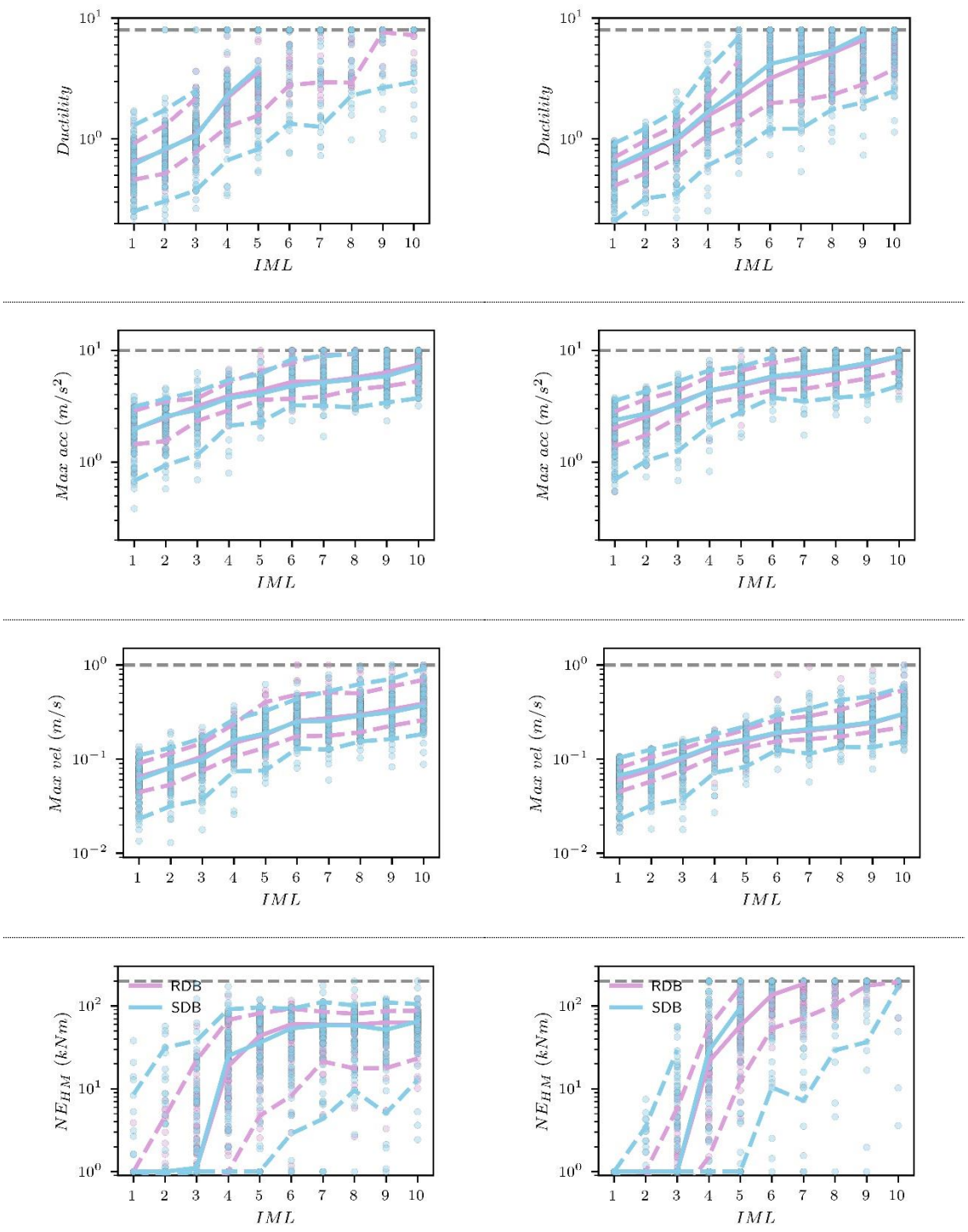

Appendix 29. EDPs obtained via NLTHA of the SDoF with $T_1 = 0.2s$ using 40 records at each IML, selected from the RDB and SDB. Ductility ratio, Peak Floor acceleration, Peak floor velocity, and dissipated energy, from first to the last row, respectively. In the figure, the median is represented by the solid line and 5th and 95th percentiles by the dashed lines.

Degradation (Pinching)	Elastic Hardening

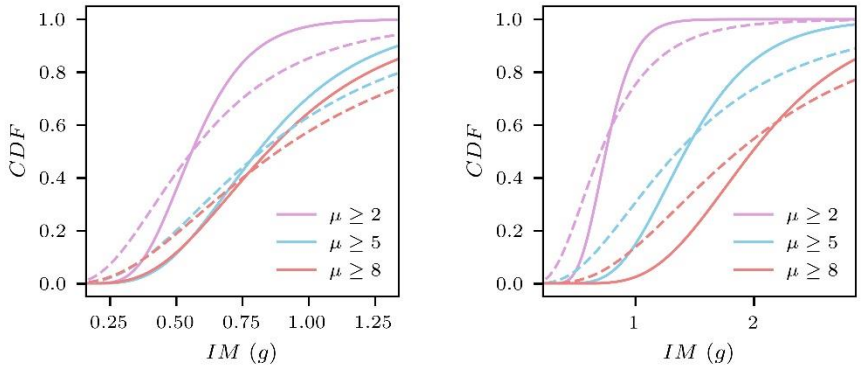

Appendix 30. Fragility curves obtained for ductility and via NLTHA of the SDoF with $T_1 = 0.2s$ using 40 records at each IML, selected from the RDB and SDB. The solid line represents the results obtained from the RDB whereas the dashed mine represents the results obtained from the SDB

Degradation (Pinching)	Elastic Hardening

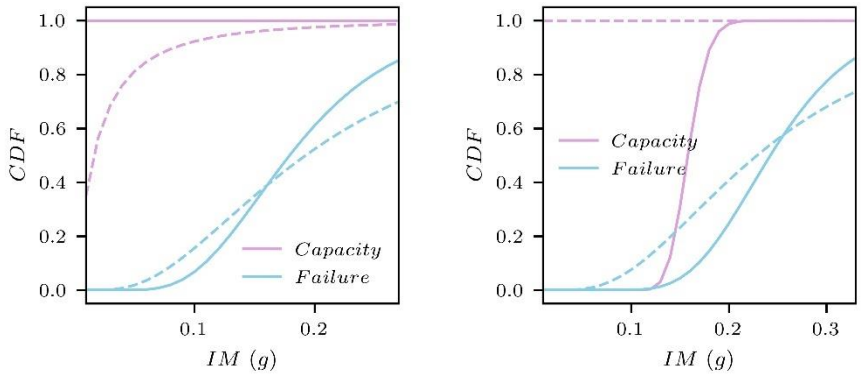

Appendix 31. Fragility curves obtained for the LVSG and via NLTHA of the SDoF with $T_1 = 0.2s$ using 40 records at each IML, selected from the RDB and SDB. The solid line represents the results obtained from the RDB whereas the dashed mine represents the results obtained from the SDB

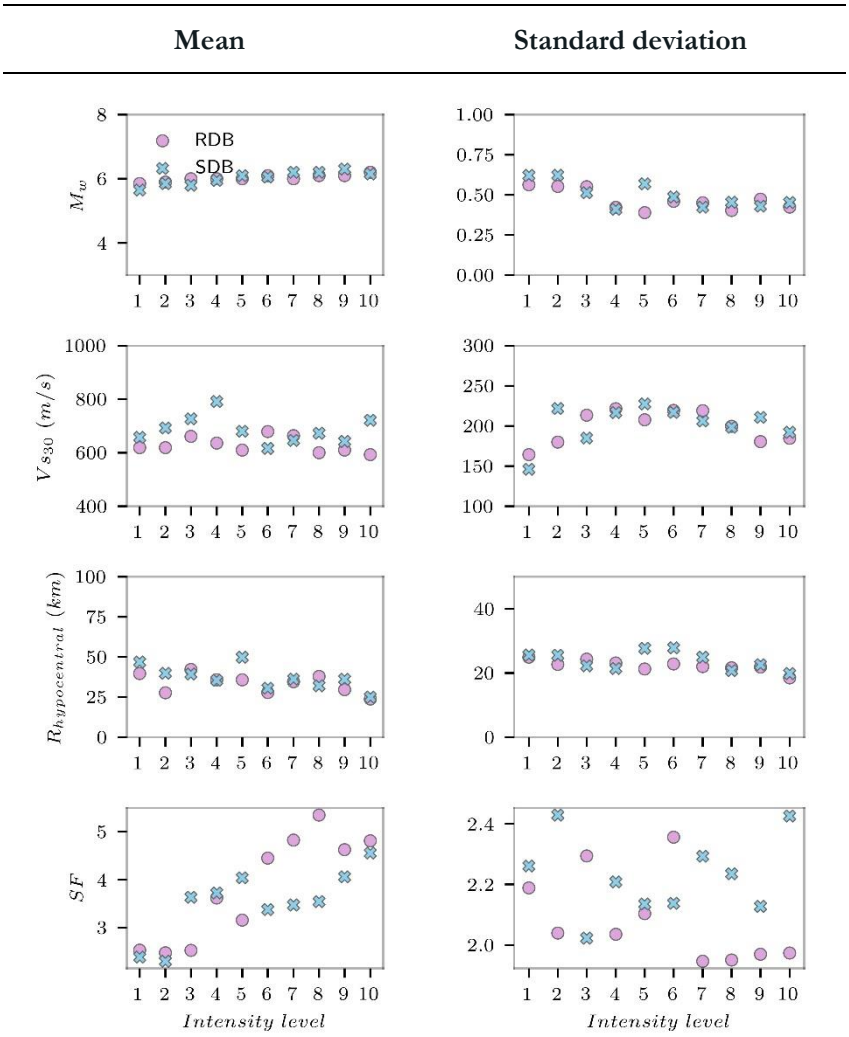

Appendix 32. Causative parameters of the CS-selected records for $Sa(T_1) = 0.5s$, namely moment magnitude (M_w), average shear propagation velocity of the upper 30m (Vs_{30}), hypocentral distance (R_{hyp}), and scaling factor (SF), from first to the last row, respectively.

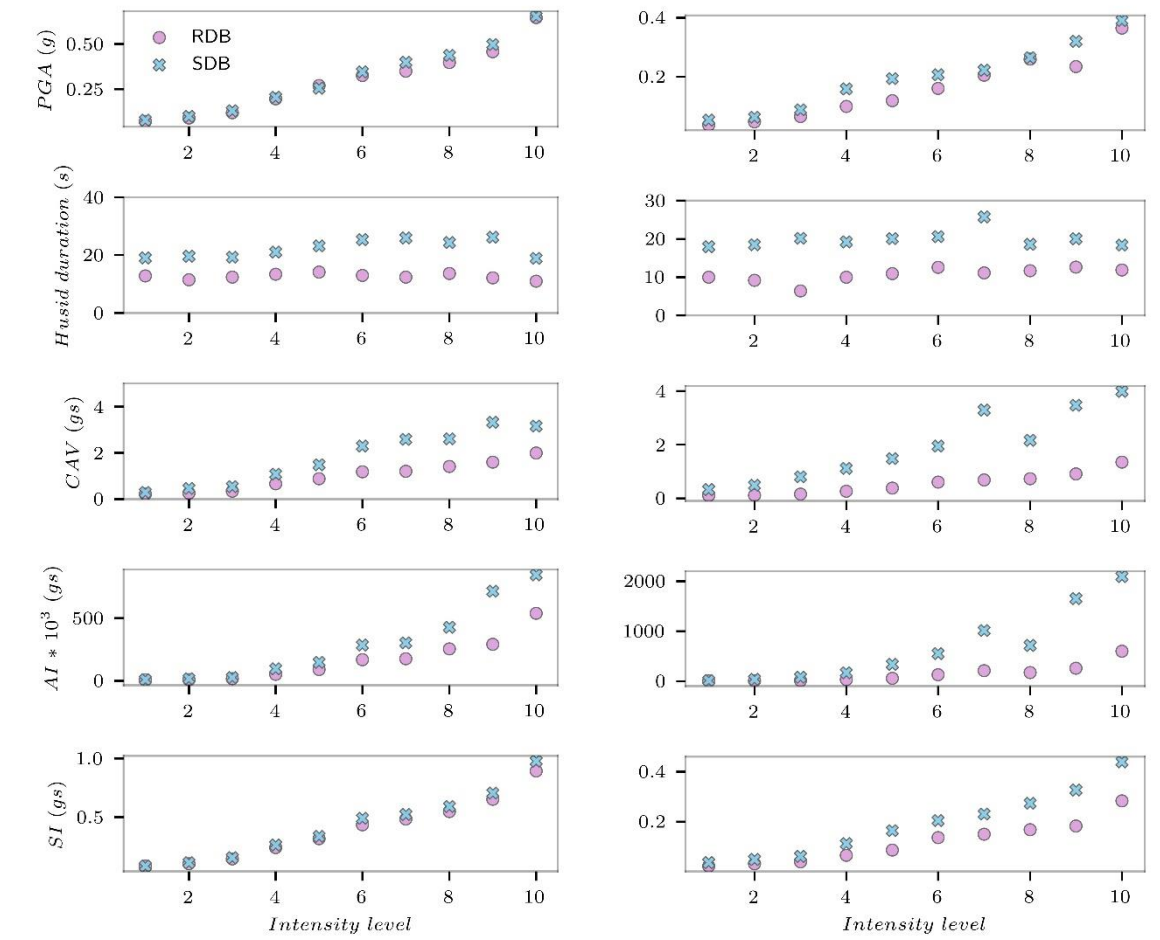

Appendix 33. IMs of the CS-selected records for $Sa(T_1) = 0.5s$, namely moment magnitude (M_w), average shear propagation velocity of the upper 30m (Vs_{30}), hypocentral distance (R_{hyp}), and scaling factor (SF), from first to the last row, respectively.

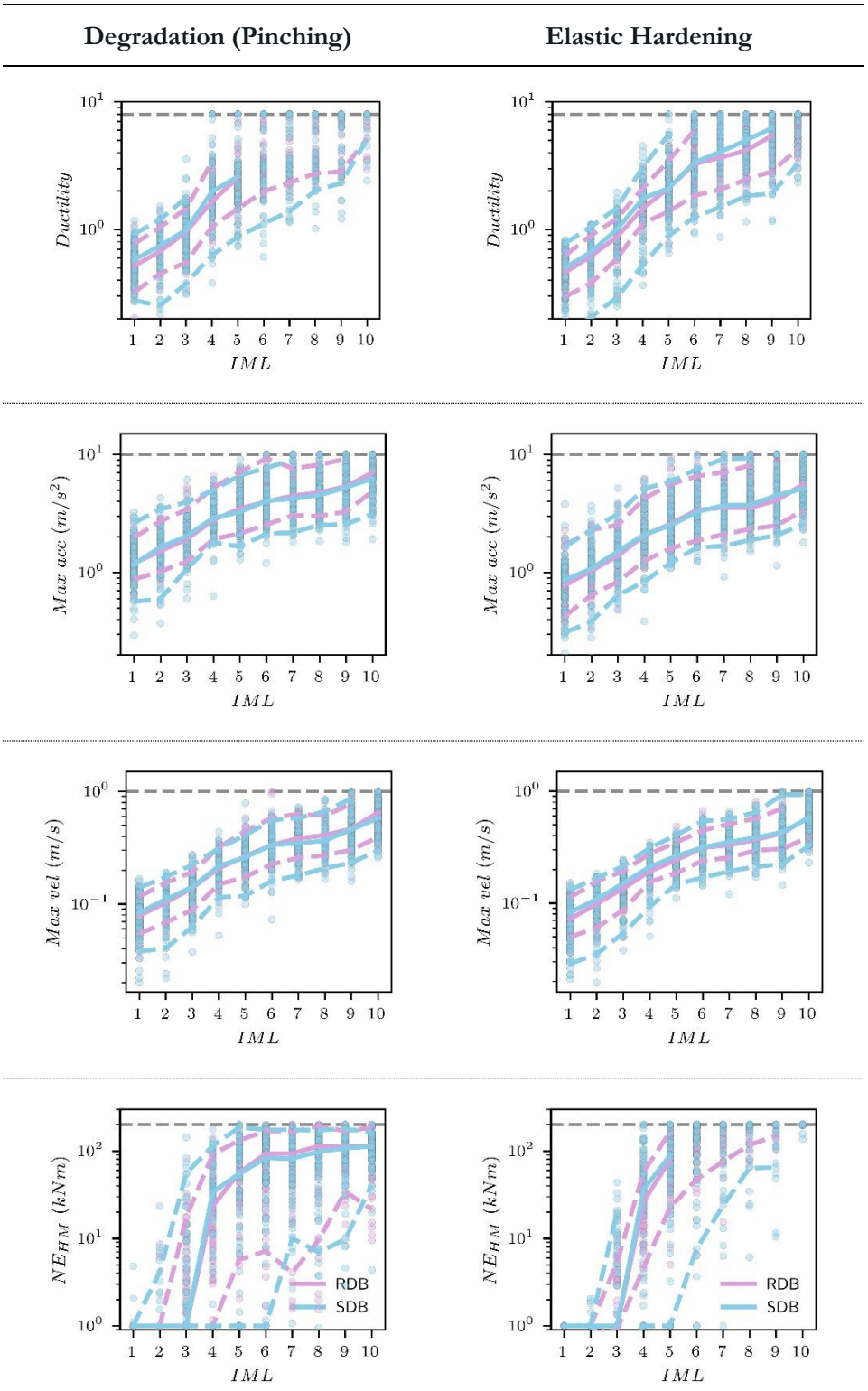

Appendix 34. EDPs obtained via NLTHA of the SDoF with $T_1 = 0.5s$ using 40 records at each IML, selected from the RDB and SDB. Ductility ratio, Peak Floor acceleration, Peak floor velocity, and dissipated energy, from first to the last row, respectively. In the figure, the median is represented by the solid line and 5th and 95th percentiles by the dashed lines.

Degradation (Pinching)	Elastic Hardening

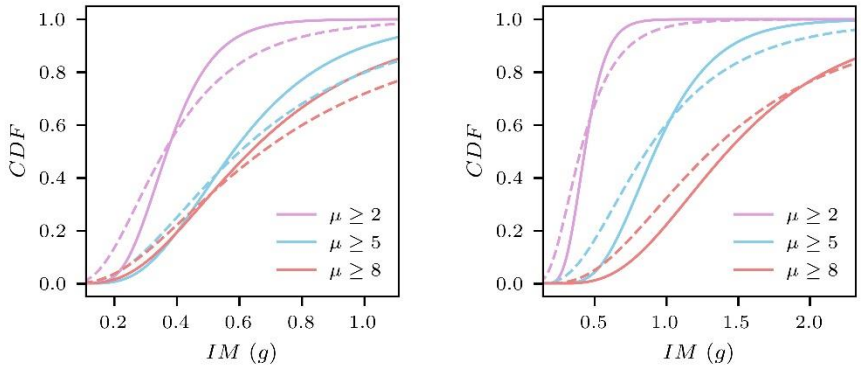

Appendix 35. Fragility curves obtained for ductility and via NLTHA of the SDoF with $T_1 = 0.5s$ using 40 records at each IML, selected from the RDB and SDB. The solid line represents the results obtained from the RDB whereas the dashed mine represents the results obtained from the SDB

Degradation (Pinching)	Elastic Hardening

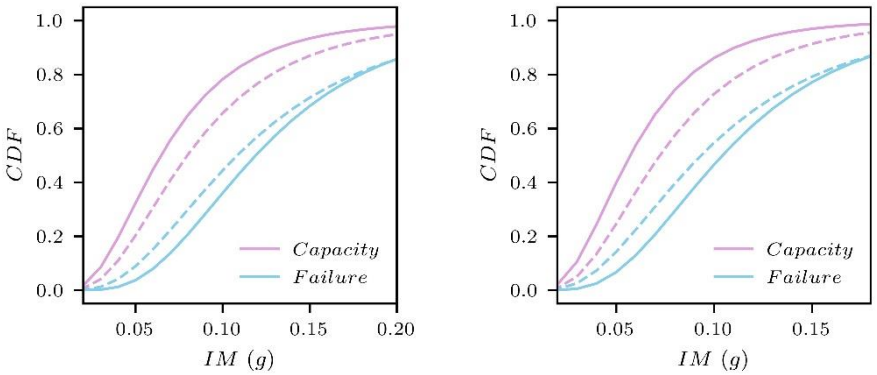

Appendix 36. Fragility curves obtained for the LVSG and via NLTHA of the SDoF with $T_1 = 0.5s$ using 40 records at each IML, selected from the RDB and SDB. The solid line represents the results obtained from the RDB whereas the dashed mine represents the results obtained from the SDB

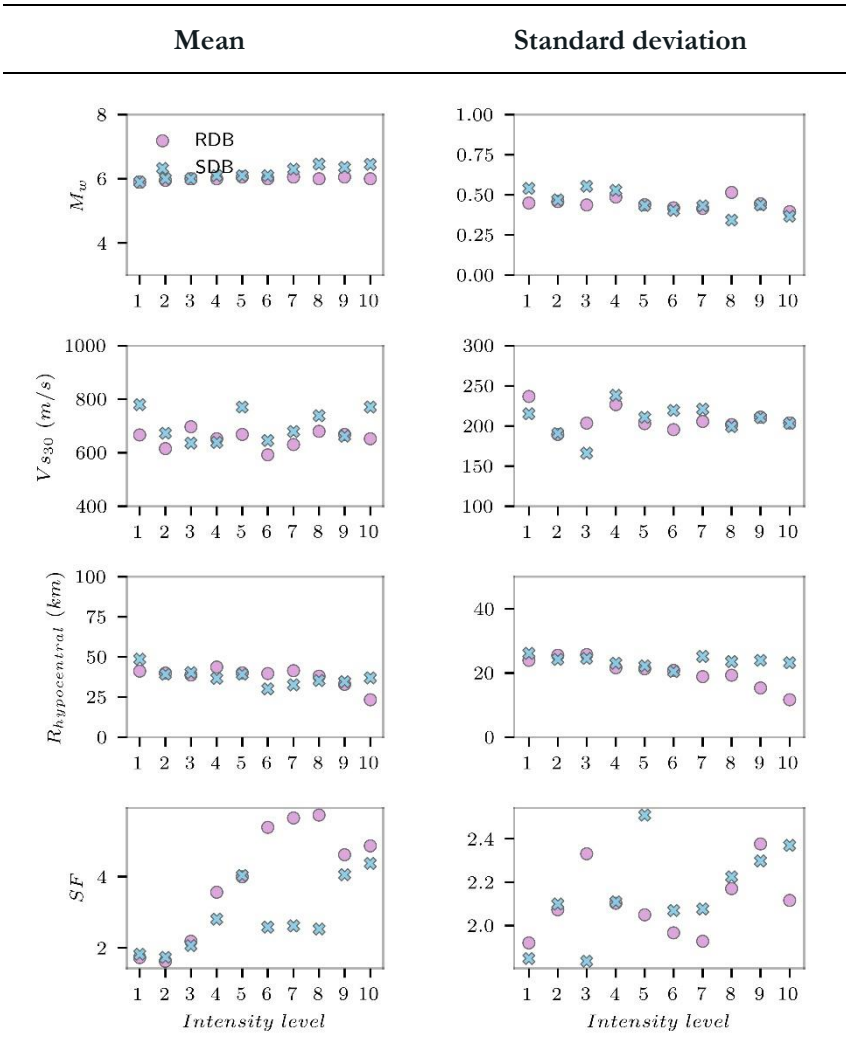

Appendix 37. Causative parameters of the CS-selected records for $Sa(T_1) = 1.0s$, namely moment magnitude (M_w), average shear propagation velocity of the upper 30m (Vs_{30}), hypocentral distance (R_{hyp}), and scaling factor (SF), from first to the last row, respectively.

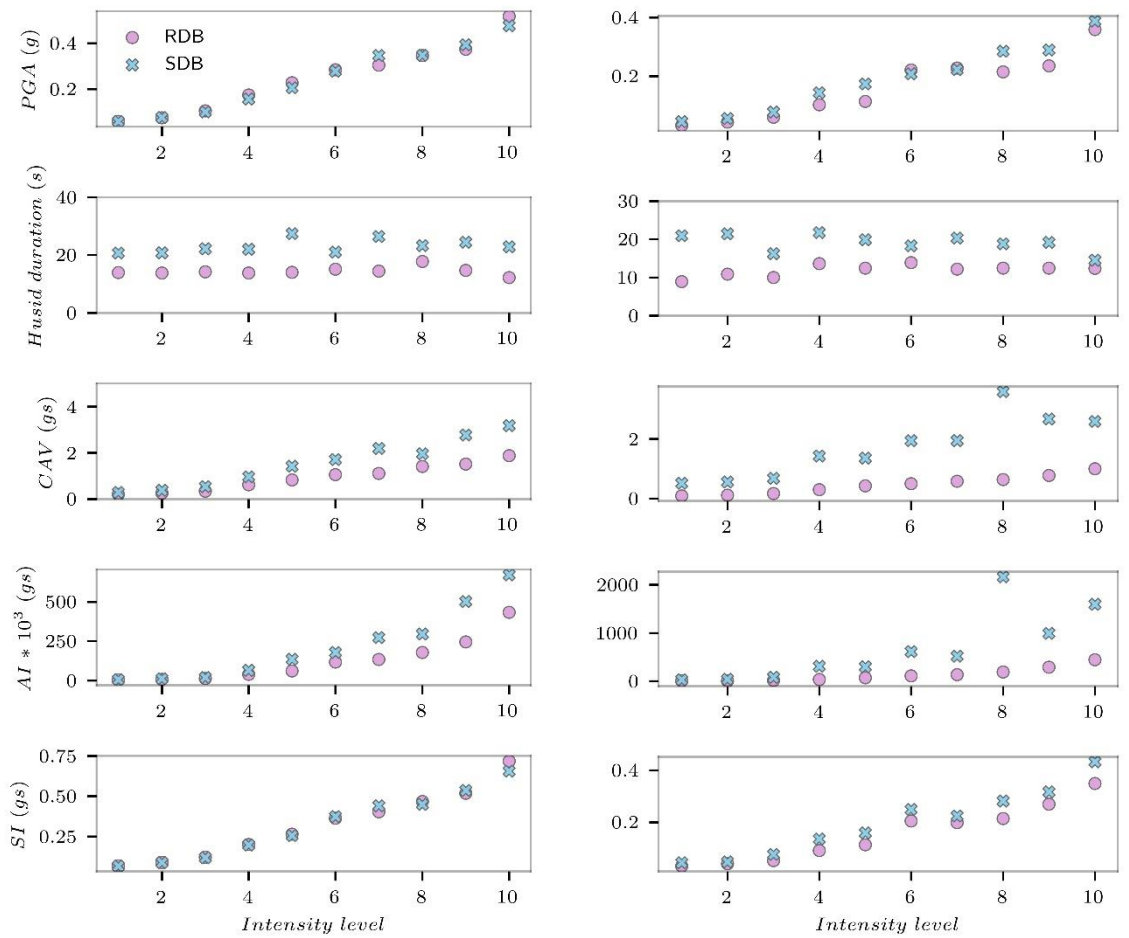

Appendix 38. IMs of the CS-selected records for $Sa(T_1) = 1.0s$, namely moment magnitude (M_w), average shear propagation velocity of the upper 30m (Vs_{30}), hypocentral distance (R_{hyp}), and scaling factor (SF), from first to the last row, respectively.

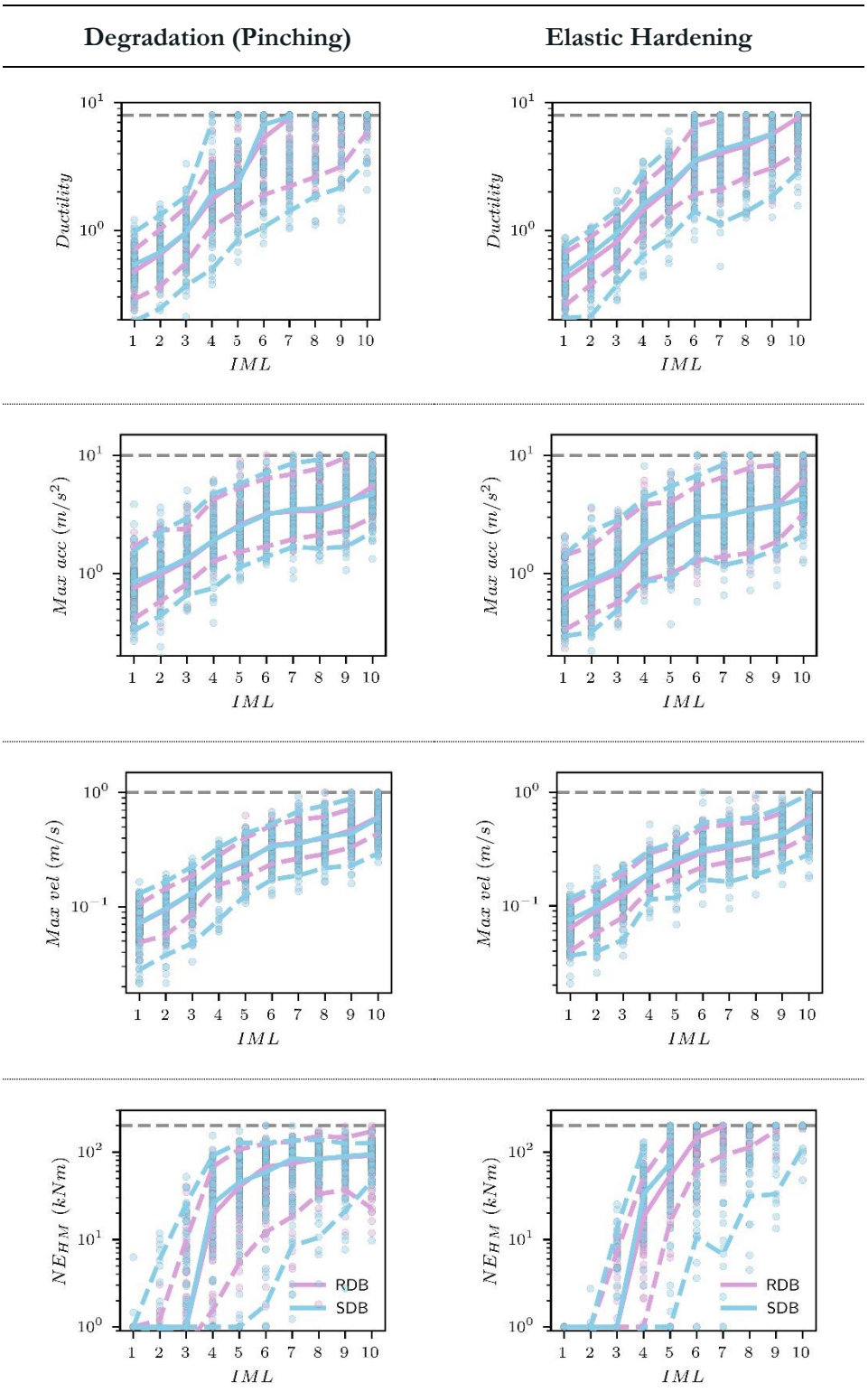

Appendix 39. EDPs obtained via NLTHA of the SDoF with $T_1 = 1.0s$ using 40 records at each IML, selected from the RDB and SDB. Ductility ratio, Peak Floor acceleration, Peak floor velocity, and dissipated energy, from first to the last row, respectively. In the figure, the median is represented by the solid line and 5th and 95th percentiles by the dashed lines.

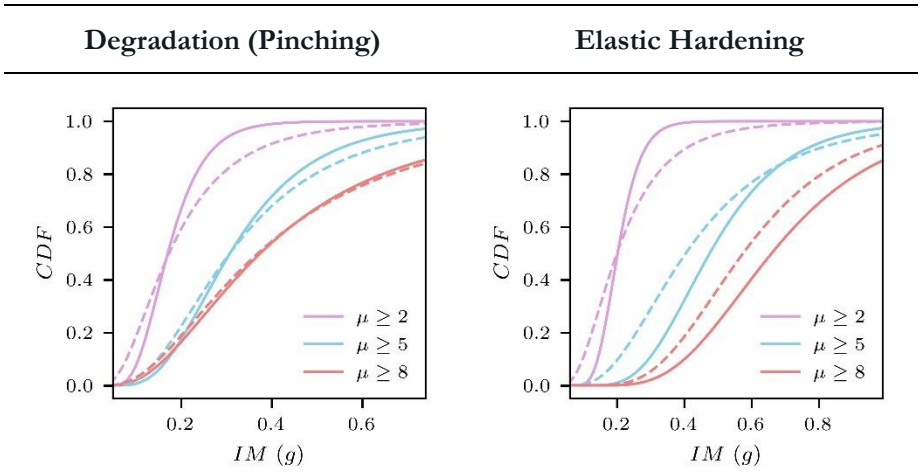

Appendix 40. Fragility curves obtained for ductility and via NLTHA of the SDoF with $T_1 = 1.0s$ using 40 records at each IML, selected from the RDB and SDB. The solid line represents the results obtained from the RDB whereas the dashed mine represents the results obtained from the SDB

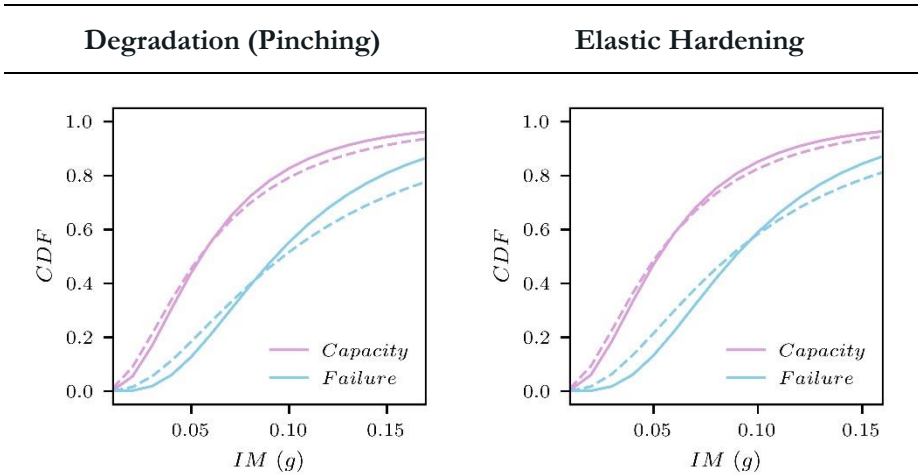

Appendix 41. Fragility curves obtained for the LVSG and via NLTHA of the SDoF with $T_1 = 1.0s$ using 40 records at each IML, selected from the RDB and SDB. The solid line represents the results obtained from the RDB whereas the dashed mine represents the results obtained from the SDB

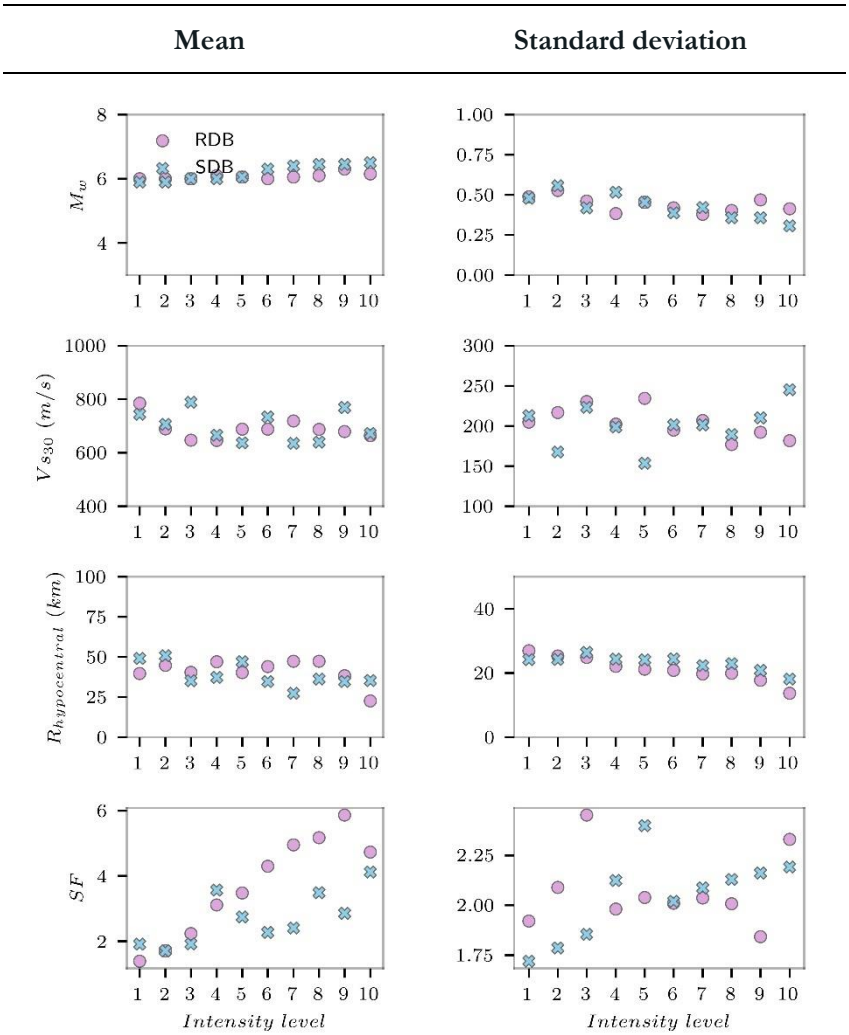

Appendix 42. Causative parameters of the CS-selected records for $Sa(T_1) = 1.50$, namely moment magnitude (M_w), average shear propagation velocity of the upper 30m (Vs_{30}), hypocentral distance (R_{hyp}), and scaling factor (SF), from first to the last row, respectively.

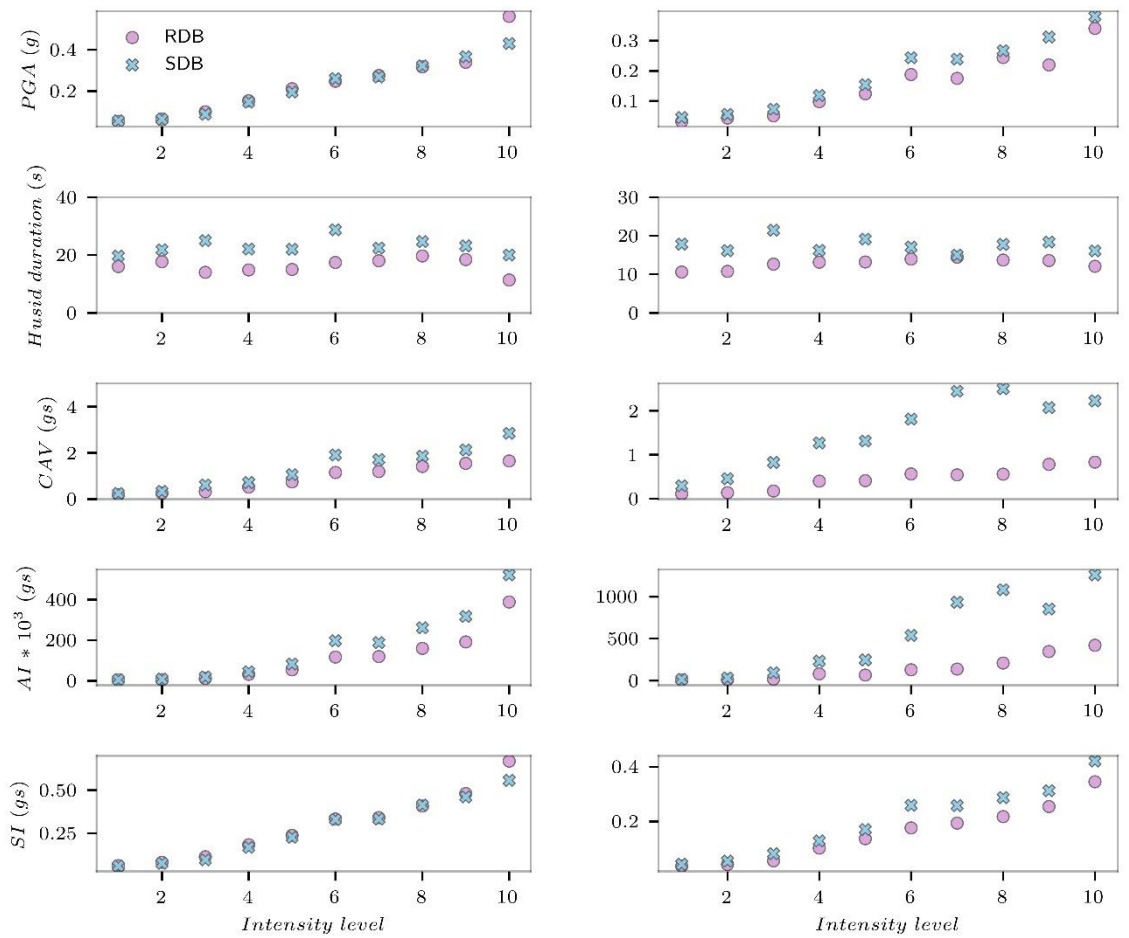

Appendix 43. IMs of the CS-selected records for $Sa(T_1) = 1.5s$, namely moment magnitude (M_w), average shear propagation velocity of the upper 30m (Vs_{30}), hypocentral distance (R_{hyp}), and scaling factor (SF), from first to the last row, respectively.

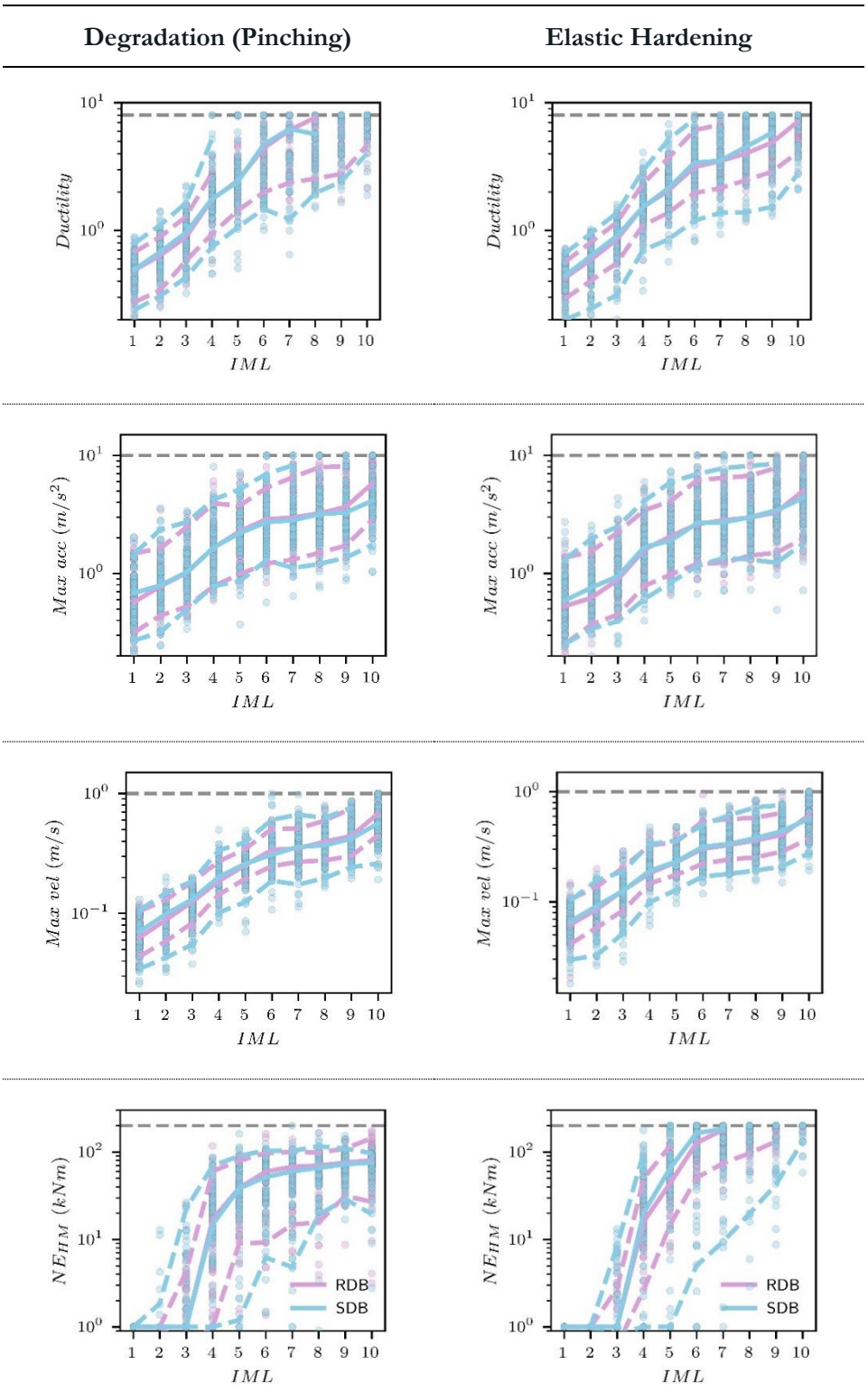

Appendix 44. EDPs obtained via NLTHA of the SDoF with $T_1 = 1.5s$ using 40 records at each IML, selected from the RDB and SDB. Ductility ratio, Peak Floor acceleration, Peak floor velocity, and dissipated energy, from first to the last row, respectively. In the figure, the median is represented by the solid line and 5th and 95th percentiles by the dashed lines.

Degradation (Pinching)	Elastic Hardening

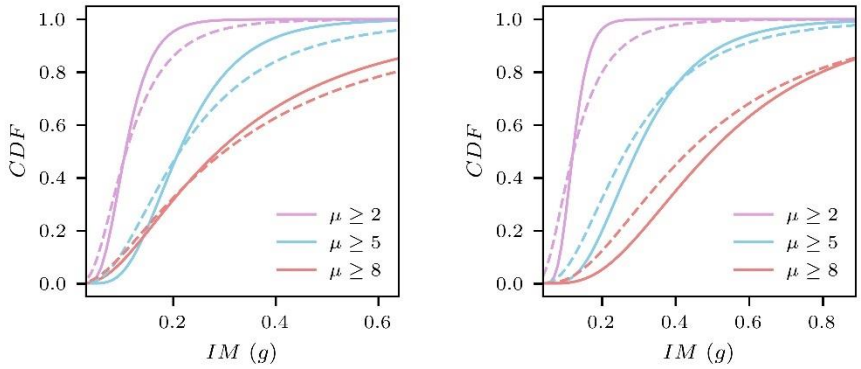

Appendix 45. Fragility curves obtained for ductility and via NLTHA of the SDoF with $T_1 = 1.5s$ using 40 records at each IML, selected from the RDB and SDB. The solid line represents the results obtained from the RDB whereas the dashed mine represents the results obtained from the SDB

Degradation (Pinching)	Elastic Hardening

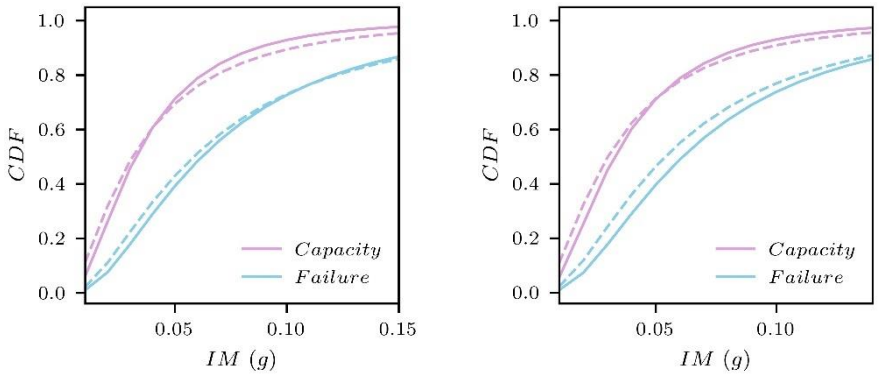

Appendix 46. Fragility curves obtained for the LVSG and via NLTHA of the SDoF with $T_1 = 1.5s$ using 40 records at each IML, selected from the RDB and SDB. The solid line represents the results obtained from the RDB whereas the dashed mine represents the results obtained from the SDB

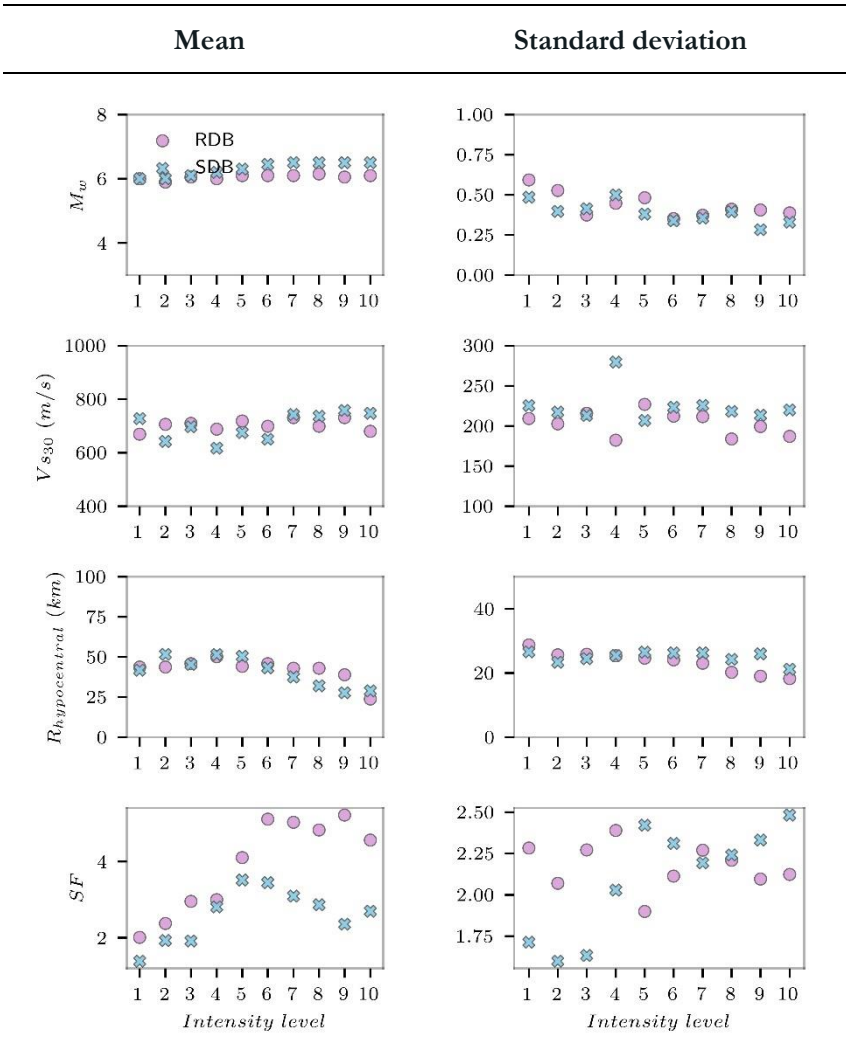

Appendix 47. Causative parameters of the CS-selected records for $Sa(T_1) = 2.0$, namely moment magnitude (M_w), average shear propagation velocity of the upper 30m (Vs_{30}), hypocentral distance (R_{hyp}), and scaling factor (SF), from first to the last row, respectively.

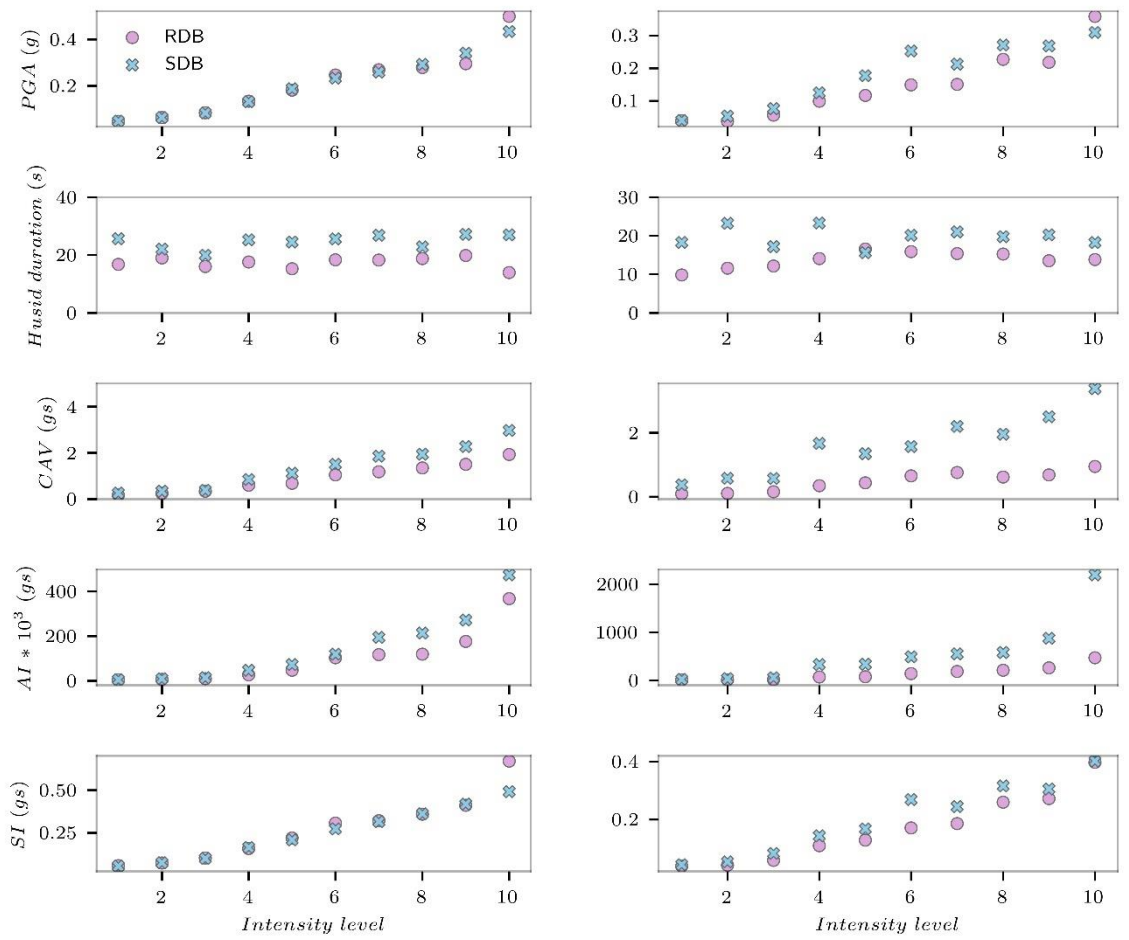

Appendix 48. IMs of the CS-selected records for $Sa(T_1) = 2.0s$, namely moment magnitude (M_w), average shear propagation velocity of the upper 30m (Vs_{30}), hypocentral distance (R_{hyp}), and scaling factor (SF), from first to the last row, respectively.

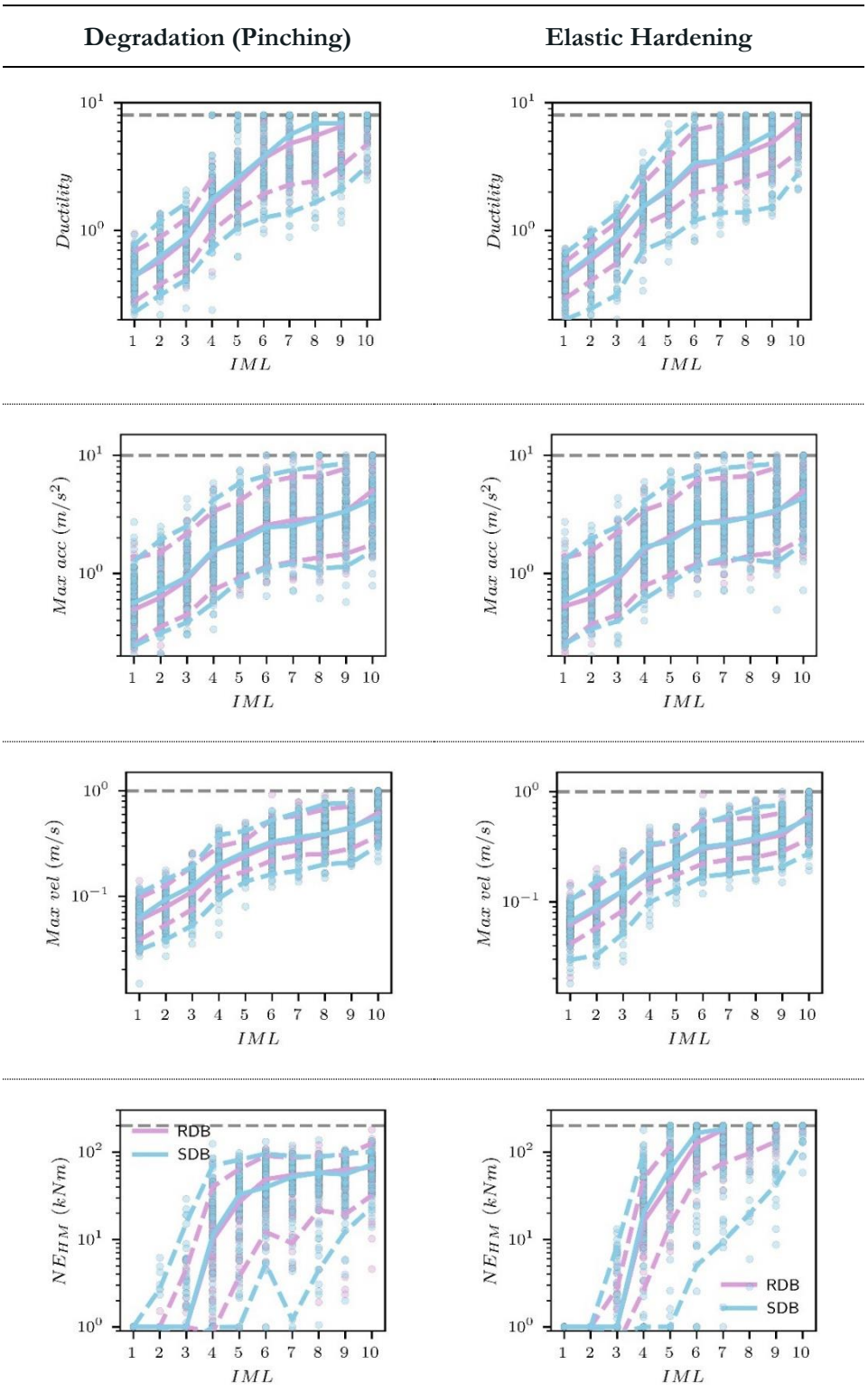

Appendix 49. EDPs obtained via NLTHA of the SDoF with $T_1 = 2.0s$ using 40 records at each IML, selected from the RDB and SDB. Ductility ratio, Peak Floor acceleration, Peak floor velocity, and dissipated energy, from first to the last row, respectively. In the figure, the median is represented by the solid line and 5th and 95th percentiles by the dashed lines.

Degradation (Pinching)	Elastic Hardening

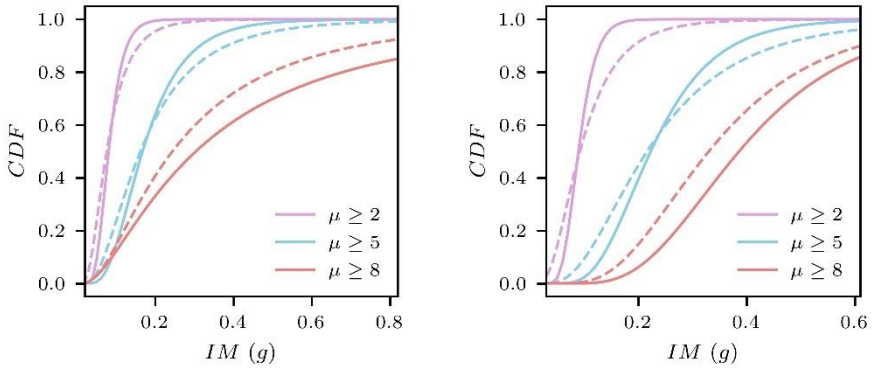

Appendix 50. Fragility curves obtained for ductility and via NLTHA of the SDoF with $T_1 = 2.0s$ using 40 records at each IML, selected from the RDB and SDB. The solid line represents the results obtained from the RDB whereas the dashed mine represents the results obtained from the SDB

Degradation (Pinching)	Elastic Hardening

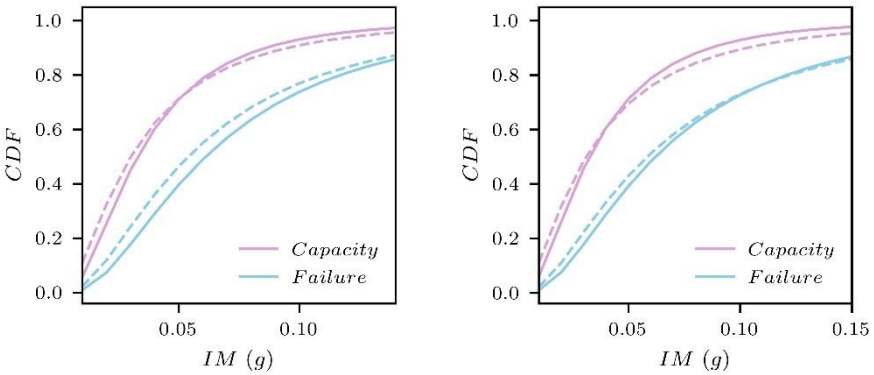

Appendix 51. Fragility curves obtained for the LVSG and via NLTHA of the SDoF with $T_1 = 2.0s$ using 40 records at each IML, selected from the RDB and SDB. The solid line represents the results obtained from the RDB whereas the dashed mine represents the results obtained from the SDB